-OptoRiboGenetics-

Post-transcriptional control of gene expression by light

Dissertation

zur

Erlangung des Doktorgrades (Dr. rer. nat.)

der

Mathematisch-Naturwissenschaftlichen Fakultät

der

Rheinischen Friedrich-Wilhelms-Universität Bonn

vorgelegt von

Sebastian Pilsl

aus

Vilshofen an der Donau

Bonn 2021

Angefertigt mit der Genehmigung der Mathematisch-Naturwissenschaftlichen Fakultät der
Rheinischen Friedrich-Wilhelms-Universität Bonn

1. Gutachter: Prof. Dr. Günter Mayer
2. Gutachter: Prof. Dr. Andreas Möglich

Tag der Promotion: 16.07.2021
Erscheinungsjahr: 2021

Parts of this dissertation have been published in:

Pilsl, S., et al., *Optoribogenetic control of regulatory RNA molecules.* Nature Communications, 2020. **11**(1): p. 4825. DOI: 10.1038/s41467-020-18673-5.

Weber, A.M., et al., *A blue light receptor that mediates RNA binding and translational regulation.* Nature chemical biology, 2019. **15**(11): p. 1085-1092. DOI: 10.1038/s41589-019-0346-y.

Content

1 Abstract

Gene expression is tightly regulated in mammalian cells at the post transcriptional level and its precise manipulation has proven to be valuable for protein overexpression and gene therapy. Implementation of light-responsive photoreceptors into gene regulatory networks has been shown to enable spatiotemporal control modalities. The discovery of the bacterial light-oxygen-voltage (LOV) photoreceptor **P**AS-**A**NTAR-**L**OV (PAL) depicts a direct link between light-control and RNA biology and, thus, led to the foundation of optoribogenetics. Light-adapted PAL binds RNA stem-loop structures in a sequence dependent manner *via* its ANTAR domain.

The control of gene expression as a function of light was achieved in mammalian cells when PAL-binding stem-loops were embedded in 5' untranslated regions (UTRs) of mRNA transcripts. Increased light-control was achieved when PAL was fused to eukaryotic translation initiation factor 4E binding protein 1 (4E-BP1), an inhibitor of cap-dependent translation. Besides these "off-switches", "on-switches" were generated when PAL-binding stem-loops replaced the apical loop domain of *pre*-micro RNAs (*pre*-miRs) or short-hairpin RNAs (shRNAs). The performance of shRNAs was improved *via* single nucleotide insertions that conjoin the small-interfering- (si-) RNA to the PAL-responsive RNA stem-loops. Such shRNAs can be designed and applied in a near-arbitrary fashion with minimal efforts as exemplified by controlling the physiologic function of several target proteins.

Taken together this thesis presents optoribogenetic methodologies which offer a hitherto unavailable access point that connects light-mediated precision with RNA biology in a genetically encodable system. These methods will facilitate the study of RNA and protein function *in vivo*. As next step, they could be used in future gene therapies or in basic research, for example to study the onset of cancer.

1 Zusammenfassung

Die Genexpression von Säugetierzellen wird maßgeblich auf post-transkriptioneller Ebene reguliert und das Eingreifen auf dieser Ebene hat sich sowohl bei der Überexpression von Proteinen als auch bei der Gentherapie bewährt. Durch das Einbringen von Fotorezeptorproteinen in derartige Genregulationsnetzwerke können Eingriffe räumlich und zeitlich präzise gesteuert werden. Bis heute ist das bakterielle Licht-Sauerstoff-Spannungs- (LOV) Fotorezeptorprotein **P**AS-**A**NTAR-**L**OV (PAL) der einzig beschriebene fotosensible Rezeptor, welcher direkt mit RNA wechselwirkt. Diese Entdeckung legte den Grundstein für die Optoribogenetik. Licht-aktiviertes PAL bindet RNA Stammschleifen sequenzabhängig durch eine veränderte Zugänglichkeit dessen ANTAR Domäne.

Eine lichtabhängige Kontrolle der Genexpression konnte durch den Einbau von PAL-bindenden RNA-Stammschleifen in den 5‘ nicht-translatierten Bereich (5’UTR) bestimmter mRNA Transkripte erreicht werden. Durch die Fusion von PAL mit dem eukaryotischen Translationsinitiationsfaktor 4E bindenden Protein 1 (4E-BP1), einem Inhibitor der Cap-abhängigen Translation, konnten die lichtabhängigen Unterschiede bei der Genexpression weiter verstärkt werden. Neben derartigen „off-switches” können auch „on-switches“ generiert werden, indem PAL-bindende RNA-Stammschleifen in die apikale Domäne von *pre*-micro RNAs (*pre*-miRs) oder short-hairpin RNAs (shRNAs) eingebaut werden. Die von den shRNA hervorgerufenen lichtabhängigen Unterschiede in der Genexpression konnte durch das Einsetzen zusätzlicher Nukleotide zwischen der small-interfering (si-) RNA und den PAL-bindenden RNA-Stammschleifen verstärkt werden. Derartige shRNAs können mit nur geringem Aufwand gegen nahezu jedes Wunschgen gerichtet werden, wie durch die Kontrolle der physiologischen Funktion von drei Zielproteinen gezeigt wurde.

Zusammengefasst beschreibt diese Dissertation optoribogenetische Methoden, welche den direkten Eingriff auf die RNA-Ebene mit der Präzision von Licht und als vollständig genetisch kodierbares System erlauben. Damit können diese Methoden zukünftige *in vivo* Untersuchungen von Abläufen auf RNA- und Proteinebene vereinfachen. Ferner könnten diese Methoden in zukünftigen Gentherapien und der Grundlagenforschung genutzt werden, beispielsweise um die Entstehung von Krebs besser verstehen zu können.

2 Introduction

Throughout progression in life sciences, fundamental knowledge was gathered by observing biological processes and our understanding has been constantly increased together with advances in detection techniques. With the development of methods for the observation of biological events at the relevant time scales such as calcium imaging [1] and size scales such as stimulated emission depletion (STED) microscopy [2], fundamental questions could be tackled. Many techniques for detection use light because it has the potential to give precise information about time and space. Contrarily, the development of light-controlled techniques for biological manipulation could not keep up with methods which have been developed for observation [3]. In one approach, photocaged compounds have been used to control biological function by light. They are generated by chemical synthesis. Subsequently, these compounds can be introduced into cells or animals [4]. Upon illumination with UV-light they become activated to control a biological event. Photocaged compounds have been applied in various fields such as neurosciences [5] or therapeutics [6]. However, the use of UV light as trigger might have disadvantages because it harms the genetic information. Therefore, organismal applications may be limited to short time periods [7].

2.1 Optogenetics

The term optogenetics summarizes approaches that combine optical methods using visible light with genetic encodability to study and control biological processes [8]. As such, no further external addition of substrates is needed. For example, light-responsive photoreceptors can be targeted to the cell membrane of neurons in alive mice [9]. These implementations can be used to control neuromodulation, and thus, the animal's behavior by light. They combine the use of light as a controllable trigger for reversible activation with the benefit that such photoreceptors can be permanently expressed. Furthermore, they enable the observation of activation effects in a distinct subpopulation of neurons [9].

2.1.1 Optogenetic technologies and applications

After the introduction of optogenetics in neuroscience, it also gained attention in various scientific fields [10]. This led to the development of many optogenetic actuators that offer broad functionality by controlling the fate of various target structures within a cell (for an overview, see **Figure 1.1**).

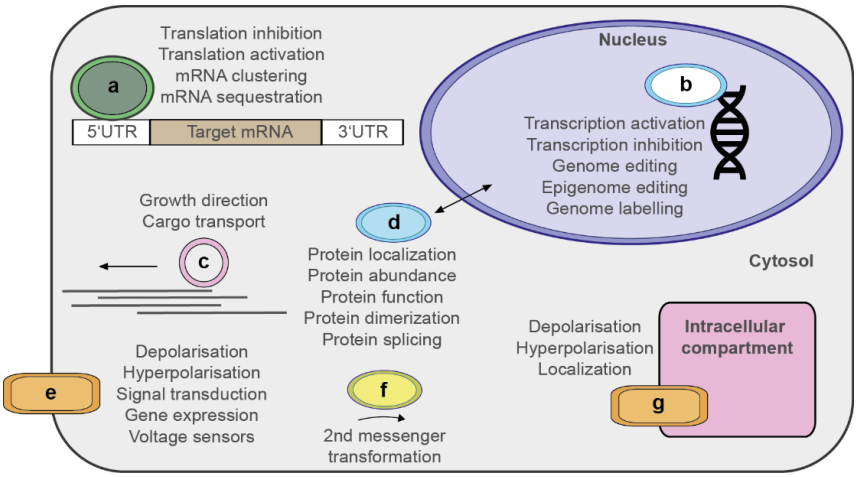

Figure 1.1: Subcellular structures as targets for optogenetic actuators and potential light-induced effects. Shown is a schematic of a mammalian cell. Optogenetic actuators (**a**-**g**) are targeted to various structures in a cell (**a**: mRNA, **b**: genomic DNA, **c**: cytoskeleton, **d**: fusion protein, **e**: cell membranes, **f**: enzymes, **g**: organelles and intracellular compartments) to gain control of distinct functions. Adapted in parts from [11].

Optogenetic membrane-bound channel proteins

First optogenetic applications in neurons of alive rodents were performed using algal channelrhodopsin-2 protein (ChR2, [9, 12]). ChR2 is a membrane-bound photoreceptor which allows blue light-induced influx of mono- and divalent cations (**Figure 1.2**, [13]). This is facilitated by conformational changes of the covalent-bound cofactor retinal which leads to channel opening and neuronal firing [13]. ChR2 was applied in different subsets of neurons for controlling various biological functions such as bladder pain or voiding [14] and ChR2 mutants were created and examined for their ability to restore vision [15, 16]. Further mutational studies revealed ChR2 variants with delayed desensitization that were suitable for the generation of long-term action potentials [17].

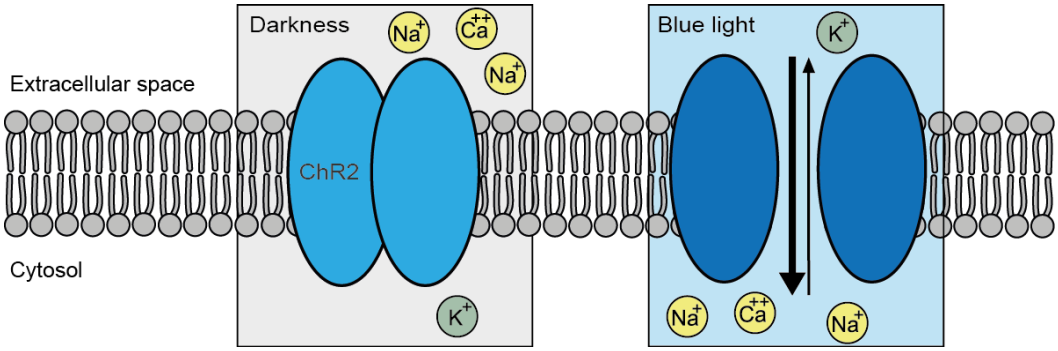

Figure 1.2: Genetically encoded channelrhodopsin 2 (ChR2) as optogenetic actuator for the control of neuronal activity. In darkness, the transmembrane protein acts as a barrier which blocks the influx of mono- and divalent cations and the efflux of potassium cations. Under blue light conditions, the protein opens a transmembrane channel which leads to the cationic flux (bold arrow: Na^+ and Ca^{++}, thin arrow: K^+) and neuronal firing. Adapted from [18].

In parallel, other channelrhodopsins with different biophysical properties were found in nature or generated artificially. Their discovery broadens the fields of application and offers the possibility for multiplexing. Dual color neural activation and behavioral control in *C. elegans* were demonstrated by simultaneous application of Chrimson, a red-shifted, proton-selective channelrhodopsin together with channelrhodopsin from *Chloromonas oogama* (CoChR), which is five times more sensitive to blue light compared to ChR2 [19]. ReaChR, an engineered ChR that can be excited with orange to red light, was successfully applied for sight restoration in blind mice [20, 21].

In turn, inhibitory synaptic potentials can be light-induced by anion conducting channelrhodopsins, such as GtACR1 or GtACR2 as demonstrated in *Drosophila* and Zebrafish for reversible silencing in neurons [22, 23]. Neuronal silencing can also be achieved by using archaeal Halorhodopsins (HRs, [24]). However, GtACRs are used more often than HRs due to increased light-responsiveness [25]. Intracellular membrane hyperpolarization can be achieved by using the light-driven proton pump archaerhodopsin-3 (Arch) [26]. When this protein is recruited to the membranes of synaptic vesicles and lysosomes, the acidification of these compartments gets light-inducible [27]. As the fluorogenic properties of the engineered Arch variants are dependent on the electrical state, these proteins can also be used as voltage indicators in parallel to optogenetic perturbations in awake animals [28-30]. Long-term inhibition could be achieved with the engineered potassium channel BLINK2 (blue-light-induced K^+ channel, [31]), for which the *Chlorella* virus potassium channel was conjoined with a photo-responsive light-oxygen-voltage 2 (LOV2-)Jα domain from *Avena sativa*. Fusion with LOV2-Jα domain renders the channel blue-light dependent. BLINK2 displays improved surface expression compared to a previously described version (BLINK1, [32]).

G-protein coupled signaling

Animal-derived opsins are G-protein coupled receptors that have a retinal-based chromophore. Retinal enables the protein's photo-responsiveness *via cis*/*trans* isomerization (**Figure 1.3**, [33, 34]). Considerable work has been done on engineering optogenetic chimeras (so-called "OptoXRs") consisting of an opsin fused to parts of G-protein coupled receptors. In this way, the targeted signal transduction pathways were made light-dependent [35]. OptoXRs were used to control G_t, G_s and G_q signaling pathways [33]. They were designed to either mimic endogenous receptor activity closely or to display altered signaling properties [36]. Besides from engineering of receptor chimeras, transgene expression of opsins also enables light-responsive signaling networks. This was shown by the introduction of melanopsin (Opn4) into cardiomyocytes for the investigation of G_q signaling in heart function [37]. Alternatively, the introduction of jellyfish opsin (JellyOp) into these cells enabled optogenetic control of the G_s signaling cascade [34].

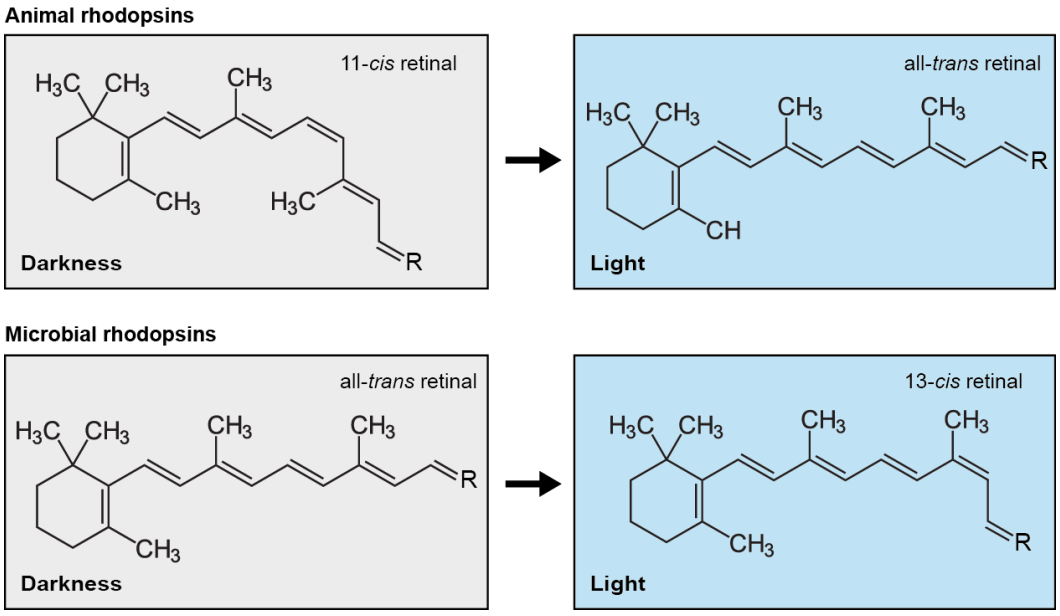

Figure 1.3: Retinal is the chromophore in rhodopsins. In animal rhodopsin, light absorption leads to the isomerization of 11-*cis* to all-*trans* retinal. In microbial rhodopsin, light absorption leads to the isomerization of all-*trans* to 13-*cis* retinal. R: The protein rest is coupled to the retinal *via* Schiff base linkage between an aldehyde group of retinal and a specific lysine residue. Adapted from [38] and [39].

One advantage of controlling signal transduction cascades at the receptor level is the amplification of the input signal [40]. Consequently, lower doses of input signal are needed when light-regulation occurs at early steps of signal transduction.

Light-activated enzymes for second messenger production

Downstream to the receptors, enzymes that produce second messenger molecules amplify the input signal. Optical control of these enzymes might be of relevance when the role of distinct second messengers should be studied and the direct activation of the upstream receptor would lead to unwanted side reactions [41]. For example, photoactivated adenylyl cyclase which originates from *Beggiatoa* (bPAC) was introduced into sperm cilia cells of mice to study the role of cyclic AMP (cAMP) in motility and fertilization [42]. Photo-responsiveness in bPAC is assured by a BLUF (sensors of blue-light using FAD) domain which harbors a flavin adenine dinucleotide (FAD) molecule as light-sensing co-factor [43]. However, with a penetration depth of 1 mm (**Figure 1.4**), blue light does not reach deep tissue [44]. For applications which require >5 mm penetration of tissue by light, bacteriophytochrome-based tools were applied [45]. Bacteriophytochrome-based tools are capable of sensing near-infrared light which penetrates tissue deeper than visible and UV light [45]. In these proteins, near-infrared light is sensed by the co-factor biliverdin Ixα. Likewise, a bacteriophytochrome coupled diguanylate cyclase was engineered to be capable of photoactivating the synthesis of cyclic dimeric GMP (c-di-GMP) from GTP [46]. Also, the hydrolysis of the second messengers cAMP and cGMP can be controlled by a light-activated phosphodiesterase (LAPD) in CHO cells and zebrafish embryos [47].

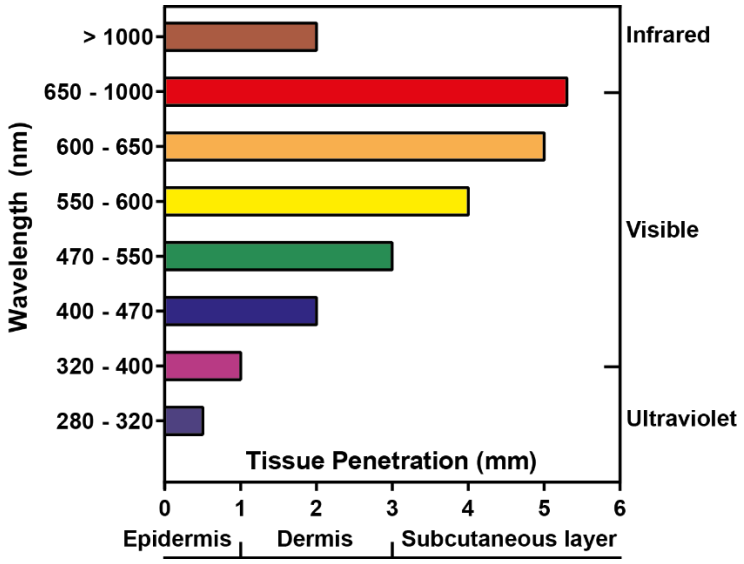

Figure 1.4: The tissue penetration by light depends on the wavelength. The thickness of the three different layers of the human skin is indicated (left to right: exterior to interior). Adapted from [44] and [48].

LOV-based protein activation, localization, and abundance

Besides the control of signal transduction pathways, the function of distinct proteins and peptides can be also controlled by light. The activity, localization and abundance can be light-controlled by fusing the target peptide or protein to LOV-based photo-responsive protein domains (**Figure 1.5**, [49-51]). For example, the GTPases Rac1 and RhoA are involved in cytoskeletal dynamics, which controls cell movement [52-54]. Fusion of Rac1 to a LOV-domain rendered Rac1 signaling and the cell movement responsive to blue light [52]. This was achieved by controlling either the activation (PA-Rac1, [52]) or the membrane recruitment of Rac1 (Opto-Rac1 [53]). Two complementary studies described the light-control of protein localization by fusion of the target protein to a LOV2 domain, originating from *Avena sativa* (AsLOV). The exposure of mammalian cells to blue light induced LOV2-mediated unfolding of the J-α helix that either unmasked a nuclear export or a nuclear import signal leading to controlled protein localization [50, 55]. In another approach, protein abundance was controlled by photoactivated protein degradation. In this case, a photosensitive degradation-inducing (degron) module was fused to a LOV2 domain from *Arabidopsis thaliana* and a target protein of interest [51]. Under blue light, degron-mediated ubiquitin-independent proteasomal degradation took place for the respective fusion protein [51].

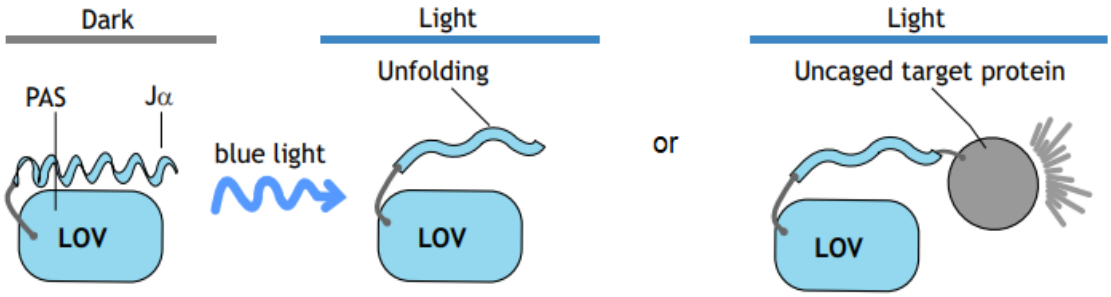

Figure 1.5: Mechanism of light-regulation in LOV-based proteins. In darkness, the Jα helix is closely aligned to a LOV domain. The irradiation with blue light induces the unfolding of the Jα helix. LOV-based proteins can be fused to target proteins and peptides (e.g. GTPase RAC1, nuclear export/import signals or degron modules) which become uncaged and activated under blue light conditions. Adapted from [56].

Strickland *et al.* constructed tunable light-inducible dimerization tags (TULIPs). Here, the light-dependent interaction of an AsLOV domain with an engineered PDZ domain was harnessed to induce a protein interaction. In this way, the protein was recruited to the cell membrane to light-control cell polarization in yeast [57].

2.1.2 Light-dependent control of gene expression in mammalian cells

As shown above, protein and peptide function can be controlled directly by light. Additionally, the expression of proteins itself can be light-controlled to study their function and to control cellular fate and physiological behavior [58-63]. Synthetic signaling cascades were engineered to gain light-control of gene expression. In one example, the membrane-bound photoreceptor OPN4 was used to light-control a downstream genetic network for the expression of glucagon-like peptide 1 (**Figure 1.7**, [58]). When this strategy was applied, glycemic excursions in mice could be prevented [58].

Light-control of transcription *via* engineered signal transduction was also achieved in bacteria. Recruitment of transcription factor FixJ to a target DNA locus could be induced by the engineered light-responsive histidine-kinase YF-1, which activates FixJ upon phosphorylation (**Figure 1.7** ,[59]). Several applications were developed in which the transcription was directly controlled by light. Most of them are based on the recruitment of DNA-binding proteins Gal4 or TetR to their DNA-binding sites in mammalian cells [64]. Gal4 and TetR were fused to additional factors that are capable to interact with their interaction partners. Upon light-irradiation, this strategy enables the recruitment of transcription factors such as VP16 ([60, 65], VP64 [66] and p65 [61] which then induce gene transcription (**Figure 1.7**). Alternatively, transcriptional repressors such as KRAB (Krüppel associated box) or tryptophan-repressor from *E. coli* [67, 68] were utilized to repress transcription [62]. In all these cases, tethering of transcription factors for gene targeting was mediated by the photo-responsive interaction of a protein pair. One protein component is constitutively anchored to a DNA-binding site which is located near the target gene locus. The other protein was fused to transcription factors and bound its counterpart under light conditions.

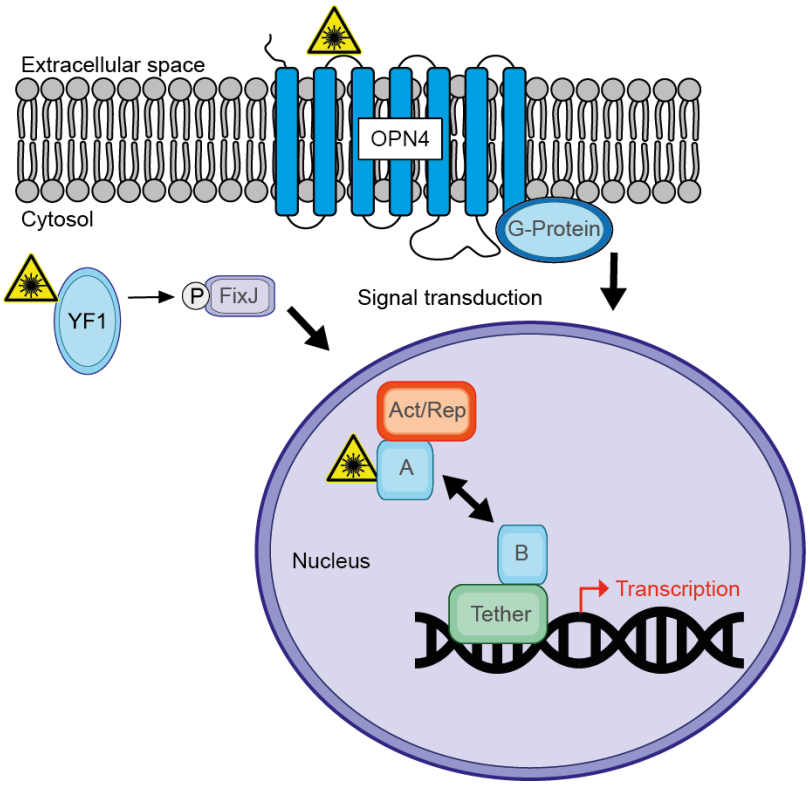

Figure 1.6: Strategies for the light-control of gene expression. Signal transduction cascades can be induced upon light-activation of membrane-bound optogenetic actuators (OPN4) by G-protein mediated signaling. In the cytosol, signal transduction can be achieved *via* light-activated phosphorylation of transcription factors (FixJ) by kinases (YF1). In the nucleus, the interaction of a light-responsive protein pair (depicted as A and B) leads to the recruitment of transcription factors which can induce transcriptional activation or repression (Act/Rep). The recruitment of the system to the DNA is ensured by a DNA-tether protein fused to one of the light-responsive proteins. The light-activation of optogenetic actuators is indicated by a yellow laser sign. Adapted from [58-60].

Water-soluble protein pairs consisting of phytochromes (Phy) and phytochrome interacting factors (PIFs) were used to control gene expression [64]. Their interaction is inducible upon illumination with red light and can be reverted by far-red light, a behavior that is routinely utilized for tethering transcription factors to target gene loci or bringing protein fractions in proximity. Phytochromes incorporate linear tetrapyrrole rings as their chromophores. In bacteria or fungi, biliverdin IXα is used, whereas plants use phytochromobilin as a chromophore [69]. Phytochromobilin is not present in eukaryotic cells and therefore must be supplemented [69]. Frequently, cryptochrome (CRY) proteins are used for the control of gene expression with blue light. They can be found in plants and in animals [70]. In these proteins, light-responsiveness is mediated by a flavin-binding PAS-domain that is closely related to BLUF domains which can be found in bacteria and lower eukaryotes [71]. In BLUFs, a hydrogen bond is formed with FAD upon light-irradiation, whereas CRYs undergo a redox reaction with their co-factor [70, 71]. CRY proteins are known for their ability to dimerize to hetero- and homodimers [72]. In plants, CRY2 interacts with the transcription factor cryptochrome-interacting basic-helix-loop-helix (CIB1) and a truncated version thereof was developed for optogenetic applications (CIBN, [73]). This system was expanded with mammalian transcription factors and used to gain light-control of Cre recombinase expression [73], an enzyme that is used for the generation of gene knock in and knock out animals [74].

Alternatively, LOV-based photosensory modules were used for the light-induced manipulation of gene expression. The formation of a protein-flavin adduct under light conditions induces a conformational change in this protein (**Figure 1.7**, [75]).

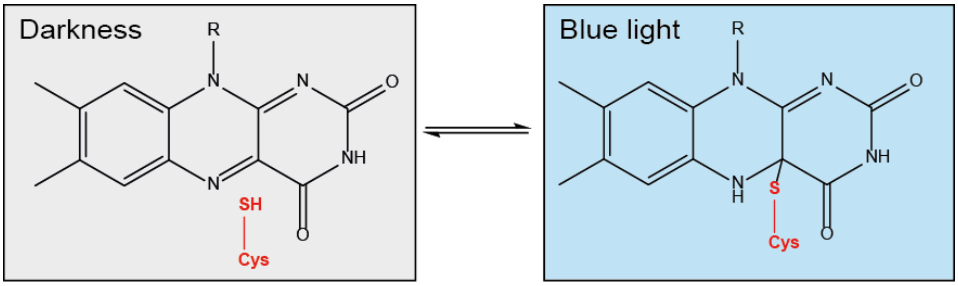

Figure 1.7: Photocycle in LOV domains. In darkness, the cofactor FMN is bound non-covalently to the LOV domain. Under blue light conditions a covalent bond formation occurs between a cysteine of the LOV protein (red: Thiol group from the reacting cysteine) and the C4a position of the isoalloxazine ring of FMN. The reaction is reverted when the LOV domain returns to its dark-adapted state [76].

Some LOV-proteins feature this light-responsiveness with the ability to bind to DNA. For example, the fungal flavoprotein Vivid (VVD) is capable to form a homodimer upon blue-light exposure [77]. VVD was fused to a dimerization-deficient variant of Gal4 [74]. Irradiation with blue light led to the homo-dimerization of the Gal4-VVD fusion protein and, thus, restored the protein's ability to bind to DNA. The additional modification of Gal4-VVD with the transcription activators p65 or VP16 enabled the light-control of transcription [74, 77]. Another example is EL222, which consists of a LOV-domain and a helix-turn-helix (HTH) domain that is unmasked from a bound Jα-helix upon light exposure [78]. This leads to the homo-dimerization of the protein which enables DNA-binding *via* the HTH domain. Similar to Gal4-VVD, EL222 was fused to transcription activators and EL222 used subsequently to control transcription in zebrafish [78].

As the application of these systems is limited to distinct DNA binding sites for transcription activation or repression, more generally applicable approaches were developed. Such approaches allow for programmable targeting of DNA sequences [79]. Initially, this was demonstrated by using transcription activator-like effector nucleases (TALEN). Furthermore, TALENs were conjoined with enzymes which introduce epigenetic modifications at the targeted genetic locus [63]. However, the application of TALE requires protein engineering. One alternative to this approach would be the CRISPR-CAS (Clustered Regularly Interspaced Short Palindromic Repeats) system, which allows for programmable DNA targeting by a short guide RNA sequence [80]. Due to the simplicity, CRISPR-CAS technology has been widely applied for genetic targeting [50, 81].

Optogenetic control of translation

Optogenetic control of translation is barely described in literature. One innovative approach capitalizes on the recruitment of the eukaryotic translation initiation factor 4E (eIF4E) which induces the translation of a target mRNA (**Figure 1.8**, [82]). Light responsiveness was introduced by a CRY2-CIBN protein pair which is capable to interact under light exposure [82]. The binding to mRNA was achieved by fusion of CIBN to a protein tether that constitutively interacts either with boxB aptamers or with PUF domains that were incorporated upstream to the RNA coding region of interest [82, 83]. In these cases, the translation was increased by light-dependent recruitment of CRY2 which was fused to eIF4E [82, 83].

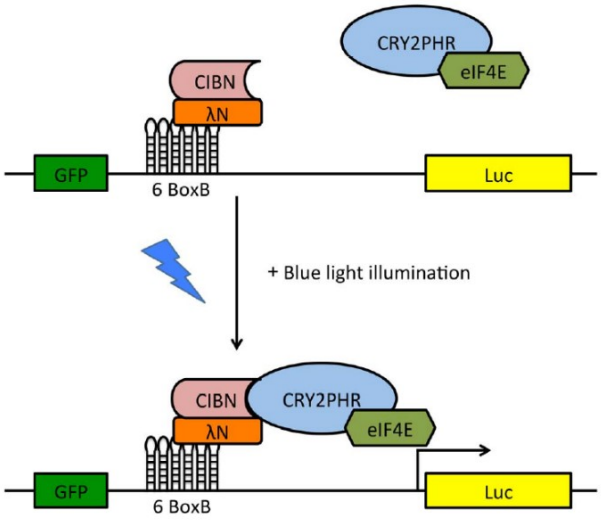

Figure 1.8: Light-induced activation of translation *via* recruitment of eIF4E. A target mRNA is modified with six boxB aptamers which interact constitutively with the λN peptide fused to CIBN. In darkness, CRY2PHR fused to eIF4E is not recruited to the mRNA. Under light conditions, CRY2PHR-eIF4E interacts with CIBN which induces the translation of luciferase (Luc), whereas GFP is translated irrespective to the light state. λN: λ bacteriophage antiterminator protein N. CIBN: NLS-deficient truncated version of the CIB1 protein. CRY2PHR: N-terminal photolyase homology region of *A. thaliana* Cryptochrome 2 protein. Adapted from [82].

In another approach, termed mRNA-light-activated reversible inactivation by assembled trap (mRNA-LARIAT), the light interaction of CRY2-CIB1 was harnessed to induce mRNA clustering and, thereby inhibiting translation [84, 85]. Here, mRNA molecules were anchored by a GFP tagged MS2 coat protein (MCP) which binds to MS2 aptamers embedded in the mRNA sequence of interest. Additionally, the GFP protein was constitutively bound by a GFP nanobody which was conjoined with the CRY2 protein. Upon exposure to light, the cluster formation was induced *via* the light-induced interaction of CRY2 with CIB1 which was fused to a multimeric protein (MP) [84]. However, these tools are not suited for viral delivery, because they consist of many functional protein domains which need to be encoded on large genetic fragments. Therefore, they exceed the maximal packing load of AAVs, which tolerate only up to 8.7 kilobase pairs [86]. Few optogenetic systems to control gene expression were reused by others.

Partially, this is owed to the lack of simple applicability and the potential for targeting endogenous genes in a programmable manner which should be key considerations for developing these systems [11].

2.2 Synthetic gene expression in mammalian cells

A great number of synthetic gene expression circuits have been developed to address a large variety of potential applications [87, 88]. For example, synthetic genetic circuits have been developed to create oscillating networks [89] and logic gates which can be used to create artificial biocomputers [90]. Furthermore, they have been developed for tumor diagnosis, tumor cell- and gene-based therapy and drug delivery [88]. In many of these approaches, known biological elements have been rearranged to obtain networks with novel functionalities.

2.2.1 RNA aptamers and their expression in mammalian cells

Aptamers are relatively short (~20-80 nts [91]) single-stranded nucleic acid sequences that fold into distinct three-dimensional structures [92]. Similar to other affinity reagents such as antibodies, aptamers bind their target ligands with high specificity and affinity that can surpass the nanomolar-range [93]. Aptamers are identified by an *in vitro* selection procedure called Systematic Evolution of Ligands by Exponential Enrichment (SELEX, [94, 95]). Through a cyclic process of binding, retention and elution, SELEX enriches candidate aptamer molecules from an initial pool of up to 10^{15} sequences that are subsequently identified by sequencing [96]. By using SELEX, RNA aptamers were identified with the capability to bind to small target structures with the size of single ions [97], small molecules [98], macromolecules [99] or to complex targets such as cell subpopulations [100]. Advantageously, the SELEX procedure for RNA aptamer selection can be largely automated and parallelized [101]. Downstream high-throughput evaluation methods such as Next Generation Sequencing (NGS, [96, 102]) allow deep insight into the SELEX procedure.

Classical antibodies are not suited for the reductive intracellular environment, which may lead to misfolding and loss of functionality. To circumvent this, engineered antibodies, so-called intrabodies were developed. However, most of them suffer from low expression levels [103]. Today's approach consists of a single heavy chain-only antibody fragment from *Camelidae*, termed nanobodies. These tools work considerably well and can be light-controlled [104], but they necessitate transgenic protein translation which requires high energy consumption [105]. This might impact cellular physiology which renders them less useful for specific applications, e.g. the investigation of energy homeostasis. As described above, RNA aptamers are identified *de novo* by SELEX and their selection conditions is tailored to meet the specific conditions in which the aptamer is capable to bind. RNA aptamers which were engineered for intracellular environments (so-called intramers) were selected under precise ion concentrations that mimic the intracellular environment [106]. Since a pioneering study has shown that transgenic RNA could alter HIV virus replication in 1990 [107], just few intramers were described in the literature. Intramers are delivered to cells by RNA transfection or through a patch-clamp pipette [108].

Alternatively, they are expressed following plasmid transfection, where the RNA expression level is set under the control of RNA polymerase II or III dependent promoters [109, 110]. Other delivery options are microinjection [111], a delivery with nanoparticles [112] or viral transduction using engineered adeno-associated viruses (AAVs, [110]), lentiviruses [113] or vaccina viruses [114]. One future goal would certainly be a direct uptake and cytosolic delivery of RNA by distinct RNA sequences [115].

Seminal studies attempted to control the function of RNA intramers, either *via* allosteric aptamers [116] or catalytically active RNA moieties (e.g. self-cleaving ribozymes, [117, 118]). The stability of RNA intramers could be enhanced by using tRNA scaffolds [119] or, recently, by expression systems that feature RNA circularization [120]. RNA circularization will greatly enhance intramer applicability in the future due to increased stability as they cannot be degraded by exonucleases. Intramers were employed to manipulate biological functions of a cell such as signaling [120] or to develop small molecule inhibitor screening platforms [121]. They were engineered to target a variety of ligands such as nucleic acid binding proteins (p50 subdomain of the transcription factor NFκB or yeast Polymerase II, [122, 123]), kinases (ERK1/2, [124]), guanine nucleotide exchange factors (Sec7 domain of Cytohesin1 [125]), *pre*-mRNA splicing proteins (B52, [126]) and metabolites (ADP and SAM [127, 128]), thereby addressing different cellular compartments. Besides the functionalities named above, intramers which bind exogenously added or transgenic target moieties were applied for the construction of orthogonal pathways in eukaryotic cells. Prominent examples are intramers which bind to theophylline [129], tetR [116], tetracycline [130] and the bacteriophage MS2 coat protein [131]. They were applied to control mRNA visualization [132] and gene expression by various means such as transcription [133], translation [130], *pre*-mRNA splicing [134], editing [135], and *pri*- or *pre*-miR processing [136, 137].

2.2.2 Artificial control of Transcription

Most approaches for synthetic control of gene expression act on the transcriptional level [138]. To gain control of transcription, effector proteins such as the Tet Repressor Protein (TetR) or Gal4 can be directly tethered to DNA target loci to activate or repress transcription [139]. In case of TetR, binding to DNA is reversed upon addition of tetracycline or doxocycline which both bind TetR (**Figure 1.9a**, [139]). When TetR is fused to transcription factors such as VP16, binding of the fusion protein to DNA leads to the activation of transcription [139]. This so-called tetracycline dependent transactivator (tTA) is targeted to Tet Response Elements (TRE) which are embedded usually close to promoter sequences [116]. Using rationally designed RNA modules such as the theophylline responsive TetR aptamer, the transcription of target loci can be also reversed by addition of theophylline (**Figure 1.9b**, [116]). In this case, the presence of theophylline leads to the interaction of the TetR aptamer with tTA. Based on random mutagenesis the binding behavior of tTA to DNA could was reversed. The reverse tTA (rtTA) protein enables tetracycline-dependent binding to DNA which leads to transcription activation in presence of the ligand (**Figure 1.9c**, [140]).

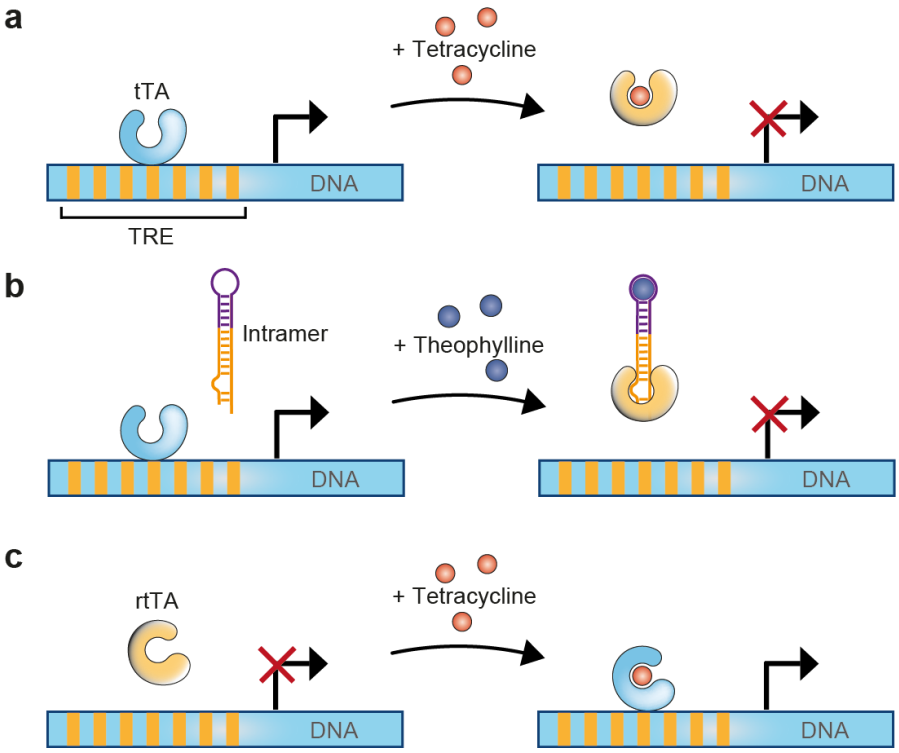

Figure 1.9: Conditional control of transcription by small-molecule responsive protein-promoter interactions. Binding of the tetracycline-controlled transactivator (tTA) or the reverse tetracycline-controlled transactivator (rtTA) to the tetracycline response element (TRE) leads to transcriptional activation. **a**, In absence of tetracycline, tTA binds the TRE region of a DNA strand. When tetracycline is added, tTA binds its ligand and dissociates from the TRE. **b**, In absence of theophylline, the theophylline-responsive TetR aptamer (Intramer) does not bind to tTA. When theophylline is added, the TetR aptamer structure is restored. Consequently, the intramer binds to tTA which dissociates from the TRE. **c**, In absence of tetracycline, rtTA does not bind to the DNA. When tetracycline is added the interaction of rtTA and TRE is restored. Adapted from [116].

As an alternative to ligand-dependent binding to DNA, such an interaction can also be controlled by light to overcome the limited applicability of small molecules to organisms (**Figure 1.6**, [66]). In addition to the above-mentioned tethers which bind DNA at distinct loci, several approaches enable DNA-tethering in a programmable manner using protein domain engineering. To this end, Zinc-Finger (ZF) proteins have been used [141]. More than 140 ZF proteins domains have been described which all target different DNA loci [142]. Alternatively, Transcription Activator-Like Effectors (TALEs) have been applied. These proteins consist of 34-amino acid repeats which target single nucleotides [142]. They can be arranged to target virtually any DNA sequence of interest. Both ZFs and TALEs capitalize on protein engineering. As a powerful alternative, CRISPR-Cas systems were repurposed for genetic engineering. These systems can be tethered to distinct DNA loci *via* an associated guide RNA (gRNA) sequence [143]. In this way, Cas proteins can be recruited to the DNA sequence of interest [144]. CRISPR-based tools were applied for genome and epigenome editing [143], transcription activation or repression [145] and imaging of DNA and RNA loci [146]. However, given the large coding size of CRISPR-Cas9 based systems, viral transduction remains challenging. Nevertheless, AAV-based delivery can be realized *via* split-Cas9 systems which divide the required genetic information over two AAV vectors [147].

2.2.3 Artificial control of mRNA translation

Transcription in mammalian cells takes place in the nucleus [148]. To control gene expression in the cytosol, artificial regulation of mRNA translation can be conducted. Researchers continue to incorporate a great variety of aptamers into the 5'UTR of mRNAs of interest to control translation by binding of the aptamers to their ligands. The aptamer incorporation in the 5'UTR was studied with respect to the relative positioning in the 5'UTR, suggesting that the translation is mostly inhibited when aptamers are embedded near the cap structure rather than the start codon [149, 150]. Contrariwise, the positioning of the tetracycline aptamer (free energy = -16.5 kcal/mol) close to the start codon already in absence of the ligand led to a more efficient translational suppression compared to positioning near the cap structure [130]. Depending on the positioning on the mRNA's 5'UTR, it was suggested that the aptamer either interferes with cap binding of eIF4F or with ribosomal scanning mediated by the 43S preinitiation complex (**Figure 1.10**, [130]).

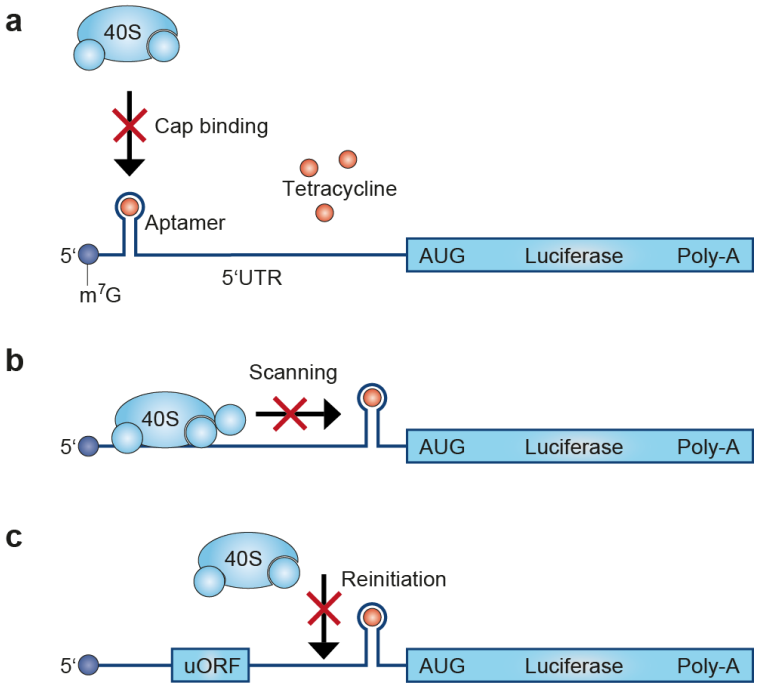

Figure 1.10: The positioning of the tetracycline-dependent aptamer inhibits translation initiation at different steps. Inhibition of translation initiation can only be observed in presence of tetracycline. **a**, A cap-proximal insertion of the aptamer prevents the small ribosomal subunit (40S) from binding to the cap structure (m^7G) of the mRNA. **b**, A cap-distal insertion of the aptamer interferes with ribosomal scanning for the AUG starting codon. **c**, An insertion of the aptamer between an upstream open reading frame (uORF) and a downstream ORF may prevent the small ribosomal subunit from another round of translation initiation. Adapted from [130].

It was observed that the translation is mostly regulated at the initiation step [151-153] and in 1989, Kozak suggested that the limited controllability of the 80S translation elongation complex might be due to the increased tolerance towards structured RNA elements [150]. The presence of structured RNA elements (e.g. stem-loops or aptamers) in the 5' UTR was shown to negatively affect translation initiation rates [154, 155]. Therefore, it was suggested for conditional systems to finetune the stem-loop stability within

free Gibbs energies between -25 to -35 kcal/mol at which the translation efficiency might be modulated [149].

Several attempts used protein-responsive aptamers binding the MS2 coat [156] or L7Ae protein [157] which reduce the translation upon protein binding. Oppositely, by taking advantage of these transgenic scaffolds, the recruitment of aptamer-responsive fusion proteins in conjunction with the translation initiation factors eIF4E or eIF4G were shown to be sufficient for initiation of translation when tethered to cap distal regions at intercistronic regions upstream of the target gene [158]. Naturally, structured RNA elements are recognized by RNA binding proteins (RBPs). The affinity of RBPs towards structured RNA elements can be controlled by environmental conditions such as small molecule concentrations [159]. RBPs may affect mRNA translation by different means such as transcription, export, localization, and decay [159]. Effects on mRNA which are mediated by RBPs are also dependent on the mRNA region to which they are targeted. For example, the iron responsive element (IRE), a short stem-loop, mediates the inhibition of translation initiation when interacting with an IRE binding protein and embedded in the 5'UTR [160]. This interaction takes place upon iron depletion. However, when the IRE is embedded in the 3'UTR of an mRNA, the interaction with an IRE binding protein leads to increased mRNA stability by limiting accessibility of the mRNA to RNAses [160].

Also, small molecule-responsive aptamers such as the Hoechst 33342 [161], tetracycline [130] or theophylline [162] aptamers were embedded into the 5'UTR to control mRNA translation. Whereas protein concentrations are routinely controlled by inducible promoters [163], small molecule-responsive systems bear the advantage that they can be adjusted directly by titration of the ligand [164]. Initially, artificial small-molecule dependent translation regulation systems had been demonstrated in mammalian cells [161]. However, it later became clear that these systems also occur naturally in bacteria to control mRNA translation of genes responsible for the biosynthesis of the respective small molecule [165]. Subsequently, flow cytometry [166] and genetic selection [167] based screens were applied in bacteria and yeast cells [168] to generate synthetic riboswitches with altered substrate specificity. In some cases, these riboswitches exceeded the performance characteristics of previously described natural and synthetic riboswitches [166].

When synthetic approaches target 3'UTRs, the output is often controlled by a modulation of the mRNAs stability. This is achieved by incorporation of self-cleaving RNA motifs. These so-called ribozymes are capable to cleave themselves which leads to mRNA degradation [169, 170]. mRNA degradation can be inhibited by antisense oligonucleotides that are complementary to the self-cleaving region or the incorporation of artificial nucleotides into the mRNA [170, 171]. It was shown that ribozymes can be modified with aptamers that render the self-cleavage event ligand-dependent [172]. In case of the natural hammerhead ribozyme (HHR), the cleavage event is mediated by the tertiary interaction of two loop structures [173]. After modification of the HHR with a tetracycline or theophylline aptamer, the self-cleavage event occurs only in absence of the aptamer's ligand [173, 174]. Such a modified HHR was applied for the conditional induction of gene expression in disease models in *C. elegans* [172]. Furthermore, the principle of two interacting loops to induce self-cleavage was applied for the screening

of ribozyme libraries. Candidate ribozymes were incorporated in a modular ribozyme scaffold which was embedded in an expression platform for bacteria and mammalian cells [169]. Subsequently, one stem-loop of the candidate ribozymes was modified with a boxB RNA aptamer motif and used for conditional gene expression [169].

All above-mentioned approaches capitalize on the regulation of the mRNA in *cis*. Alternatively, mRNA can be regulated in *trans*. In these cases, a second, *trans*-acting RNA strand is used to control mRNA translation. This principle was first demonstrated in bacteria [175]. Here, the spontaneous formation of a stem-loop structure located in the 5'UTR of a GFP mRNA inhibited the translation. Upon addition of a *trans*-acting RNA, the stem-loop structure was shifted which led to the expression of GFP [175]. Bayer and Smolke developed an approach in which they controlled reporter gene expression in mammalian cells. In this case, *trans*-acting RNAs were modified with theophylline or tetracycline aptamer sequences [164]. In presence of the aptamer's ligands, the *trans*-acting RNA modules hybridized with the translation initiation site of target mRNA to inhibit its translation [164]. Upon rational design, they were further able to reverse the binding behavior of these *trans*-acting RNAs, that is, inhibition of target gene expression in absence of the ligand [164]. Liu *et al.* created an approach in which the CRISPR-Cas9 system was used as a roadblock to inhibit translation when tethered to target mRNAs. The tethering could be programmed by single guide RNAs (sgRNAs) which hybridize to their complementary target mRNA sequences [176]. In general, the modulation of translation by *trans*-acting RNAs is of interest as it can be adapted easily to any target mRNA of interest *via* the design of short RNA sequences.

2.2.4 Artificial control of RNA interference

RNA interference (RNAi) depicts the mechanism in eukaryotes where gene expression is suppressed by small double-stranded RNA of which one strand is partially or fully complementary to target mRNA molecules (**Figure 1.11**). Together with other mechanisms such as epigenetics, RNAi adds an additional layer of complexity towards gene expression. The human genome itself encodes for ~20.000 different genes [177]. To date, roughly 2500 genes which encode for intrinsic dsRNAs were discovered. These so-called micro RNAs (miRs) regulate ~60% of all mRNAs to control cellular processes [178]. RNAi influences development, differentiation and apoptosis in a spatiotemporally controlled manner, and its dysregulation is linked to the onset of various diseases such as cancer or cardiovascular diseases [179, 180]. Therefore, artificial control of RNAi is highly desired as it promises further insights into RNAi function and can contribute to the development of novel therapeutic approaches.

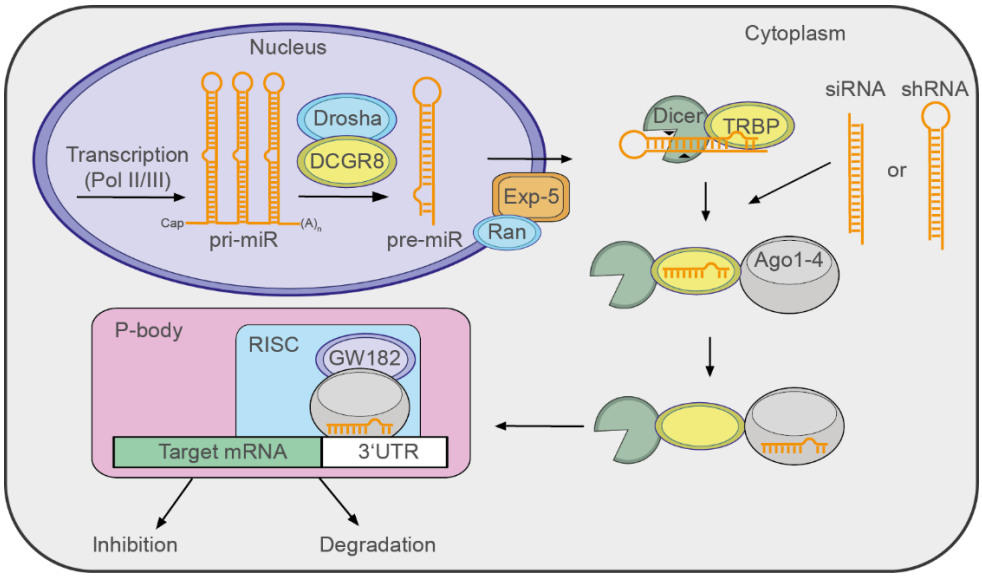

Figure 1.11: The mechanism of RNA interference and micro RNA biogenesis. Primary micro RNAs (*pri*-miRs) are transcribed in the nucleus by Polymerase (Pol) II or III. In the case of transcription by Pol II, *pri*-miRs are capped, spliced and poly-adenylated. After that, *pri*-miRs are truncated by the microprocessor complex comprising of Drosha and DCGR8. The shorter hairpin-shaped constructs bear a 2 nt 3' overhang and are now called precursor micro RNAs (*pre*-miRs). *Pre*-miRs are recognized by Exportin 5 (Exp-5), which functions together with Ran-GTP to translocate the *pre*-miRs into the cytoplasm. In the cytoplasm, *pre*-miRs are cleaved by dicer to form a mature miR duplex. This cleavage step is supported by additional dsRNA binding proteins such as TRBP which impact dicer's cleavage action and facilitate the loading of one of the mature miR strands into an Argonaute (AGO1-4) protein to form the RNA induced silencing complex (RISC). Alternatively, RNA from exogenous sources (e.g. siRNAs or shRNAs) may be loaded into the RISC complex. The RISC complex hybridizes with a target mRNA that needs to display at least a matching seed sequence which is located in its untranslated region. These complexes can be found in P-bodies. Additional protein factors such as the scaffold protein GW182 are also present and mediate translational repression. In case of perfect hybridization, AGO2-mediated cleavage and subsequent degradation of the target mRNA may occur. Adapted from [181] and [182].

The control of endogenous miR activity has been achieved using antagomirs [183]. These artificial oligonucleotides silence miR activity after hybridization a complementary miR [183]. Therefore, these miRs are no longer available for target gene suppression. Alternatively, miR sponges can be used [184]. miR sponges are genetically encodable RNA molecules that harbor a multitude of miR binding sites which can potentially suppress the activity of several miRs at once [184]. To overcome the limitations of oligonucleotide delivery, small molecules can also be administered to silence intrinsic miR activity [185]. In this approach, the interaction of precursor miR molecules with lead compounds from large libraries could be predicted by the miR sequence [185].

As an alternative to the control of endogenous miR activity, gene expression can be controlled extrinsically by administration of RNAi triggers such as small interfering RNAs (siRNAs). siRNAs are short single- or double-stranded nucleic acids that are designed to hybridize perfectly with target sequences to induce their hydrolysis [186]. In nature, siRNAs were predominantly found in plants and viruses [179]. Since siRNA have been artificially introduced into mammalian cells for the first time [187], they were applied to program the expression of protein targets, thereby offering an alternative to small-molecule based approaches [188]. Few years later, in 2002 and 2005, Paddison *et al.* and Siolas *et al.*

showed that RNAi potency could be improved when short hairpin RNAs (shRNAs) were used [189, 190]. shRNAs consist of a small loop structure that connects two stem regions [189]. One of this stem regions contains a siRNA sequence that is liberated after dicer processing [189]. The potency of both classes of synthetic RNAi triggers was modulated by altering their structures (e.g. branching [191] or segmentation [192]), or by the introduction of chemical modification with which various compounds could enter clinical trials [193]. Among them, patisiran was the first FDA-approved antisense therapeutic in 2018 for the treatment of hereditary transthyretin amyloidosis (hATTR) [193].

However, one general obstacle when using chemically modified antisense molecules is the delivery of sufficient concentrations into the cell [193]. As unmodified RNA is genetically encodable, it can be transcribed directly in cells which can provide high steady-state levels of the si- or shRNA [194]. In some cases, e.g. for studying spatiotemporally controlled events, it may not be wanted to provoke RNAi continuously. Thus, multiple routes for obtaining conditional control of RNAi were pursued. Systems were developed that use small-molecule responsive promoters to control transcription of RNAi triggers [194]. Alternatively, the processing of *pri*-miRs was controlled by binding to aptamers [136] or small molecules [117] after the transcription step. Also, at the next step of the miR biogenesis, the maturation of *pre*-miR was controlled by interaction with small molecules [195] or proteins [137, 196]. To this end, the loop domain of the *pre*-miR was replaced by aptamers which are capable to sense their interaction partner. When the interaction takes place, the processing by dicer is hampered. In turn, limiting the accessibility of the RISC complex to mRNA target sequences by structured RNA elements is another option to control target gene suppression. These systems can be regulated by the administration of small molecules that can bind to these RNA elements [197, 198].

Light is another tenable option to control RNAi as it provides increased spatiotemporal resolution compared to diffusion-based systems which use small molecules or proteins. Initial synthesis routes for light-responsive RNAi triggers relied on random integration of photolabile caging groups (e.g. DMNPE) by alkylation of the backbone or nucleobases of a given siRNA duplex [199]. Whereas incompletely caged RNAi triggers might not be prevented from inducing RNAi, the uncaging of heavily caged RNAi triggers may remain incomplete which hampers RNAi [200, 201]. Therefore, approaches with site-specific installation of caging groups were elaborated as by the incorporation of 2-(*o*-nitrophenyl)-propyl (NPP) modified deoxynucleotides by solid-phase synthesis [200]. Rational approaches were undertaken to cage either the seed region or the region of the antisense strand that hybridizes with the cleavage point of the mRNA to suppress RNAi more efficiently [202]. The differences in gene expression between the light states could also be increased when siRNA duplexes were modified at their termini which prevents RISC loading [203]. This approach could be improved further by introducing bulkier side chains in conjunction with caging moieties to prevent unwanted RNAi in the caged state [204, 205]. By using this rationale, Ji *et al.* designed siRNA molecules that were modified with a photocleavable vitamin E moiety at the siRNA's 5'-termini and obtained a 18.6-fold change in eGFP expression, which is among the strongest post-transcriptional systems that aim to control RNAi [205].

To increase the stability of antisense agents, backbone modifications such as 2'fluoro- or phosphorothioate- groups were introduced to prevent degradation in biological systems [206, 207]. Alternatively, the stability of unmodified RNA moieties was increased in a recent approach that

capitalizes on uncaging of two cyclized siRNA molecules. When cyclized, these siRNAs cannot be hydrolyzed by exonucleases. Upon light-induction, both molecules linearize to induce RNAi [208]. As an alternative to siRNAs, hairpin RNAs comprising of a PNA or morpholine backbone can also be uncaged intracellularly from single photolabile groups as it was demonstrated in zebrafish embryos [199, 209]. Because all the systems above use UV light that is toxic to cells [7], alternative approaches were developed which respond to different wavelengths [210]. In 2015, Huang *et al.* developed nanoparticles that release siRNA cargos upon irradiation with near-infrared light and demonstrated the utility of the system by controlling the differentiation of human embryonic stem cells [210]. However, the activation of RNAi remains irreversible for all these examples. By using azobenzene modified siRNAs (siRNAzos) instead, RNAi can be switched off by UV light and on again by visible light in a reversible manner [211]. The underlying mechanism harnesses a bistable *cis*/*trans* isomerization of the azobenzene's N=N bond within the modified siRNA which can only induce RNAi in the *trans* state. Instead, the *cis* isoform cannot be incorporated into the RISC complex due to sterical hindrance. Reversible activation of siRNAzos was suggested to reduce off-target effects and toxicity due to high quantum yields in photoswitching, thus requiring low light doses [211]. However, because of a spectral overlap which induces either *cis* or *trans* isomerization, switching of azobenzenes is not quantitative [211].

2.3 The mammalian cell cycle and its artificial regulation

The cell cycle is a cellular program that allows for duplication of genetic information which then is equally distributed between two genetically identical dividing cells. This procedure is tightly organized over several phases in which different key steps are chronologically arranged [212]. In Gap1 (G_1) phase, the cell increases its size due to the synthesis of organelles and distinct proteins, both required to enter the subsequent synthesis (S) phase, in which the haploid set of chromosomes is replicated [213, 214]. Once the diploid set of chromosomes is formed, the cell initiates the Gap2 (G_2) phase, the synthesis of proteins that are necessary for cell division and the cell changes its morphology to a rounded shape which is required for cellular division [215]. This is followed by the mitosis (M) phase at which the cell divides into two daughter cells that are again bearing a haploid set of chromosomes [215]. After division, the cell has the option to escape the cell cycle by entering a quiescent phase (G_0) in which many cells differentiate terminally (e.g. erythrocytes, neurons, or muscle cells) or die after entering the senescence program [216]. Other cells may reenter the cell cycle by specific stimuli (e.g. stem cells) or continue the cell cycle progression directly *via* scheduled (e.g. healthy cells) or unscheduled (e.g. cancer cells) re-entry in G_1 phase [217]. The timing of the cell cycle progression is tightly regulated at several checkpoints at which the cell status is checked by integrating the status of several extrinsic and intrinsic stimuli [217]. A failure in the cell cycle progression, caused by abnormal events such as chromosomal damage or incomplete DNA replication, allows the cell to respond to the problem [217]. When abnormalities cannot be solved readily, cell death *via* apoptosis might be initiated [214]. Bypassing such control mechanisms is associated with malignant growth as it can be observed in cancerous cells [212].

Due to its importance in cellular function in both health and disease, it is of interest to gain control of the cell cycle progression. To study effects that are specific to distinct cell cycle phases, techniques were

developed to halt cells at the same phase of the cycle. This strategy enables the implementation of an exact starting point into the experimental setup and allows to study the entire population rather than single cells in the desired cell cycle phase [215]. Studying cell populations rather than single cells increases the experimental throughput and helps to identify outliers inherent to cell polymorphism. Cell cycle control in culture can be achieved by controlling confluency, serum concentrations, application of small molecules and by genetic strategies [218, 219].

In culture, cell-to-cell contacts are facilitated when they are highly confluent [218]. This forces cells to accumulate in early G_1 phase. As a considerable number of cells may escape from synchronization, this technique can be multiplexed with serum deprivation which forces cells into the quiescent phase (G_0) [218]. The underlying mechanisms are not fully understood and may lead to desynchronization because cells reenter the cell cycle at different time points. The efficiency of cell-to-cell contacts and serum deprivation on the cell cycle is highly dependent on the cell type and especially the latter technique is not useful for the synchronization of cancer cells which usually do not enter G_0 phase [218]. The double thymidine block is among the most widely used small molecule-based approaches and accumulates cells at the G_1/S boundary of the cell cycle (**Figure 1.12**, [220]). By using this method, cell cycle inhibition is achieved by an autoregulatory feedback loop that stops nucleotide synthesis in the presence of excess thymidine. Two treatments with thymidine are necessary because cells that resided in later stages of S phase during the first treatment may now also reach G_1/S boundary after the second treatment [220].

In other approaches the function of proteins that are crucial for cell cycle progression is inhibited. For example, cyclin-dependent kinase (CDK) 4/6 inhibitors such as Palbociclib or Ribociclib [221] may be used to accumulate cells reversibly in G_1 phase, whereas an inhibition of CDK1 by RO-3306 accumulates cells at the G_2/M boundary [222]. A prolonged inhibition of the cell cycle increases the likelihood of cell death *via* apoptosis [222, 223]. The inhibition of the cell cycle by CDK-specific inhibitors is of interest in basic research as well as in therapeutics, e.g. the inhibition of tumor cell proliferation, as tumor cells are more susceptible to the inhibition of certain key CDKs compared to non-transformed cells [224]. Especially targeting the M phase is of therapeutic interest because the deregulation of this phase is linked to severe types of cancer, partially because its dysregulation leads to genomic instability [224]. Besides targeting CDKs, spindle poisons such as nocodazole, paclitaxel, or colchicine that either inhibit microtubule polymerization or de-polymerization are among the most applied cancer therapeutics worldwide [225]. However, they display severe side effects as microtubule function is also important in other cell cycle phases than mitosis, especially in neuron cells [225]. The overall toxicity of small molecule-based approaches to alter the cell cycle largely limits them to therapeutics in animals and humans.

Alongside with cyclin/CDK dependent progression through mitosis, additional factors such as polo-like serine/threonine kinases (PLKs) are involved. PLK1 is overexpressed in various types of cancer. The knockdown of PLK1 by RNAi in these cells leads to apoptosis at early mitosis (at the boundaries of metaphase to anaphase), which is caused by activation of the spindle assembly checkpoint [226, 227]. The PLK1 protein is mainly active in the late G_2 and M phase. Therefore, the inhibition of PLK1 for cancer therapy potentially results in less side effects because non-dividing cells are no target of the

treatment [225]. To date, several small molecules that target the ATP binding domain of PLK1 are under clinical investigation (e.g. Volasertib or Onvansertib [228]) [225].

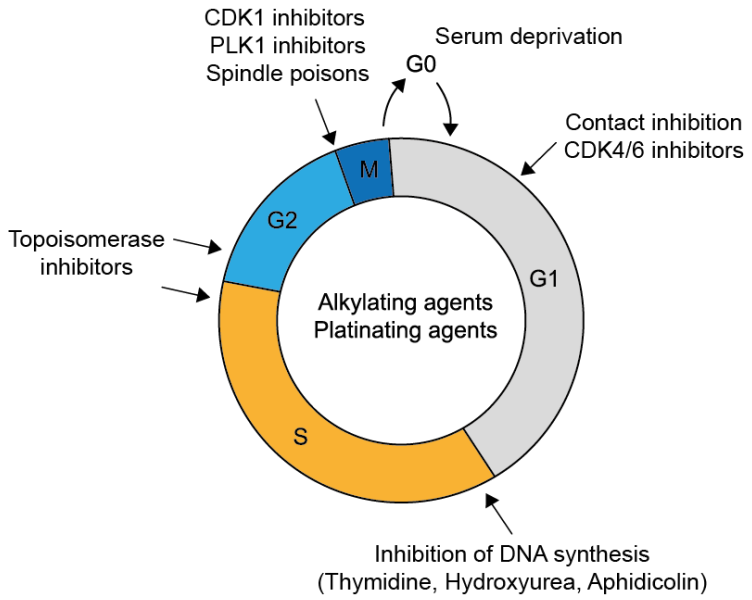

Figure 1.12: Inhibition of the cell cycle at distinct phases by small molecules. Shown are examples for small molecule-based compound groups that are routinely used for inhibition of the cell cycle at different phases in both basic research and therapeutics. Alkylating or Platinating agents inhibit the cell cycle irrespective to the phase.

Furthermore, genetic targeting systems were developed for both cells in culture and animals [229]. Especially in early years of cell cycle research, many working groups performed genomic knockout studies in *Xenopus* and yeast [230]. More recently, RNAi-based approaches were applied as they are adaptable to a broad range of target molecules. Extensive RNAi-based screenings were performed in various cell types, which helped to decipher the complexity and function of the cell cycle network [231]. Complementarily, inducible RNA interference was used as a tool to study the role of essential cell cycle genes during embryonic development and their roles as potential therapeutic targets [232]. However, the spatiotemporal controllability of the current methodology should be further improved to gain deeper insights into cell cycle dynamics.

2.4 PAS-ANTAR-LOV (PAL)

2.4.1 PAL – A light-oxygen-voltage photoreceptor that mediates RNA binding

Light-oxygen-voltage (LOV) photoreceptors can be found throughout all kingdoms of life [233]. They absorb blue light of the visible spectrum and are part of the Per-ARNT-Sim protein superfamily [234]. LOV proteins govern a large variety of cellular processes including circadian rhythm in fungi upon protein dimerization (VIVID, [235]), phototropism in plants *via* autophosphorylation [236] or modulate DNA

binding in bacteria (e.g. EL222 [75]). This large variety of functions is facilitated by the conjunction of a LOV domain to different signal transduction output domains [234] that are predominantly, but not exclusively conjoined to the C-terminus of LOV domains [237]. Together with some other examples for naturally occurring LOV proteins [238], PAL (PAS-ANTAR-LOV) displays an uncommon domain architecture (**Figure 1.13a**).

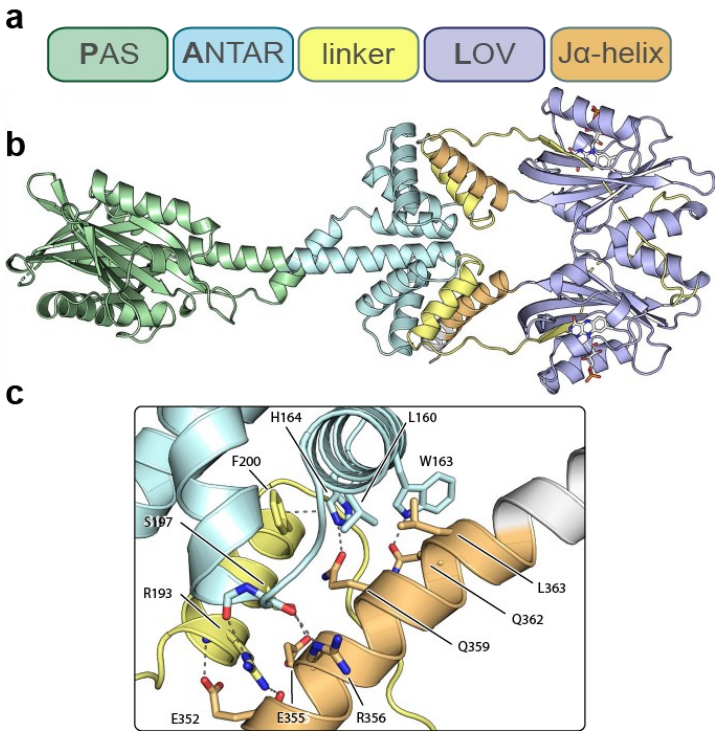

Figure 1.13: Structure of PAL incubated in darkness (pdb: 6hmj). a, Domain architecture (N to C-terminal) of PAL consists of a PAS (green), ANTAR (blue), linker (yellow), LOV (violet) domain and a Jα-helix (orange). **b**, Crystal structure of PALs dark-adapted state as a constitutive homodimer. **c**, The Jα-helix is in contact with residues from the ANTAR domain and the linker domain (adapted from [237]).

PAL was discovered using an automated bioinformatic approach which screened sequence databases for novel LOV-containing proteins. The PAL sequence was found in the genome of *Nakamurella multipartita* [237]. Similar to the LOV proteins YtvA and YF1, PAL forms a constitutive homodimer [239]. PAL consists of an N-terminal PAS domain, an AmiR and NasR transcription antitermination regulators (ANTAR) domain and a C-terminal LOV domain that is connected to a Jα-helix. Unlike other described LOV-containing proteins, PAL's LOV domain is located at the C-terminus of the protein. To rationalize how light signals are transduced in PAL's uncommon domain structure, the protein's crystal structure was resolved [237]. ANTAR domains are known for their ability to bind to RNA in bacteria as it can be found in transcriptional anti-terminal mechanisms [240]. PAL's ANTAR domain is connected to the LOV domain by a proline-rich linker sequence that is crucial for the protein's structure and function. In PAL's dark-adapted state, the linker domain features helix-helix interactions with the ANTAR domain and impacts the orientation of the LOV domain in a way that the Jα helix is oriented towards the ANTAR

domain (**Figure 1.13b**). Therefore, hydrogen and salt bridges are formed with both the linker helix and the ANTAR domain (**Figure 1.13c**). Thus, the accessibility of the ANTAR domain by RNA is hampered in the proteins dark-adapted state. Upon light exposure, PAL undergoes a reversible cysteinyl-C4(a) adduct formation that is mediated by a triplet intermediate, similar as it is described for other LOV proteins (**Figure 1.7**, [241, 242]). The structural rearrangement of the LOV domain upon light-activation affects the positioning of the Jα-helix. This leads to altered interactions with the linker and the ANTAR domain that finally result in a relief of autoinhibition [237]. To date, PAL is the sole photoreceptor which is known to interact with RNA directly. To gain precise control over the interaction, RNA aptamers have been developed which bind to PAL in a light-dependent manner.

2.4.2 RNA aptamers targeting PAL

Recently discovered PAL aptamers bridge the gap between optogenetics and RNA biology [237]. In 2019, Weber *et al.* identified the aptamer motifs named Motif1 and Motif2 which target the light-conformation of the photoreceptor PAL *via* SELEX (**Figure 1.14a**). The two selected aptamer motifs recognize similar regions within the PAL protein, as shown in a competitive displacement assay where one aptamer displaced the other. Secondary structure prediction analysis indicated that the aptamers comprise a stem-loop structure which is bridged by an AGCAG sequence in their loop regions.

Respectively, Motif1 and Motif2 could be truncated down to 17 (aptamer 04.17) and 19 (aptamer 53.19) nucleotides (**Figure 1.14b**, [237]) and the functionality of both motifs was exhaustively characterized. In both cases, this indicated some degree of freedom for nucleotide compositions concerning the stem and less freedom for engineering the loop regions. The binding affinity of Motif1 to PAL drops at the physiological temperature of 37 °C, but not for Motif2. This indicates that that the latter motif might be more suitable for cellular applications such as the post-transcriptional control of gene expression in mammalian cells [237].

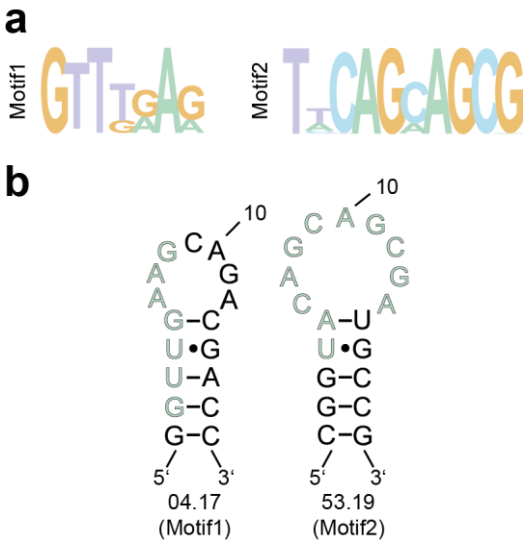

Figure 1.14: Consensus sequences of Motif1 and Motif2 aptamers targeting PAL. a, Consensus sequences of Motif1 and Motif2 based on NGS analysis of selection cycle 15. **b**, Secondary structure predictions of aptamer 04.17 and 53.19 bearing Motif1 and Motif2. The two aptamers were truncated down to 17 and 19 nucleotides, respectively. Green nucleotides depict the aptamer Motifs in the stem-loop structures. Adapted from [237].

3 Aim of the study

The aim of the study was to develop a generalizable system that enables light-control of gene expression at the RNA level. The system could be used to broaden the current understanding about protein and miR function. This goal can be achieved when several key features are combined in the novel approach. The approach should be reversible, genetically encodable and spatiotemporally controllable. This can be potentially achieved by harnessing the interaction of the PAL protein to RNA stem-loop structures. Therefore, one aim of this study was to demonstrate spatiotemporal controllability of the PAL/RNA stem-loop interaction in mammalian cells.

Most available tools light-control gene expression on the transcriptional or the protein level. In this study it is assumed that the genetic encodability of RNA may also have advantages. The RNA stem-loops can be genetically encoded into virtually any target RNA structure to gain precise light-control. To demonstrate the broad applicability, the function of several types of RNA should be controlled. For example, the RNA stem-loops will be incorporated into mRNA molecules to control protein translation. Furthermore, the RNA stem-loops will be conjoined with mature miR and siRNA sequences to enable light-control of RNA interference. To monitor the effects, the development of bioreporter systems for all these cases is indispensable.

To improve the light-regulation in all these contexts, the nucleotide compositions which flank the RNA stem-loops will be optimized. Finally, it should be demonstrated that these RNA elements represent an alternative layer to control intrinsic target gene expression.

4 Results

In this chapter, several optoribogenetic modalities in mammalian cells are presented. All of them control gene expression on the post-transcriptional level. In section 4.1, the PAL aptamer 53.19 was directly embedded into the UTRs of reporter mRNAs, thereby an “off-switch” was created which enabled target gene expression control by blue light. To create an “on-switch”, the PAL aptamers 04.17 and 53.19 were introduced into the apical loop domain of *pre*-miRs (section 4.2) or shRNA molecules (section 4.3). The impact of light intensity and pulsing was investigated in section 4.4. Ultimately, shRNA molecules have been applied to control intrinsic protein levels and cellular function (section 4.5).

4.1 Light-control of protein translation in mammalian cells

4.1.1 Characterization and application of mCherry-PAL for translational control

To visualize the PAL protein in mammalian cells, a fusion protein with the fluorescent mCherry protein was created [237]. The mCherry tag was introduced as N-terminal fusion to PAL as the C-terminus of the protein is responsible for light-adapted conformational changes which should not be disturbed.

4.1.1.1 Assessment of mCherry-PAL photochemistry

As the PAL protein was discovered in bacteria, it was investigated whether PAL can be expressed in a eukaryotic cell environment with an intact photochemistry. To this end, HEK293 cells have been transiently transfected with plasmids which encode for either mCherry or mCherry-PAL. The expression of both constructs was set under the control of a Human Cytomegalovirus Immediate-Early Gene Promoter (CMV) which promotes strong protein expression [243]. 48 h after transfection and incubation in darkness, cells were subjected to fluorescence microscopy (**Figure 4.1**)[1]. A mCherry fluorescence was detectable in cells which express the mCherry (**Figure 4.1a**) or the mCherry-PAL (**Figure 4.1b**) protein, whereas PAL fluorescence was only detectable for the latter construct. After the exposure of the cells to blue light (1 min), which was immediately followed by imaging, the PAL fluorescence was not detectable in cells that express the mCherry or the mCherry-PAL protein. This indicates a conformational switching of mCherry-PAL to the non-fluorescent light state of PAL. After a 10 min recovery phase in darkness, the fluorescence of PAL could be detected as before the irradiation. Among all applied conditions, no PAL fluorescence was detected in cells that have been transfected with mCherry.

[1] Establishment of the experimental setup by Anna Maria Weber.

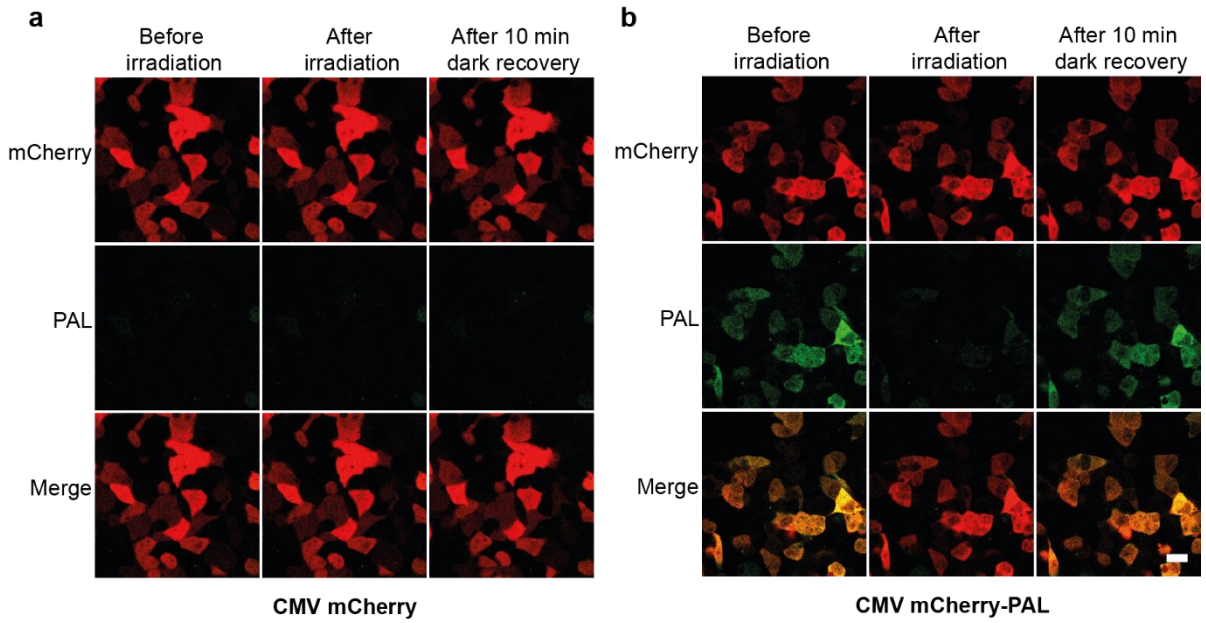

Figure 4.1: PAL photochemistry in mCherry-PAL is reversible in mammalian cells. HEK293 cells were transfected with mCherry (**a**) or mCherry-PAL (**b**) and fluorescence of mCherry and PAL was determined after cells have been exposed to the indicated light conditions (incubation in darkness, immediately after irradiation with blue light for 1 min or after 10 min further incubation of these cells in darkness) by using fluorescence microscopy. This experiment was performed in duplicates and in two independent replications. Scale bar: 20 µm.

These results indicate an intact and reversible photochemistry of mCherry-PAL for one irradiation cycle in a cellular context. It is rather unlikely that the loss of PAL fluorescence is a result of photobleaching, as the translation of initial levels of the PAL protein might be slower than the observed dark recovery time [244].

4.1.1.2 Investigation of mCherry-PAL protein localization and translational control as a function of expression strength

The localization of PAL to the cytosol might be necessary to control translation initiation [245]. Therefore, it should be investigated whether the PAL protein can be detected in the cytosol and at various expression levels. Hence, a mCherry-PAL plasmid variant was generated in which the transcription was set under the control of a CMV promoter to produce high transcript levels. Further mCherry-PAL plasmid variants were generated by using a human ubiquitin C promoter (Ubc), which produces intermediate transcript levels and a mouse metallothionein I (MT) promoter, which produces low transcript levels. Expression of mCherry under the control of a CMV promoter was used as control. Then, cells were transfected with these plasmids. Subsequently cells were incubated under light or dark conditions to determine whether the light state influences the abundance of mCherry-PAL protein. Fluorescence microscopy studies were performed 24 h and 48 h after transfection, in which the expression of mCherry fluorescence was monitored (**Figure 4.2**). After 24 h, small spots of increased mCherry fluorescence were observed only in cells which were transfected with CMV-mCherry-PAL irrespective to the light irradiation protocol (**Figure 4.2a**). All other conditions indicated homologous distribution of mCherry

fluorescence throughout the cells which was irrespective to the applied light protocol. 48 h after transfection, increased formation of spots with increased mCherry fluorescence was observed under both light conditions in cells that were transfected with CMV-mCherry-PAL and to less extent in cells which were transfected with Ubc-mCherry-PAL (**Figure 4.2b**). A co-transfection of mCherry under the control of a CMV promoter together with MT-mCherry-PAL did not or to very little extent show spots of increased mCherry fluorescence in neither of the applied light conditions.

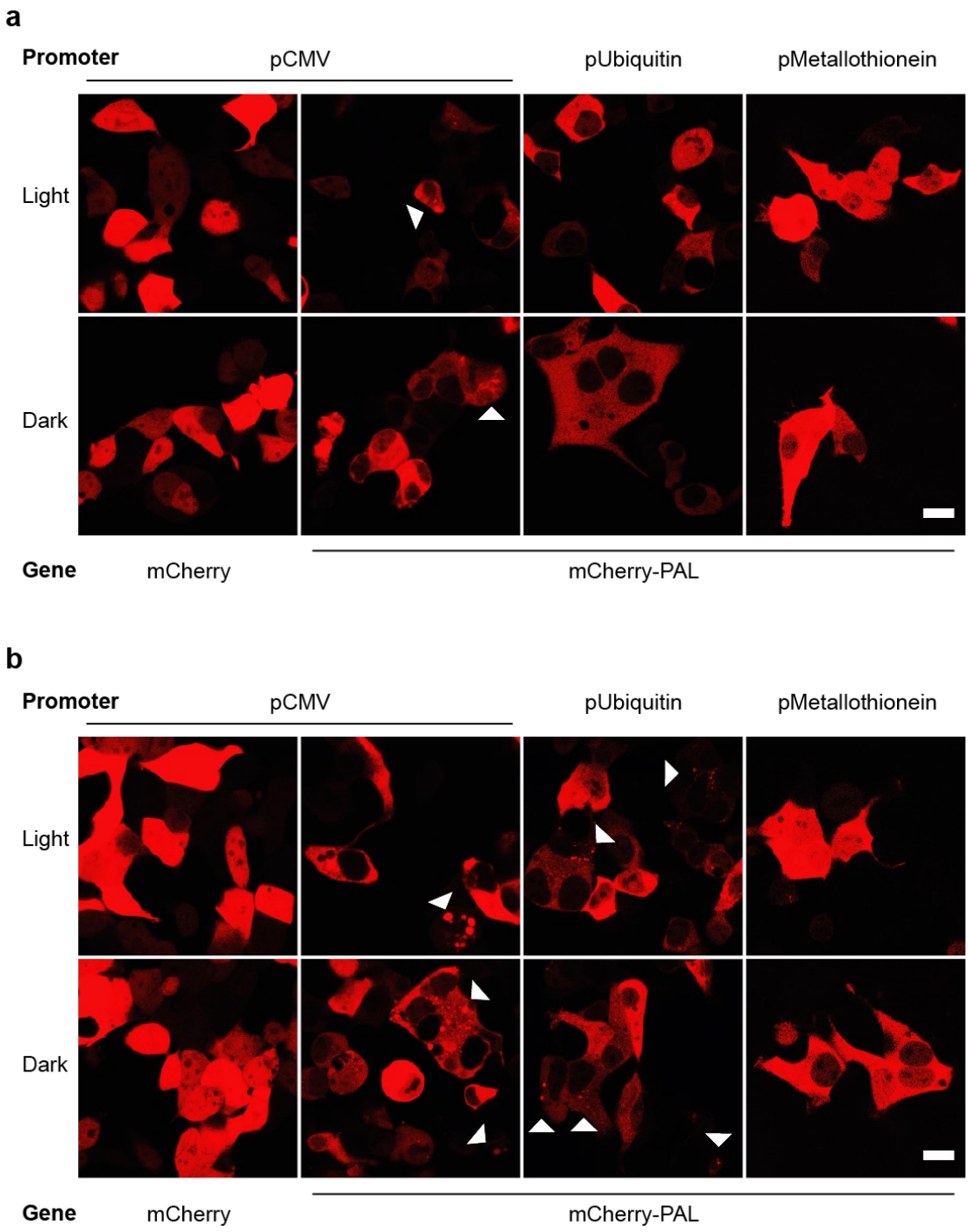

Figure 4.2: Spots of increased mCherry fluorescence from mCherry-PAL protein correlate with expression strength. Fluorescence microscopy images of HEK293 cells 24 h (**a**) or 48 h (**b**) after transfection with mCherry or mCherry-PAL expressed

under the control of the indicated promoter. The cells were incubated in presence of blue light or in darkness. The experiment was performed in duplicates and at least in two independent replications. The fluorescence of mCherry (ex/em: 543/578-696 nm) was monitored. Please note that different laser settings for the excitation of mCherry were used among the samples to avoid image oversaturation (for microscopy settings, see **Table 7.5**). White bar: 20 µm.

These results indicate that the concentration dependent accumulation of mCherry-PAL but not mCherry leads to the formation of spots of increased mCherry fluorescence in mammalian cells. Furthermore, the experiment indicates that mCherry-PAL is present in the cytosol under all tested conditions.

4.1.1.3 Translational control of *Metridia* Luciferase using mCherry-PAL and the PAL aptamer 53.19

Subsequently, a gene reporter assay was established to demonstrate that the photoreceptor PAL can be used as optogenetic tool that transduces light-triggered signaling to control the translational fate of a target mRNA. To realize the signal transfer between PAL and a target mRNA, the PAL aptamer 53.19 (see also section 2.4.2) was used as an interface and incorporated into the 5'UTR of a *Metridia* luciferase reporter plasmid. As a control, a four base mutant of the aptamer 53.19 was used which does not bind to PAL (A7U, G8C, A10U and G11C: M4, [237]). The position of the aptamer was chosen to be close to the translational start codon (18 bases upstream the translation start site, **Figure 4.3a**, see also section 8.5.2) by taking advantage of the *AgeI* restriction site that was present on the unmodified plasmid, at the 5'UTR of the mRNA. HEK293 cells were co-transfected with reporter plasmid variants which express the aptamer (Mot2), the light-independent four base mutant of the aptamer (M4), or no insertion (Luc, **Figure 4.3b**) together with mCherry-PAL. The transcription of mCherry-PAL was set under the control of the intermediate Ubc (pUbiquitin) or the weak MT (pMetallothionein) promoter in these plasmids. The expression of luciferase relative to the control in cells, which were incubated in light and transfected with Mot2 was found to be 28 % in case of pUbiquitin and 35 % in case of pMetallothionein and the expression increased to 48 % for pUbiquitin and 43 % for pMetallothionein in darkness (**Figure 4.3c**). Consequently, light-dependent fold changes decreased gradually to 0.6-fold (Ubc) and 0.8-fold (MT) for weaker promoters (**Figure 4.3d**). Control transfections with Luc and M4 plasmids revealed no light-dependency when co-transfected with one of the mCherry-PAL promoter variants. The luciferase expression of the Luc plasmid was elevated about 1.1-fold compared to M4 and both variants did not show light-dependency (**Figure 4.3c**). Both Luc and M4 expression levels were very similar for either co-transfecting pUbiquitin or pMetallothionein (**Figure 4.3c**).

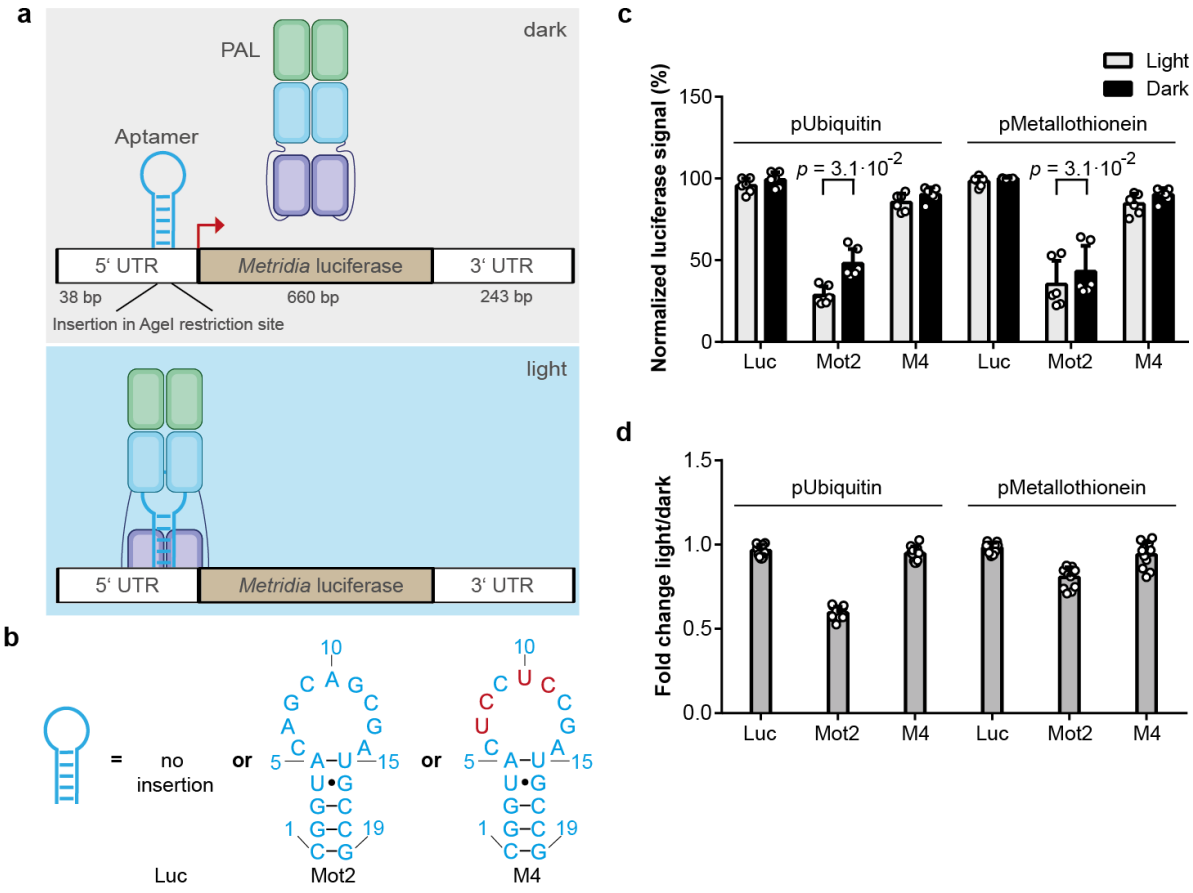

Figure 4.3: Translational control is mediated by interaction of the PAL aptamer 53.19 which was incorporated in the 5'UTR of a reporter mRNA and PAL. a, Schematic representation of the translational control system. The PAL aptamer was incorporated near the translation start site (18 bases upstream to the start codon). In darkness, protein translation can occur as the aptamer interacts with PAL to a negligible extent. Under light conditions, PAL binds to the aptamer, which inhibits the translation initiation. **b**, Schematic representation of the aptamer variants which were used in this experiment. Either no aptamer (Luc), functional aptamer (Mot2) or a non-functional mutated variant of the aptamer (A7U, G8C, A10U and G11C, M4) were tested. **c**, The luciferase expression of HEK293 cells after transfection with the indicated luciferase reporter plasmid variants (Luc, Mot2 or M4) and mCherry-PAL under the control of promoters resulted in intermediate (pUbiquitin) or weak (pMetallothionein) protein expression levels. The values are normalized to Luc co-transfected with mCherry-PAL under the control of pMetallothionein and incubated in darkness. **c**, Grey bars: cells incubated under light conditions, black bars: cells incubated in darkness. A Wilcoxon two-sided signed-rank test was used for statistical analysis as a paired observation was assumed. **d**, Fold changes calculated from light *vs*. dark conditions from (**c**). **d**, Dark grey bars: Fold changes. **c**, **d**, N = Three biologically independent experiments performed in duplicates. Values are means ± s.d.

Based on these results, it was concluded that the *Metridia* luciferase protein abundance can be light-controlled most likely by the interaction of the PAL protein with its RNA aptamer 53.19 incorporated into the 5'UTR of the target mRNA.

The results shown in **Figure 4.3b** indicate that the expression levels of luciferase in darkness were lower for Mot2 compared to the control levels (Luc and M4). To demonstrate whether this observation is a consequence of binding to PAL in darkness or an effect that is inherent to Mot2, Luc (no insertion in 5'UTR), Mot2 (the functional aptamer 53.19) and M4 (a control aptamer bearing four mutated bases) were co-transfected with mCherry. Furthermore, the differences in luciferase expression under light

conditions or in darkness were intended to be increased. In **Figure 4.3**, it was observed that the Ubiquitin promoter of intermediate strength surpassed the weak Metallothionein promoter for the light-dependent differences in reporter protein expression. To find out whether strong transcription of mCherry-PAL is necessary for efficient light-responsiveness in the luciferase reporter assay, Luc, Mot2 and M4 luciferase plasmid variants were co-transfected in HEK293 cells with plasmids which encode for mCherry-PAL. Therefore, the expression of mCherry-PAL and mCherry was set under the control of a CMV promoter. As already observed before (**Figure 4.3c**,**d**), light-dependency was also observed for samples in which mCherry-PAL was set under the control of the CMV promoter and co-transfected with Mot2, albeit to a greater extent (**Figure 4.4**). In these cells the expression of luciferase relative to the control was found to be 10 % under light conditions and 25 % in darkness (**Figure 4.4a**). Elevated, but light-independent levels of luciferase expression was monitored in samples that were co-transfected with M4 and mCherry-PAL (72 % of under light conditions and 74 % in darkness, **Figure 4.4a**). Decreased luciferase expression (22 %) for both light irradiation states and no light-dependency was observed in samples which were co-transfected with Mot2 and mCherry (**Figure 4.4**). Additionally, no light-dependency was detected for control transfections with an unmodified luciferase plasmid (Luc) or M4 and the values were similar for co-transfection of mCherry or mCherry-PAL (**Figure 4.4**). Again, luciferase levels were slightly elevated (1.1-fold) when cells were transfected with Luc compared to M4 (**Figure 4.4a**).

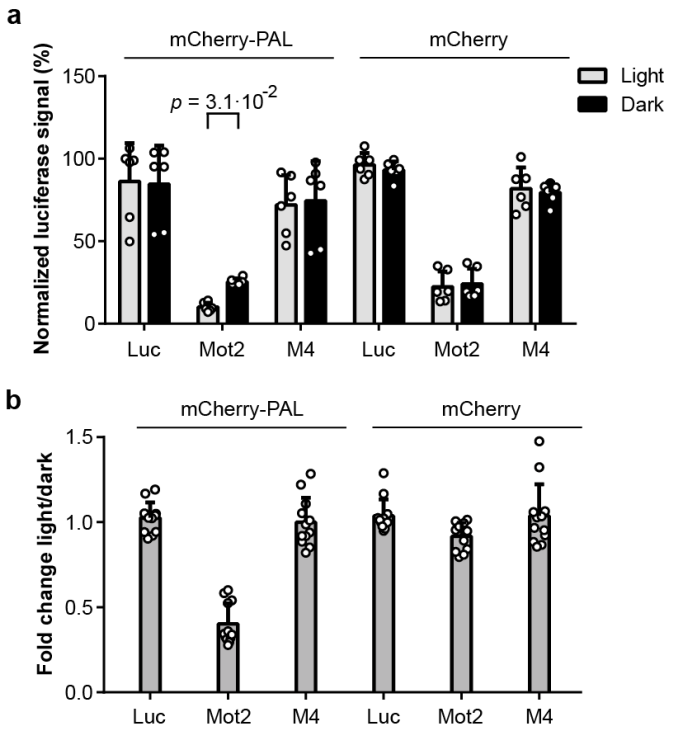

Figure 4.4: A strong CMV promoter for the expression of mCherry-PAL increases the light-dependent translational control. a, Luciferase expression after transfection of HEK293 cells with the indicated luciferase reporter plasmid variants (Luc, Mot2, M4, **Figure 4.3b**) and a mCherry(-PAL) plasmid variant which was expressed from a strong CMV promoter. For better comparison, values are normalized to Luc which was co-transfected with mCherry-PAL under the control of the weak Metallothionein promoter and incubated in darkness (shown in **Figure 4.3c**), as these experiments were performed simultaneously. Grey bars: cells incubated under light conditions, black bars: cells incubated in darkness. A Wilcoxon two-sided signed-rank test was used for statistical analysis as a paired observation was assumed. **b**, Fold changes calculated from light *vs.*

dark conditions from (**a**). Dark grey bars: Fold changes. N = Three biologically independent experiments performed in duplicates. Values are means ± s.d.

Based on this experiment, it was concluded that the decreased expression levels of luciferase for Mot2 was not a consequence of PAL-binding in darkness but rather an Mot2 inherent effect. It was further concluded that the expression of mCherry-PAL needs to be controlled by a strong promoter (e.g. CMV) to increase the light-dependent fold change of target mRNA expression.

4.1.2 Characterization and application of 4E-BP1-mCherry-PAL for translational control

It had been described before that the eukaryotic translation initiation factor 4E-binding protein 1 (4E-BP1) represses cap-dependent translation [246, 247]. As its interacting protein eIF4E had been tethered to target mRNAs before, which led to an increased translational initiation [158], it was hypothesized that the tethering of 4E-BP1 to target mRNAs by fusion with mCherry-PAL could induce the opposite effect. Hence, a 4E-BP1-mCherry-PAL fusion protein was created and applied in mammalian cells. As the results shown in **Figure 4.4** indicate, mCherry-PAL and its conditional interaction to the RNA aptamer 53.19 might be a suitable mRNA tethering system.

4.1.2.1 Assessment of 4E-BP1-mCherry-PAL photochemistry

It was unclear whether 4E-BP1 could influence PAL abundance and negatively impact conformational switching capabilities. Hence, HEK293 cells have been transiently transfected with 4E-BP1-mCherry-PAL expressed under the control of a CMV promoter. 48 h after transfection and incubation in darkness, the cells were subjected to fluorescence microscopy (**Figure 4.5**). Both, mCherry and PAL fluorescence could be detected at this point. After the exposure of cells to a 1 min blue light pulse which was immediately followed by imaging, no more PAL fluorescence was detectable. This indicates a conformational switching to the non-fluorescent light state of the fusion protein. After a recovery step, comprising of 10 min incubation in darkness, fluorescence of PAL could be detected as before the blue light irradiation. Throughout all applied conditions, mCherry fluorescence could be detected.

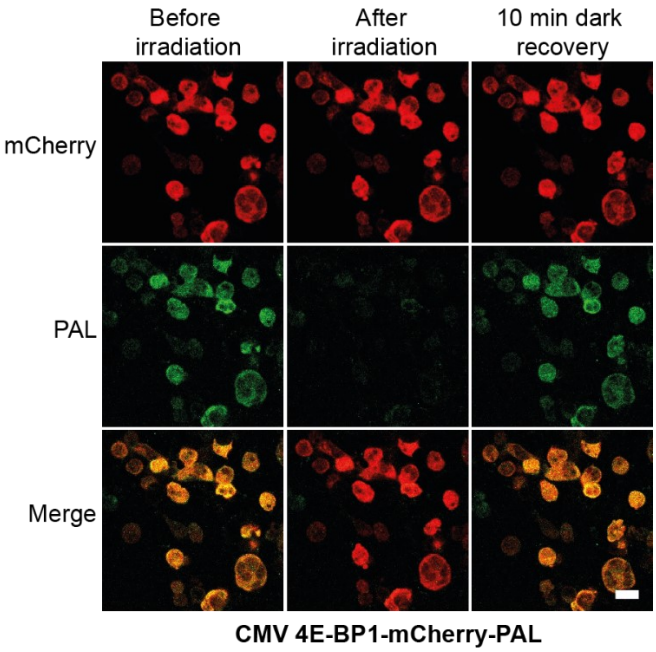

Figure 4.5: 4E-BP1-mCherry-PAL protein photochemistry is reversible in mammalian cells. HEK293 cells were transfected with 4E-BP1-mCherry-PAL or mCherry (see **Figure 4.1a**) under the control of a CMV promoter and fluorescence of mCherry and PAL was determined after cells had been exposed to the indicated light conditions (incubation in darkness, immediately after irradiation with blue light for 1 min or after 10 min further incubation of these cells in darkness) by using fluorescence microscopy. The experiment was performed in duplicates and in two independent replications. White bar: 20 µm.

These results indicate reversible photochemistry of 4E-BP1-mCherry-PAL for one irradiation cycle in a cellular context. Comparable results have been obtained for mCherry-PAL (**Figure 4.1b**).

4.1.2.2 Translational control of *Metridia* Luciferase using 4E-BP1-mCherry-PAL and the aptamer 53.19

Subsequently, 4E-BP1-mCherry-PAL was tested in the luciferase reporter system to determine whether the light-responsiveness can be improved by the inhibitory effect of 4E-BP1 on cap-dependent mRNA translation. Here, cells were transfected with mCherry-PAL or 4E-BP1-mCherry-PAL together with luciferase reporter plasmids which have either no aptamer insertion (Luc), a functional aptamer 53.19 (Mot2) or a four base pair non-functional aptamer variant (M4) which was embedded in the 5'UTR of the reporter mRNA. Untransfected cells (None) were used as further control, where no luciferase expression was expected (**Figure 4.6a**). 19 h after incubation in presence of blue light or darkness, a luciferase assay was performed. The luciferase expression decreased generally when cells were transfected with 4E-BP1-mCherry-PAL compared to the respective mCherry-PAL transfections (**Figure 4.6b**). For cells which express 4E-BP1-mCherry-PAL and Mot2, a 0.27-fold light induced reduction in luciferase expression was detected, compared to a 0.44-fold reduction for cells which express mCherry-PAL and Mot2 (**Figure 4.6c**). All controls (Luc, M4, None) irrespective of the co-transfected PAL variant, did not show light-dependency (**Figure 4.6c**). In contrast to cells which express mCherry-PAL, where a slight, light-independent decrease of luciferase expression in cells which express M4 compared to Luc was

detected (~5 %, see also **Figure 4.4b**), no substantial difference in luciferase expression was detected among these variants in cells which express 4E-BP1-mCherry-PAL (**Figure 4.6b**). No luciferase expression was detected for untransfected cells (None, **Figure 4.6b**).

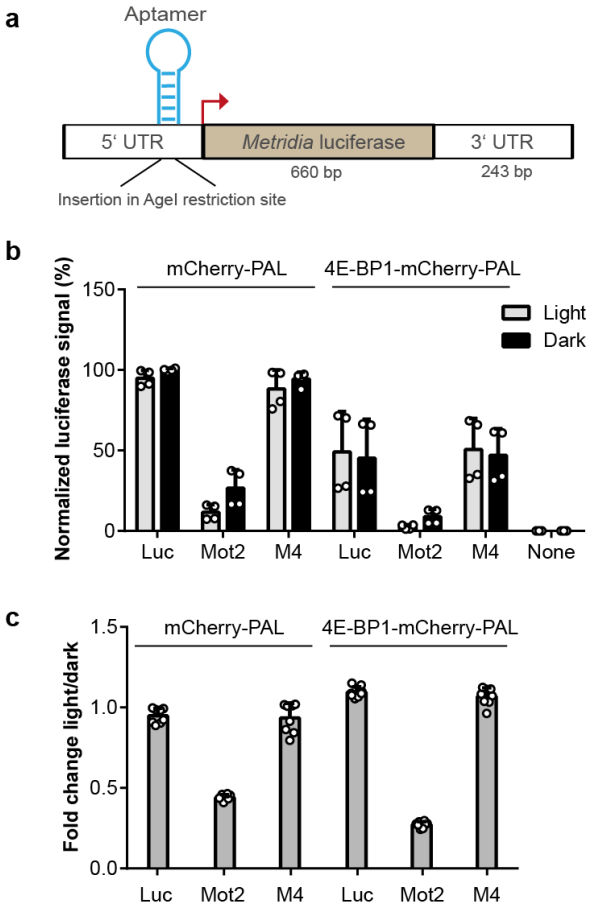

Figure 4.6: 4E-BP1-mCherry-PAL increases the differences of reporter protein expression between the light states when aptamer 53.19 is incorporated in the 5'UTR of a reporter mRNA. a, Schematic representation of the reporter mRNA applied in **b** and **c**. PAL aptamer was incorporated 18 bases upstream to the translation start site in the 5'UTR. Red arrow: Translation start site. **b**, Luciferase expression of HEK293 cells after transfection with the indicated luciferase reporter plasmid variants (Luc, Mot2 or M4, **Figure 4.4b**) and either mCherry-PAL or 4E-BP1-mCherry-PAL. **c**, Fold changes calculated from light *vs*. dark conditions from (**b**). **b**, Values are normalized to Luc co-transfected with mCherry-PAL and incubated in darkness. **b**, Grey bars: cells incubated under light conditions, black bars: cells incubated in darkness. **c**, Dark grey bars: Fold changes. **b**,**c**, The experiment was performed in duplicates, once in HEK293 cells and once in HeLa cells and results for both cell types were combined in the figures. Values are means ± s.d.

Based on this experiment, it was concluded that the tethering of 4E-BP1-mCherry-PAL to the aptamer 53.19 is capable to increase the light-dependent differences in luciferase expression compared to mCherry-PAL. It was furthermore observed that the overexpression of 4E-BP1-mCherry-PAL decreases the reporter protein expression *per se*. This could a consequence from the inhibitory effect of 4E-BP1 overexpression on cap-dependent mRNA translation [248].

4.2 Light-control of *pre*-miR activity

Besides the possibility of regulating target mRNAs directly in *cis* [82, 83], systems have been developed that employ the gene regulation in *trans* [249]. In these cases, the target of regulation is controlled by the RNA's sequence. Therefore, these approaches are easily adaptable to a target of interest. Several attempts described the small-molecule controlled biogenesis of synthetic *pre*-miRs [137, 195], which represent genetically encodable "off-switches". These systems hold great potential upon the study of miR biogenesis and function [250]. They further enable the concerted regulation of several target proteins on the posttranscriptional level at once to control multifactorial processes and cellular fate [251]. Within this thesis, two types of regulatory RNA molecules have been engineered to gain full genetic control about their processivity by light: *pre*-miRs and shRNAs (**Figure 4.7**). Initially, an altered processivity of *pre*-miR21 constructs was anticipated by altered PAL binding to the aptamer-modified apical loop domain. In naturally occurring *pre*-miRs, the apical loop sequence is not part of the mature miR sequence and therefore it is degraded after miR maturation. Thus, replacing the apical loop domain provides a strategy to alter *pre*-miR processing while the conveyed mature miR information is left unaltered.

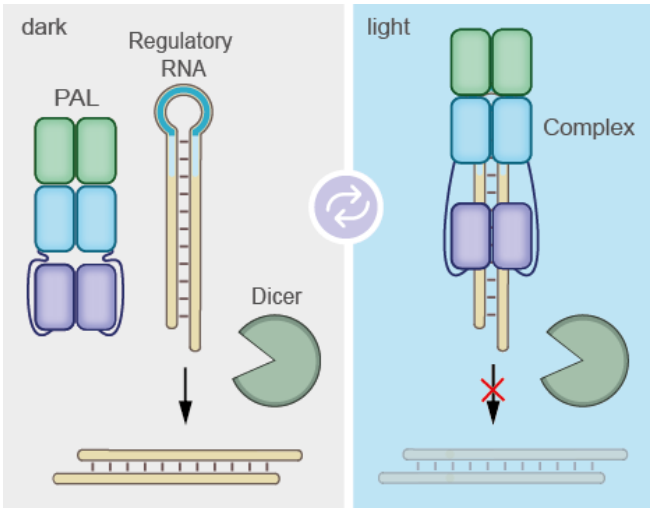

Figure 4.7: General design of light-dependent regulatory RNAs. The PAL protein reversibly binds to its cognate RNA aptamer (highlighted in blue) embedded in the apical loop domain of a regulatory RNA (highlighted in light orange) under light conditions and thereby influences regulatory RNA function.

4.2.1 Characterization of purified PAL and *in vitro* binding studies with *pre*-miR21 variants

To demonstrate PAL-binding to *pre*-miR21 variants, *in vitro* interaction studies were performed. To this end, the PAL protein was purified and characterized *in vitro*. Subsequently, PAL was biotinylated to enable protein immobilization on streptavidin coated wells. With this strategy, PAL remains bound to the well throughout the assay and molecules that bind to PAL can be separated from non-binding molecules

only by washing. The successful protein expression and purification was verified by SDS-PAGE (**Figure 4.8a**). Indeed, a protein band can be observed after induction of protein overexpression (**Figure 4.8a**, 2, before induction, see **Figure 10.1**) and this band accumulates after elution from the column (**Figure 4.8a,** 7). After protein purification, a PAL absorption spectrum was recorded to determine whether the protein is capable to accomplish conformational switching (**Figure 4.8b**). When the protein was incubated in darkness (dark state), three peaks that are characteristic for LOV photoreceptors could be observed with respective maxima at 420, 444 and 471 nm. Then, PAL was irradiated for 1 min with blue light (λ_{max}= 465 nm) and the absorption spectrum was measured directly afterwards. Under this condition, no more absorption peaks could be observed within the tested wavelengths, which indicates a conformational switching to the light state of the protein. After one additional hour of incubation in darkness (**Figure 4.8b**), the initial spectrum with the characteristic three absorption peaks could be observed again, indicating a restoration of PAL's conformational dark state. Subsequently, the PAL protein was biotinylated (see also section 7.3.8) and a dot blot was performed to verify the status of the protein's biotinylation (**Figure 4.8c**). Here, increased chemiluminescence indicated the presence of biotin moieties. Chemiluminescence of spots covered with protein was detectable to an increasing extent in accordance with increasing protein concentration from 10 over 25 to 50 pmol for the biotinylated PAL variant, but not for unbiotinylated PAL (**Figure 4.8c**). Afterwards, the PAL absorption spectrum was recorded again (**Figure 4.8d)** which indicated similar results as observed before biotinylation (**Figure 4.8b**).

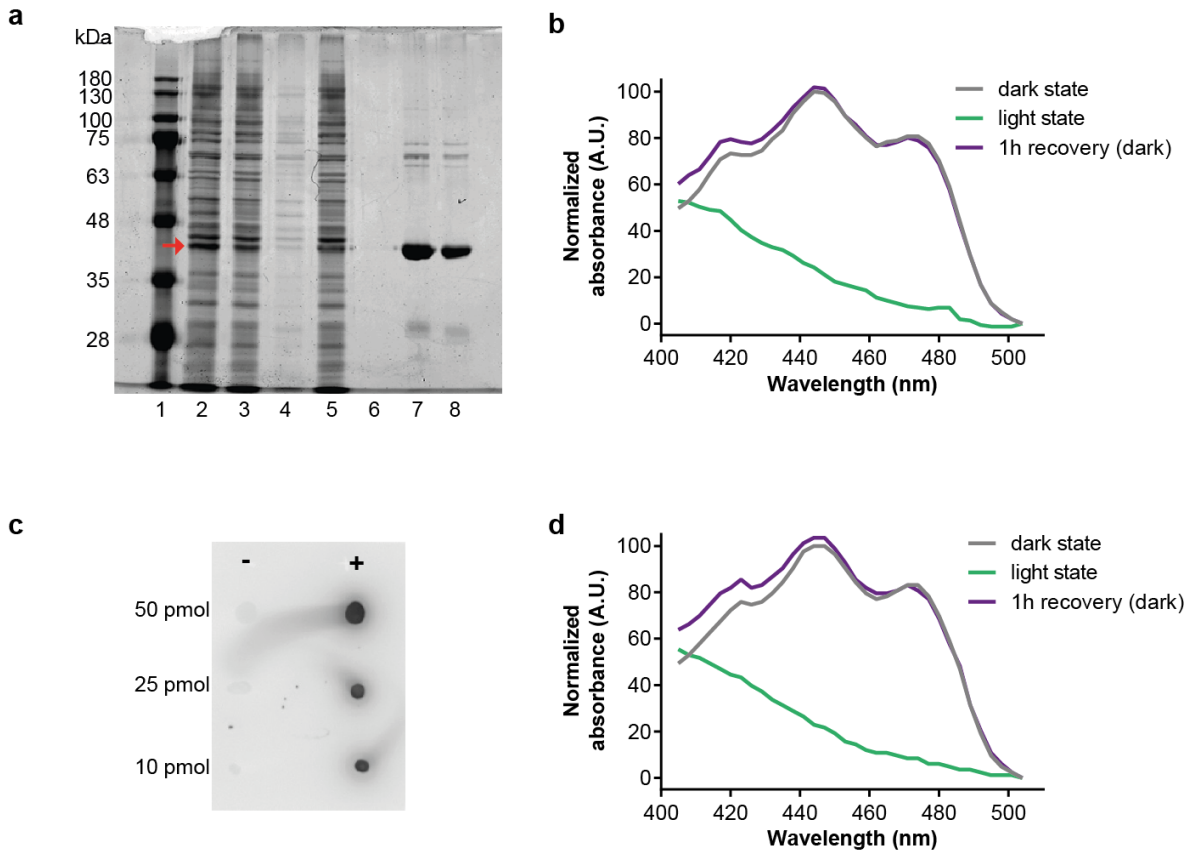

Figure 4.8: PAL purification, biotinylation and characterization. a, Gel electrophoresis of samples at different PAL purification steps (1: Prism Protein Ladder, 2: Cell lysate after induction, 3: Lysate supernatant, 4: Lysate pellet, 5: Column flow through, 6:

Washes, 7: Dialyzed elution, 8: Biotinylated Protein). Red arrow: putative PAL band[2]. For comparison of the cell lysate before and after induction of protein expression, see **Figure 10.1**. **b**, Normalized absorption spectrum (405 – 505 nm) of PAL incubated under different light conditions before biotinylation reaction. **c**, Dot blot of PAL before (**-**) and after (**+**) biotinylation reaction to visualize the biotinylation status of the protein[3]. **d**, Normalized absorption spectrum (405 – 505 nm) of PAL incubated under different light conditions after biotinylation reaction. **b**, **d**, Absorption spectra reveal three characteristic peaks (420, 444, 471 nm, respectively) of PAL in its dark conformation whereas no absorption peaks are identifiable for PAL when switched to its light conformation within the tested range. **b**, **d**, Values are processed by normalization to the absorption at 444 nm in the dark state and before irradiation (grey bars) after subtraction of the background (absorption at 504 nm).

Based on these results, it was concluded, that intact PAL could be successfully purified and biotinylated. Thus, the protein was used for downstream *in vitro* binding experiments.

In parallel, artificial *pre*-miR21 variants were designed and *in vitro* transcribed. As miR21 is among the best characterized miRs [252], presumably because its central role in cellular metabolism [253] and because there is already large experience in the laboratory with miR21 application in cells [254], the *pre*-miR21 processivity was intended to be controlled in a light-dependent manner. Therefore, sequences of mature miR21-5p and -3p were conjoined with the PAL aptamer 53.19 as connecting apical loop domain (SHA, **Figure 4.9a**). As controls, *pre*-miR-21 variants that bear a single (G11C; SHC) or a four base mutation (A7U, G8C, A10U and G11C; SHC_M4) within the PAL aptamer that renders them incompetent of binding, a non-functional mature miR domain (SHB, SHD, [255]), or with both domains altered (SHD) have been constructed (**Figure 4.9a**). As further controls for *in vitro* binding experiments, previously described full length aptamers of 04.17 (04) a non-binding sequence (46mu) and the full length aptamer of 53.19 (53) were additionally implemented in the assay [237]. All RNA constructs were tested at two different concentrations and in the absence of a competitor (1000 nM: **Figure 4.9b**, 100 nM: **Figure 4.9c**). Additionally, the *pre*-miR-21 variants 46mu, 53, SHA, SHB, SHC and SHD were incubated in presence of a competitor (1000 nM: **Figure 4.9d**, 100 nM: **Figure 4.9e**) to reduce unspecific interactions.

For assays in presence of 1000 nM RNA, the binding of SHA under light conditions is similar to the binding of 53 (108 % *vs*. 94 % in absence or presence of competitor), whereas SHB binds to a slightly weaker extent (74 % *vs*. 77 % in absence or presence of competitor) which is similar to the binding of 04 (77 % in absence of competitor). In absence of a competitor, control variants show weak binding under light conditions (36 % for 46mu, 31 % for SHC and SHD, 9 % for SHC_M4), which decreases in presence of a competitor (2 % for 46mu, 10 % for SHC, 6 % for SHD). For dark conditions, 53 shows the highest rate of binding (48 % *vs*. 49 % in absence or presence of competitor) followed by other variants that were modified with functional aptamers (31 % *vs*. 28 % for SHA, 28 % for 04, 23 % *vs*. 25 % for SHB in absence or presence of competitor). Non-binding variants show a slight binding in absence of a competitor (12 % for 46mu, 11 % for SHC_M4, 5 % for SHC and 6 % for SHD) that further decreases in presence of a competitor (1 % for 46mu, 2 % for SHC and 3 for SHD).

[2] Experiment shown in **Figure 4.8a** was performed by Charles Morgan.
[3] Experiment shown in **Figure 4.8c** was performed by Léa Angèle Dugrosprez.

For assays in presence of 100 nM RNA, the binding of SHA under light conditions is below the binding of 53 (82 % *vs*. 67 % in absence or presence of competitor), and SHB binds to a weaker extent (39 % *vs*. 51 % in absence or presence of competitor), which is below the binding level of 04 (84 % in absence of competitor). In absence of a competitor, non-binding variants show weak binding (20 % for 46mu, 44 % for SHC, 30 % for SHD, 11 % for SHC_M4), which decreases in presence of a competitor (2 % for 46mu, 6 % for SHC, 3 % for SHD) under light conditions. For dark conditions, 53 shows the highest rate of binding (56 % *vs*. 33 % in absence or presence of competitor), followed by other variants that were modified with functional aptamers (28 % *vs*. 19 % for SHA, 23 % *vs*. 14 % for SHB and 14 % for 04, in absence or presence of competitor). Non-binding variants show a slight binding in absence of competitor (10 % for 46mu, 8 % for SHC_M4, 11 % for SHC and 14 % for SHD) that further decreases in presence of a competitor (2 % for 46mu, 4 % for SHC and SHD, respectively).

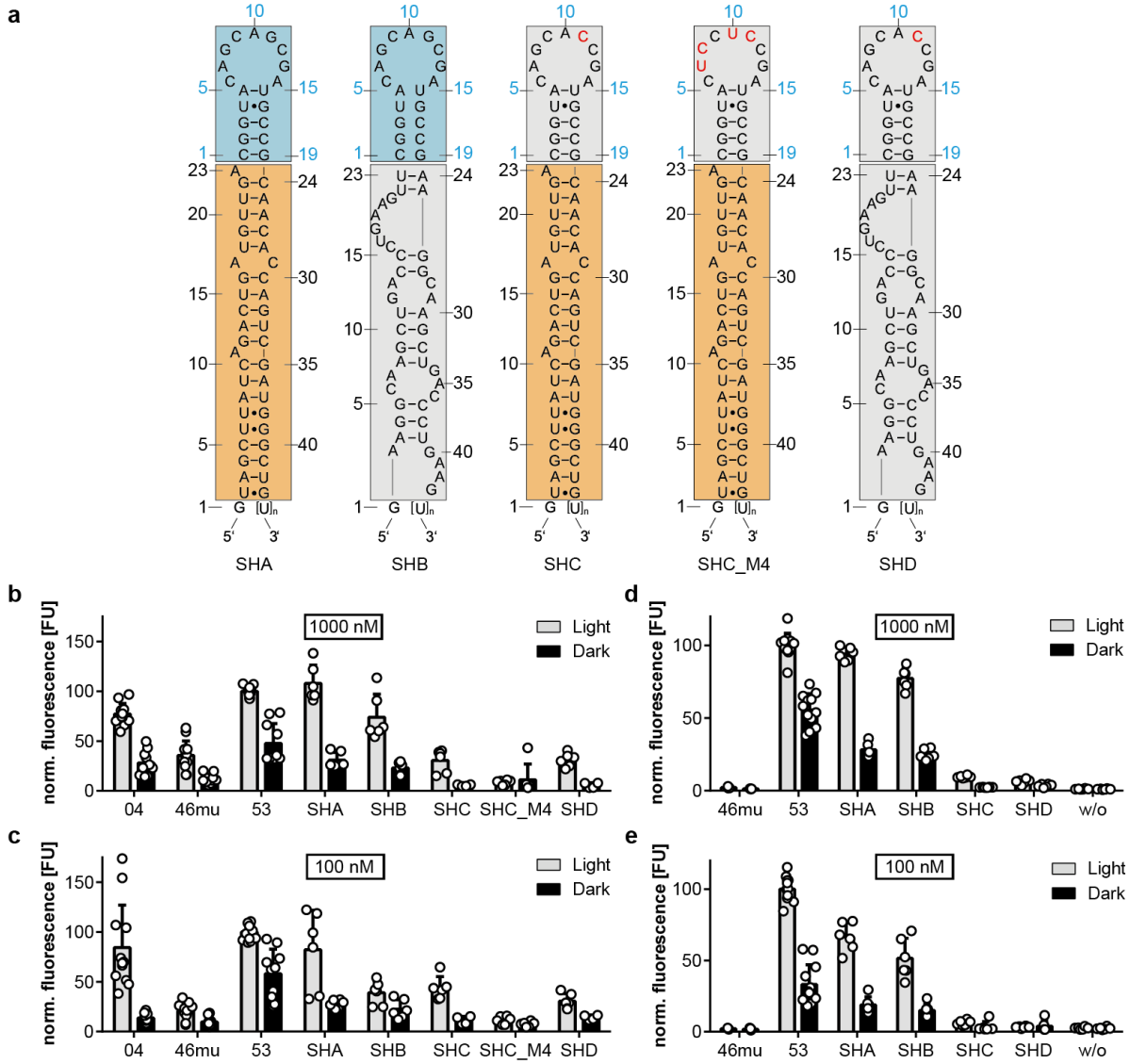

Figure 4.9: Aptamer 53.19-conjoined *pre*-miR variants bind to PAL light-dependently *in vitro*, whereas the binding is reduced for respective point mutants. a, Schematic representation of the *pre*-miR variants and corresponding controls. Blue boxes: aptamer domain, orange boxes: miR21 domain, grey boxes: aptamer point mutant or control miR. The biotinylated PAL protein was immobilized on streptavidin coated wells. Binding of 1000 nM (**b**) or 100 nM (**c**) *pre*-miR constructs was quantified in

absence of a competitor by RiboGreen fluorescence. **b**,**c**, N = At least two independent experiments performed in duplicates. The binding of 1000 nM (**d**) or 100 nM (**e**) *pre*-miR constructs in presence of 0.5 mg mL^{-1} heparin and 0.5 mg mL^{-1} BSA was quantified by RiboGreen fluorescence. **d**,**e**, N = At least three independent experiments performed in duplicates[4]. **b**-**e**, The values are processed by subtracting background fluorescence from equally treated wells without immobilized PAL and subsequent normalization to 53 incubated under light conditions. **b**-**e**, Grey bars: light conditions, black bars: darkness. Values are means ± s.d.

In conclusion, *pre*-miR variants SHA and SHB bind to PAL light-dependently *in vitro* whereas a specific binding of SHC, SHC_M4 and SHD is negligible. For the variants which bind to PAL (53, SHA, SHB), dark binding was also observed in presence of a competitor. However, effects in darkness have not been observed in a cellular context (**Figure 4.4**), which suggests that the dark binding may be an assay specific observation.

4.2.2 Development and optimization of a light-controllable *pre*-miR21 reporter system

Next, *in vitro* tested *pre*-miR21 variants have been tested in mammalian cells for their ability to control target gene expression in a light-dependent manner when PAL is present. To this end, a cell line that stably expresses mCherry-PAL and a cell reporter system was established.

4.2.2.1 Generation and characterization of a cell line stably expressing mCherry-PAL (HEK293PAL)

To facilitate transient transfection experiments, a mCherry-PAL cell line was generated. Direct translational control by incorporating aptamer 53.19 into the 5'UTR of a target mRNA was realized by co-transfecting two plasmids, with one plasmid which encodes for the photoreceptor PAL and another plasmid which encodes for aptamer 53.19-modified luciferase mRNA (**Figure 4.4**). In case of gene expression control using regulatory RNAs, the functionality of reporter mRNA and the *pre*-miRs variants is separated into two plasmids. This circumstance prompts triple-transfections, with the potential risk of reducing the light-responsiveness. Initial attempts in which *pre*-miR21 variants were co-transfected together with mCherry-PAL and luciferase reporter did not reveal promising results (data not shown). Thus, a HEK293 cell line that expresses mCherry-PAL stably (HEK293PAL) was generated (see also section 7.5.4). This cell line ensures steady-state levels of PAL in the cell, thereby reducing protein fluctuations that would be obtained potentially from transient transfections. To characterize the mCherry-PAL protein amount and function in HEK293PAL cells, flow cytometry (**Figure 4.10a**,**b**), fluorescence microscopy (**Figure 4.10b**) and *in vitro* mCherry protein quantification experiments (**Figure 4.10d**-**f**) were performed.

For flow cytometry, the fluorescence of mCherry and PAL was compared between HEK293 cells and HEK293PAL cells. Mean fluorescence of HEK293PAL cells was ~28 times higher in the mCherry

[4] Experiments shown in **Figure 4.9d**,**e** were performed by Charles Morgan

channel (**Figure 4.10a**) and ~2.5 times higher in the PAL channel (**Figure 4.10b**), compared to HEK293 cells. Both measured fluorescence channels featured a normally distributed expression pattern which indicates homogenous mCherry-PAL expression throughout the cell population (**Figure 4.10a**,**b**). Subsequently, HEK293PAL had been seeded and incubated 24 h in darkness, before the cells were analyzed by fluorescence microscopy (**Figure 4.10c**). At this time point, the fluorescence of both mCherry and PAL could be detected. Immediately after subsequent exposure of cells to blue light, imaging had been performed. This revealed a strongly decreased PAL fluorescence which indicates conformational switching to the non-fluorescent light state of the PAL protein. After a 10 min recovery step in darkness, fluorescence of PAL could be detected to the same extent as before the blue light irradiation (**Figure 4.10c**). Throughout all applied conditions, mCherry fluorescence was equally detectable. Next, mCherry protein quantification was performed to determine the average number of mCherry-PAL molecules per cell. For that purpose, the volume of the cell's cytosol was estimated (1333 μm^3, [256]). Then, a mCherry standard curve (**Figure 4.10d**) was prepared by using a mCherry protein standard. The corresponding mCherry fluorescence was recorded together with fluorescence that was measured from protein lysates which were prepared from 10^6 HEK293PAL cells. The standard curve gave insight about the linear range between the measured fluorescence and the mCherry protein mass. As a distinct number of HEK293PAL cells was subjected to lysis, the number of proteins per cell could be calculated resulting in a mean value of ~840.000 mCherry-PAL molecules per cell (**Figure 4.10e**). By assuming a cell volume of 4000 μm^3 and the cytosol to occupy one third of the cell's volume, the molarity of mCherry-PAL in the cytosol was calculated which led to a value of ~1.1 µM (**Figure 4.10f**).

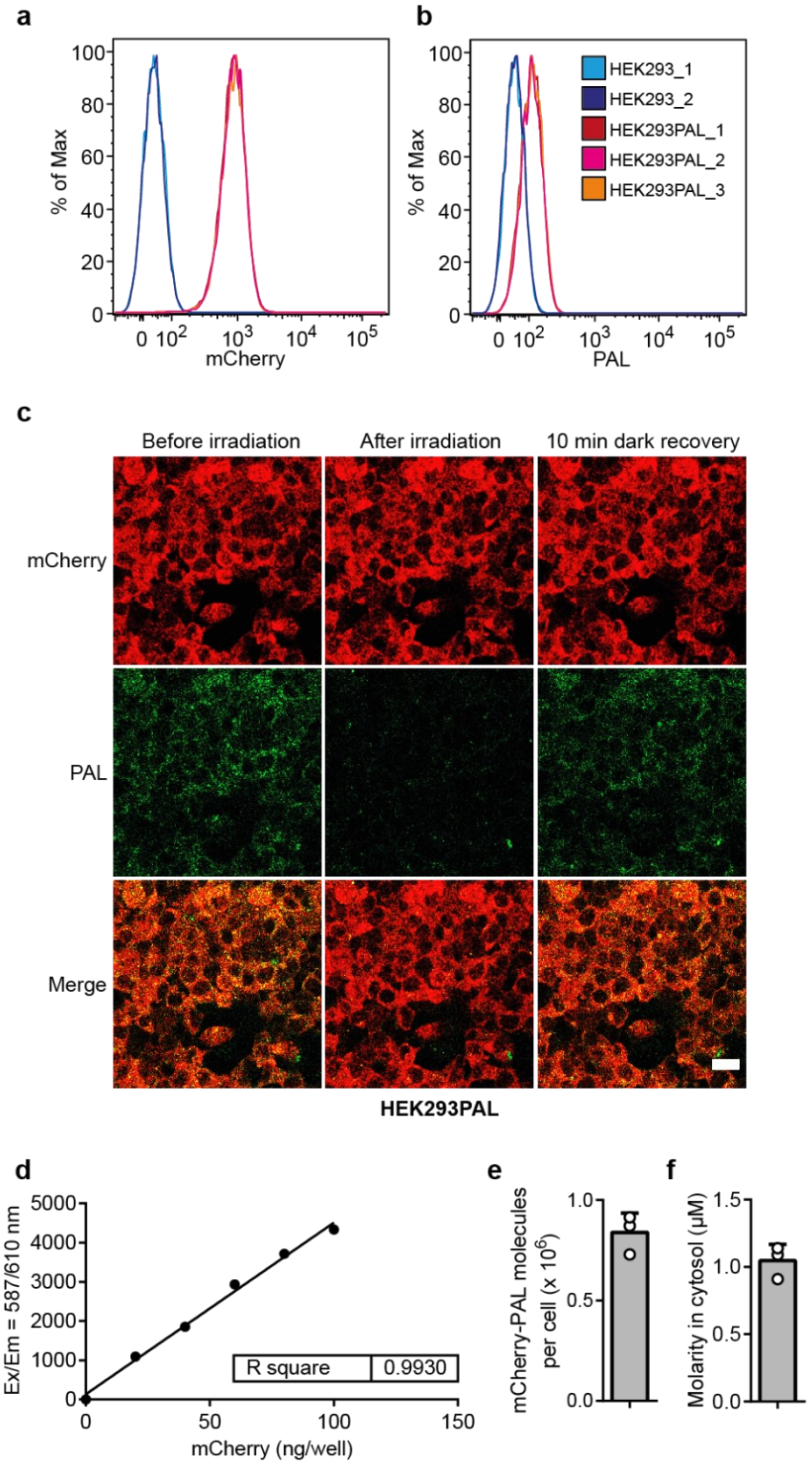

Figure 4.10: Characterization of the Hek293 cell line stably expressing mCherry-PAL (HEK293PAL). Flow cytometry histograms of mCherry (**a**) and PAL (**b**) fluorescence measured from HEK293 and HEK293PAL cells (legend for **a**: see **b**). **a**,**b**, Singlet cells were detected using side scatter area (SSC-A) *vs*. forward scatter area (FSC-A). **a**,**b**, The experiment was performed one time. **c**, HEK293PAL cells were seeded and fluorescence of mCherry and PAL was determined after the cells had been exposed to the indicated light conditions (incubation in darkness, immediately after irradiation with blue light for 1 min or after 10 min further incubation of these cells in darkness) by using fluorescence microscopy. **c**, The experiment was performed in duplicates and in two independent replications and together with constructs shown in **Figure 4.1**. Scale bar: 20 µm. **d**, The representative standard curve for determination of the linear range of mCherry quantification. **e**, Determination of average mCherry-PAL molecules per cell by using the corresponding mCherry standard curve. **f**, Calculation of the mCherry-PAL molarity

in the cytosol based on the measurements of (**e**). **d-f**, N = Three biologically independent experiments performed with three different cell concentrations, each.

Taken together, the HEK293PAL cell line expresses mCherry-PAL homogeneously at an average molarity of 1.1 µM mCherry-PAL in the cytosol and the protein displays intact photochemistry. All these arguments suggest that HEK293PAL cells might be a suitable cell line for hosting regulatory RNA reporter gene experiments.

4.2.2.2 Optimization of plasmid transfection ratios for regulatory RNA experiments

One question that arose when beginning to work with regulatory RNAs in cells was whether the plasmid ratio of regulatory RNA *vs*. reporter plasmid would influence the differences of reporter protein expression between the light states. To answer this question, an experiment was conducted in which the ratio of both plasmids was altered when transfected into HEK293PAL cells. However, the total amount of transfected plasmid per well (500 ng) was kept constant to ensure that a comparable total amount of total DNA was transfected for all samples.

pSilencer plasmid variants either coding for SHA or SHC_M4 (**Figure 4.9a**) were transfected in mass excess (99:1, 66:1, 49:1, 24:1, 9:1) or in equal mass amounts (1:1) to the luciferase reporter plasmid (pLuciferase). The pLuciferase plasmid has four miR21-5p binding sites that were incorporated into the 3'UTR of its mRNA which enables miR21-depenent gene suppression (**Figure 4.12a**). Increasing proportions of the pSilencer plasmid SHA led to increased fold changes in luciferase expression for 9:1 (1.3-fold) and 24:1 (1.6-fold) and reached a plateau for 49:1 (2.0-fold), 66:1 (2.2-fold) and 99:1 (2.1-fold), respectively (**Figure 4.11b**). No light-dependent difference in luciferase expression was observed for a 1:1 plasmid ratio of SHA and for all tested plasmid ratios using SHC_M4 (**Figure 4.11b**). Furthermore, it was observed that the total level of luciferase expression peaked when equal amounts of plasmid were transfected (1:1, **Figure 4.11a**) independently to the tested pSilencer variant. Conversely, a gradual increase in the amount of transfected pSilencer plasmid (and the simultaneous decrease in the amount of transfected pLuciferase) correlated with a decrease of luciferase expression levels.

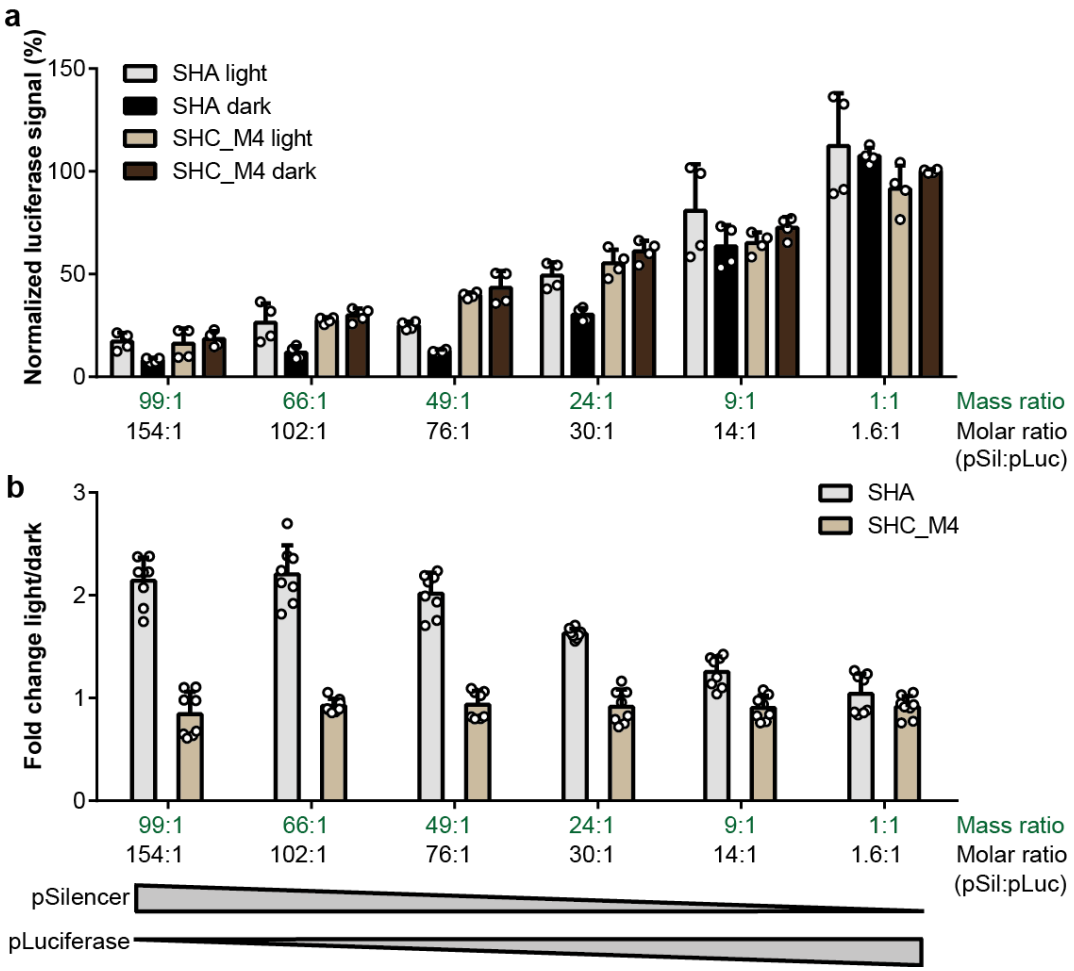

Figure 4.11: Mass excess transfection of pSilencer plasmid displays increased light-responsiveness. a, Luciferase expression of HEK293PAL cells after transfection at the indicated mass ratio (green) or molar ratio (black) with the indicated pSilencer plasmid variant (SHA or SHC_M4, see also **Figure 4.9a**) and a luciferase reporter plasmid (pLuciferase) which has four binding sites complementary to miR21-5p incorporated in its 3'UTR (Luc-5p, **Figure 4.12:a**). The values are normalized to SHC_M4 which was transfected with pLuciferase at a mass ratio of 1:1 and incubated in darkness. **b**, Fold changes for SHA and SHC_M4 which were calculated from light *vs*. dark conditions from (**a**). **a**,**b**, N = Two biologically independent experiments performed in duplicates. Values are means ± s.d.

From this experiment, it was concluded that a high plasmid ratio of pSilencer *vs*. *Metridia* Luciferase leads to higher light-dependent fold changes. Among the three candidate ratios (100:1, 75:1 and 50:1), a ratio of 100:1 was selected arbitrarily for further experiments. However, it needs to be stated that this might not be the optimal condition at which the highest possible light-dependent fold changes may be achieved. To determine this point, the amount of pLuciferase should be kept constant while the amount of pSilencer may be titrated. In such an experiment higher fold changes could be potentially achieved because a potential excess of pSilencer plasmid compared to luciferase plasmid could be adjusted. Furthermore, the plasmid mass ratio was used as a measure in this experiment. A more comprehensive measure may be the molar ratio, because it directly compares the number of transfected molecules.

4.2.2.3 Investigation of reporter gene suppression by miR21-5p, miR21-3p and miR21-5p-3p

Based on the idea, that in principle, either the -5p (upstream) or -3p (downstream to the loop sequence) mature miR strand processed from a *pre*-miR can be loaded into the RISC complex [257], the impact of both mature miR strands in the artificial *pre*-miR21 SHA on reporter gene expression was tested together with further controls. Therefore, three luciferase reporter plasmids which bear either four binding sites for mature miR21-5p (**Figure 4.12a**), miR21-3p (**Figure 4.12e**) or both strands (**Figure 4.12c**) were co-transfected with either SHA, SHB or SHC_M4. Light-dependent expression in darkness for SHA could be observed together with all three luciferase plasmids with 18 % for Luc-5p (**Figure 4.12b**), 15 % for Luc-5p-3p (**Figure 4.12d**) and 64 % for Luc-3p (**Figure 4.12f**) of luciferase expression compared to SHB which was also incubated in darkness for each luciferase construct. Under light conditions, the expression for SHA reached 35 % for Luc-5p (**Figure 4.12b**), 34 % for Luc-5p-3p (**Figure 4.12d**) and 80 % for Luc-3p (**Figure 4.12f**). This leads to fold changes of 2.0 (Luc-5p), 2.3 (Luc-5p-3p) and 1.3 (Luc-3p), respectively (**Figure 4.12g**). No light-dependent fold changes could be detected for SHC_M4 and SHB (**Figure 4.12g**). Expression levels of SHC_M4 under light conditions were 21 % for Luc-5p, 20 % for Luc-5p-3p and 64 % for Luc-3p (**Figure 4.12b**,**d**,**f**) and 26 % for Luc-5p, 24 % for Luc-5p-3p and 69 % for Luc-3p in darkness (**Figure 4.12b**,**d**,**f**). Thus, luciferase expression levels for SHC_M4 for both light states were comparable to the levels of luciferase expression which were obtained by the corresponding SHA transfections in darkness (**Figure 4.12b**,**d**,**f**). SHB did not display suppression of luciferase expression (**Figure 4.12b**,**d**,**f**).

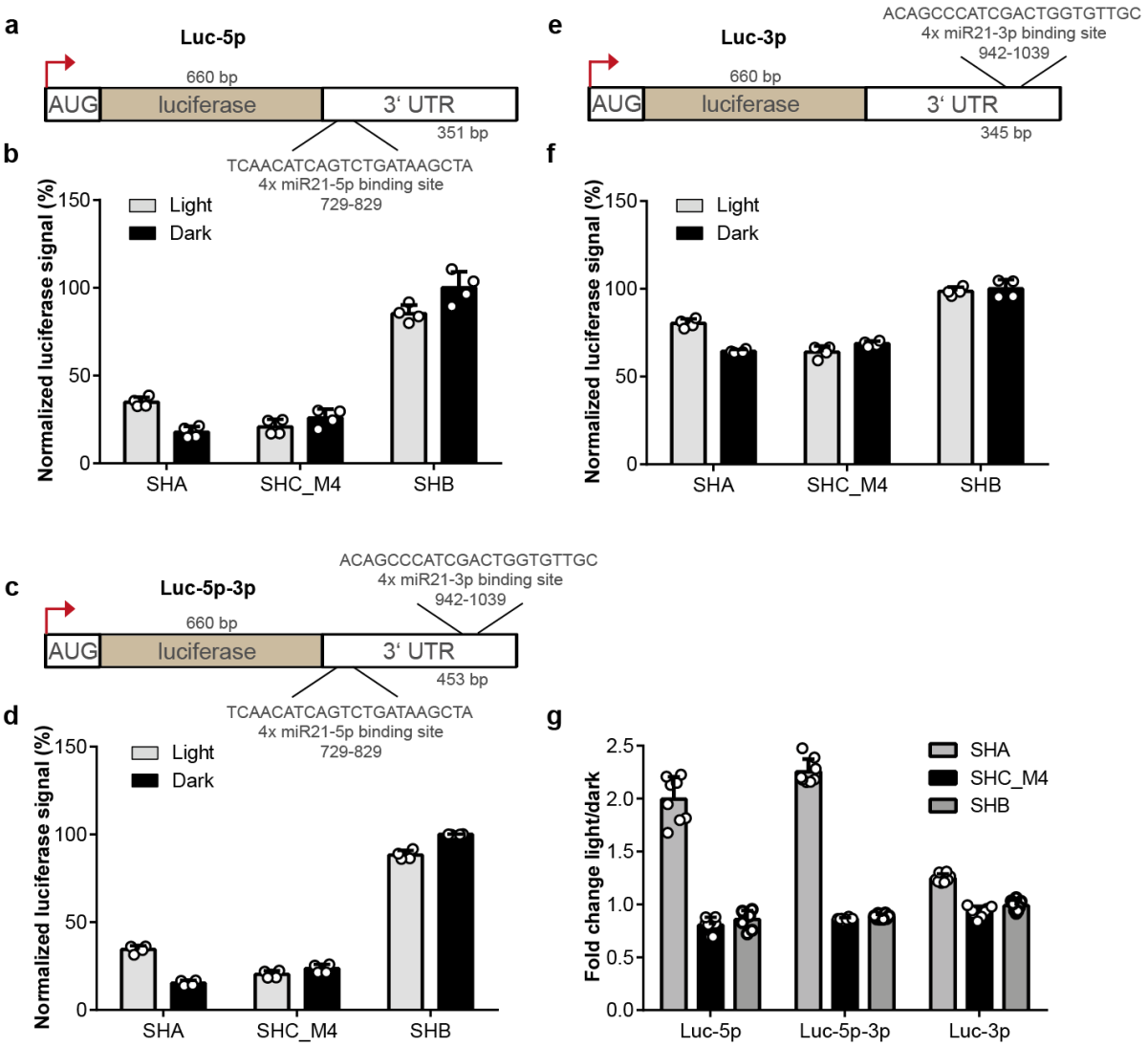

Figure 4.12: miR21-5p but not -3p is predominantly responsible for reporter protein suppression. **a**, Schematic representation of the luciferase reporter mRNA which has four binding sites complementary to miR21-5p incorporated in its 3'UTR (Luc-5p) that was applied in (**b**). **b**, Luciferase expression of HEK293PAL cells after transfection with the indicated pSilencer plasmid variants (SHA; SHC_M4, SHB) and Luc-5p. **c**, Schematic representation of the luciferase reporter mRNA which has four binding sites complementary to miR21-3p incorporated in its 3'UTR (Luc-3p) that was applied in (**d**). **d**, Luciferase expression of HEK293PAL cells after transfection with the indicated pSilencer plasmid variants (SHA; SHC_M4, SHB) and Luc-3p. **e**, Schematic representation of the luciferase reporter mRNA which has four binding sites complementary to both mature miR21 strands incorporated in its 3'UTR (Luc-5p-3p) that was applied in (**f**). **f**, Luciferase expression of HEK293PAL cells after transfection with the indicated pSilencer plasmid variants (SHA; SHC_M4, SHB) and Luc-5p-3p. **a**,**c**,**e**, red arrow: Translation start site. **g**, Fold changes calculated from light *vs*. dark conditions from (**b**), **(d)** and **(f)**. **b**,**d**,**f**, Values are normalized to cells which express SHB and were incubated in darkness. **b**-**g**, N = Two biologically independent experiments performed in duplicates. Values are means ± s.d.

It was concluded that miR21-5p decreases target gene knockdown more effectively compared to miR21-3p. Furthermore, an incorporation of both binding sites in the 3'UTR of target mRNA (Luc-5p-3p) increases the light-dependent differences in luciferase expression slightly.

4.2.2.4 Screening of PAL-responsive *pre*-miR21 variants

Next, different *pre*-miR21 variants based on SHA have been generated by rational design. As it had been described before, unpaired 5' nucleotide overhangs may impair dicer processing [258]. In order to enable base pairing at the starting nucleotide, the nucleotide sequence of SHA was modified (SHA_V1, **Figure 4.13a**). Transcription under the control of a U6 promoter results in a heterogenous number of uridine residues at the 3' end of the transcription product [259]. As the dicer protein preferentially recognizes two nucleobase overhangs at the 3' end [260], a hammer head ribozyme [261] was embedded downstream of the sequence of SHA to generate *pre*-miRs with precise 3' termini consisting of two uracil nucleotide overhangs (SHA_V2). For SHA_V3, the stem-loop of the aptamer was shortened and the unpaired adenine bulge (A23 of SHA) was removed, thereby bringing the PAL aptamer and the putative dicer cleavage site in closer proximity [196]. In principle, this could favor steric hindrance of dicer cleavage of the *pre*-miR in the PAL-bound state. SHA_V4 was generated to test the impact of a perfectly hybridized stem with an intact miR21-5p and adjusted -3p stem sequence on the target gene expression. HEK293PAL cells were transfected with one of the SHA variants or a control variant (SHB, SHC, SHC_M4 or SHD) together with Luc-5p-3p and a luciferase expression was measured 19 h after incubation under the indicated light conditions (**Figure 4.13b**). In darkness, SHA_V4 displayed the lowest luciferase expression (6 %), followed by SHA (15 %), SHA_V3 (18 %), SHA_V2 (47 %) and SHA_V1 (61 %). Furthermore, the luciferase expression under light conditions followed the same order (SHA_V4 = 10 %, SHA = 37 %, SHA_V3 = 40 %, SHA_V2 = 66 % and SHA_V1 = 76 %). The highest light-dependent fold change was calculated for SHA (2.6), followed by SHA_V3 (2.4), SHA_V4 (1.7), SHA_V2 (1.4) and SHA_V1 (1.3) and no notable fold changes were observed for the controls SHB, SHC, SHC_M4 and SHD (**Figure 4.13c**). A reduced luciferase expression was displayed by SHC and SHC_M4 (13 – 18 %), whereas no decrease in luciferase expression was detected for SHB and SHD (**Figure 4.13b**).

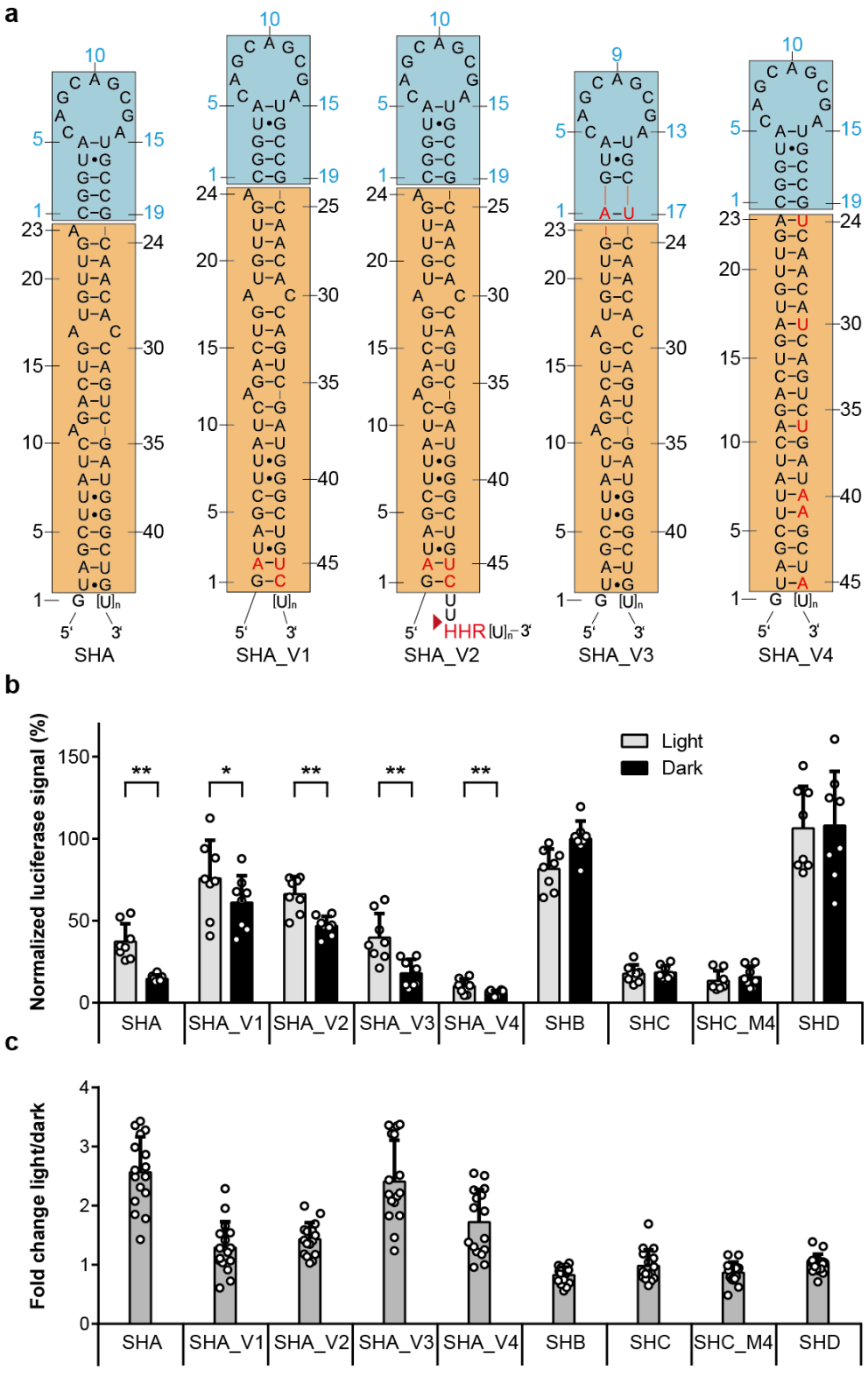

Figure 4.13: Structural variants of *pre*-miR21 SHA reveal altered light-responsiveness. a, Schematic representation of the tested *pre*-miR21 variants of SHA (for schematics of controls, see **Figure 4.9a**). Blue boxes: aptamer domain, orange boxes: miR21 domain, red nucleotides: nucleotide variations deviating from original SHA. HHR: hammer head ribozyme. Red arrow: putative HHR cleavage site. **b**, Luciferase expression of HEK293PAL cells after transfection with the indicated *pre*-miR21 variants and Luc-5p-3p. Values are normalized to SHB incubated in darkness. Grey bars: light conditions, black bars: dark conditions. **b**, Wilcoxon two-sided signed-rank test was used for statistical analysis as a paired observation was assumed: **p* = 0.0234, ***p* = 0.0078. **c**, Fold changes calculated from light *vs*. dark conditions from (**b**). Dark grey bars: Fold changes. N = four biologically independent experiments that were performed in duplicates. Values are means ± s.d.

These results indicate that SHA displays the highest light-dependent difference in luciferase expression with intermediate luciferase levels under light conditions and relatively low expression levels in darkness among the tested *pre*-miR21 variants.

As an alternative to motif2-based aptamer 53.19, the motif1-based aptamer 04.17 should also be tested for its potential to light-control gene expression. To this end, aptamer 04.17 was conjoined with *pre*-miR21 as apical loop domain (see also section 2.4.2) and tested for binding to PAL *in vitro* (**Figure 4.14**) as well as for reporter assay performance in mammalian cells (**Figure 4.15**). For *in vitro* binding assays, the functional pre-miR21-04.17 variant (SHI) was tested along with a *pre*-miR-21 variants which has a point mutation within the 04.17 sequence that renders the construct incompetent of binding (A7U, SHJ) and a variant which has a non-functional miR-21 domain and a functional aptamer 04.17 domain (SHK, **Figure 4.14a**). As additional controls, the full length aptamer of 04.17 (04), a non-binding sequence (46mu) and the full length aptamer of 53.19 (53) were implemented in the assay and all constructs were tested at two different concentrations of RNA in absence of a competitor (1000 nM: **Figure 4.14b**, 100 nM: **Figure 4.14c**). As the experiment that is shown in **Figure 4.14** had been performed before the experiment that is shown in **Figure 4.9**, no competitor was used because it was still not known if the presence of a competitor would reduce the unspecific binding. For assays under light conditions and in presence of 1000 nM RNA, the binding of SHI was at the level of negative control 46mu (25 % *vs*. 24 %), while SHK showed an increased binding (41 %) which was about half the binding of the positive control 04 (81 %). SHJ almost showed no binding (11 %). Under dark conditions, the binding of all *pre*-miR21 variants was remarkably low (9 %, 8 % and 15 % for SHI, SHJ and SHK, respectively) and within the range of the negative control 46mu (11 %), whereas positive controls showed an increased binding (32 % and 57 % for 04 and 53, respectively). For assays under light conditions and in presence of 100 nM RNA, binding of SHI was more than half of the positive control 04 (25 % *vs*. 41 %) and SHK showed a slightly increased binding compared to SHI (33 %), whereas 46mu and SHJ displayed a weak binding (11 % and 9 %, respectively). Under dark conditions, the binding of all *pre*-miR21 variants was again remarkably low (9 % for SHI and SHJ and 8 % for SHK) and within the range of the negative control 46mu and the positive control 04 (8 % and 9 %, respectively), while the positive control 53 indicated a binding to some extent (35 %).

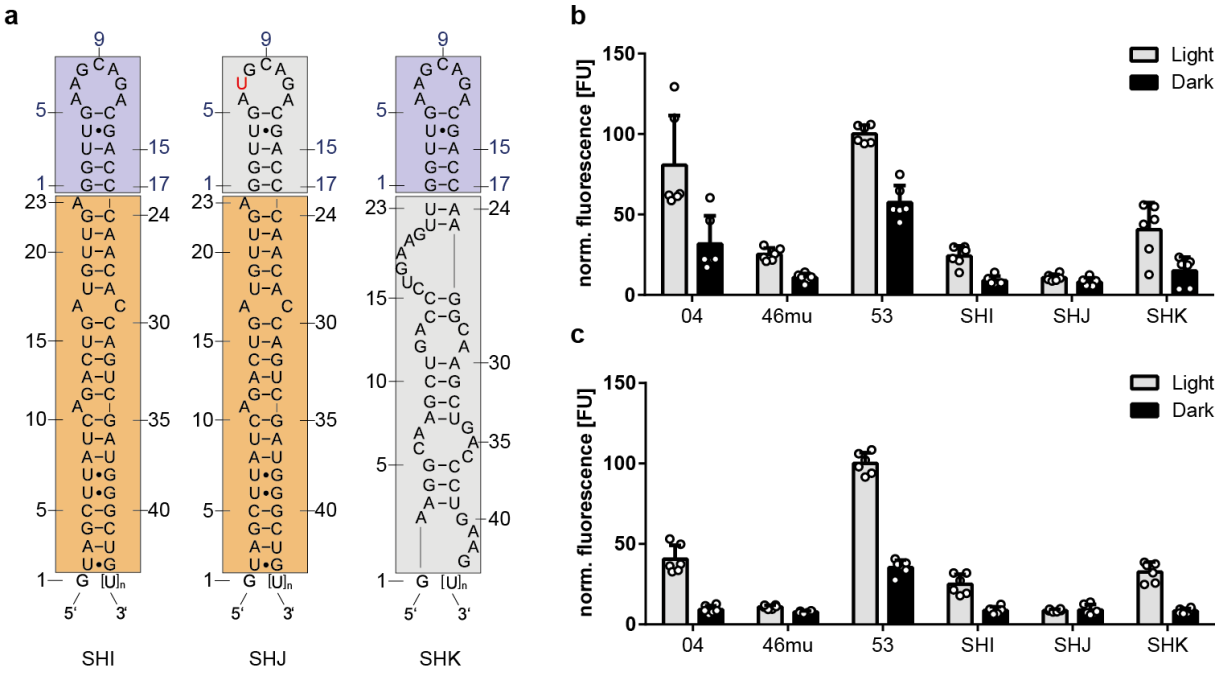

Figure 4.14: Aptamer 04.17-conjoined *pre*-miR21 variants bind weakly to PAL light-dependently *in vitro* and the binding is reduced for respective point mutant. a, Schematic representation of the *pre*-miR variants and corresponding controls. Violet boxes: aptamer domain, orange boxes: miR21 domain, grey boxes: aptamer point mutant or control miR. Biotinylated PAL protein was immobilized on streptavidin coated wells. Binding of 1000 nM (**b**) or 100 nM (**c**) *pre*-miR constructs were quantified by RiboGreen fluorescence. **b**,**c**, Values are processed by subtracting background fluorescence from equally treated wells without immobilized PAL and subsequent normalization to 53 which was incubated under light conditions. **b**,**c**, N = Three independent experiments performed in duplicates. Grey bars: light conditions, black bars: darkness. Values are means ± s.d.[5]

Taken together, aptamer 04.17-modified *pre*-miR variants SHI and SHK bind weakly to PAL *in vitro*, whereas SHJ does not bind to PAL.

As weak to no binding of SHI and SHK to PAL was observed *in vitro* (**Figure 4.14**), extended stem variants of SHI with increasing aptamer 04.17 lengths were constructed with the aim to restore binding to PAL. The stem extensions were derived from the full length aptamer 04. Thus, three (SHI_V1) or five (SHI_V2) additional base pairs were added to the stem region of SHI (**Figure 4.15a**). To test whether the three aptamer 04-modified *pre*-miR21 variants (SHI, SHI_V1 and SHI_V2) are capable to control luciferase expression light-dependently, HEK293PAL cells were co-transfected with the respective pSilencer plasmid or control plasmids (SHJ, SHK) and Luc-5p-3p (**Figure 4.12c**). Unexpectedly, none of the tested transfections displayed light-dependent gene expression (**Figure 4.15c**). Transfections with SHI and SHJ showed a reduction in luciferase expression (13 % *vs*. 15 % for SHI in light and dark, 19 % *vs*. 23 % for SHJ in light and dark), whereas a decrease in luciferase expression could not be detected in case of a transfection with SHI_V1 (145 % under light conditions and 148 % in darkness), SHI_V2 (107 % under light conditions and 121 % in darkness) or SHK (85 % under light conditions and 100 % in darkness). Untransfected cells (None) did not indicate an expression of luciferase (< 1 %, **Figure 4.15b**).

[5] Experiment shown in **Figure 4.14** was performed by Léa Angèle Dugrosprez.

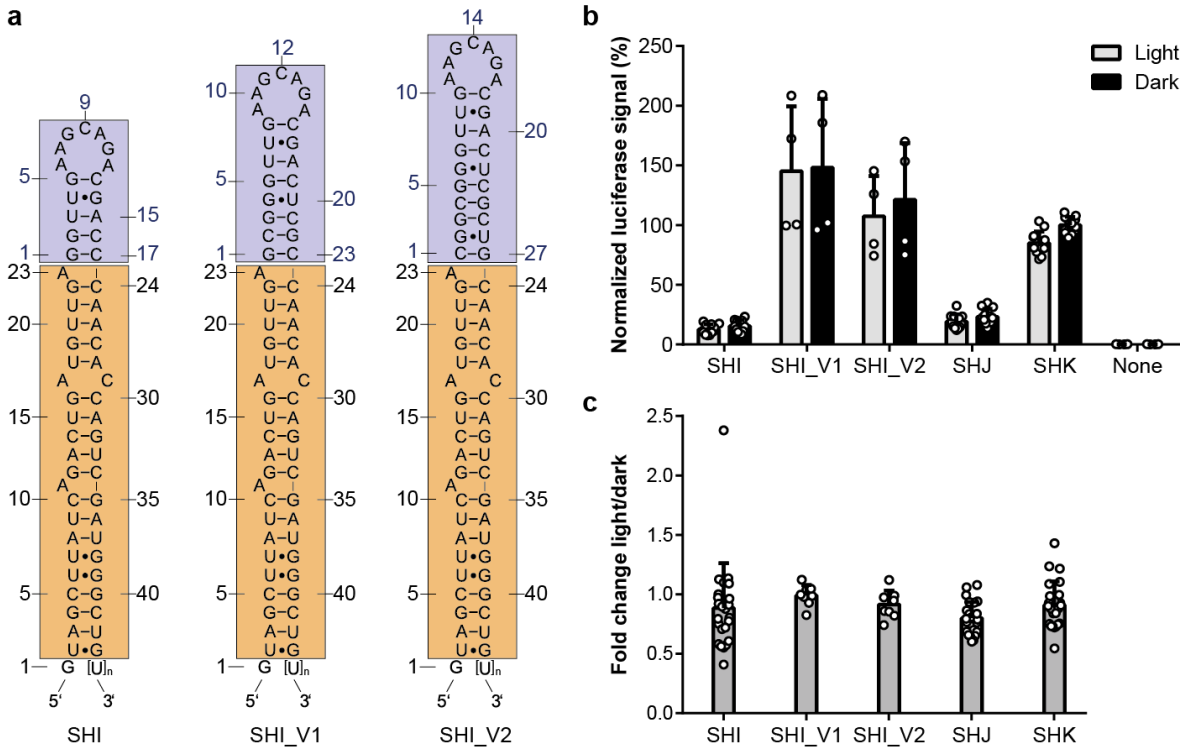

Figure 4.15: Aptamer 04.17-conjoined *pre*-miR21 variants do not display light-dependent gene expression in mammalian cells. a, Schematic representation of the tested *pre*-miR21 variants with extended aptamer 04 stems were derived from full length aptamer 04 (for schematics of controls, see **Figure 4.14a**). Violet boxes: aptamer domain, orange boxes: miR21 domain. **b**, Luciferase expression of HEK293PAL cells after transfection with the indicated *pre*-miR21 variants and Luc-5p-3p. Values are normalized to SHK incubated in darkness. Grey bars: light conditions, black bars: dark conditions. **c**, Fold changes calculated from light *vs*. dark conditions from (**a**). Dark grey bars: Fold changes. N = Two (SHI_V1, SHI_V2 and None) or six (all others) biologically independent experiments performed in duplicates. Values are means ± s.d.

It was concluded that the light-regulation of the target gene expression cannot be achieved with aptamer 04 conjoined to *pre*-miR21. This might be due to the temperature sensitivity of aptamer 04 [237] and limited possibilities for construct optimization. Therefore, it was decided to conduct further studies with the most promising *pre*-miR21-53.19 variant SHA.

4.2.2.5 Light-regulation of reporter gene expression using a transfection protocol without FCS

Until now, the transfection was performed in presence of FCS for *pre*-miR21 experiments in cells (**Figure 4.13**). However, the presence of FCS might limit the transfection efficiency [262, 263]. Consequently, a two-days transfection protocol was applied in which cells were transfected in DMEM containing no FCS one day after seeding. Four hours after transfection, FCS was added to ensure cell growth. Therefore, the *pre*-miR21 construct SHA and further controls (SHB, SHC or SHD) were co-transfected with Luc-5p-3p (**Figure 4.17a**). Only when SHA was transfected, a light-dependent increase in luciferase expression could be observed (4.4-fold, **Figure 4.17c**). These samples displayed 27 % of luciferase expression in light, whereas only 6 % of expression was observed in darkness (**Figure 4.17b**). Moreover, dark expression was comparable to the expression levels when SHC was transfected (8 % in light and darkness, **Figure 4.17b**). Neither an increased luciferase expression under light conditions

compared to dark conditions, nor a global decrease of luciferase expression was observed for the transfection of SHB (99 % under light conditions *vs*. 98 % in darkness) and SHD (91 % under light conditions *vs*. 100 % in darkness, **Figure 4.17b**).

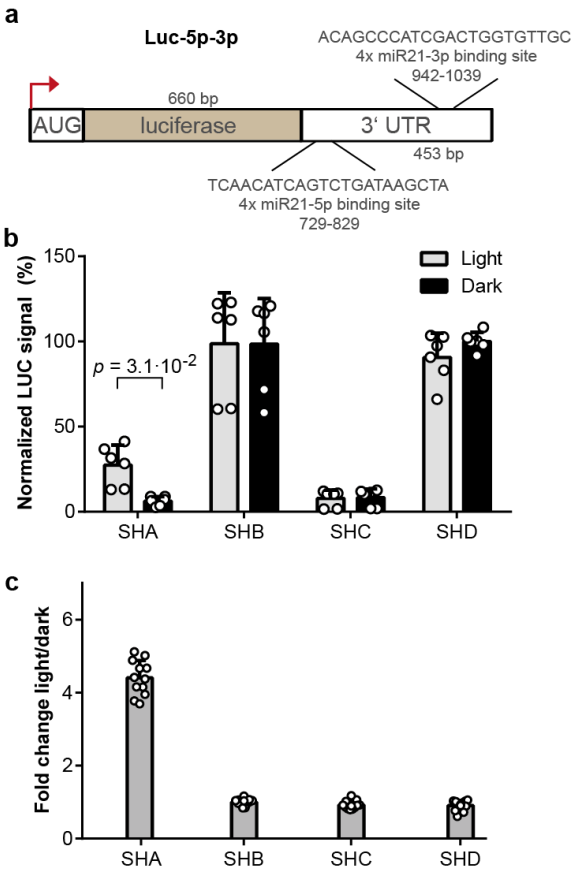

Figure 4.16: The light-regulation of luciferase expression by SHA can be increased when the transfection is performed in absence of FCS. a, Schematic representation of the luciferase reporter mRNA which has four binding sites complementary to both mature miR21 strands incorporated in its 3'UTR (Luc-5p-3p) that was applied in **b** and **c**. **b**, Luciferase expression after transfection of the indicated *pre*-miR21 variants. Values are normalized to SHD incubated in darkness. **c**, Fold changes were calculated from light *vs*. dark conditions from (**b**). **b**,**c**, N = Three biologically independent experiments performed in duplicates. **b**, Grey bars: light conditions, black bars: dark conditions. **c**, Dark grey bars: Fold changes. **b**, Wilcoxon two-sided signed-rank test was used for statistical analysis as a paired observation was assumed. Values are means ± s.d.

To demonstrate the spatial controllability in later experiments, the expression of the fluorogenic protein eGFP was also set under the control of the *pre*-miR21 variant SHA. Other than the *Metridia* luciferase, eGFP can be directly observed in living cells. Whereas the *Metridia* luciferase, a secretable protein, is translated into the lumen of the endoplasmic reticulum [264], the eGFP reporter protein is both translated and subsequently accumulated in the cytosol. Therefore, it should be tested whether the reporter assay is transferrable to eGFP. The plasmids for both reporter proteins share the same 3'UTR design except for one nucleobase that is part of the stop codon (not shown). As in case of the luciferase mRNA, the 3'UTR sequence of eGFP was modified with four binding sites that match to the miR21-5p and miR21-3p strands (eGFP-5p-3p, **Figure 4.17a**). For the eGFP assay, the same *pre*-miR variants as for the luciferase assay (**Figure 4.16**) had been co-transfected with eGFP-5p-3p. As an additional control group

for the eGFP experiment, SHA was co-transfected with eGFP which has no miR21 binding sites (SHA + eGFP, **Figure 4.17b**,**c**). Here, cells which express SHA together with eGFP-5p-3p indicated light-dependency uniquely (4.4-fold, **Figure 4.17c**) and displayed 32 % of eGFP expression in light, whereas only 8 % of expression was observed in darkness (**Figure 4.17b**). The dark expression of cells transfected with SHA was slightly lower, compared to SHC (17 % in light and darkness). Transfections with SHB (77 % in light and darkness) and SHD (100 % in light and darkness) showed increased, light-independent eGFP expression levels and no light-dependent differences (**Figure 4.17b**). When SHA was co-transfected with eGFP that has no miR21 binding sites, elevated light independent eGFP expression levels (144 % under light conditions *vs*. 146 % in darkness) could be detected compared to the non-targeting control transfections (SHB, SHC) with eGFP-5p-3p (**Figure 4.17b**).

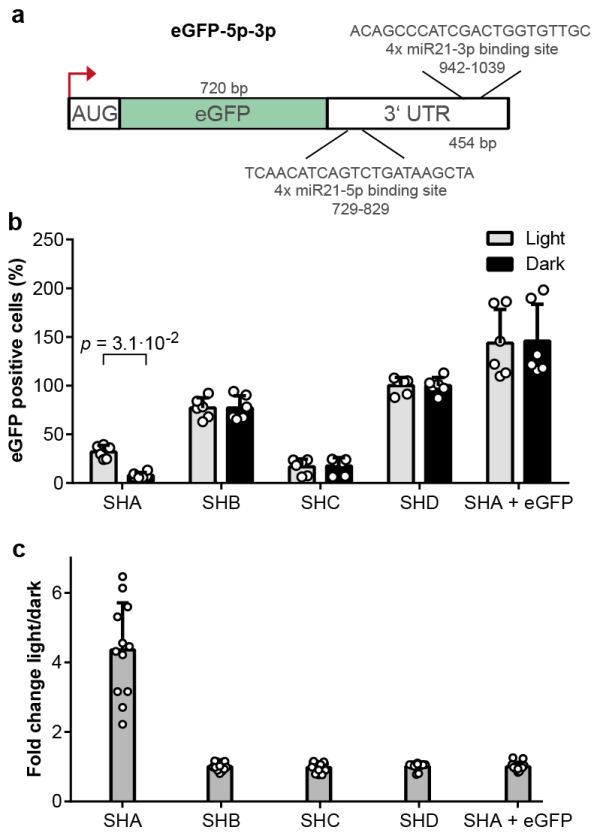

Figure 4.17: The reporter gene identity for SHA-mediated expression control is exchangeable. a, Schematic representation of the eGFP reporter mRNA which has four binding sites complementary to both mature miR21 strands incorporated in its 3'UTR (eGFP-5p-3p) that was applied in **b** and **c**. **b**, Number of cells expressing eGFP after transfection of the indicated *pre*-miR21 variants. Values are normalized to SHD incubated in darkness. **c**, Fold changes calculated from light *vs*. dark conditions from (**b**). **b**,**c**, N = Three biologically independent experiments performed in duplicates. **b**, Grey bars: light conditions, black bars: dark conditions. **c**, Dark grey bars: Fold changes. **b**, Wilcoxon two-sided signed-rank test was used for statistical analysis as a paired observation was assumed. Values are means ± s.d.

Taken together, the transfection in absence of FCS showed increased light responsiveness for the luciferase reporter assay compared to the transfection in presence of FCS. The light-responsive *pre*-miR21 system could be modified to control a second reporter protein which demonstrates the modular

applicability of the approach. Finally, it was observed that the presence of miR21 binding sites in the 3'UTR decreases the eGFP reporter protein expression slightly in a light-independent manner (**Figure 4.17c**: SHA + eGFP *vs*. SHB/SHD).

4.2.2.6 Light-regulation of reporter gene expression in presence of elevated AGO2 levels

It is described in literature, that an overexpression of regulatory RNAs such as *pre*-miRs or shRNAs might saturate the intrinsic RNA interference machinery. In this case intrinsic AGO2 levels might be exceeded. This leads to incomplete suppression of overexpressed mRNAs [186]. To investigate the target gene suppression of SHA on eGFP-5p-3p regulation in presence of elevated AGO2 levels, the experiment that is shown in **Figure 4.17b**,**c** was repeated and extended for co-transfection of AGO2 [265]. To this end, SHA, SHB, SHC, SHD (encoded on pSilencer plasmids, **Figure 4.9a**) were co-transfected with eGFP-5p-3p (**Figure 4.17a**). As additional control, 10 nM miR21 mimic was transfected instead of a pSilencer plasmid together with eGFP-5p-3p. Furthermore, SHA was co-transfected with eGFP which has no miR21 binding sites (SHA + eGFP). Here, transfection of HEK293PAL cells with SHA and eGFP-5p-3p indicated light-dependency (9-fold, **Figure 4.18b**) and displayed 48 % of luciferase expression in light, whereas only 6 % of expression was observed in darkness (**Figure 4.18a**). The dark expression of SHA was close to the expression range of SHC (3 % under light conditions *vs*. 5 % in darkness) and the expression was suppressed completely in cells which express miR21 mimic (below 1 % in light and darkness, **Figure 4.18a**). SHB (110 % under light conditions *vs*. 99 % in darkness) and SHD (112 % under light conditions *vs*. 100 % in darkness) showed increased eGFP expression levels with negligible light-dependency that indicates no regulatory effect (**Figure 4.18a**). When SHA was co-transfected with eGFP which has no miR21 binding sites, elevated light-independent eGFP expression levels (141 % under light conditions *vs*. 125 % in darkness) could be detected compared to the non-targeting control transfections (SHB, SHC) with eGFP-5p-3p (**Figure 4.18a**).

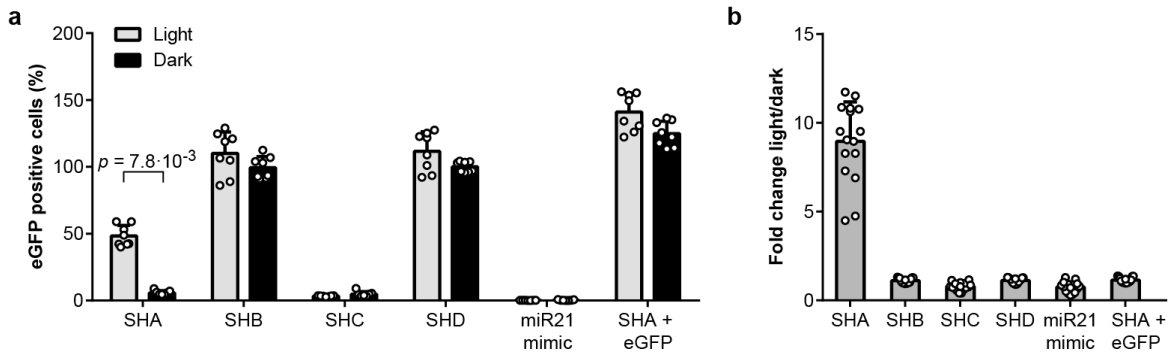

Figure 4.18: Elevated levels of AGO2 increase the differences in light-dependent eGFP expression levels. a, Number of cells which express eGFP in the presence of elevated levels of AGO2 and after transfection of the indicated *pre*-miR21 variants with eGFP-5p-3p (**Figure 4.17a**) or eGFP and miR21 mimic with eGFP-5p-3p. Values are normalized to SHD incubated in darkness. **b**, Fold changes calculated from light *vs*. dark conditions from (**a**). N = four biologically independent experiments performed in duplicates. Grey bars: light conditions, black bars: dark conditions. Dark grey bars: Fold changes. **a**, Wilcoxon two-sided signed-rank test was used for statistical analysis as a paired observation was assumed. Values are means ± s.d.

These results indicate that elevated levels of AGO2 lead to an increased difference in light-dependent eGFP expression under the control of the aptamer 53.19-modified *pre*-miR21 SHA.

4.2.3 Spatiotemporal control of reporter protein abundance

The temporal control of gene expression by using regulatory RNAs has been described before [194]. However, a regulation of these systems is based on the interaction with small molecules such as doxocycline or tetracycline [266], which renders the reversibility a diffusion-controlled process. Also, the spatial control of gene expression by light using regulatory RNAs has been shown before [250], but these RNA moieties need to be chemically synthesized and are therefore not genetically encodable. Besides that, most of these approaches are not reversible.

Theoretically, optoribogenetic control of regulatory RNA molecules is only limited by the speed and precision of light with the further benefit of full genetic encodability. To demonstrate a temporal and spatial control of gene expression with optoribogenetic RNA molecules, two experiments (**Figure 4.19** and **Figure 4.20**) have been designed and performed in the following.

4.2.3.1 Temporal control of reporter protein abundance

To demonstrate the reversibility of the approach, the *Metridia* Luciferase reporter system was used by taking advantage of the reporter protein to be secreted into the cell's supernatant. This enables repeated measurements at different time points without the need to sacrifice the cells. Here, HEK293PAL cells that harbor SHA or SHC and Luc-5p-3p were incubated for 19 h under blue light. Subsequently, the cells were kept in darkness for further 24 h (**Figure 4.19a**). In cells harboring SHA, an increase of luciferase activity was observed in the cell culture supernatants after 19 h in light (4.8-fold) and a reduction when these cells were further incubated in darkness afterwards (2.8-fold after further 8 h and 1.8-fold after further 24 h, **Figure 4.19b**,**c, Figure 10.2**). Cells which express SHC did not reveal light-induced luciferase expression (0.89-fold after 19 h, 0.92-fold after further 8 h and 0.81-fold after further 24 h, **Figure 4.19b**,**c**, **Figure 10.2**), which indicates no susceptibility to light. In turn, cells which were kept first in darkness for 19 h did not reveal an increased luciferase expression (1.1-fold), but an increased luciferase activity was detected when cells were subsequently exposed to light conditions for further 24 h (2.0-fold for further 10 h and 1.8-fold for further 24 h, **Figure 4.19d-f**, **Figure 10.3**). Again, cells which express SHC did not reveal light-dependent luciferase expression (1.00-fold after 19 h, 0.93-fold for further 10 h and 24 h, respectively, **Figure 4.19f**, **Figure 10.3**).

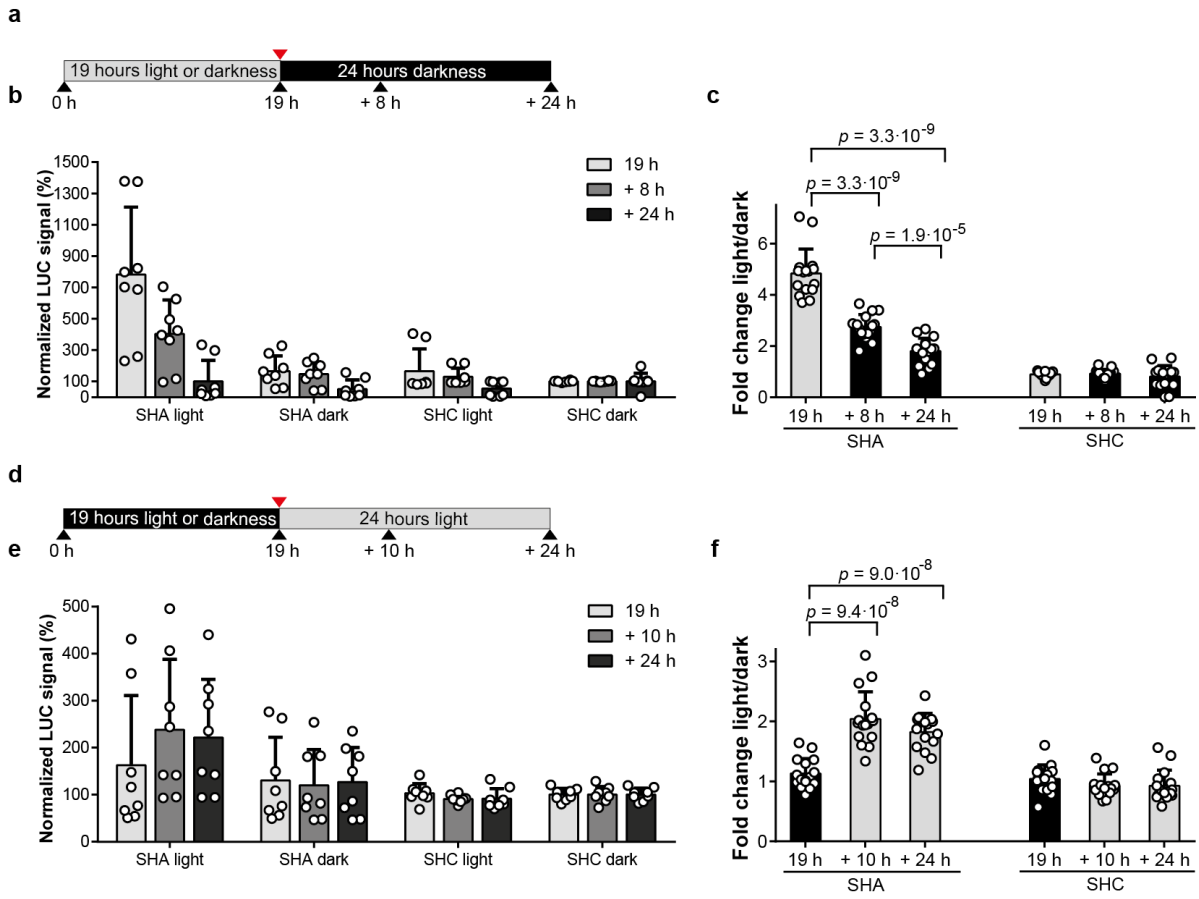

Figure 4.19: Light-control of luciferase expression is reversible. a, Illumination protocol applied in (**b**) and (**c**). Red arrow: time point of medium exchange and switching of light irradiation state. Black arrows: time points of sample taking. **b**, Luciferase expression level of cells which express SHA or SHC. Shown are normalized values to SHC in darkness. **d**, Fold changes were calculated from light *vs*. dark conditions from (**b**). **d**, Illumination protocol applied in (**e**) and (**f**). Red arrow: time point of medium exchange and switching of light irradiation state. Black arrows: time points of sample taking. **e**, Expression level of luciferase of cells that express SHA or SHC. Shown are normalized values to SHC in darkness. **f**, Fold changes calculated from light *vs*. dark conditions from (**e**). **b-f,** N = four biologically independent cultures in duplicates. **c**,**f**, Two-sided Mann-Whitney *U* test was used for statistical analysis as an unpaired observation was assumed. Values are means ± s.d.

Taken together, the luciferase expression under the control of the *pre*-miR21 variant SHA is reversible in both directions of the light-irradiation state. This suggests that the target gene suppression can be reversibly switched on and off.

4.2.3.2 Spatial control of reporter protein abundance

To demonstrate that the light-responsive *pre*-miR21/eGFP reporter system can also be spatially controlled, a photomask[6] (**Figure 4.20b**) was used to cover wells which were seeded with HEK293PAL cells that have been transfected with SHA or SHB and eGFP-5p-3p. After subsequent irradiation with blue light, the expression of SHA resulted in eGFP expression predominantly in light-illuminated areas, whereas an eGFP expression was observed independently of the irradiation status in the presence of

[6] Idea of spatial patterning experiment by Christian Renzl. Photomask was a gift from Julia Patricia Deisinger.

SHB. Strikingly, mCherry-fluorescence was reduced in light-illuminated areas for both transfections (**Figure 4.20a**).

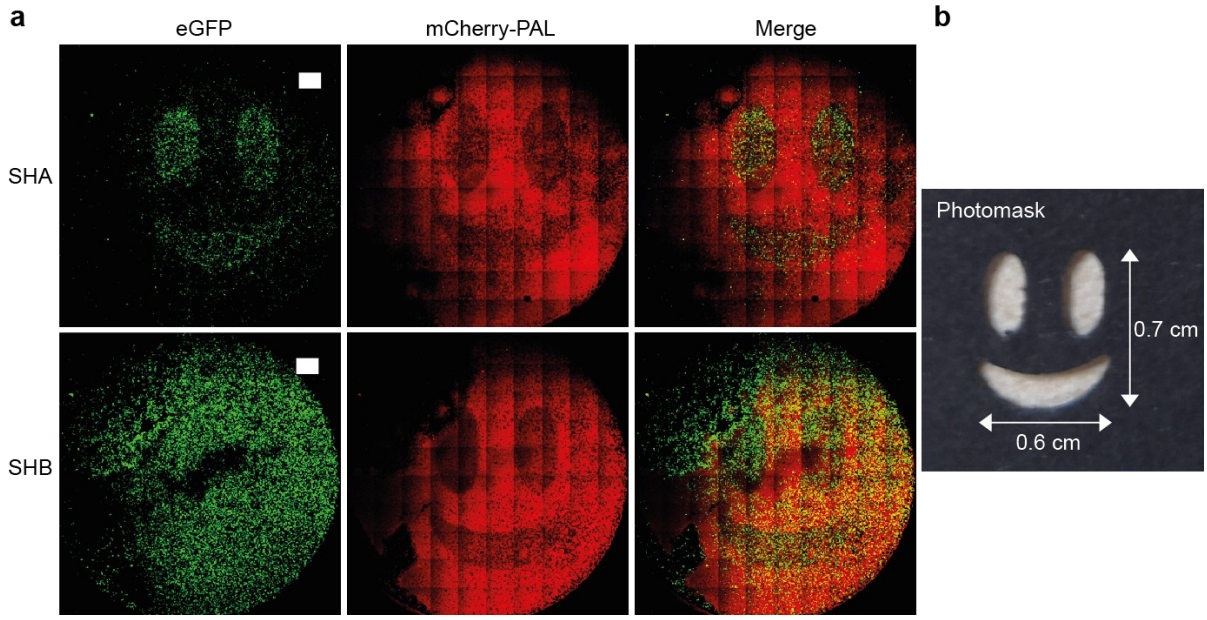

Figure 4.20: Spatial control of *pre*-miR21 mediated gene knockdown. a, Fluorescence microscopy images which show eGFP and mCherry-PAL expression in HEK293PAL cells after the transfection with eGFP-5p-3p and SHA (top panels) or SHB (lower panels). White bars: 1000 µm. Irradiation was done on cells which were covered with a photomask (**b**). The experiment was performed one time.

It was concluded from this experiment that the eGFP reporter gene expression in HEK293PAL cells which express SHA is spatially controllable by light.

As it was observed that the fluorescence of mCherry from the mCherry-PAL fusion protein was reduced in regions that have been illuminated by light, a control experiment was performed to investigate whether this effect is mCherry-PAL specific or it can also be observed for unmodified mCherry protein (**Figure 4.21**). Here, HEK293 cells have been transfected with plasmids that encode for mCherry, PAL, mCherry-PAL (500 ng plasmid per well) and all possible two-plasmid combinations thereof (250 ng of each plasmid per well). After 44 h of incubation under blue light conditions or in darkness, the cells were subjected to flow cytometry analysis for quantification of mCherry (**Figure 4.21a**) and PAL (**Figure 4.21b**) fluorescence. Strikingly, mCherry fluorescence was higher in darkness for cells which contain mCherry-PAL (1.3-fold for mCherry-PAL/mCherry, 1.6-fold for mCherry-PAL and 1.5-fold for mCherry-PAL/PAL), whereas samples with unfused mCherry or PAL protein showed weak to no light-dependent differences (1.2-fold for mCherry/PAL and 1.1-fold for mCherry and PAL, respectively). A transfection with mCherry indicated the highest and a transfection with PAL indicated the lowest mCherry fluorescence among all tested combinations irrespective to the light irradiation state (**Figure 4.21a**). A light-dependency of PAL fluorescence was observed for all tested constructs that contain PAL and was highest for mCherry-PAL (1.7-fold), followed by PAL/mCherry-PAL and PAL transfections (both 1.6-fold, **Figure 4.21b**). The light-dependency of PAL fluorescence was reduced when mCherry was co-

transfected (1.4-fold for mCherry/mCherry-PAL and 1.3-fold for mCherry/PAL) and not detectable when only mCherry was transfected (0.98-fold, **Figure 4.21b**). The PAL fluorescence intensity in cells which were incubated in darkness was highest for transfection with mCherry-PAL, lowest for transfection with mCherry and remained mainly at background level for all tested combinations which were incubated under light conditions (**Figure 4.21b**).

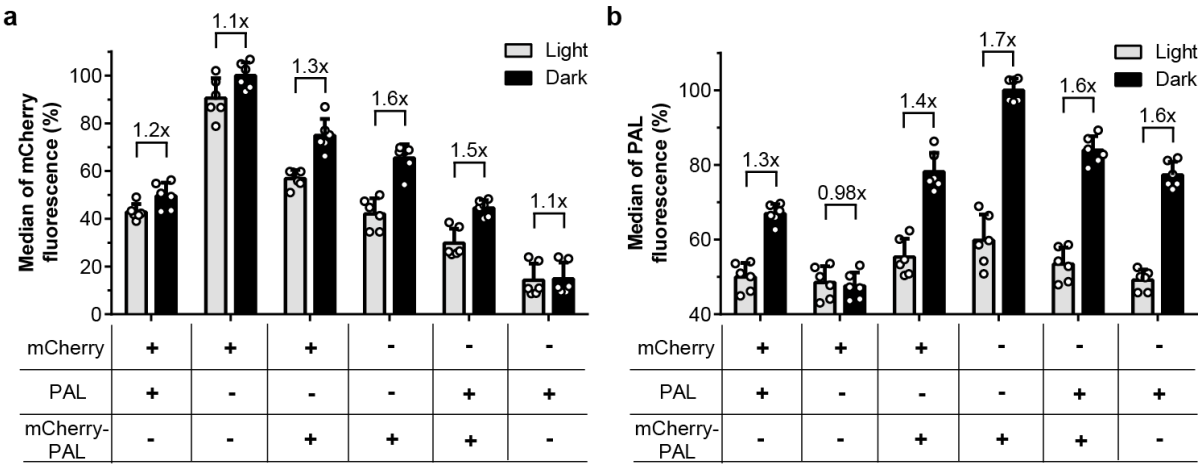

Figure 4.21: A light-dependent reduction in mCherry fluorescence is only observed for the mCherry-PAL fusion protein. Median fluorescence intensity of mCherry (**a**) or PAL (**b**) after transfection of Hek293 cells with plasmid(s) which express the indicated protein(s). Grey bars: light conditions, black bars: dark conditions. Values are normalized to cells that were transfected with mCherry (**a**) or mCherry-PAL (**b**) which were incubated in darkness. Values are means ± s.d. N = Three biological independent experiments in duplicates. Values are means ± s.d.

These results indicate that the mCherry fluorescence from mCherry-PAL but not from mCherry decreases in HEK293 cells which were incubated under blue light conditions. Interestingly, the PAL fluorescence from PAL and mCherry-PAL decreases in cells which were incubated under blue light conditions.

4.2.4 Investigation of 3'-isomiR formation after *pre*-miR21-aptamer maturation

The suppressive capacity of mature miR molecules depends greatly on its length and the sequence identity. This is determined upon imprecise dicer processing, a process that is known as isomiR formation [267]. To get an idea whether the 3'-isomiR formation of the miR21-5p strand processed from the artificial *pre*-miR21-53.19 chimera is similar to its natural counterpart, HEK293PAL cells had been transfected with SHA and incubated in darkness for 19 h. Thereafter, total RNA was extracted, poly-adenylated and reverse transcribed by using a poly-T primer equipped with a barcode sequence. Subsequently, cDNA containing mature miR21-5p molecules were amplified by using a miR21-5p specific forward primer and a reverse primer which was specific to the barcode sequence that flanks the poly-T sequence which was introduced during the reverse transcription step. Next, PCR-products were subjected to TOPO TA cloning into a corresponding plasmid backbone. After transformation, 17 clones

had been collected for plasmid preparation and purified plasmids were sent for sequencing. 12 out of these 17 plasmids contained a mature-miR21-5p insertion and therefore they have been considered as 3'-isomiR representatives (**Table 4.1**).

Table 4.1: The sequencing of mature miR21-5p clones which were derived from SHA transfection indicates altered 3'-isomiR formation compared to natural *pre*-miR21. Percentage was calculated from the number of clones which were obtained for the respective 3'-isomiR from the 12 clones that have been considered in total. Blue: Nucleotides that encode for the PAL aptamer.

Name	# Clones	Percentage (%)	RNA Sequence
Mature miR21-5p	0	0	UAGCUUAUCAGACUGAUGUUGA
Mature miR21-5p – 1 nts	2	17	UAGCUUAUCAGACUGAUGUUG_
Mature miR21-5p + 1 nts	2	17	UAGCUUAUCAGACUGAUGUUGAC
Mature miR21-5p + 2 nts	8	67	UAGCUUAUCAGACUGAUGUUGACG

Eight plasmids contained a mature miR21-5p sequence that was two nucleotides longer than its natural counterpart. Two plasmids could be detected individually with a one nucleotide longer and with a one nucleotide shorter sequence compared to the natural miR21-5p sequence. No clone contained the natural miR21-5p sequence. This indicates that the maturation of the artificial *pre*-miR21-53.19 chimera SHA might be altered compared to the natural counterpart.

4.3 Light-control of shRNA activity

Up to this point, the processivity of a *pre*-miR21-53.19 chimera for the spatial and temporal control of target reporter gene expression could be regulated successfully by light. However, this requires an exchange of the apical loop domain of endogenously occurring *pre*-miRs that might also be processed alternatively by dicer compared to the natural counterpart (see **Table 4.1**). Other than for miRs, which hybridize imperfectly to the 3'UTR of various intrinsic target genes (**Figure 4.22a**), siRNAs hybridize within the coding region of a target mRNA (**Figure 4.22b**).

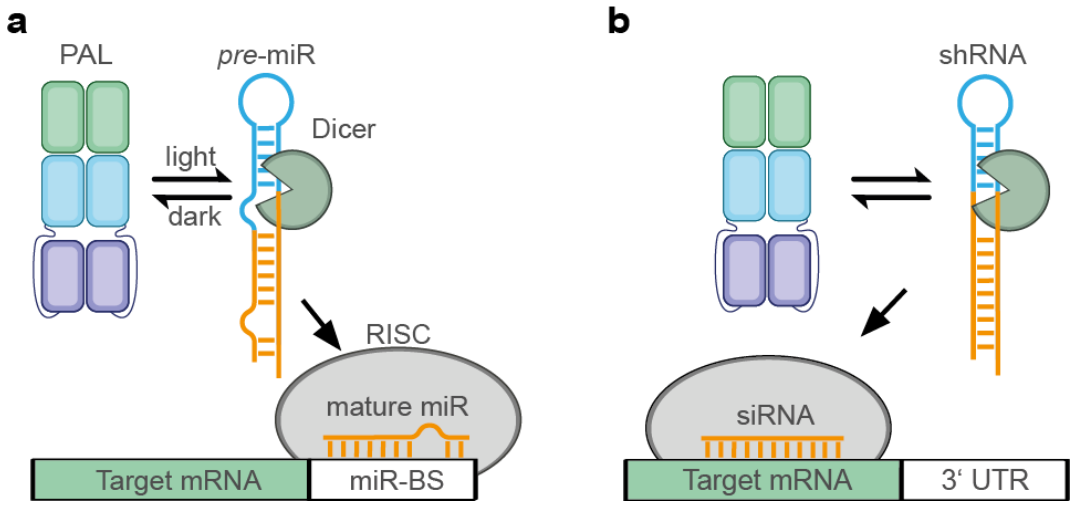

Figure 4.22: Light-control of target gene expression by regulatory RNAs. Regulation by *pre*-miRs (**a**) or shRNAs (**b**), which are processed by dicer in darkness to form mature miRs (orange, **a**) or siRNAs (orange, **b**) that are loaded into the RISC complex. This leads to target mRNA inhibition or hydrolysis depending on the degree of hybridization. The PAL protein binds light-dependently to the apical loop domain of both regulatory RNAs which contains the PAL aptamer sequence (blue). This might convey an alternative processing of the regulatory RNA under light conditions.

4.3.1 Screening of eGFP shRNAs

In principle, siRNA sequences can be targeted to any mRNA molecules of interest. Therefore, they can be used to create a generalizable and modular approach for the regulation of distinct target genes. To this end, light responsive shRNAs were designed. Subsequently, these constructs had been tested for their differences on the light-dependent eGFP reporter gene expression. Because it is known that the efficiency of target gene suppression may vary among the tested siRNAs, three different siRNA sequences were conjoined with the PAL aptamer 53.19 as apical loop domain (SH2, SH3 and SH4, **Figure 4.23a**,**b**,**c**). All of them target the coding region of the eGFP mRNA. Furthermore, SH2 was also conjoined with a published loop sequence (SH1, UUCAAGAGA, [268], **Figure 4.23a**), which renders this shRNA incompetent for binding to PAL. As negative control, SHA was implemented into the assay. The corresponding pSilencer plasmid variants were co-transfected into HEK293PAL cells with plasmids for AGO2 overexpression and with an eGFP reporter plasmid which has no miR21 binding sites. These cells were incubated subsequently under light conditions or in darkness for 44 h. A strong light-dependent increase in eGFP positive cells could be observed when SH2 was transfected (20 % under light conditions, 5 % in darkness, **Figure 4.23**). This corresponded to a 4-fold change in expression, while transfections with SH3 and SH4 also displayed elevated levels of eGFP positive cells in darkness (42 % under light conditions, 32 % in darkness for both SH3 and SH4, respectively) which reduced the calculated fold change to 1.5 and 1.3 for SH3 and SH4, respectively (**Figure 4.23d**,**e**, for calculation of fold changes, see section 7.6.1). The eGFP expression was remained unaffected in cells which express SHA (**Figure 4.23d**,**e**). In case of SH1 transfection, the eGFP expression was equally suppressed for both light states (**Figure 4.23d**,**e**).

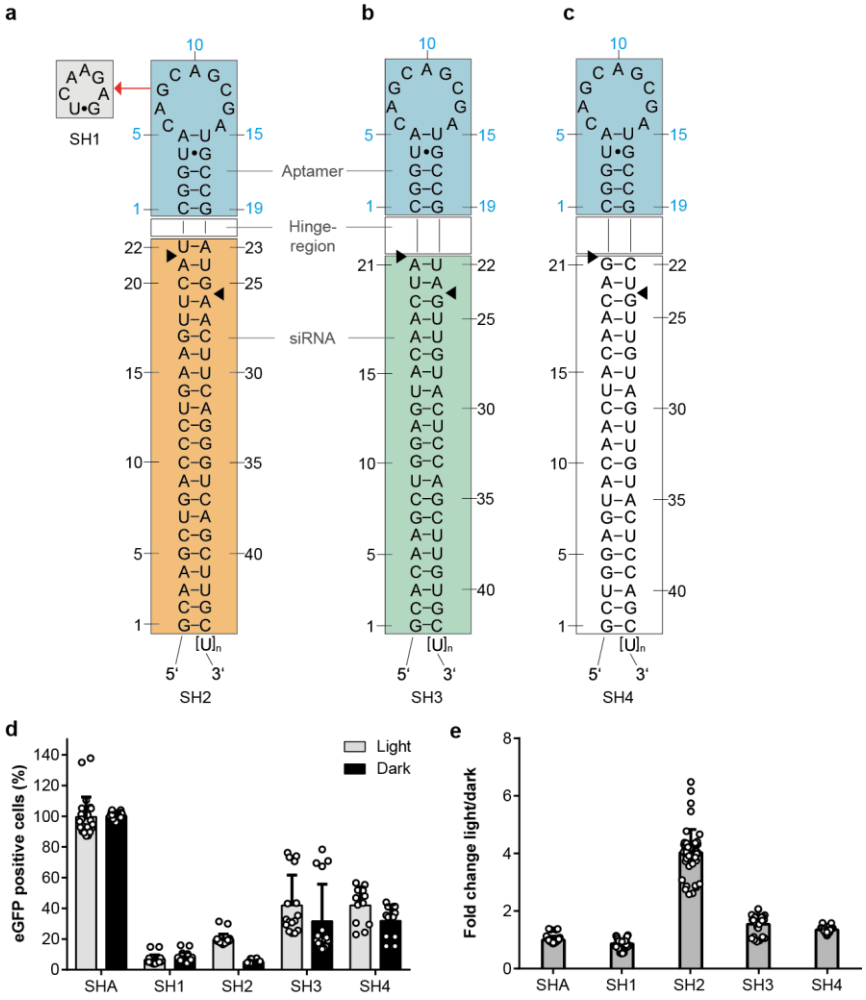

Figure 4.23: Screening of shRNAs for light-dependent control of eGFP expression. Three different siRNA sequences SH2 (orange box, **a**), SH3 (green box, **b**) and SH4 (white box, **c**) which target the eGFP mRNA were conjoined with the PAL aptamer (53.19, blue boxes) or a control hairpin (SH1, grey box, **a**) as apical loop domain. Black arrows indicate putative preferential dicer cleavage sites [193]. **d**, Number of cells which express eGFP after transfection with the indicated shRNA. Values are normalized to SHA (**Figure 4.13a**) incubated in darkness. **e**, Fold changes were calculated from light *vs.* dark conditions from (**d**). N = At least six biologically independent experiments performed in duplicates. Grey bars: light conditions, black bars: dark conditions. Dark grey bars: Fold changes. Values are means ± s.d.

From this experiment it was concluded that conjoining a siRNA sequence with aptamer 53.19 as apical loop domain results in optoribogenetically functional shRNAs with low to intermediate light-responsiveness. Among the tested variants, SH2 was the most potent candidate.

4.3.2 Investigating the impact of shRNA hinge region insertions on shRNA structure and reporter gene regulation

The next question was how the light-responsiveness of shRNAs could be improved in a general manner. It is described in literature that structural variations of one or two nucleotides close to the dicer cleavage

site are common motifs found in natural *pre*-miRs and shRNAs [269]. As these motifs impact the accuracy of shRNA processing, they influence shRNA performance and gene silencing efficacy [270].

4.3.2.1 Investigating the impact of one-or two nucleotide bulges implemented into the hinge region of shRNAs targeting eGFP

To increase the light-responsiveness of eGFP shRNAs, one- (SH5, SH6 and SH8) or two-nucleotide (SH7) bulges of which SH5 was asymmetric, were implemented into the hinge region of SH2 (**Figure 4.24a)** and the experimental setup that is shown in **Figure 4.23** was extended for these constructs. As additional constructs, mutations in the aptamer loop region of SH7 at the positions C9G (SH9), C12G (SH10) and at both positions (SH11) were tested alongside. The mutations were tested as putative controls because it was assumed that they cannot bind to PAL (**Figure 4.24b)**. Strikingly, transfection of constructs with one-nucleotide bulges consisting of adenines (asymmetric: SH5, symmetric: SH8) resulted in increased eGFP expression under light conditions (30 % *vs*. 36 % for SH5 and SH8, respectively). eGFP expression under light conditions was at a similar level when the two-nucleotide bulge construct was transfected (SH7, 33 %). A decreased eGFP expression under light conditions was observed for the transfection of a symmetric one-nucleotide cytosine bulge and the unmodified construct (20 % for SH2 and SH6, respectively, **Figure 4.24c**). The number of eGFP positive cells in darkness was within the same range for all tested constructs except for SHA (5 % for SH2, SH5 and SH6, 7 % for SH7 and 6 % for SH8, **Figure 4.24c**). Increased fold changes were calculated for SH5 (6.4), followed by SH8 (5.8, **Figure 4.24d**). Reduced fold changes slightly above the level of SH2 (4.0) were calculated for SH7 (4.5) and SH6 (4.3, **Figure 4.24d**), in which the C1G12 base pair of the aptamer 53.19 was replaced by hinge nucleotide insertions. For transfections of the three 53.19-modified controls (SH9 - SH11), a low eGFP expression was measured irrespective to the light-irradiation state (9 % in light *vs*. 7 % in darkness for SH9, 12 % in light *vs*. 11 % in darkness for SH10 and 9% light and darkness for SH11) and no notable light-dependent fold changes could be calculated for these constructs (**Figure 4.24c**,**d**).

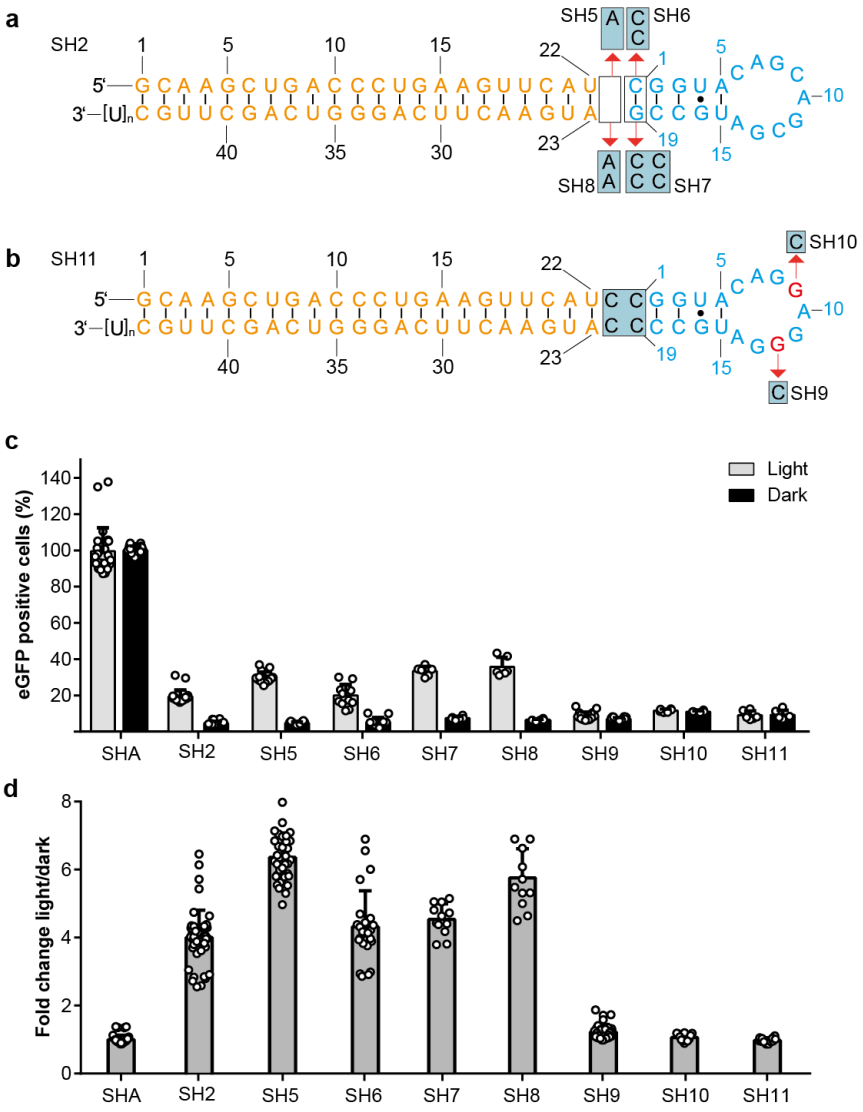

Figure 4.24: One- or two nucleotide bulges inserted into the hinge region of shRNA influences the light-dependent reporter gene expression. a, Structural variations were implemented in the hinge region (blue boxes) that connects the siRNA (orange) to the aptamer (53.19, blue) as apical loop domain. **b**, Point mutations were introduced into the aptamer domain. **c**, Number of cells which express eGFP after transfection with the indicated shRNA. Values are normalized to SHA (**Figure 4.13a**) which was incubated in darkness. **d**, Fold changes calculated from light *vs.* dark conditions from (**c**). N = At least six biologically independent experiments performed in duplicates. Grey bars: light conditions, black bars: dark conditions. Dark grey bars: Fold changes. Values are means ± s.d.

Based on this experiment, it was concluded that single-nucleotide bulges (both symmetric and asymmetric) increase the differences in reporter protein expression between the light states when the integrity of C1G19 base pairing of aptamer 53.19 is not disturbed. It was decided to continue working with single asymmetric nucleotides which were incorporated into the hinge region, because the highest fold change was observed for SH5. Furthermore, all tested shRNAs which contained loop mutations suppressed reporter gene expression irrespective to the light state.

4.3.2.2 Investigating the impact of single nucleotide bulges implemented into the hinge region of shRNAs targeting eGFP

As the implementation of a single nucleotide into the hinge region improved both the number of eGFP positive cells under light conditions and light-dependent fold changes, the impact of the nucleotide identity was tested next. To this end, all canonical nucleobases (adenine, uracil, guanine and cytosine) were embedded into the hinge region of SH2 either up- or downstream of the aptamer, respectively (**Figure 4.25a**). SHA was used as control as the transfection of the construct induces no eGFP suppression (**Figure 4.25a**). All variants were tested in the eGFP reporter assay system in HEK293PAL cells (**Figure 4.25b**,**c)**.

The highest level of eGFP positive cells under light conditions was observed for an uridine insertion upstream to the aptamer (SH12, 65 %), followed by a guanine (SH13, 45 %) at this position (**Figure 4.25b**). Intermediate levels of eGFP expressing cells were obtained by insertion of an adenine up-(SH5, 31 %) or downstream (SH15, 29 %) of the aptamer similar to insertion of a uridine (SH16, 31 %) or cytosine (SH18, 27 %) at the latter position (**Figure 4.25b**). Low levels of eGFP expressing cells under light conditions were obtained by insertion of an adenine up- (SH14, 16 %) or a guanine downstream (SH17, 9 %) to the aptamer (**Figure 4.25b**). The order of eGFP expressing cells incubated in darkness was equal to the observed order under light conditions and was within the range of 2 – 10 % of eGFP expressing cells (**Figure 4.25b**). This resulted in fold changes within the same range (6.1 – 6.5-fold) for most of the tested constructs except for SH15 which displayed the highest fold change (8.0-fold), while SH14 (5.4-fold) and SH17 (3.9-fold) displayed the lowest fold changes (**Figure 4.25c**). eGFP expression was not repressed in cells that were transfected with SHA (**Figure 4.25b**).

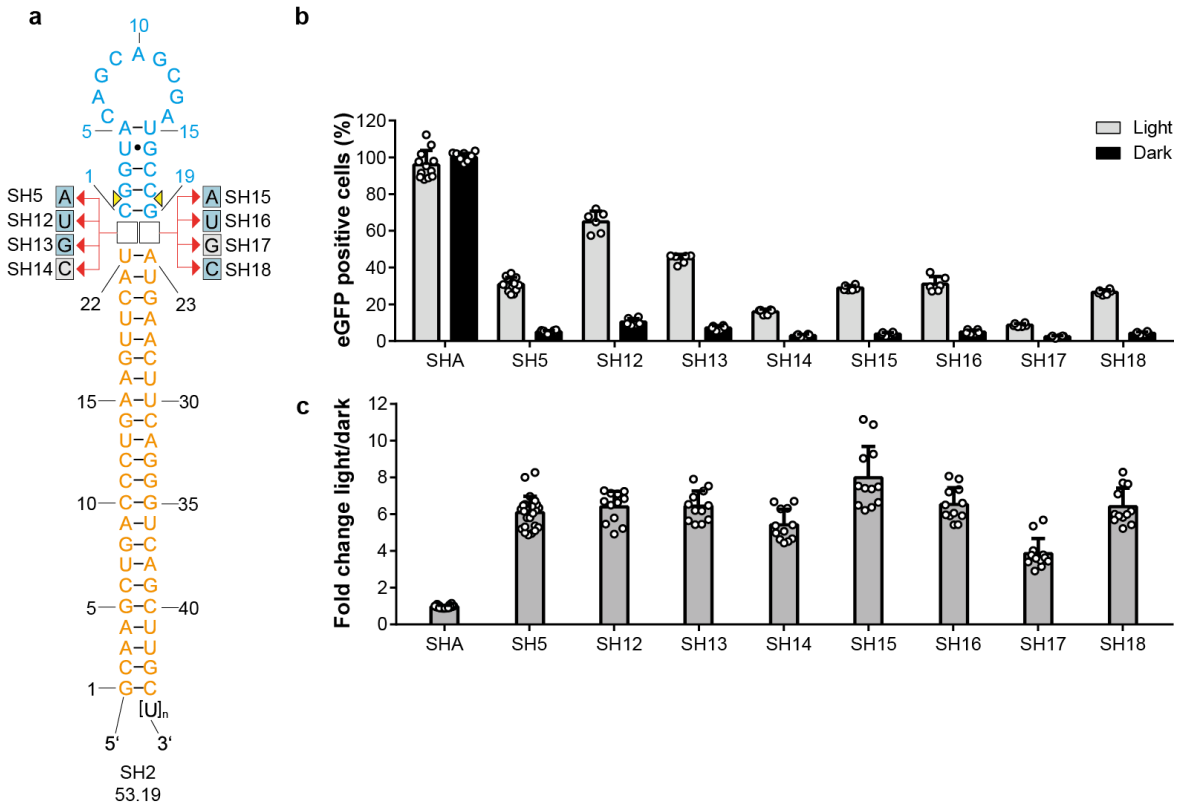

Figure 4.25: ShRNA hinge region nucleotide identity influences the light responsiveness. a, Single nucleotide permutations were implemented into the hinge region of SH2 (blue boxes) that connects the siRNA targeting eGFP (orange) to the aptamer (53.19, blue) as apical loop domain. Yellow arrows: Structural rearrangements shift the single nucleotide bulge of SH14 (left arrow) and SH17 (right) into the aptamer region as revealed by secondary structure predictions. **b**, Number of cells expressing eGFP after transfection with the indicated shRNA. Values are normalized to SHA (**Figure 4.13a**) which was incubated in darkness. Grey bars: light conditions, black bars: dark conditions. **c**, Fold changes calculated from light *vs*. dark conditions from (**b**). Dark grey bars: Fold changes. N = At least three biologically independent experiments performed in duplicates. Values are means ± s.d.

The experiments indicate that an insertion of an adenine or uridine in both tested positions (up- or downstream to the aptamer) leads to high numbers of eGFP expressing cells under light conditions. Similar results can also be obtained by an insertion of a guanine up- and cytosine downstream to the aptamer. However, an insertion of cytosine up- and guanine downstream to the aptamer indicated small fold changes and low numbers of eGFP-expressing cells under light conditions probably due to unintended structural rearrangements. Therefore, it was decided to continue working with adenine and uridine as representatives in hinge region variants, while a downstream guanine as putative “negative” control was further included.

The difference in eGFP expression might be a consequence of structural alterations between the shRNA variants. Hence, two- and three- dimensional structure predictions were conducted to identify structural differences (**Figure 4.26**). The U4G16 Wobble base pair is an important structural feature of the aptamer 53.19 and might influence the aptamer’s three-dimensional conformation [237]. Therefore, the structure of aptamer 53.19 was predicted and compared to a 53.19 variant in which the Wobble base pair was replaced by a Watson Crick base pair (U4C, **Figure 4.26a**). To verify whether the same folding of 53.19 takes place when the aptamer is conjoined to the siRNA, similar predictions were performed for SH2

and a variant, in which the Wobble base pair was replaced by a Watson Crick base pair (U4C, **Figure 4.26a**). Next, it was verified whether the single nucleotide insertions into the hinge region of SH2 would disturb the U4G16 Wobble base pair formation. To this end, hydrogen bond formation of the U4G16 Wobble base pair was predicted for the construct having no hinge nucleotide insertion (SH2) and the construct which induced the highest number of eGFP expressing cells for both light conditions (SH12). As additional construct, SH15 was chosen because its transfection resulted in a low number of eGFP expressing cells (**Figure 4.26b**). Furthermore, two- and three- (**Figure 4.26c**,**d**) dimensional structure predictions were conducted for the single nucleotide hinge region variants and the structural alterations were compared to the shRNA variant which lacks hinge region insertions (SH2).

Secondary and tertiary structure predictions of 53.19 suggest that the aptamer folds into a stem-loop structure (**Figure 4.26a**). A similar structure was observed when 53.19 was conjoined with the siRNA (SH2, **Figure 4.26a**). When the U4G16 Wobble base pair was replaced by a Watson-Crick base pair (C4G16), a shift of the loop away from the radial axis could be observed for 53.19. This was not observed in case of SH2. Instead, similar structures were observed for both the Wobble and the Watson-Crick base pair (**Figure 4.26a**). One reason for this observation could be that prolonged stem structures might facilitate correct folding of aptamer 53.19. For all tested constructs (SH2, SH12 and SH15), a Wobble base pair formation could be observed in their tertiary structure predictions (**Figure 4.26b**).

Secondary structure predictions for the insertion of cytosine up- (SH14) and guanine downstream (SH17) to the aptamer indicated structural rearrangements. This rearrangement leads to the formation of an unpaired nucleotide bulge within the aptamer region (position 2 for SH14 and position 19 for SH17, see yellow arrow in **Figure 4.25a**), which was not observed for the rest of the constructs (**Figure 4.25a**). Three-dimensional predictions were performed for all other constructs which did no indicate a bulge formation in the aptamer region. In the prediction, the apical loop structure of SH12 was deviating strongly from the loop structure of SH2 (**Figure 4.26c**). Apparently, the uridine insertion into the hinge region of SH12 interfered with the helical winding compared to SH2, which led to a shift of the two abundant apical SH12 loops (loops 2 and 3) towards the opposite side of the radial axis compared to the single loop observed for SH2 (loop 1, **Figure 4.26c**). To a smaller extent, this effect was also observed for SH13 whereas only one loop (2) was located on the opposite side of the radial axis and the other loop (3) was aligned close to the radial axis (**Figure 4.26c**). For SH5, loop 3 was aligned on the same side as loop 1 from SH2 with a small shift towards the radial axis, whereas loop 2 was enlarged nearly perpendicular to loop 1 (**Figure 4.26c**). For hinge region variants which were implemented downstream to the aptamer, all three tested variants showed structural deviations from SH2 to a comparably small extent (**Figure 4.26d**). For all three tested constructs (SH16, SH15 and SH18), loop 3 was aligned on the same side as loop 1 from SH2 with a small shift towards the radial axis (**Figure 4.26d**). SH16 and SH18 displayed a shift of loop 2 towards the center of the helical axis which led to an enlargement of loop 3 (**Figure 4.26d**). For SH15, loop 2 was shifted towards the opposite side of the radial axis compared to loop 1 from SH2, which led to a parallel shift of loop 3 towards the center of the radial axis (**Figure 4.26d**).

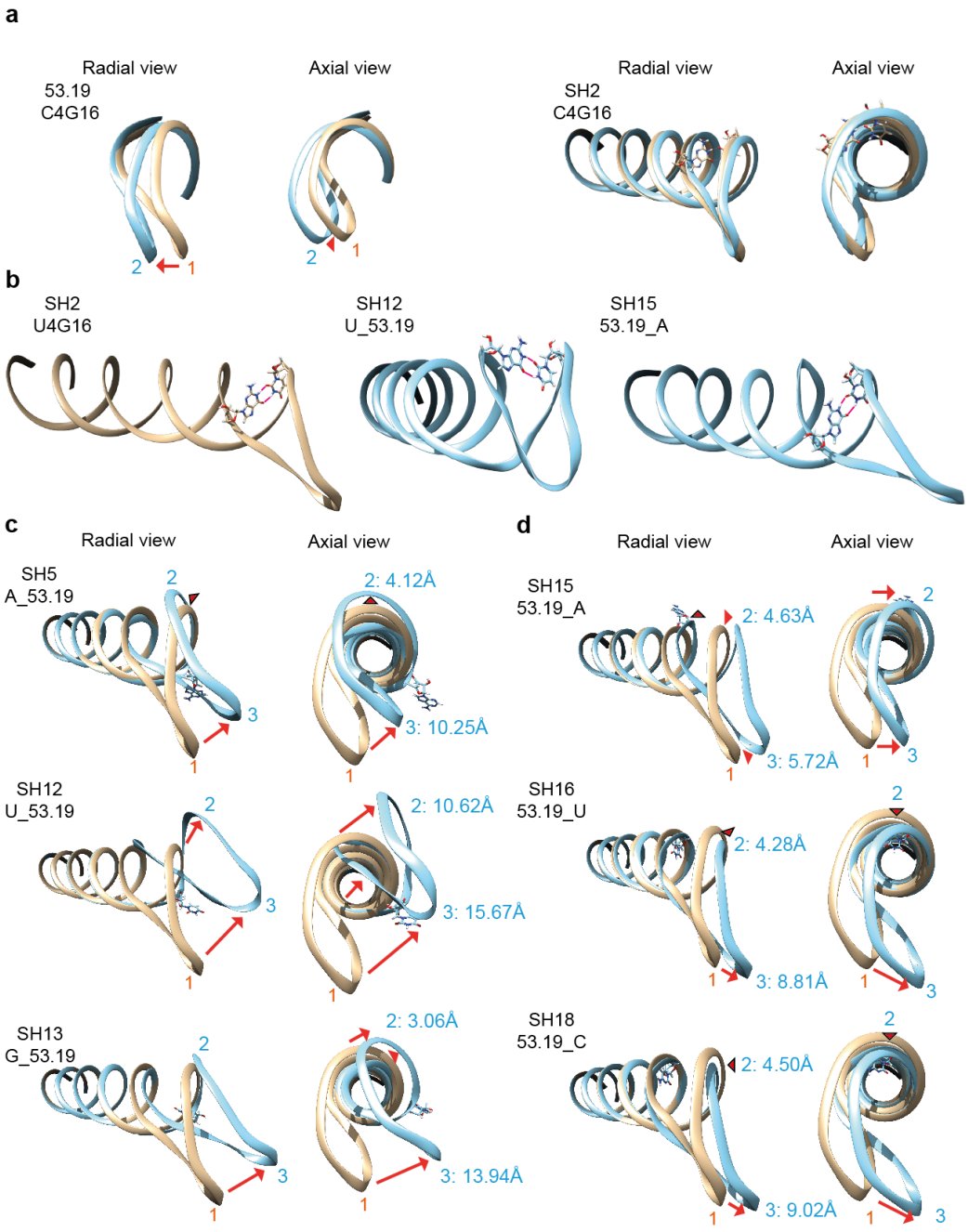

Figure 4.26: Influence of the Wobble base pair and single nucleotide insertions on the tertiary structure of SH2. a, Tertiary structure predictions of 53.19 (left) and SH2 (right) with a Wobble base pair (U4G16, orange) or a Watson-Crick base pair (C4G16, blue) within the aptamer sequence. The presence of the Wobble base pair is shown as ball stick model within the structure of SH2 (orange structure, right). **b**, Tertiary structure predictions (radial view) of SH2 (orange), SH12 and SH15 (both blue). Predicted hydrogen bonds of the U4G16 Wobble base pair are shown as pink lines between the two nucleobases (shown as ball stick model). **c**,**d**, Tertiary structure predictions of the shRNA variants (blue) which have single nucleotide insertions upstream (**c**) or downstream (**d**) to the aptamer region in overlay with SH2 (orange). Red arrows: Striking structural changes of the apical loop domain were caused by nucleotide insertion (shown as ball stick model) into the hinge region. The distance of the oxygen atom in the ribose ring from the A5 nucleoside (depicted as 2) or the G9 nucleoside (depicted as 3) of the aptamer 53.19 was predicted between the single nucleotide insertion variants and SH2.

According to tertiary structure predictions, 53.19 might fold into a stem-loop structure and the structure may be altered by a U4G nucleotide replacement. This might explain why a C4G16 variant of aptamer 53 does not bind to PAL *in vitro* [237]. In all predicted shRNA variants, the Wobble base pair formation remained intact. Additionally, the number of eGFP positive cells among the constructs correlates with the increased structural rearrangements in the loop region. Furthermore, a higher eGFP background in darkness could be observed for constructs that show increased structural rearrangements in the loop region. Structural distortions through hinge nucleotide implementation led to a shift of the two abundant apical loops towards the opposite side of the radial axis compared to the single loop observed in the structure without hinge region insertion (SH2).

Next, the experiments that are shown in **Figure 4.25** and **Figure 4.26** were recapitulated by using another shRNA targeting eGFP. In this shRNA the neighboring nucleotides to the hinge region were swapped (U22A23 for SH2, A21U22 for SH3) to elucidate whether any general rules apply for insertion of the hinge region nucleotides. Hinge region implementations of adenine and uridine were tested up- (SH19 and SH20) and downstream (SH21 and SH22) to the aptamer as well as a guanine insertion (SH23) at the latter position. A G11C mutation within the aptamer region of SH3 (SH24, **Figure 4.27a)** and SHA (**Figure 4.13a**) were used as controls. The highest level of eGFP positive cells was observed for an insertion of uridine upstream to the aptamer (SH20, 52 %) followed by an insertion of adenine (SH19, 45 %) at this position (**Figure 4.27b)**. Intermediate to low levels of eGFP expressing cells were obtained by insertion of a uridine (SH22, 29 %), a guanine (SH23, 18 %) and an adenine (SH21, 16 %) downstream of the aptamer (**Figure 4.27b)**. The order of eGFP expressing cells which were incubated in darkness varied between 1 % to 8 % and was not equal to the order under light conditions which led to various fold changes (**Figure 4.27c**). A uridine insertion downstream to the aptamer (SH22, 15.3-fold) showed the highest fold change, followed by adenine (SH21, 11-fold) and guanine (SH23, 4.3-fold) insertions at this position. Insertions of uridine (SH20, 9.3-fold) and adenine upstream (SH19, 5.8-fold) to the aptamer displayed high to intermediate fold changes. The G11C aptamer mutant (SH24) showed a reduced eGFP expression irrespective to the light irradiation state (15 %, **Figure 4.27b**). The eGFP expression was not reduced in neither of the applied conditions in cells that harbor SHA (**Figure 4.27b**).

The secondary structure prediction for an insertion of a guanine downstream to the aptamer (SH23) indicated structural rearrangement which leads to an unpaired nucleotide bulge within the aptamer region (position 19 for SH23, see yellow arrow in **Figure 4.27a**). This was not observed for the rest of the constructs (**Figure 4.27a**). Next, the hydrogen bond formation for the U4G16 Wobble base pair was predicted for the construct having no insertion (SH3) and the construct which induced the highest number of eGFP expressing cells for both light conditions (SH20). As additional construct, SH21 was chosen because its transfection resulted in a low number of eGFP expressing cells (**Figure 4.27b**). For the three tested shRNA constructs, a Wobble base pair formation could be predicted within their tertiary structure (**Figure 4.27d**). Three-dimensional predictions for correctly folded hinge region variants (no bulges within the aptamer region according to secondary structure predictions) upstream to the aptamer (SH19 and SH20) showed structural deviations from SH3 to a comparable extent (**Figure 4.27e)**. For both a uridine (SH20) and an adenine (SH19) at this position, loop 2 was shifted towards the opposite

direction of the radial axis compared to loop 1 from SH3, which leads to a parallel shift of loop 3 towards the center of the radial axis (**Figure 4.27e)**. For a uridine downstream of the aptamer (SH22), no loop 2 was observed (**Figure 4.27f)**. Loop 3 was located on the same side on the radial axis as loop 1 from SH3, however, with a small shift towards the center of the radial axis (**Figure 4.27f)**. For an adenine at this position (SH21), loop 2 and an additional loop 4 formed a structural kink on the opposite side of the radial axis compared to loop 1 from SH3, whereas loop 3 was aligned close to the center of the radial axis (**Figure 4.27f)**.

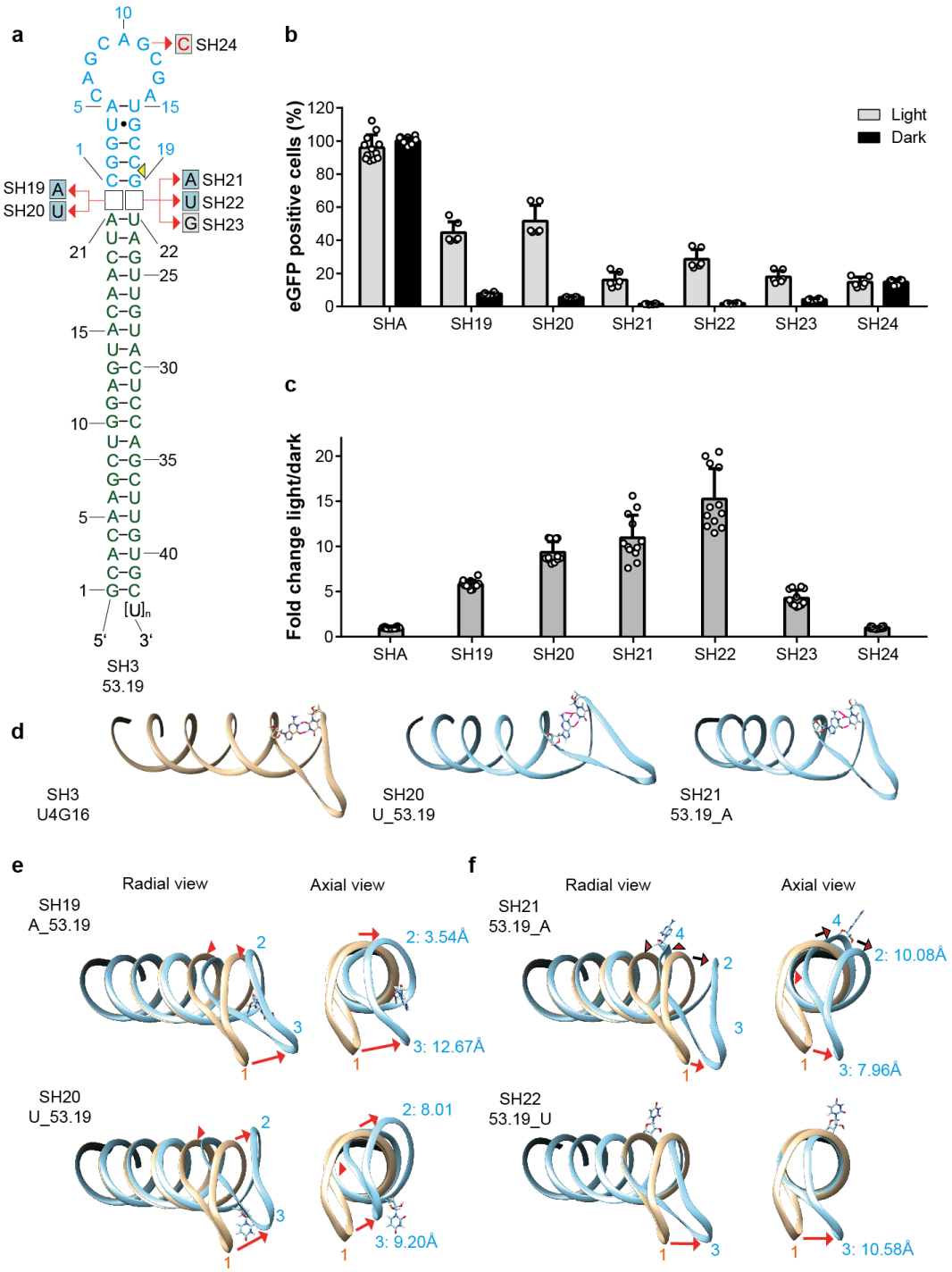

Figure 4.27: Single-nucleotide insertions into shRNA hinge regions commonly influences the light-responsiveness. a, Single nucleotide permutations were implemented into the hinge region of SH3 (blue boxes) that connects the siRNA targeting eGFP (green) to the aptamer (53.19, blue) as apical loop domain. An aptamer-point mutated variant of SH3 was generated to remove light-dependency (G11C, SH24). Yellow arrow: Structural rearrangements shift the single nucleotide bulge of SH23 into the aptamer region as revealed by secondary structure predictions. **b**, Number of cells expressing eGFP after transfection with the indicated shRNA. Values are normalized to SHA (**Figure 4.13a**) which was incubated in darkness. Grey bars: light conditions, black bars: dark conditions. **c**, Fold changes calculated from light *vs*. dark conditions from (**b**). Dark grey bars: Fold changes. N = At least three biologically independent experiments performed in duplicates. Values are means ± s.d. **d**, Tertiary structure predictions (radial view) of SH3 (orange), SH20 and SH21 (both blue). Predicted hydrogen bonds of the U4G16 Wobble base pair are shown as pink lines between the two nucleobases (shown as ball stick model). **e**,**f**, Tertiary structure predictions of the shRNA variants (blue) which have single nucleotide insertions upstream (**e**) or downstream (**f**) to the aptamer region in overlay with SH3

(orange). Red arrows: Striking structural changes of the apical loop domain were caused by nucleotide insertion (shown as ball stick model) into the hinge region. The distance of the oxygen atom in the ribose ring from the A5 nucleoside (depicted as 2) or the G9 nucleoside (depicted as 3) of 53.19 was predicted between the single nucleotide insertion variants and SH2.

For single nucleotide implementations into the hinge region of SH3, it could be concluded that an insertion of a uridine upstream to the aptamer leads to the highest number of eGFP positive cells and this observation correlated with structural features (loops 2 and 3) in tertiary structure predictions and similar observations for SH2. The highest fold changes were observed for an insertion of an adenine (SH15) or a uridine (SH22) downstream to the aptamer for SH2 and SH3, respectively, which points for nucleotide insertion at this position. The number of cells which express eGFP in darkness was greatly reduced for nucleotide implementations into the hinge region of SH3. However, higher eGFP expression in darkness was observed for the transfection of constructs which showed structural rearrangements in the loop region according to tertiary structure predictions. Additionally, in all predicted shRNA variants, the Wobble base pair formation remained intact.

4.3.2.3 Fluorescence microscopy studies of representative shRNA variants controlling eGFP expression

To verify the light-dependent eGFP expression mediated by light-responsive shRNAs with a second independent method, fluorescence microscopy experiments were performed (**Figure 4.28**, **Figure 10.4**). To this end, HEK293PAL cells were co-transfected with eGFP, AGO2 plasmids and shRNA plasmids which induced strong eGFP expression under light conditions (SH12, SH20), the construct that induced the highest fold change (SH22) and constructs of low to intermediate performance in terms of light-activated eGFP expression and fold changes (SH2, SH5). As additional controls, aptamer-deficient shRNAs (SH1 and SH9), an aptamer-containing variant with low inhibitory activity (SH4) or untransfected cells (None) were tested as well. An increased eGFP fluorescence could be observed for cells that were incubated in light and transfected with SH5, SH12, SH20 or SH22 whereas the fluorescence was reduced when cells of that kind were incubated in darkness (**Figure 4.28**, **Figure 10.4**). As for flow cytometry experiments (see **Figure 4.23d**), SH4 showed intermediate levels of eGFP fluorescence which were nearly independent to the light irradiation state. SH2, SH9 and untransfected cells showed weak to no eGFP fluorescence independent to the light irradiation state (**Figure 4.28**, **Figure 10.4**). Interestingly, SH1 as the sole variant displayed slightly increased eGFP fluorescence in darkness compared to the light condition (**Figure 4.28**, **Figure 10.4**).

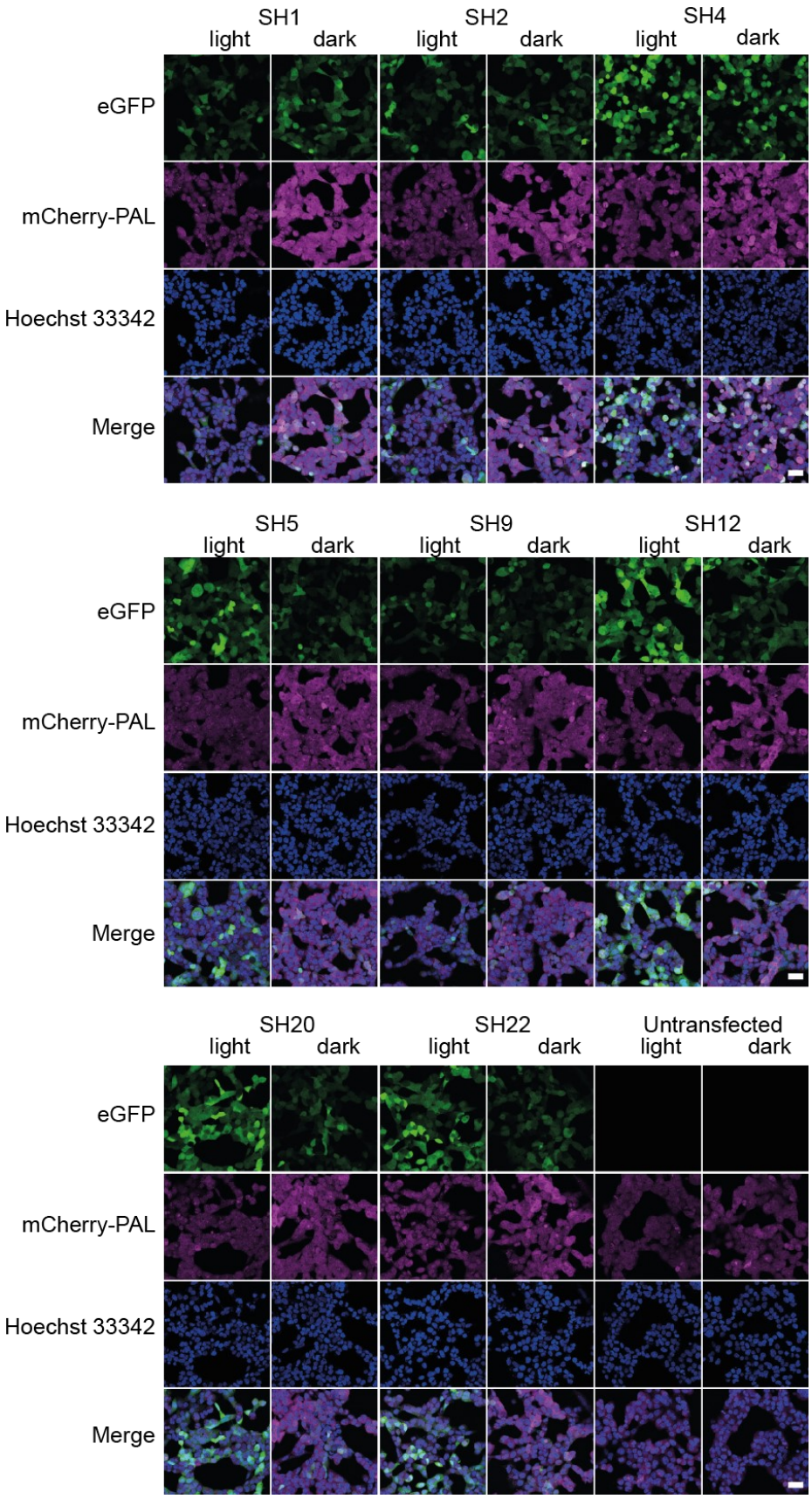

Figure 4.28: Fluorescence microscopy reveals light-dependent eGFP expression mediated by shRNAs. Fluorescence microscopy images of HEK293PAL cells which were transfected with the indicated shRNA variants. Cells were incubated under either light or dark conditions. Green: Fluorescence of reporter eGFP, magenta: Fluorescence of mCherry-PAL, blue: Nuclear

staining with Hoechst 33342, merge: Superposition of all fluorescence images that were generated per sample. N = Three biologically independent experiments performed in duplicates. Scale bar: 40 µm.

Taken together, the light-dependent increase in eGFP expression which was observed in flow cytometry experiments could be reproduced in fluorescence microscopy experiments for SH5, SH12, SH20 and SH22. A light-dependent increase in eGFP expression was not observed for the controls SH1 and SH9 and for the unmodified hinge region variants SH2 and SH4 due to light-dependent fold changes which may lie below the threshold of the method [271].

4.3.2.4 *In vitro* validation of eGFP shRNA binding to PAL

Additionally, *in vitro* binding studies were conducted to verify light-dependent interaction of selected shRNA variants to PAL in presence of 1000 nM (**Figure 4.29a**) or 100 nM (**Figure 4.29b**) shRNA. shRNA constructs that induced strong eGFP expression under light conditions (SH12, SH20), the construct that displayed the highest fold change (SH22), constructs of low to intermediate performance in terms of light-activated eGFP expression and fold changes (SH5, SH18) and a variant with predicted secondary structure rearrangement in the hinge region (SH23) were tested (**Figure 4.25a**, **Figure 4.27a**). As additional controls, a full length aptamer of 53.19 (53) and an shRNA which carries an aptamer point mutation (C9G, SH9, **Figure 4.24b**) were implemented into the assay. For assays in presence of 1000 nM RNA (**Figure 4.29a**), all shRNA constructs except for SH9 showed a similar interaction pattern which was within the binding range of the aptamer 53 (e.g. 99 % for SH5 and SH12, 90 % for SH18, 108 % for SH20, 113 % for SH22, 104 % for SH23 of 53 under light conditions and 39% for SH5 and SH12, 26 % for SH18, 34 % for SH20, SH22, SH23 and 49 % for 53 in darkness, **Figure 4.29a**). The aptamer point mutant SH9 indicated a binding to PAL to a lower extent compared to all other tested constructs (49 % under light conditions and 4 % in darkness, **Figure 4.29a**). For assays in presence of 100 nM shRNA, all shRNA constructs indicated a slightly decreased binding to PAL compared to the aptamer 53 (e.g. 82 % for SH5, 68 % for SH12, 77 % for SH18, 83 % for both SH20 and SH22, 81 % for SH22 of 53 under light conditions and 14 % for SH5, 8 % for SH12, 12 % for SH18, SH20, SH22, SH23 and 19 % for 53 in darkness, **Figure 4.29b**). The aptamer point mutant SH9 indicated a strongly decreased capability for light-dependent PAL binding (38 % under light conditions and 2 % in darkness, **Figure 4.29b**).

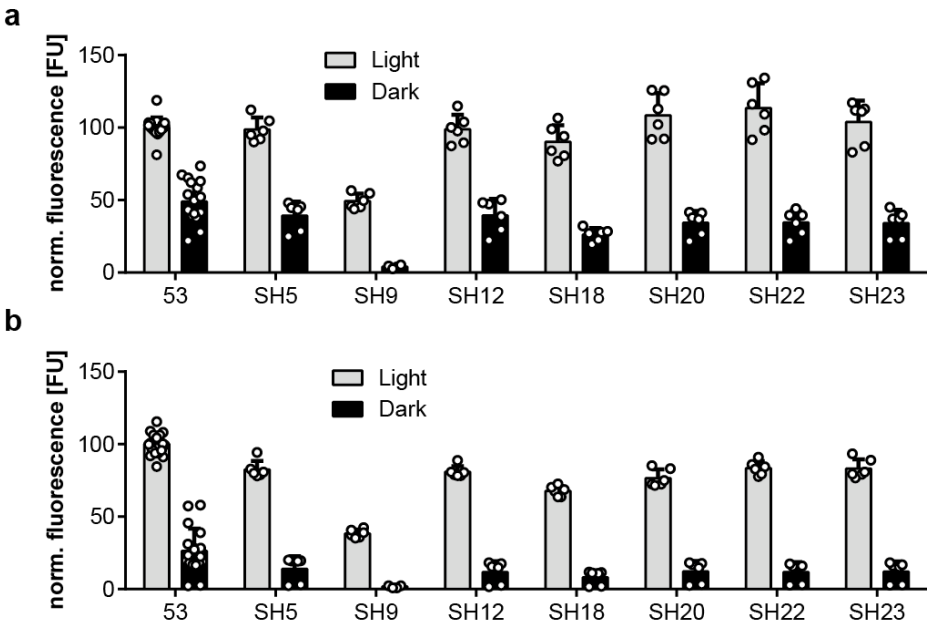

Figure 4.29: Aptamer 53.19-conjoined shRNA variants bind to PAL light-dependently *in vitro*, whereas a binding is reduced for the aptamer point mutant[7]. Biotinylated PAL protein was immobilized on streptavidin coated wells. A binding of 1000 nM (**a**) or 100 nM (**b**) shRNA constructs was quantified in presence of 0.5 mg mL^{-1} heparin and 0.5 mg mL^{-1} BSA by RiboGreen fluorescence. **a**,**b**, Values are processed by subtracting background fluorescence from equally treated wells without immobilized PAL and subsequent normalization to the aptamer 53 which was incubated under light conditions. **a**,**b**, N = Three independent experiments performed in duplicates. Grey bars: light conditions, black bars: darkness. Values are means ± s.d.

Compared to the full length aptamer 53, eGFP shRNAs indicated a decreased binding to PAL in darkness. This might be due to the nucleotide insertions which were embedded into the hinge regions of the eGFP shRNAs that may impact the interaction. The binding to PAL under light conditions varied slightly among the constructs but had no apparent correlation to the tertiary structure predictions. As expected, the aptamer point mutant (SH9) showed strongly decreased binding to PAL. The residual binding under light conditions suggests a tolerance for PAL binding to the C9G mutation of aptamer 53.19 and was not observed for C11G mutations (**Figure 4.9**).

4.3.2.5 Investigating the impact of kink motifs implemented into the hinge region of shRNAs targeting eGFP

In section 4.3.2.2, the shifting of the two abundant apical loops towards the opposite side of the radial axis compared to the loop from the original construct SH2 indicated high numbers of eGFP positive cells under light conditions. Due to this this observation, known structural RNA motifs which lead to strong conformational changes (kink-turn motifs, [272, 273]) were implemented into the hinge region. In principle, they could alter the orientation of the apical shRNA loops. At first, it was first asked whether the implementation of a kink-turn motif (SH26) or a modified variant thereof (SH25, **Figure 4.30a**) would disturb the base pairing in the stem region of aptamer 53.19. To this end, the hydrogen bond formation

[7] Experiment shown in **Figure 4.29** was performed by Charles Morgan.

of the aptamer's Wobble base pair (and all Watson Crick base pairs) was predicted (U4G16, **Figure 4.30b**). Next, three-dimensional RNA structure predictions were performed in overlay with SH2 to gain further insights into the aptamer's orientation (**Figure 4.30c**). Subsequently, HEK293PAL cells were co-transfected with plasmids which encode for eGFP, AGO2 and the respective shRNA variants that were encoded on pSilencer plasmids. Transfections of SHA, SH2 and SH12 served as control measures. After incubation of these cells under either light conditions or in darkness, flow cytometry analysis was performed (**Figure 4.30d**,**e**).

According to tertiary structure predictions for SH25 and SH26, hydrogen bond formation occurs for all anticipated Watson-Crick base pairs in the stem region of the aptamer 53.19 (not shown) and the Wobble base pair (**Figure 4.30b**). Furthermore, strong structural differences in the loop region could be observed for SH25 and SH26 compared to SH2 (**Figure 4.30c**). In both cases, loop 3 was located on the opposite side of the radial axis compared to loop 1 from SH2 (**Figure 4.30c**). A structural kink towards the center of the stem helix was observed in the hinge region for SH25, which leads to an additional twist within the region of loop 2 compared to SH26. This results in opposite orientations for loop 3 for SH25 compared to SH26 (**Figure 4.30c**). The highest number of eGFP expressing cells which were incubated under light conditions was observed in case of SH26 (82 %), followed by SH12 (58 %), SH25 (51 %) and SH2 (22 %, **Figure 4.30d**). The eGFP expressing cells in darkness were lowest for SH2 (6 %), followed by SH12 (11%), 25 (18 %) and SH26 (47 %, **Figure 4.30d**). This resulted in the highest calculated fold change of 5.3 for SH12, followed by SH2 (4.0), SH25 (2.8) and SH26 (1.8, **Figure 4.30e**). Transfections with SHA did not show a decrease of eGFP expression irrespective to the light irradiation state (**Figure 4.30d**).

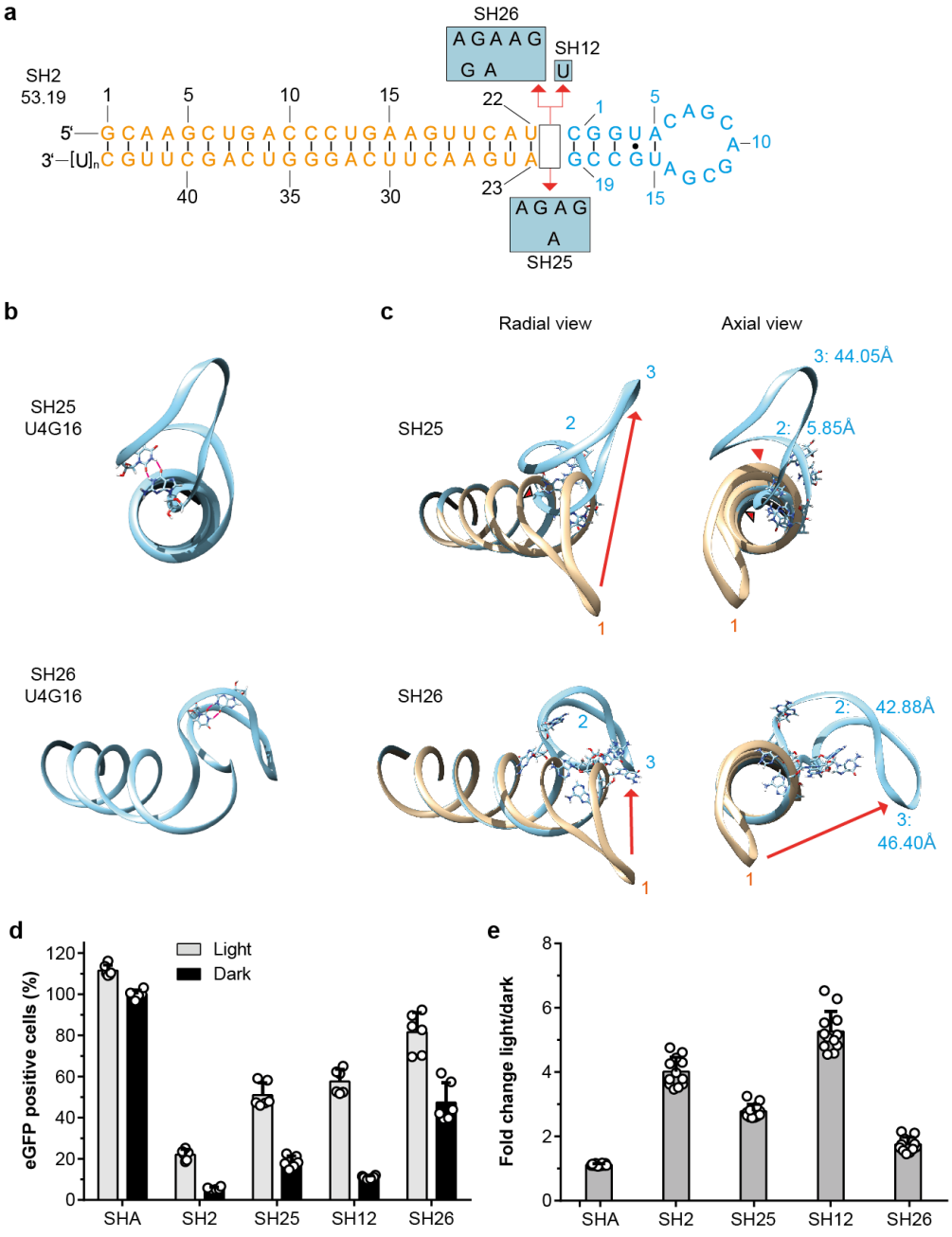

Figure 4.30: Characterization of light-responsive eGFP shRNAs with kinked hinge regions. Sequences which are known to provoke structural kinks were implemented in the hinge region (blue boxes) of SH2 that connects the siRNA (orange) to the aptamer (53.19, blue) as apical loop domain. **b**, Tertiary structure predictions of SH25 and SH26. Predicted hydrogen bonds of the U4G16 Wobble base pair are shown as pink lines between the two nucleobases (shown as ball stick model). **c**, RNA tertiary structure predictions of SH25 or SH26 (blue) in overlay with SH2 (orange). Red arrows: Striking structural changes of the apical loop domain were caused by nucleotide insertions (shown as ball stick model) into the hinge region. The distance of the oxygen atom in the ribose ring from the A5 nucleoside (depicted as 2) or the G9 nucleoside (depicted as 3) of 53.19 was predicted between the single nucleotide insertion variants and SH2. **d**, Number of cells which express eGFP after transfection with the indicated shRNA. Values are normalized to SHA (**Figure 4.13a**) which was incubated in darkness. **e**, Fold changes were calculated from light *vs*. dark conditions from (**d**). **d**,**e**, The results that are shown **Figure 4.31c**,**d** are part of the same experiment and therefore share the same controls (SHA, SH2 and SH12). N = Three biologically independent experiments performed in duplicates. Grey bars: light conditions, black bars: dark conditions. Dark grey bars: Fold changes. Values are means ± s.d.

These results indicated that a shift of the apical loop compared to the loop of SH2 correlated indeed with a higher number of eGFP positive cells in light but also led to an increased eGFP expression in darkness. Therefore, no constructs with increased fold change could be identified.

4.3.3 Investigation of Nm60 as potential optoribogenetic tool

Another promising PAL aptamer sequence (Nm60) was found by Anna Maria Weber within the next generation sequencing data of the PAL SELEX as well as in the genome of *Nakamurella multipartita*. Nm60 differs marginally from the original aptamer 53.19 sequence and both belong to the Motif2 aptamer family (**Figure 4.31a**). To test whether this sequence is capable to mediate light-activated gene expression, Nm60 was used to replace the aptamer 53.19 as the apical loop domain of the eGFP shRNA SH2 (**Figure 4.23**). To screen several aptamer orientations, a kink variant was designed (60_1) as well as a single nucleotide insertion variant upstream to the aptamer (60_2, **Figure 4.31a**). An enlarged aptamer stem variant of 60_2 which has an additional base pair at the aptamer's termini was tested as well (60_3, **Figure 4.31a**). Next, the tertiary structure of different hinge region variants was predicted (**Figure 4.31b**) and the shRNA variants were subsequently tested in HEK293PAL cells by using the eGFP reporter assay.

The tertiary structure predictions (**Figure 4.31b**) revealed two loops (loops 2 and 3) for all hinge region variants with different orientations compared to the loop 1 which was observed for the variant that has no hinge region implementations (Nm60, **Figure 4.31a**). Whereas loop 2 of 60_1 showed an orientation perpendicular to loop 1, loops 2 of 60_2 and 60_3 which were orientated on the opposite side of the radial axis compared to Nm60. For all three constructs loop 3 was orientated on the opposite side of loop 2.

The highest number for eGFP positive cells under light conditions was observed for the transfection of 60_3 (90 %), followed by 60_2 (80 %), SH12 (58 %), SH_1 (56 %) and SH2 (22 %) and highest number in darkness was displayed when 60_3 was transfected (32 %), followed by 60_1 (25 %), 60_2 (23 %), SH12 (11 %) and SH2 (6 %, **Figure 4.31c**). Thus, the highest fold change was observed for SH12 (5.3-fold), followed by SH2 (4.0-fold), 60_2 (3.9-fold), 60_3 (2.8-fold) and 60_1 (2.2-fold, **Figure 4.31d**). Transfections with SHA did not show a light-dependent reduction in the eGFP expression.

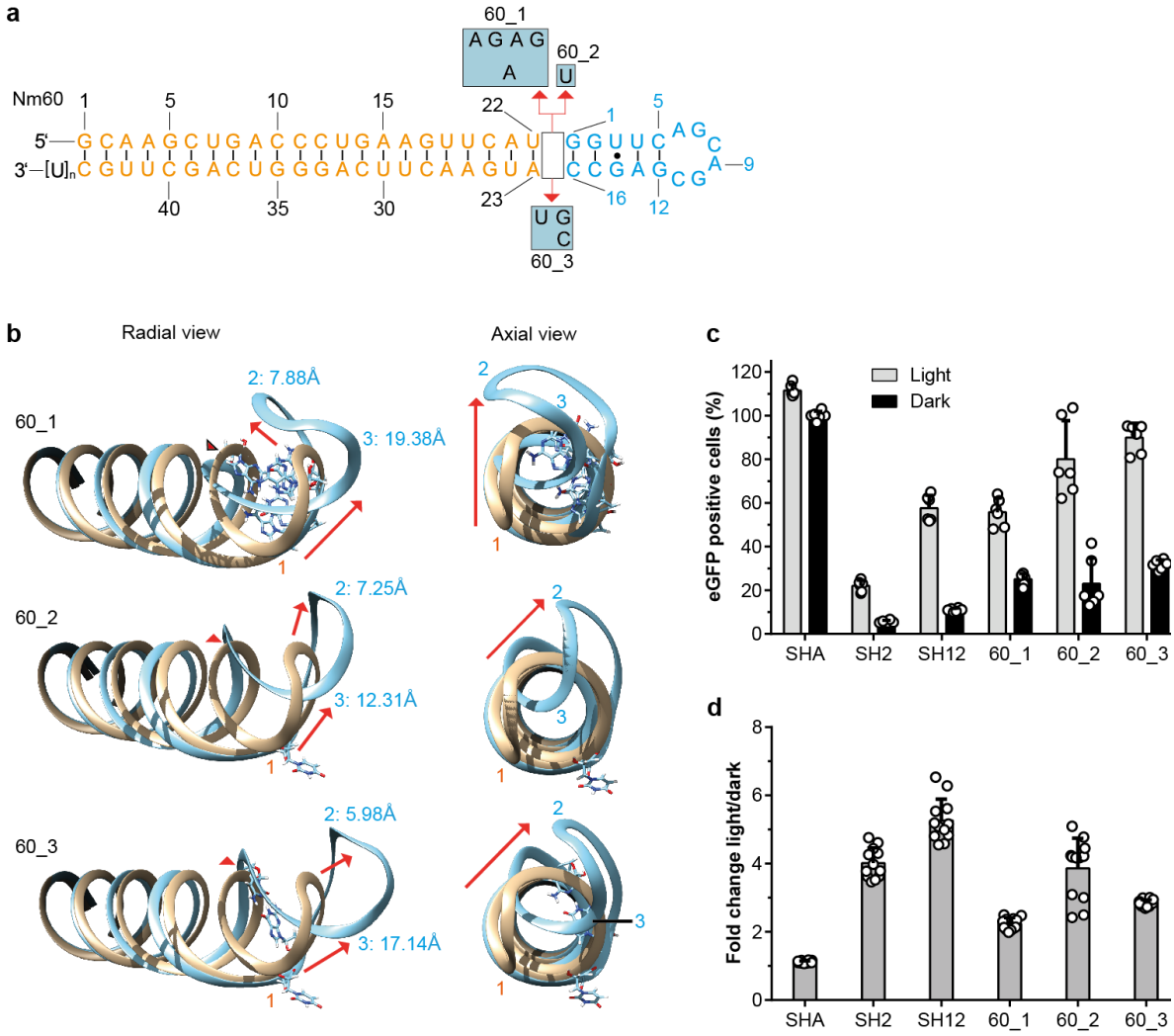

Figure 4.31: Validation of Nm60 as optoribogenetic tool in mammalian cells. a, Nm60 (blue) as apical loop domain was tested in conjunction with structural variations in the hinge region (blue boxes) and a siRNA (orange) targeting eGFP. **b**, RNA tertiary structure predictions of hinge region variants (blue) in overlay with no hinge region nucleotide insertions (Nm60, orange). Red arrows: Striking structural changes of the apical loop domain which were caused by nucleotide insertions (shown as ball stick model) into the hinge region. **c**, Number of cells which express eGFP after transfection with the indicated shRNA. Values are normalized to SHA (**Figure 4.13a**) which was incubated in darkness. **d**, Fold changes were calculated from light *vs*. dark conditions from (**c**). **c**,**d**, The results shown **Figure 4.30c**,**d** are part of the same experiment and therefore share the same controls (SHA, SH2 and SH12). N = Three biologically independent experiments performed in duplicates. Grey bars: light conditions, black bars: dark conditions. Dark grey bars: Fold changes. Values are means ± s.d.

In conclusion, Nm60 might be a useful tool for optoribogenetics because all tested variants showed high levels of eGFP expression under light conditions. Tertiary structure predictions of the apical loop orientation towards the opposite side of the radial axis compared to Nm60 correlated with this observation. However, and similar to what was described in section 4.3.2.5, the eGFP expression in darkness increased together with the altered apical loop orientation. Consequently, no variants with increased light-dependency could be identified. Therefore, the *in-silico* design of shRNA variants cannot be used to predict shRNA variants with enhanced light-regulatory properties. To further increase the

light responsiveness of Nm60 in conjunction with the eGFP siRNA, the identity of the single hinge region nucleotide could be screened in future experiments.

4.4 Investigating the impact of light intensity and timing on light-dependent reporter protein abundance

Similar than diffusion-based regulatory systems that are controlled by the concentration of small-molecules [164], light-dependent systems are tunable *via* the applied light dose. Furthermore, as it was demonstrated in section 4.2.3.1 that the optoribogenetic control of gene expression is reversible, the timing of light may also play an important role in regulation. To investigate the impact of both parameters on the light-dependent eGFP expression in cells, two experiments were conducted within this section. In the first experiment which focused on the effect of different light intensities (**Figure 4.32**), HEK293PAL cells were co-transfected with AGO2, eGFP and either SH5 or SH9. Then, cells were incubated under continuous light conditions at different intensities (450, 220, 100, 55, 12.5, 8, 4 or 0 µW/cm^2) at λ = 465 nm. 44 h after transfection, the cells were subjected to flow cytometry analysis. A maximal number of eGFP positive cells was achieved when the cells were transfected with SH5 and incubated under 100 µW/cm^2 blue light (21 %, **Figure 4.32a,** 4.1-fold change compared to incubation in darkness, **Figure 4.32b**). The number of eGFP positive cells decreased, when the light intensity was either increased or decreased (**Figure 4.32a)**, which also led to reduced fold changes (**Figure 4.32b**). The eGFP expression was comparably low (4.5 – 5.6 %) for cells which harbor SH9 under all tested light conditions and for cells that harbor SH5 in darkness (**Figure 4.32a)**. No light-responsiveness could be observed for SH9 (**Figure 4.32b**).

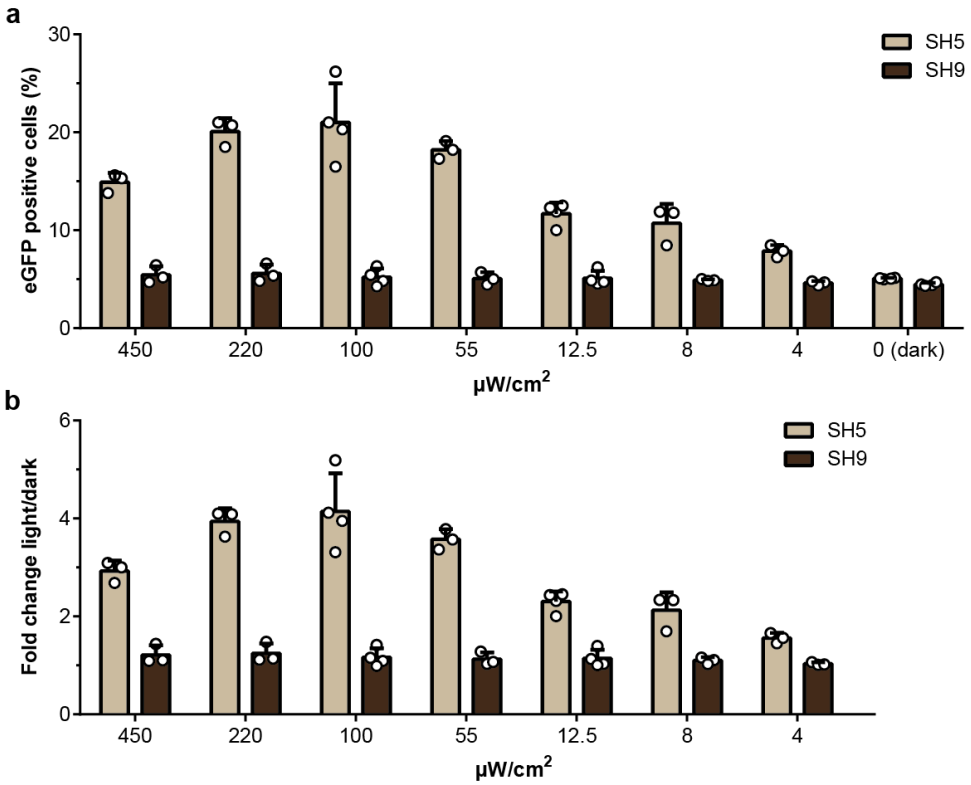

Figure 4.32: Optimization of the light intensity to maximize the number of eGFP positive cells. HEK293PAL cells were transfected with SH5 (light brown bars) or SH9 (dark brown bars) and incubated under constant light at the indicated intensities. **a**, Number of eGFP positive cells. **b**, Fold changes which were calculated from light *vs*. dark conditions from (**a**). For gating strategy, see section 7.5.11. N = At least three biologically independent experiments performed as single value determination. Values are means ± s.d.

Subsequently, the impact of pulsed light illumination on the eGFP expression under the control of light-responsive shRNAs was tested. HEK293PAL cells were transfected similarly as described above (**Figure 4.32**) and these cells were incubated under light pulses of fixed illumination time periods (30 sec) and fixed light intensities (100 µW/cm^2), whereas the time of incubation in darkness between the light pulses was varied (0, 20, 30, 40, 60, 90, 120 and 300 sec). Here it was observed that constant light (0 sec) indicated the highest number of eGFP positive cells that were transfected with SH5 (17 %, **Figure 4.33**, 3.3.-fold compared to incubation in darkness, **Figure 4.33b**). The number of eGFP positive cells (**Figure 4.33a**) and consequently, the light-dependent fold changes (**Figure 4.33b**) decreased continuously, when prolonged time periods in darkness were applied to the cells (**Figure 4.33b**). The eGFP expression was comparably low (5.9 % – 7.4 %) for cells which harbor SH9 under all tested conditions and for cells that harbor SH5 in darkness (**Figure 4.33a**). Again, no light-responsiveness could be detected for SH9 (**Figure 4.33b**).

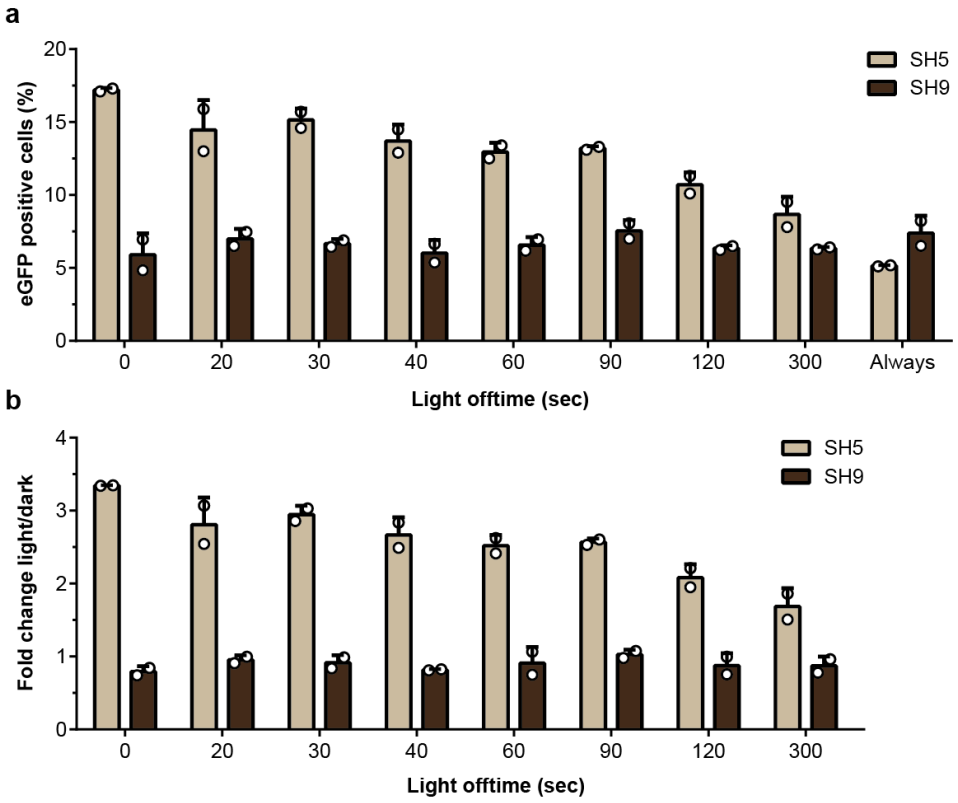

Figure 4.33: Optimization of the light pulse period to maximize the number of eGFP positive cells. HEK293PAL cells were transfected with SH5 (light brown bars) or SH9 (dark brown bars) and incubated under 30 sec blue light pulses (100 µW/cm^2), followed by time intervals of the indicated lengths of incubation in darkness. **a**, Number of eGFP positive cells. **b**, Fold changes were calculated from light *vs*. dark conditions from (**a**). For gating strategy, see section 7.5.11. N = At least two biologically independent experiments performed as single value determination. Values are means ± s.d.

These two experiments revealed that the highest eGFP expression can be achieved when HEK293PAL cells are treated with constant blue light at an intensity of 100 µW/cm^2. This also results in the highest achievable fold change among all tested light conditions.

4.5 Optoribogenetic control of physiological processes

4.5.1 Light-control of cell cycle progression

It was reasoned that the mammalian cell cycle would be suitable physiological process to demonstrate the generic applicability of light-responsive shRNAs, because it has been studied for a long time and has been controlled before by using shRNAs [274]. Therefore, large methodological and theoretical repository is accessible in the literature. As optoribogenetic approaches are reversible as shown in section 4.2.3.1, the cell cycle progression could be switched on and off reversibly in later applications. This can be of interest for cellular reprogramming, as new approach for studying cancer, novel gene therapies and improved protein production for medical and industrial applications [230].

4.5.1.1 Light-control of the cell cycle using shRNAs targeting cyclin B1 and CDK1

Cyclin B1 and CDK1 are both essential proteins for the transition from gap 2 (G_2) to the mitosis (M) phase of the mammalian cell cycle [275]. To accumulate the cells in G_2/M phase, two shRNAs that target cyclin B1 (SHCBi and SHCBii) and two shRNAs that target CDK1 (SCDKi and SHCDKii) were tested for their impact on cell cycle distribution in a first light-independent screening experiment. For these shRNA variants, a control sequence was used as apical loop domain and conjoined with the respective siRNAs without the implementation of any hinge region modifications (**Table 8.5**). In additional samples, SHCBi and SHCDKi were co-transfected together (50 ng or 100 ng of each pSilencer variant). As controls, cells were transfected with SH5 (shRNA that targets eGFP, **Figure 4.25a**) or remained untransfected (None, **Figure 4.34**). All above-named shRNA variants were co-transfected with AGO2 into HEK293PAL cells and incubated for 44 h in darkness. For SHCBi or SHCDKi, an increased accumulation of cells in G_2/M was observed (24 % and 25 %, respectively, **Figure 4.34**). Transfecting both plasmids together, the accumulation could be further increased when 100 ng of each pSilencer plasmid were transfected (28 %), but not when 50 ng of each plasmid were transfected per well (25 %, **Figure 4.34**). SHCBii and SHCDKii did not display an accumulation of cells in G_2/M phase (16 % *vs*. 15 %), as these values were also observed within the range for the control samples (15 % for SH15 and 13 % for untransfected cells, **Figure 4.34**).

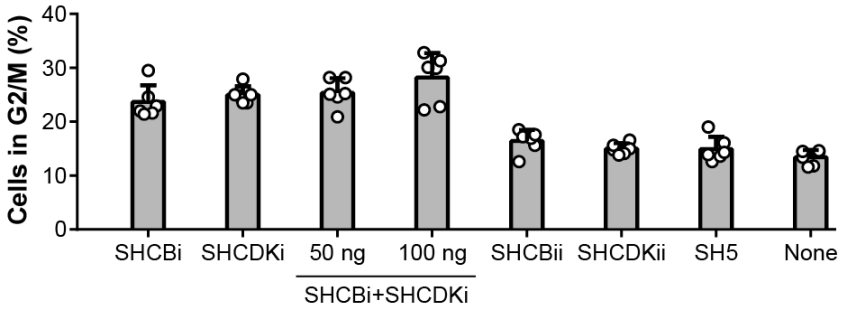

Figure 4.34: Screening of shRNAs targeting cyclin B1 or CDK1. Percentages of HEK293PAL cells in G_2/M phase of the cell cycle when transfected with indicated shRNAs. SHCBi+SHCDKi: 50 ng or 100 ng of each plasmid were transfected together. N = Three biologically independent experiments performed in duplicates. Values are means ± s.d.

After successful accumulation of cells in G_2/M phase by using SHCBi and SHCDKi, these shRNAs should be rendered light-dependently. To this end, the control loop sequence was exchanged to the aptamer 53.19 and an additional adenine upstream to the aptamer was implemented into the hinge region of SHCBi (SHCB1, **Figure 4.35a**) and SHCDKi (SHCDK1, **Figure 4.35b**). As controls, a G11C mutation was introduced within the aptamer region into both shRNAs to form SHCB1m (**Figure 4.35a**) and SHCDK1m (**Figure 4.35b**). To verify whether these shRNA variants are capable to bind to PAL*, in vitro* binding studies were performed in presence of 1000 nM (**Figure 4.35c**) or 100 nM (**Figure 4.35d**) shRNA under light conditions or in darkness. For assays in presence of 1000 nM shRNA that was incubated in light, SHCB1 showed an increased binding (110 %) and SHCDK1 showed a similar binding (102 %) compared to the full length aptamer 53 (**Figure 4.35c**). A reduced binding in darkness was

observed for all three variants (31 % for SHCB1, 23 % for SHCDK1 and 49 % for 53, **Figure 4.35c**). Control shRNAs which have an aptamer point mutation showed weak to no binding, irrespective to the applied light conditions (9 % *vs*. 8% under light conditions and 2 % *vs*. 1 % in darkness for SHCB1m and SHCDK1m, respectively, **Figure 4.35c**). For assays in presence of 100 nM shRNA that was incubated in light, SHCB1 showed an increased binding (110 %) and SHCDK1 showed a slightly reduced binding (95 %) compared to the full length aptamer 53 (**Figure 4.35d**). A strongly reduced binding in darkness was observed for these variants (21 % for SHCB1, 15 % for SHCDK1 and 26 % for 53, **Figure 4.35d**). Control shRNAs which have an aptamer point mutation showed weak to no binding, irrespective to the applied light conditions (4 % *vs*. -28% for SHCB1m and 4 % for SHCDK1m under light and dark conditions, respectively, **Figure 4.35d**).

Having shown that the shRNA variants SHCB1 and SHCDK1 are capable to bind to PAL light-dependently *in vitro*, it was tested next whether these constructs are suitable for the light-control of the cell cycle progression through the G_2/M phase. Here, HEK293PAL cells were co-transfected with plasmids which encode for SHCB1 and/or SHCDK1 and a plasmid that encodes for AGO2. Control transfections were performed by using the corresponding aptamer point mutants (SHCB1m and/or SHCDK1m), an eGFP shRNA (SH5, **Figure 4.25a**) or cells which remained untreated (None). Subsequently, the cells were incubated under light conditions or in darkness for 44 h. Weak to no light-independent accumulation of cells in the G_2/M phase was detected in transfections including SHCB1, SHCDK1 and their respective aptamer point mutants SHCB1m and SHCDK1m (24 % – 18 % among all transfections, **Figure 4.35e**). The highest accumulation was observed for SHCDK1m (24 % in light and 22 % in darkness), whereas the lowest accumulation was observed for the transfection of SHCB1 (18 % in light and 19 % in darkness, **Figure 4.35e**). Under light conditions, a very slight accumulation of cells in the G_2/M phase was observed for SH5 (14 % *vs*. 11 % in light and darkness) and for untransfected cells (None, 12 % *vs*. 9 % in light and darkness, **Figure 4.35e**) was observed.

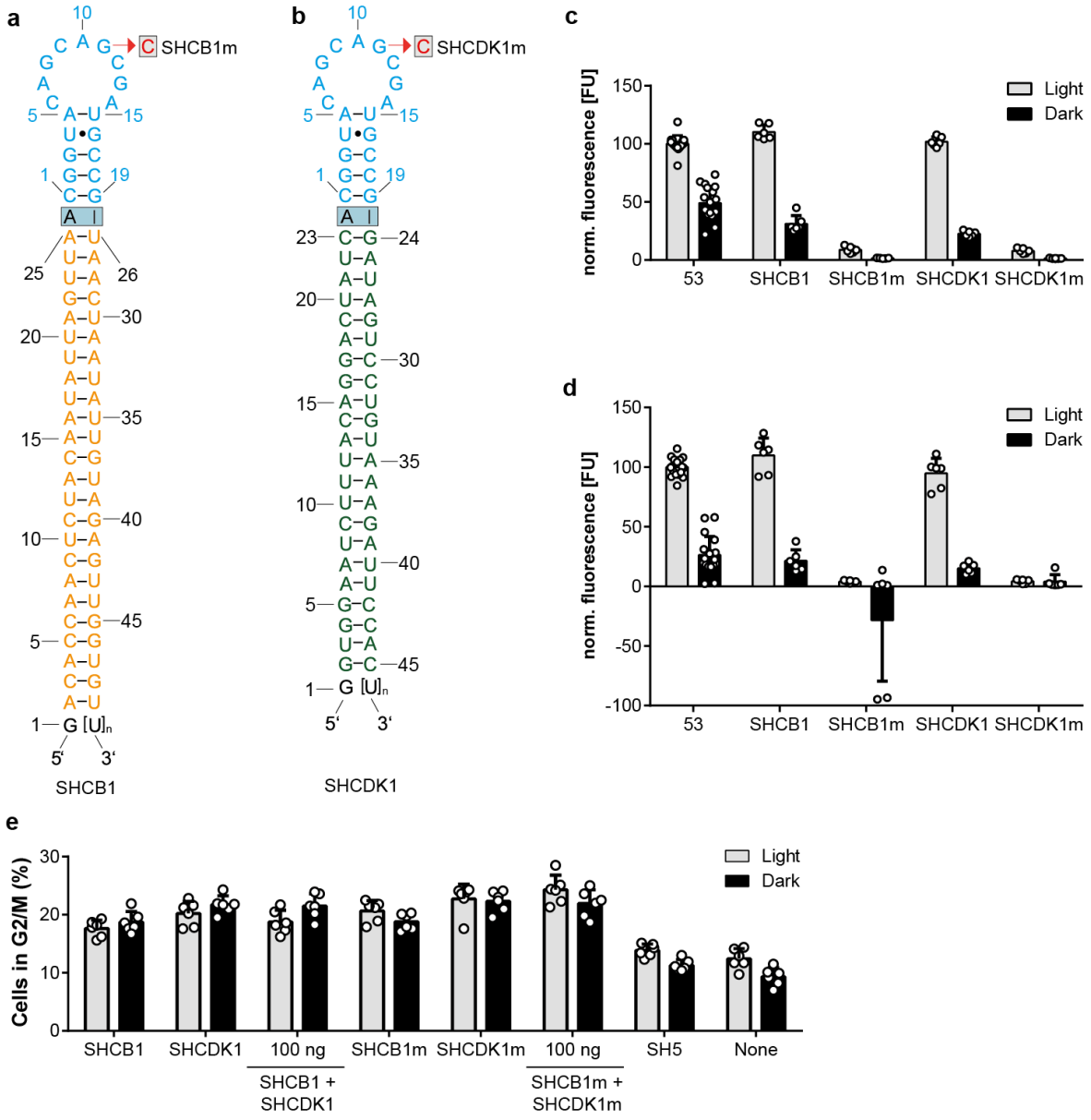

Figure 4.35: Aptamer 53.19-conjoined shRNAs targeting cyclin B1 or CDK1 bind to PAL light-dependently and accumulate cells in G_2/M phase. **a**,**b**, siRNA sequences targeting cyclin B1 (orange, **a**) or CDK1 (green, **b**) mRNA were conjoined with the PAL aptamer (53.19, blue boxes) *via* an unpaired adenine upstream to the aptamer. **a**,**b**, Aptamer-point mutated variants thereof were generated to remove light-dependency (G11C, grey boxes). **c**,**d**, Biotinylated PAL protein was immobilized on streptavidin coated wells. Binding of 1000 nM (**c**) or 100 nM (**d**) shRNA constructs were quantified in presence of 0.5 mg mL^{-1} heparin and 0.5 mg mL^{-1} BSA by RiboGreen fluorescence. **c**,**d**, Values are processed by subtracting background fluorescence from equally treated wells without immobilized PAL and subsequent normalization to 53 which was incubated under light conditions[8]. **e**, Percentages of HEK293PAL cells in G_2/M phase of the cell cycle when transfected with indicated shRNAs. **c-e**, N = At least three independent experiments performed in duplicates. Grey bars: light conditions, black bars: darkness. Values are means ± s.d.

In summary, aptamer-modified shRNA variants that target cyclin B1 and CDK1 have been generated. These shRNAs are capable to bind to PAL light-dependently *in vitro*. Furthermore, they were capable

[8] Experiments that are shown in **Figure 4.35c**,**d** were performed by Charles Morgan.

to accumulate cells in G_2/M phase of the cell cycle. However, no light-dependent accumulation of cells in G_2/M phase was observed at this point.

Up to this point it was reasoned that a co-transfection of AGO2 improves the knockdown efficiency and fold changes as it was observed for the light-control of eGFP expression in section 4.2.2.6. However, as the number of transcripts for intrinsic mRNAs is much lower compared to the CMV promoter driven reporter transcript levels [276], it was reasoned that no elevated levels of AGO2 protein might be needed to suppress cyclin B1 or CDK1 efficiently in order to accumulate cells in the G_2/M phase. Together with this hypothesis, the impact of the hinge nucleotide identity was studied for cyclin B1 shRNA. Besides SHCB1, which has an adenine implemented in the hinge region upstream to the aptamer, a uridine was tested at this position (SHCB2) and at the position downstream to the aptamer (SHCB3). As a control, a G11C aptamer point-mutant of SHCB1 was tested alongside in cells (SHCB1m, **Figure 4.36a**). Therefore, HEK293PAL cells were transfected solely with the pSilencer plasmid that encodes for the indicated shRNA variant and the impact of light on the G_2/M phase accumulation was quantified after 44 h of incubation (**Figure 4.36b**). Interestingly, an accumulation in the G_2/M phase in cells that harbor SHCB1 was elevated in darkness (17 %) and reduced under light conditions (13 %), whereas an accumulation in the G_2/M phase was observed irrespective to the light conditions in cells that harbor SHCB1m (18 %, **Figure 4.36b**). SHCB2 and SHCB3 did not show an accumulation in G_2/M phase irrespective to the light irradiation state (13 % – 14 %, **Figure 4.36b**). Concerning CDK1, a hinge region variant which has an unpaired adenine upstream to the aptamer (SHCDK1) and its respective aptamer point mutant (SHCDK1m, **Figure 4.36c**) were also tested for light-dependent accumulation of cells in the G_2/M phase (**Figure 4.36d**) together with eGFP shRNA (SH5, **Figure 4.25a**) and untransfected cells (None). Similar as for SHCB1, an accumulation of the G_2/M phase in cells which harbor SHCDK1 was elevated in darkness (21 %) and decreased under light conditions (16 %), whereas an accumulation in the G_2/M phase was observed irrespective to the light conditions in cells that were transfected with SHCDK1m (20 % under light conditions, 22 % in darkness, **Figure 4.36d**). Instead, SH5 and untransfected cells indicated a very slight accumulation of cells in the G_2/M only under light conditions (13 % for SH5 and 12 % for None) compared to incubation in darkness (12 % for SH5 and 11 % for None, **Figure 4.36d**).

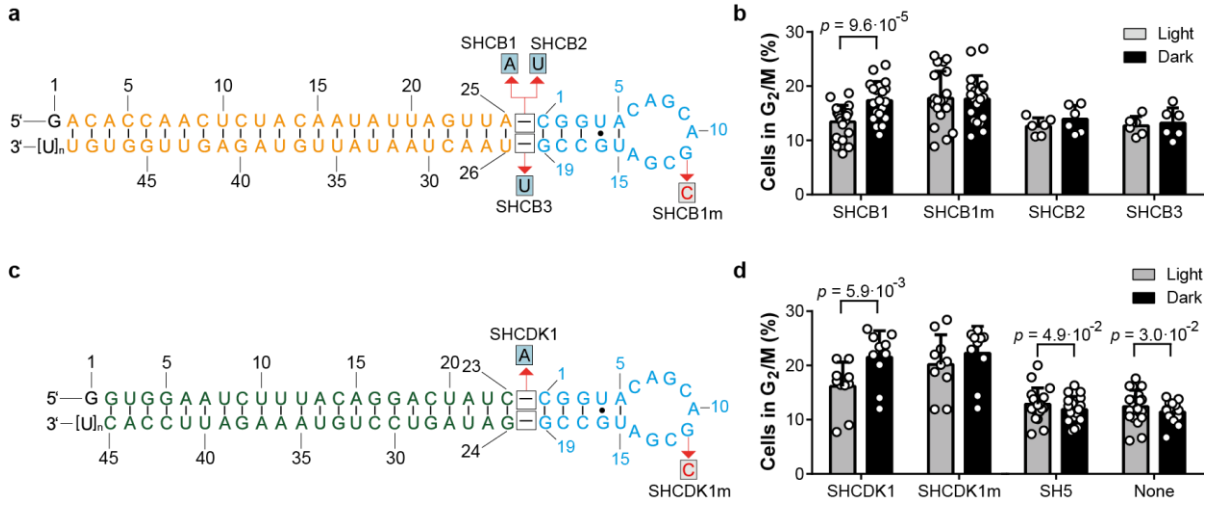

Figure 4.36: Optoribogenetic control of the mammalian cell cycle. a, shRNA variants were used to control cyclin B1 gene expression. Blue: aptamer domain; orange: siRNA domain. **b**, Percentages of HEK293PAL cells in G_2/M phase of the cell cycle when transfected with indicated shRNAs that target cyclin B1. **c**, shRNA variants were used to control CDK1 gene expression. Blue: aptamer domain; green: siRNA domain. **d**, Percentages of HEK293PAL cells in G_2/M phase of the cell cycle when transfected with indicated shRNAs that target CDK1. **b**,**d**, For representative flow cytometry cytograms, see **Figure 10.5**. **b**,**d**, N = At least three biologically independent experiments performed in duplicates. **b**, The identity of SHCB1 and SHCB1m was blinded and double-blinded in one experiment. **d**, The identity of SHCDK1 and SHCDK1m was blinded and double-blinded in one experiment. **b**,**d**, Wilcoxon two-sided signed-rank test was used for statistical analysis. Values are means ± s.d.

These results suggest that an optoribogenetic control of the mammalian cell cycle is accessible for two intrinsic target genes by using regulatory RNAs that were equipped with the PAL aptamer 53.19 which is connected with a suitable nucleotide in the hinge region and a functional siRNA.

4.5.1.2 Light-control of cell cycle using shRNAs targeting PLK1

As an additional intrinsic target protein, PLK1 was chosen. This protein is essential for both entry and progression through the mitosis phase [277]. Decreased PLK1 protein levels lead to an accumulation of cells in the G_2/M phase and eventually to cell death [226]. To establish an optoribogenetic control of the PLK1 protein levels, a series of hinge region variants (SHPLK1 – 7, **Figure 4.37a**) were generated and screened for their ability to alter the cycle distribution light-dependently (**Figure 4.37b**). These hinge region variants either consisted of single or two-nucleotide adenine or uridine insertions that were either symmetrically or asymmetrically incorporated (**Figure 4.37a)**. The aptamer point-mutant (G11C, SHPLK1m) for an asymmetrically implemented adenine upstream to the aptamer (SHPLK1) was used as a control along with an eGFP shRNA (SH5, **Figure 4.25a**) and untransfected cells (None). The cells were incubated for 29 h after transfection under the indicated light conditions. For SHPLK2 and SHPLK4, decreased levels of cells in the G_2/M phase were detected under light conditions (22 % *vs*. 31 %) while the G_2/M phase levels increased, when cells were incubated in darkness (36 % *vs*. 39 %, **Figure 4.37b**). All other tested shRNA variants which target PLK1 indicated an accumulation of cells in the G_2/M phase irrespective to the light irradiation state (SHPLK1, SHPLK1m and SHPLK3 - 7: 28 % – 39 % among all tested transfections, **Figure 4.37b**). SH5 and the untransfected cells did not indicate an accumulation

of cells in the G_2/M phase irrespective to the applied light conditions (15 % - 17 %, **Figure 4.37b**). As SHPLK2 indicated the highest light-dependent difference of the G_2/M phase levels by far, an aptamer point mutant thereof (G11C, SHPLK2m) was constructed and the experiment was repeated 44 h after transfection (**Figure 4.37c**). SHPLK2 indicated decreased levels of cells in the G_2/M phase when incubated in light (14 %), compared to the incubation in darkness (21 %) and the latter value was identical to the levels which were observed for SHPLK2m, irrespective to the applied light conditions (**Figure 4.37c**).

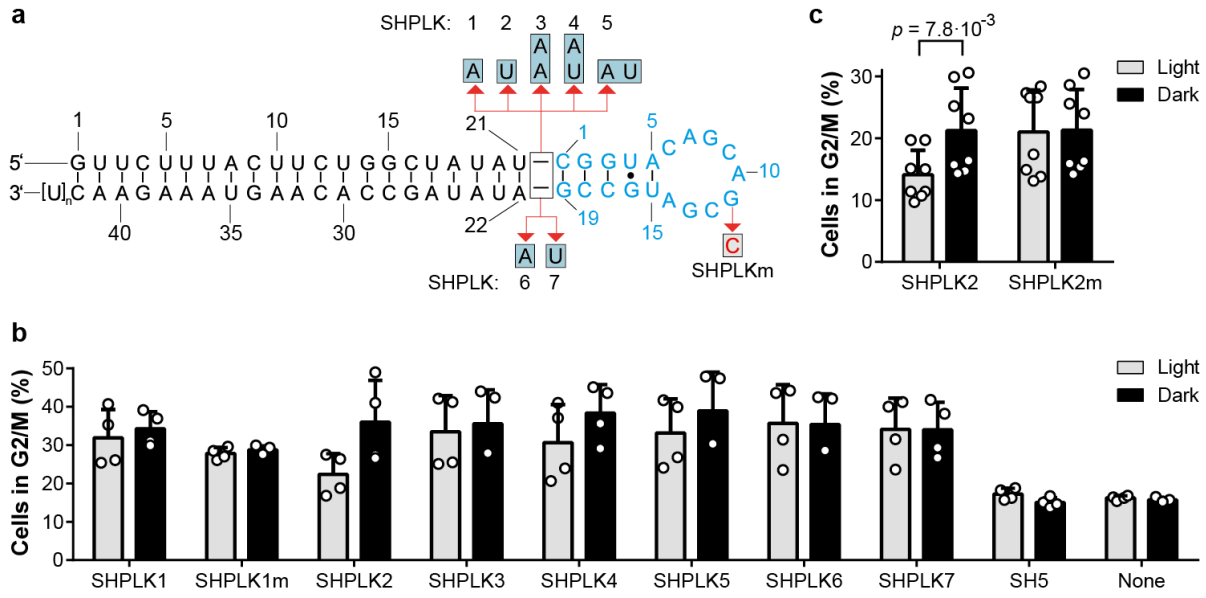

Figure 4.37: Optoribogenetic approach can be extended to additional intrinsic targets. a, shRNA variants were used to control PLK1 gene expression. Blue: aptamer domain; black: siRNA domain, red: aptamer point mutants. **b**, Percentages of HEK293PAL cells in G_2/M phase of the cell cycle when transfected with indicated shRNAs that target PLK1 29 h after transfection. **c**, Percentages of HEK293PAL cells in G_2/M phase of the cell cycle when transfected with indicated shRNAs that target PLK1 44 h after transfection. **c**, For representative flow cytometry cytograms, see **Figure 10.5**. **c**, Experiment was double-blinded in one experiment. N = Two (**b**) or four (**c**) biologically independent experiments performed in duplicates. **c**, Wilcoxon two-sided signed-rank test was used for statistical analysis. Values are means ± s.d.

Taken together, the light-control of a physiological output (cell cycle accumulation) was increased with a shRNA that target PLK1 as a third intrinsic target gene.

4.5.2 Light-control of target protein abundance

It was shown that cell cycle distribution can be controlled light-dependently by using shRNAs that target cyclin B1, CDK1 and PLK1. However, so far it was not shown whether the observed effect is indeed linked to altered levels of target gene expression. To verify the target protein levels semi-quantitatively, western blot studies have been performed. Here, HEK293PAL cells were transfected with pSilencer plasmids which encode for aptamer 53.19-modified shRNAs that target cyclin B1, CDK1 and PLK1

(SHCB1, SHCDK1, **Figure 4.36** and SHPLK2, **Figure 4.37**) and their corresponding aptamer point mutants (G11C, SHCB1m, SHCDK1m, **Figure 4.36** and SHPLK2m, **Figure 4.37**). As additional controls, eGFP shRNA SH5 (**Figure 4.25a**) was transfected or cells were left untreated (None). 44 h after incubation under light conditions or in darkness, the cells were lyzed and the protein lysate was loaded onto SDS-PAGE gels. Subsequently, gels were blotted, incubated with the indicated primary and secondary antibodies and then subjected to the fluorescence readout. GAPDH was used for normalization and Histone H3 was used as additional loading control for the PLK1 gels. SHCB1 or SHCDK1 in darkness led to a decrease of the target protein expression which was reversed by irradiation (**Figure 4.38a**,**c**,**d**). Corresponding aptamer point mutants (SHCB1m and SHCDK1m) suppressed the protein expression irrespective to the light irradiation state (**Figure 4.38a**,**c**,**d**). shRNAs that target cyclin B1 did not perturb CDK1 protein levels and *vice versa*. SHPLK1 or SHPLK1m slightly suppressed protein expression under both light and dark conditions (**Figure 4.38b**,**e**). SH5 did not alter cyclin B1, CDK1, PLK1, GAPDH or Histone H3 protein expression, similar to the untransfected cells (**Figure 4.38a**-**e**).

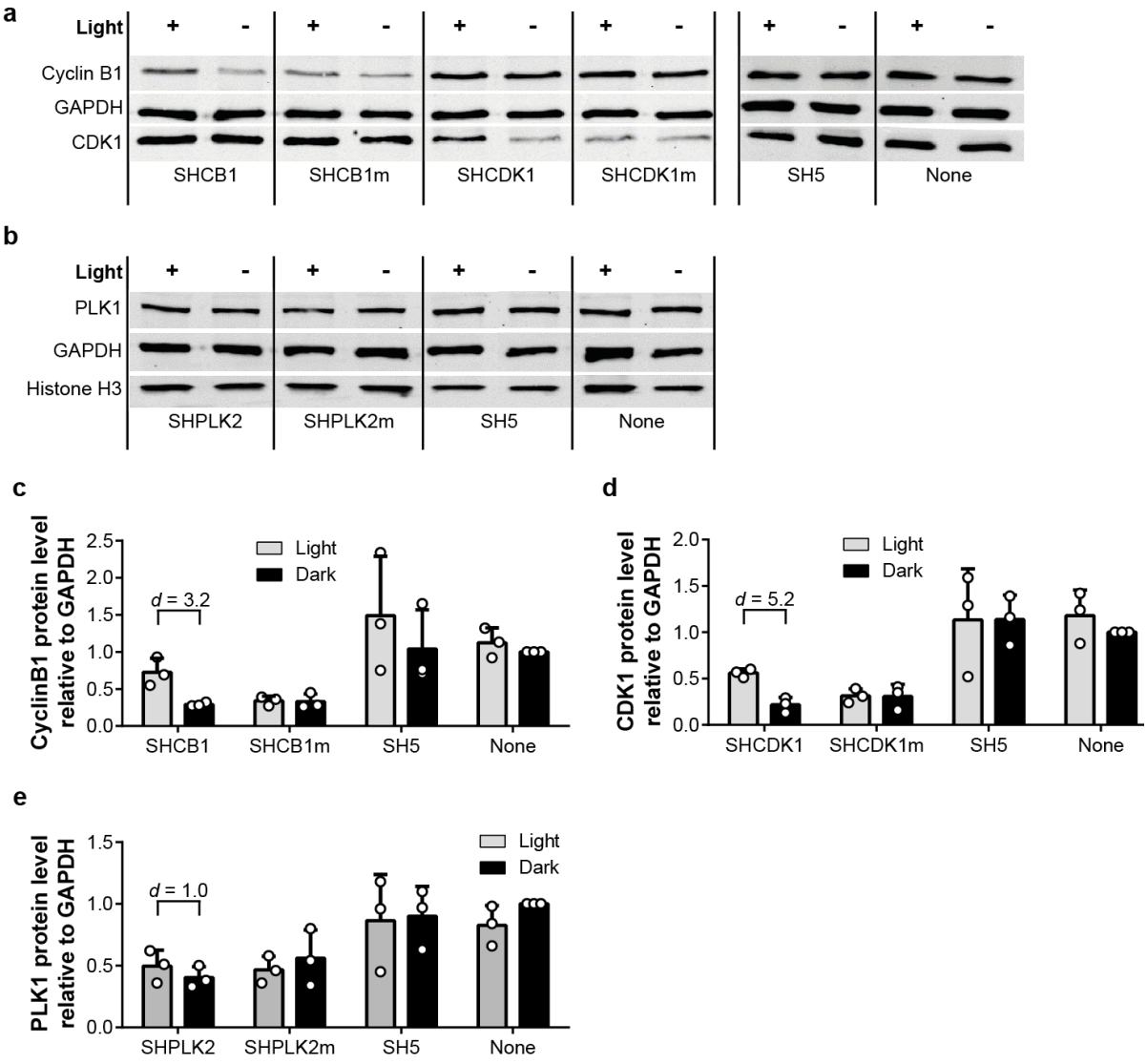

Figure 4.38: Optoribogenetic control of target protein abundance. Representative western blot images showing cyclin B1, CDK1 (a), PLK1, Histone H3 (b) and GAPDH (**a**,**b**) protein expression after transfection with the indicated shRNAs (for complete blots, see **Figure 10.6**). Pixel densitometry was used for the quantification of cyclin B1 (**c**), CDK1 (**d**) and PLK1 (**e**) protein levels. **c**,**d**, Cohen's *d* effect size was used to estimate the magnitude of difference between the different light treatments. **c**-**e**, N = Three independent experiments. Values were normalized to non-transfected cells which were incubated in darkness (None). **c**-**e**, Grey bars: cells incubated under light conditions, black bars: cells incubated under dark conditions. Values are means ± s.d.

In conclusion, cyclin B1 and CDK1 protein levels could be decreased in cells which harbor the respective shRNAs when they were incubated in darkness and the protein levels were partially restored when similar cells were incubated in light. PLK1 protein levels were found to be suppressed irrespective to the light irradiation state. This might be a consequence of the limited sensitivity of the method.

5 Discussion

5.1 Expression of PAL in mammalian cells

5.1.1 Conformational switching of PAL and its fusion proteins

Photoswitching of PAL in the mCherry-PAL fusion protein had been shown before in HeLa cells [237]. Within this thesis, this experiment was repeated in HEK293 cells as these cells are also easy to transfect. Whereas the HeLa cell line is derived from cervical cancer, HEK293 cells are derived from embryonic kidney cells which reflect a different mammalian cell type. Similar as before, the PAL fluorescence was only detectable when the protein was incubated in darkness (**Figure 4.1b**). The expression mCherry alone did not indicate PAL fluorescence (**Figure 4.1a**). Upon illumination with blue light (405 nm), the PAL fluorescence in mCherry-PAL disappeared after a short time (<1 sec). As this wavelength is also used for PAL excitation in fluorescence microscopy, it is necessary to collect quick images at the expense of image resolution (**Figure 4.1**). Similarly, switching studies were performed in HEK293 cells using 4E-BP1-mCherry-PAL (**Figure 4.5**). As the mCherry protein domain was embedded between the 4E-BP1 and the PAL domain, it was assumed that the photochemistry of PAL remained unaffected by the fusion with 4E-BP1. Indeed, similar results could be obtained for 4E-BP1-mCherry-PAL compared to mCherry-PAL (**Figure 4.5**). As for other LOV photoreceptors, the underlying mechanism for a light-triggered loss in fluorescence might be a covalent bond formation of PAL with the co-factor FMN [278] which renders FMN unable to absorb light between 405 nm to 505 nm (**Figure 4.8**)[279]. A 10 min incubation time in darkness was shown to be sufficient to switch most PAL proteins back to their dark-adapted conformational state [237]. This was indicated by the recurrence of the PAL fluorescence (**Figure 4.1b** and **Figure 4.5**). It could be argued, that the switching of the PAL protein should have been demonstrated for several photocycles in these sections. However, as the photo-responsiveness could be observed after 19 h of incubation in light (**Figure 4.4a)**, it was assumed that the light-responsiveness remained intact for at least several hours in mammalian cells.

5.1.2 Concentration-dependent expression of mCherry-PAL

To confirm the presence of the mCherry-PAL protein in the cytosol by mCherry fluorescence microscopy, high resolution images were taken. This resolution surpassed the resolution of the images that were taken to study the conformational switching. **Figure 4.2** indicates that mCherry-PAL is expressed in the cytosol but not in the nucleus. For entire clarity on this point, the experiment needs to be reperformed with nuclear staining (e.g. Höchst 33342 or DAPI). When mCherry-PAL was transiently expressed under the control of a CMV promoter, a few spots with increased fluorescence could be observed 24 h after transfection (**Figure 4.2a**) and these spots accumulated further 48 h after transfection (**Figure 4.2b**). It had been described before that the transient protein expression may peak 48 h after transfection [280]. This is in accordance with the increased mCherry-PAL fluorescence 48h after transfection compared to 24h (**Figure 4.2**). Unlike it was observed, equal protein distribution was expected. The formation of particles seems to be a mCherry-PAL specific phenomenon as this was not

observed for mCherry expressed under the same promoter (**Figure 4.2**). The aggregation of mCherry in fusion with other photoreceptors (e.g. Cry2) and under the control of strong promoters had been described before [281]. This might be a consequence of high protein levels which generally facilitate protein aggregation [282]. Furthermore, these particles do not seem to be dependent on the light irradiation state, as similar results were obtained under both light and dark conditions (**Figure 4.2**). When a weaker Ubiquitin promoter was used for expression, only slight mCherry-PAL spots could be observed 48 h after transfection and at none of the tested time points when an uninduced Metallothionein promoter was used for protein expression (**Figure 4.2**). As the Ubiquitin and Metallothionein promoters were described to induce lower expression levels, this points further at a concentration-dependent formation of mCherry-PAL particles. Of note, the basal expression from a Metallothionein was used as the weakest promoter and its expression could be increased by the titration of Zn^{2+} ions [283]. This property of the Metallothionein promoter could be used in future experiments for the determination of the critical concentration for the particle formation in these cells and to check whether these particles co-localize to specific cellular compartments (e.g. *via* fluorescence microscopy of antibody-stained compartments). To clarify if these particles consist of PAL multimers rather than dimers, gel electrophoresis under non-denaturing conditions could be performed [237].

5.2 Light-control of translation

5.2.1 Light-control using mCherry-PAL

For the aptamer-mediated regulation of mRNA translation in *cis*, the PAL aptamer 53.19 was first embedded into the 5'UTR of a *Metridia* luciferase reporter mRNA which was transcribed from a CMV promoter (**Figure 4.3**). This strategy was selected because the majority of the similar regulatory circuits also targets the 5'UTR and few synthetic systems (that do not feature the implementation of a ribozyme) have been described to target the 3'UTR for the modulation of translation [176]. For aptamer insertions into the 5'UTR, cap-proximal insertions are thought to interfere rather with the formation of the translation initiation complex [284], whereas cap-distal insertions interfere preferentially with the ribosomal scanning process (so-called "roadblocks", [285]). In this study, the aptamer 53.19 stem was extended for five additional nucleotides (section 8.5.2) to reach a stability of -30.1 kcal/mol which would be sufficiently stable to modulate translation efficiency *per se* and facilitate correct aptamer folding [149]. The insertion of the aptamer was chosen 18 bases upstream to the translation start codon, by taking advantage of the *AgeI* restriction site for restriction cloning. However, the "best" position of aptamer insertion needs to be determined experimentally. This was performed in collaboration with colleagues [237]. In this study it was found that the light-dependent fold change could be increased when the aptamer is embedded closer to the 5'end of the mRNA. Furthermore, the regulatory performance is dependent on the thermodynamic stability and the GC content [149]. The influence of the thermodynamic stability has also been investigated in the above-mentioned study [237]. Here, it was found that an aptamer stability of -30.1 kcal/mol leads to the highest fold changes among the tested stabilities. This lied within the range of what was described before [149].

Initially, it was assumed that the number of mCherry-PAL protein molecules might surpass the number of *Metridia* luciferase mRNAs per cell, as one mCherry-PAL mRNA is translated several times. Thus, enough mCherry-PAL proteins for efficient gene expression regulation might also be achieved by using promoters of weak to intermediate expression strengths which reduce the metabolic burden from transgene protein expression [105]. When mCherry-PAL was expressed under the control of a Ubiquitin or a Metallothionein promoter, a light-dependent reduction in reporter protein translation could be observed for the luciferase construct with aptamer 53.19 (Mot2), and no light-dependency could be observed for control luciferase plasmids (Luc, M4, **Figure 4.3c**). However, only small light-dependent fold changes of the reporter protein expression could be observed and compared to the weak promoter (pMetallothionein), the fold change was increased for the intermediate promoter (pUbiquitin, **Figure 4.3d**). PAL binds aptamers *in vitro* with around 20nM affinity [237]. This suggests that a strong binding may also take place in cells. Therefore, the small fold changes might be a consequence of an exceeding Mot2 mRNA number that cannot be quantitatively bound by mCherry-PAL under light conditions (**Figure 4.3c**,**d**). Thus, the expression of mCherry-PAL was set under the control of a strong CMV promoter for further experiments. Indeed, an increased light dependent difference in the reporter protein expression could be observed when mCherry-PAL was expressed from a CMV promoter in presence of Mot2 (**Figure 4.4a**). Strikingly, the translation for Mot2 was reduced in both light states compared to the unmodified plasmid (Luc). Similar expression levels as for the co-transfection of mCherry-PAL and Mot2 incubated in darkness could be obtained when Mot2 was co-transfected with mCherry irrespective to the light conditions (**Figure 4.4a**). Therefore, the decrease of luciferase expression from Mot2 in darkness might not be a consequence of dark binding to PAL but rather a result of altered translation initiation. Alternatively, this point towards an unintended interaction of Mot2 with RNA binding proteins. Instead, and similar as observed for weaker mCherry-PAL expression levels, a four-base pair mutant of Mot2 (M4) displayed strongly elevated levels of luciferase expression by almost reaching levels in cells transfected with Luc. These luciferase levels were comparable when co-transfected with mCherry-PAL or mCherry (**Figure 4.3c**, **Figure 4.4a**). Compared to mCherry-PAL expression from weaker promoters, slightly decreased levels of luciferase expression for all tested samples were measured (**Figure 4.3c** *vs.* **Figure 4.4a**). This could indicate that the increased CMV-driven mCherry-PAL expression impacts the luciferase expression or that this observation is caused by measurement inaccuracies. Furthermore, the luciferase reporter assays were performed 19 h after transfection and only few mCherry-PAL spots in the cytosol were observed 24 h after transfection (**Figure 4.2a**). Therefore, it was concluded that the mCherry-PAL particles do not decrease the light-dependent differences in target protein expression at this time point.

5.2.2 Light-control of translation using 4E-BP1-mCherry-PAL

4E-BP1 is an inhibitor of cap-dependent translation [286] and the activity of 4E-BP1 is abolished when it is phosphorylated. Thus, a mutated version of the 4E-BP1 was used in this study which cannot be phosphorylated [287]. In literature, 4E-BP1 has been fused to other proteins either *via* its N-terminus [288] or C-terminus [288], which indicates that the protein's inhibitory activity on translation remains unaffected when fused to other proteins. The fusion of 4E-BP1 to mCherry-PAL *via* its C-terminus was

chosen as the highly flexible C-terminus of PAL is a key region for light-adapted conformational changes [237]. The fusion of 4E-BP1 to mCherry-PAL was realized by a glycine-serine linker, that is described to interrupt secondary structures between two protein domains and it also provides additional flexibility (GGGGS, [289]). For the reporter studies with 4E-BP1-mCherry-PAL and Mot2, a decreased luciferase expression level was observed compared to mCherry-PAL under both light and dark conditions (**Figure 4.6b**). However, the use of 4E-BP1-mCherry-PAL induced increased fold changes compared to what was observed in presence of mCherry-PAL (**Figure 4.6c**). A reduced luciferase expression was also observed for all other samples when 4E-BP1-mCherry-PAL was overexpressed compared to mCherry-PAL. This suggests that the presence of 4E-BP1 constitutively suppresses the translation (**Figure 4.6b**). As an additional control, a 4E-BP1-mCherry-PAL fusion protein with a 4E-BP1 peptide domain that is incompetent to bind to eIF4e could be used. However, as 4E-BP1 is capable to interact with several other protein factors that could impact translation [287], this control was not included in the study [290].

5.3 Light-control of regulatory RNA activity

5.3.1 *In vitro* binding studies of *pre*-miR constructs

Prior to studying *pre*-miR activity in cells, the binding capability to PAL was investigated *in vitro*. To this end, the PAL protein was purified *in vitro*. The predicted molecular weight of the PAL monomer (~40 kDa) is in line with the enriched band that was observed in the SDS-PAGE of the PAL purification (**Figure 4.8a**, **Figure 10.1**). The additional protein bands might arise from co-purification of trace amounts of histidine-rich *E. coli* proteins (**Figure 4.8a**), which are frequently observed for His-tag affinity purification [291]. For further purification of the PAL protein, fast protein liquid chromatography could be performed. Under non-denaturing conditions, a band at ~80 kDa would be expected because PAL forms a constitutive homodimer under these conditions [237]. The PAL absorption spectrum in darkness exhibited three peaks (420 nm, 444 nm and 471 nm, **Figure 4.8b**), which are characteristic for several previously described LOV photoreceptors [279, 292, 293]. These peaks disappeared when the protein was incubated under light conditions and could be restored after one hour incubation in darkness (**Figure 4.8b**). A similar absorption spectrum was obtained after the successful biotinylation of the PAL protein (**Figure 4.8c**,**d**).

Subsequent *in vitro* interaction assays of *pre*-miR constructs with PAL were conducted in absence and presence of a competitor (**Figure 4.9**). The molarity of PAL which was applied in these assays (1.25 µM) is within the range of mCherry-PAL measured in HEK293PAL cell line (~1.1 µM, **Figure 4.10f**). The cell line was used for all subsequent cell experiments. However, due to incomplete immobilization, it could be that the actual molarity of PAL for *in vitro* assays was below the expected value. The *pre*-miR variants 53, SHA and SHB indicated a strong binding under light conditions and slight binding in darkness in both the presence and the absence of a competitor for both tested RNA concentrations (1000 nM and 100 nM, **Figure 4.9**). This argues for a specific interaction with the PAL protein under these conditions. The reason that SHA shows slightly more affinity to PAL compared to SHB might be the more complex secondary structure of SHB according to the secondary structure predictions (**Figure**

4.9a) which might influence the aptamer's affinity to PAL. A residual binding that was observed in darkness could also be a side effect of the PAL immobilization. The increased local PAL density could impact its conformational switching or alter the accessibility of PAL's ANTAR domain to the tested RNAs. Additionally, PAL monomers or misfolded PAL might be immobilized which could also have an influence on the apparent binding behavior. In presence of a competitor, the binding capability of the controls 46mu, SHC and SHD was greatly reduced for both tested RNA concentrations (1000 nM and 100 nM, **Figure 4.9d**,**e**) compared to the binding capability in absence of a competitor (**Figure 4.9b**,**c**). Similar as observed for 04 and SHC_M4 in absence of a competitor (**Figure 4.9b**,**c**), this indicates unspecific interactions to some degree which might be a consequence of PAL's general affinity to RNA.

5.3.2 Optimization of the light-controllable *pre*-miR21 reporter system

The control of reporter gene expression *via* regulatory RNAs necessitated the expression of several genetic elements, e.g. a regulatory RNA, the reporter mRNA, the photoreceptor and, in later assays, the AGO2 protein. The increased complexity of a quadruple transfection increases the likelihood of incompletely or less transfected cell subpopulations. To overcome this drawback, a HEK293PAL cell line that expresses mCherry-PAL stably was generated at this stage. This cell line exhibited solid and normally distributed expression of both mCherry and PAL fluorescence which indicates a homogenous protein distribution throughout the cell population (**Figure 4.10a**,**b**). However, the mCherry-PAL molarity in each individual cell may vary because the cell volume doubles during the cell cycle [294] and the mCherry fluorescence varied by one order of magnitude according to the FACS measurements (**Figure 4.10a**). Furthermore, conformational switching could be observed which indicates an intact photochemistry (**Figure 4.10c**). With an average mCherry-PAL protein concentration of ~1.1 µM in the cytosol (**Figure 4.10e**,**f**), the interaction of transiently transfected regulatory RNA with mCherry-PAL might be facilitated. This was assumed because the measured mCherry-PAL concentration is several magnitudes above the published K_d for PAL to the aptamer 53.19 [237]. As the regulatory RNA activity is potentially expressed at lower concentrations, this would minimize unregulated background maturation of regulatory RNA that is not bound to PAL [295].

To further increase the light regulation, the portion of the pSilencer plasmid that encodes for regulatory RNAs and the *Metridia* Luciferase reporter plasmid was optimized. To this end, the ratio of the two plasmids was varied while the total amount of DNA which was transfected was kept constant. This procedure has been described before [296, 297]. Typically, plasmid ratios are given in mass ratios. However, in future studies molar plasmid ratios could be additionally indicated because this would enable a direct comparison of the number of transfected plasmids. This can be especially useful for the comparison of plasmid variants which might vary in length. In the present study, it was found that a high mass excess of the PSilencer plasmid (99:1 – 49:1) increased the fold change (**Figure 4.11**). It has been described before that mass excess ratios up to 99:1 can be needed to maximize the regulation of luciferase reporter systems [298]. As the RISC complex is also occupied by intrinsic regulatory RNAs, a large excess of transgenic regulatory RNAs may be introduced to displace intrinsic regulatory RNAs from the RISC processing. As less transgenic regulatory RNAs are processed by the RISC complex at

lower concentrations, this might lead to inefficient gene silencing of large quantities of target mRNA molecules. This circumstance might be observed at a 1:1 transfection ratio, as a weak luciferase suppression and no fold change could be detected in these samples (**Figure 4.11**). Therefore, the amount of regulatory RNA for the transfection was increased, and the amount of reporter mRNA was further decreased. However, as stated above, large amounts of transgenic regulatory RNAs in the cell might lead to the saturation of the RISC complex [299]. This might explain the similar fold changes for SHA at transfection ratios from 99:1 – 49:1 (**Figure 4.11**). It had been described before that transcriptions from the polymerase III (PolIII) promoters that were used for regulatory RNA expression may reach up to ~$4 \cdot 10^5$ transcripts of regulatory RNA molecules per cell [295]. The measured number of mCherry-PAL molecules per cell (~$8.4 \cdot 10^6$, **Figure 4.10e**) surpasses this number by one order of magnitude. Consequently, mCherry-PAL reaches a molarity of ~1.1 µM in the cytosol (**Figure 4.10f**), which exceeds the K_d to the aptamer 53.19 by roughly one order of magnitude [237]. Therefore, the light regulation might remain unrestricted as the regulatory RNA molecules can still be efficiently bound by mCherry-PAL according to these numbers. However, it should be stated that the published K_d of PAL to the aptamer 53.19 was measured *in vitro* and may differ from the actual value in cells. Furthermore, the transfection of a smaller amount of pLuciferase might require smaller amounts of pSilencer to reach even higher fold changes. To determine the amount of pSilencer plasmid which induces the highest light-dependent fold change in such a case, an additional experiment could be set up in which the amount of pLuciferase is kept constant while the amount of pSilencer plasmid is varied.

An increase in mRNA suppression might also be achieved by taking advantage that both mature miR-5p or -3p strands can be loaded into the RISC complex [257]. The impact on target gene suppression of both artificial mature miR21 strands (miR21-5p or -3p) from SHA was not clear as only miR21-5p binding sites have been incorporated to the luciferase reporter mRNA until this point. It is described in literature, that miR21-3p is capable to suppress the expression of target mRNAs [300, 301]. Interestingly, and similar to the described natural *pre*-miR21 counterpart, it was found that the target suppression from miR21-5p was superior to miR21-3p induced target gene suppression (**Figure 4.12b** *vs*. **Figure 4.12f**). Oppositely, the luciferase suppression was increased when both types of miR binding sites were present in the luciferases 3'UTR (luc-5p-3p) which indicates an additive effect (**Figure 4.12d**). As the next generation sequencing databases indicate that miR21-5p maturation largely outweighs miR21-3p maturation [302], this could explain the small suppressive effects that were observed for miR21-3p in both natural and artificial *pre*-miR21 constructs. Because the luciferase suppression in darkness remained almost similar for luc-5p and luc-5p-3p, a slightly increased fold change was calculated for luc-5p-3p, whereas a reduced fold change was calculated for luc-5p and luc-3p (**Figure 4.12g**). The fold changes for control samples were slightly below 1.0. Probably, this was observed due to secondary irradiation effects (**Figure 4.12d**, [303]). In these cases, blue light may have led to the production of H_2O_2 by flavin-containing oxidases and the emerging radicals could be toxic to the cells [303].

Next, different artificial *pre*-miR21 variants which were derived from SHA were tested in order to increase the suppressive capacity and the light-responsiveness. In SHA_V1 and SHA_V2, the wobble base pairing of the 5'-terminal guanine was engineered to form a Watson-Crick base pair, as this structure is

also applied for the generation of shRNAs (insertions of nucleotides depicted in red, **Figure 4.13a**, [304]). However, cells that have been transfected with these constructs indicated poor luciferase suppression and fold changes below the values that were obtained for SHA (**Figure 4.13b**,**c**). This might be due to the disruption of the mature miR21-5p's seed sequence due to the implementation of an additional base pair (A2U45, **Figure 4.13a**). The seed sequence depicts a conserved sequence interval composed of the positions 2 to 8 from the mature miRs 5' end [182]. For efficient target suppression, the mature miR and the target mRNA sequence need to be fully complementary within this region. Therefore, the suppressive capacity of SHA_V1 and SHA_V2 was thought to be solely a consequence of the mature miR21-3p strand whose seed sequence remained intact (**Figure 4.13b**). SHA_V2 suppressed the luciferase expression slightly more effective in darkness compared to SHA_V1 (**Figure 4.13b**). This could be a consequence of the hammerhead ribozyme (HHR) sequence which was embedded at the 3' end of SHA_V2 [261]. While the transcription from a U6 polymerase III-dependent promoter is known to produce a random number of nucleotides at the 3' overhang (mostly ≥ 4 nucleotides, [259]), the HHR ensures precise cleavage of a two-nucleotide 3' overhang instead. This was anticipated as it is described in other studies, that the export of *pre*-miRs by exportin 5 is facilitated by two-nucleotide overhangs at the *pre*-miR's 3' end [305]. Furthermore, two-nucleotide overhangs of the *pre*-miR's 3' end ensure an efficient and more uniform dicer cleavage [260]. Both arguments could explain the slightly increased capability of SHA_V2 to suppress the luciferase expression in darkness. However, the differences are small. This argues for some tolerances of the exportin 5 or the dicer protein for different 3' overhang lengths or the presence of sufficient regulatory RNA moieties that bear a two-nucleotide overhang. To validate this hypothesis experimentally, a quantification of SHA_V1, SHA_V2 and the corresponding mature miR21 strands could be performed by RT-qPCR. Additionally, the exact number and composition of 3'-terminal nucleotide overhangs for SHA_V1 and SHA_V2 in cells could be determined by NGS analysis.

Interestingly, light-responsiveness (2.4-fold) was observed for SHA_V3 in which the aptamer stem was shortened and the single nucleotide bulge in the hinge region was avoided (**Figure 4.13**). Shortening the aptamer stem has a strong influence on the apical loop orientation which could modulate the PAL binding. Consequently, the sterical hinderance of the dicer cleavage is altered when PAL is bound to the RNA. To understand the impact of these factors, both *in vitro* dicer cleavage and PAL binding assays could be performed. On the other hand, as the results for SHA_V3 and SHA are rather similar, it seems that a shortening of the aptamer does not impact the suppressive capacity and the light-responsiveness of SHA. The results for SHA_V3 suggest that the aptamer 53.19 stem can be further modified [237]. In the case of SHA_V3, this brings the PAL aptamer in closer proximity to the putative dicer cleavage sites [196]. However, no apparent effect on the reporter gene expression could be detected in this case (**Figure 4.13b**).

SHA_V4 indicated the strongest luciferase suppression in darkness (**Figure 4.13b**). Compared to SHA, the miR21-3p strand of SHA_V4 was engineered to allow a full Watson-Crick base pairing which resulted in a shRNA-like structure [193]. Obviously, this structural feature increased the suppressive capacity at the expense of light-responsiveness (**Figure 4.13b**,**c**). One reason for these properties could be that this variant is a preferred dicer substrate [306]. Also, the regulatory RNA structure that surrounds the

dicer cleavage site impacts the position of the dicer cleavage. This could also influence the target mRNA suppression [269]. One reason for the poor light-responsiveness of SHA_V4 could be a reduced binding to PAL. Similar observations, e.g. low eGFP under light conditions have been made for eGFP shRNAs of similar structure (e.g. SH2, SH3 and SH4, **Figure 4.23**), which might be caused by the absence of the hinge region nucleotide bulge (e.g. adenine for SHA). Finally, among all tested variants, SHA indicated the highest light-dependent fold change (**Figure 4.13c**). This underpins the importance of an intact seed sequences and the presence of an unpaired nucleotide in the hinge region that flanks the aptamer 53.19.

As an alternative to the aptamer 53.19, aptamer 04.17 was implemented as a light-transducer into the apical loop domain of a synthetic *pre*-miR21 (SHI, **Figure 4.14a**). This construct was first tested *in vitro* for its capability to bind to PAL (**Figure 4.14**). However, compared to the full length aptamer 04, just a weak (**Figure 4.14c**) to no (**Figure 4.14b**) binding could be observed for both the functional variant (SHI) and the miR control (SHK). This suggests that the nucleotides which surround the truncated aptamer 04 sequence in SHI and SHK might impact the light-adapted binding to PAL. These and further constructs were subsequently tested for reporter gene suppression in mammalian cells (**Figure 4.15**). It was found that SHI is indeed capable to suppress luciferase expression, similar to the corresponding variant which is equipped with an aptamer point mutant (SHJ, **Figure 4.15b**), but without light-responsiveness (**Figure 4.15c**). To restore the light-dependency for SHI, it was suggested to extend the aptamer stem based on the original sequence of full length aptamer 04. Consequently, three (SHI_V1) and five (SHI_V2) additional base pairs were implemented in the apical loop domain of SHI (**Figure 4.15a**). Because one base pair leads to a helix rotation of 37.4° in RNA [307], the implementations shifted the apical loop orientation for 112.2° in SHI_V1 and for 187 ° in SHI_V2 compared to SHI. As no luciferase suppression was detected for these prolonged stem variants (SHI_V1 and V2) and because a weak to no binding to PAL was detected for SHI *in vitro* (**Figure 4.14**), it remains unclear whether PAL is capable to bind to these modified constructs or whether the orientation of an aptamer-bound PAL does not inhibit the dicer processing. These constructs were generated based on the previous observations that the stem length does not correlate with the suppressive activity of a regulatory RNA [308]. The same study suggested further that the placement of siRNA core needs to be adjacent to the 5'/3' ends of the regulatory RNA construct. Both rules were applied for the design of SHI_V1 and SHI_V2. NGS analysis of cells which express SHI_V1 and SHI_V2 would reveal the identity of the processed mature miR21 moieties. Such an experiment might help to explain the failed luciferase suppression. As no light responsive *pre*-miR21 variants could be generated with aptamer 04.17 as apical loop, it was decided to continue with aptamer 53.19 constructs because they already indicated light responsiveness in mammalian cells.

5.3.3 Light-control of *pre*-miR activity

It had been observed before that the presence or absence of 10 % FCS impacts the transfection efficiency [262, 263]. Performing a transfection in absence of FCS improved the light dependent fold change for the *pre*-miR21 variant SHA from 2.6-fold (**Figure 4.13c**) to 4.4-fold (**Figure 4.16c**). 15 % of

cells which were transfected with SHA in presence of FCS expressed luciferase in darkness, whereas only 8 % were measured when the transfection was performed in absence of FCS (**Figure 4.13b** *vs.* **Figure 4.16b**). Under light conditions, the luciferase expression decreased only from 37 % to 32 % when no FCS was added during the transfection (**Figure 4.13b** *vs.* **Figure 4.16b**). These results indicate that the suppressive activity was improved for SHA when the transfection was performed in absence of FCS and in darkness. The improved suppressive activity was probably caused by elevated *pre*-miR levels in these cells. The smaller difference between both transfection conditions in presence of light might be a consequence of the high mCherry-PAL levels in the cells. Consequently, mCherry-PAL binds to the aptamer of the *pre*-miR constructs with high efficiency under both conditions. Surprisingly, the aptamer point mutant SHC indicated similar levels for both transfection conditions irrespective to the light irradiation state (18 % *vs*. 17 % for transfection in presence or in absence of FCS, **Figure 4.13b** *vs.* **Figure 4.16b**). This might be explained by fluctuations in the transient transfection efficiencies or the slightly altered purity of the plasmid purifications.

The transfection setup in absence of FCS was recapitulated with eGFP as second reporter system (**Figure 4.17**). Here, similar results for SHA and SHC were obtained as for the luciferase reporter system (**Figure 4.16b** *vs.* **Figure 4.17b**). This might be a consequence of using the same promoter (CMV) for reporter mRNA expression as well as the same 3'UTR for the miR21-dependent regulation. Whereas the luciferase assay was performed 19 h after transfection, eGFP assays were performed 44 h after transfection. This indicates a robust light-regulation after transient transfection for several hours in static experiments. Whereas the control transfections with SHB or SHD and eGFP-5p-3p plasmids showed comparable levels in the eGFP expression, elevated eGFP levels were observed for the transfection of SHA with eGFP which has no miR21 binding sites incorporated in the 3'UTR (**Figure 4.17b**). The reduced eGFP protein expression from the eGFP-5p-3p plasmid may be a consequence of low intrinsic mature miR21 levels that are present in HEK293PAL cells as previously described for HEK293 cells [309]. Alternatively, factors such as a reduced transcription, an altered localization or the stability of the mRNA due to the additional nucleotide load in the 3'UTR (210 additional nucleotides) could explain the slightly reduced reporter protein expression. At this point it should be noted that the mature miR sequences of SHB and SHD point to GFP because the initial design of these controls did not foresee the application for eGFP reporter assays. However, a single-base mismatch within the seed region of these constructs explains the lack of eGFP repression for both constructs and no light-dependency for SHB (**Figure 4.16b**,**c** *vs.* **Figure 4.17b**,**c**).

In the literature it is suggested, that the transgenic expression of *pre*-miR molecules might saturate the RNA interference machinery by exceeding intrinsic AGO2 levels [186]. This could limit the silencing efficiency and influences intrinsic miR maturation pathways [186]. The AGO2 protein is the sole mammalian argonaute protein that is capable to cleave target mRNAs upon perfect hybridization with the regulatory RNA. The overexpression of AGO2 is described to reduce off-target effects that are caused by the expression of artificial regulatory RNAs and it increases the target knockdown efficiency [310]. Furthermore, there is evidence in literature that AGO2 overexpression does not adversely perturb endogenous gene expression patterns [310]. Indeed, the differences in reporter protein expression between the light states was further increased by including AGO2 overexpression into a transfection

protocol which was adapted from the literature (9-fold, **Figure 4.18b**, [299]). Here, a reduced amount of pSilencer plasmid was transfected per well (100 ng *vs*. 495 ng when the former transfection protocol was used) which enables an increased eGFP suppression by using less *pre*-miR molecules (**Figure 4.18a**). This might increase the ratio of bound *pre*-miR to mCherry-PAL under light conditions and increase the reporter suppression in darkness (**Figure 4.18a**). Additionally, the amount of transfected eGFP plasmid was increased by 10-fold (50 ng *vs*. 5 ng when the former transfection protocol was used) which indicates that the light-regulation is also robust at higher amounts of target protein expression. Whereas the number of eGFP expressing cells in darkness was reduced to 5 % in cells that harbor SHC and the number of eGFP expressing cells was further reduced to 0.3 % in cells that harbor the miR21 mimic (**Figure 4.18**). miR mimics have been described to suppress target gene expression strongly [311]. However, aberrant side effects such as the accumulation of high molecular weight RNA species were described as well [311]. These RNA species were not observed when the corresponding miR was expressed from a plasmid transfection [311]. Furthermore, as miR mimics are chemically synthesized [312], they are not genetically encodable and thus not suitable for optoribogenetic approaches.

5.3.3.1 Spatiotemporal control of *pre*-miR activity

Besides the genetic encodability, optoribogenetic approaches are reversible and spatially controllable. The reversibility was examined in **Figure 4.19** (see also **Figure 10.2** and **Figure 10.3**). Here, control cells that harbor SHA or SHC were incubated in darkness throughout the entire assay. For these transfections and the incubation of SHC under altered light conditions, the luciferase expression was comparably low for all time points throughout the assay (**Figure 4.19b**,**e**). Only when SHA was incubated under varying light-conditions, an altered luciferase expression could be detected. When the light was turned off 19 h after transfection (**Figure 4.19a**-**c**), the fold changes decreased notably after further 8 h to 24 h incubation in darkness to a final fold change of 1.8 (**Figure 4.19c**). The reason for the sustained small fold change might be a “memory effect” of the luciferase expression from the previous light state before the medium had been exchanged (**Figure 4.1**, [237]). For example, the dissociation of PAL from aptamer 53.19 might take some time at 37 °C in darkness. This assumption is supported by slow off rates that were determined in *in vitro* SPR measurements (k_{off} = 5.5 ± 0.9 · 10^{-3} s^{-1}, [237]). Additionally, only the secreted luciferase protein can be excluded from measurements by the medium replacement. As the protein secretion pathway takes roughly 1 h from protein translation to secretion [313], residual proteins might influence the apparent fold changes which may account for up to 20 % of totally expressed proteins at this time point after transfection [314]. When the light was switched on 19 h after transfection (**Figure 4.19d**-**f**), lower maximal levels in luciferase expression were achieved for SHA compared to the previous assay (**Figure 4.19e**). One reason for this observation might be that the mature miRs remain stable after the light state was altered. It is described that mature miRs are stable over several days in cells [315]. After the initial 19 h of incubation time in darkness, the mature miR moieties may accumulate and counteract the luciferase accumulation in the subsequent incubation under light conditions. Furthermore, the luciferase levels did not increase further from 10 h to 24 h after medium exchange and the incubation in light. This might be explained by a plasmid dilution after an increased time period after transient transfection. This results in decreasing transgenic protein

expression levels [316]. It is interesting that the fold changes for both end point measurements (+ 24 h) were found to be 1.8 (**Figure 4.19c,f**). However, given the complexity of the kinetics which depend on a multitude of non-linear factors (including plasmid dilution and stability, reporter protein accumulation and localization, the impact of interaction with PAL and dicer and miR kinetics), the endpoint results of both experiments are not directly comparable to each other. One way to rule out fluctuations from the transient transfection kinetics would be the generation of cell lines that express the reporter mRNA, *pre*-miR and mCherry-PAL stably.

By using the PAL-dependent *pre*-miR21 SHA, the spatial control of eGFP expression was examined with a photomask that covered well bottoms in a 24-well plate (**Figure 4.20**). Indeed, the eGFP fluorescence was elevated for SHA in light-exposed areas (**Figure 4.20a**, upper panels). For the well that was filled with cells that harbor the control SHB, the eGFP fluorescence was expected to be equally distributed. However, this was not entirely the case as some areas showed an increased eGFP fluorescence whereas other areas indicated decreased eGFP fluorescence (**Figure 4.20a**, lower panels). Because these cells grow in colonies, the cell layer was unequally distributed throughout the well. Furthermore, as HEK293PAL cells adhere only slightly to the well surface, the medium exchange for the transfection might lead to a cell detachment, particularly at the borders of the well. It is likely that some of these cells are re-attaching at different sites within the well. This leads to an unequally distributed eGFP fluorescence throughout the well. One possibility to overcome this is issue could be the treatment of wells with poly-L-lysine prior to the cell seeding which would increase the cell adherence [317]. Another point that could explain the unequally distributed eGFP and mCherry fluorescence is that no autofocusing was used for the image acquisition because of technical malfunction. Therefore, all images from one well were acquired at the same Z position. As these wells underly slight temperature fluctuations as well as mechanical stress throughout the cell treatment, the well bottoms may not be perfectly even at the time point of the experiment. A mCherry fluorescence from mCherry-PAL could be detected throughout the well for SHA and SHB which shows the presence of cells independently to the transfection state (**Figure 4.20a**). Interestingly, light-irradiated areas indicated a decreased mCherry fluorescence due to an unknown reason (**Figure 4.20a**). Because mCherry is not efficiently absorbing blue light [318] and a photoinduced protein bleaching is rather unexpected. Instead, it was found that PAL is able to absorb blue light (**Figure 4.8b**,**d**).

Therefore, the impact of blue light on the mCherry and PAL fluorescence was further investigated in presence and absence of a PAL protein tag (**Figure 4.21**). Interestingly, the light-dependent difference in mCherry fluorescence was highest for mCherry-PAL (1.6-fold) and this effect was reduced when either PAL or mCherry was co-transfected (**Figure 4.21a**). Very low light-dependent differences in mCherry fluorescence were observed when mCherry-PAL was not part of the transfection (**Figure 4.21a**). These differences might be a consequence of secondary irradiation effects such as photobleaching or altered protein levels [303]. For microscopy applications including mCherry, a ~2-fold decrease in the fluorescence has already been reported due to photobleaching [319]. This fold change is within the same order of magnitude as the observations within this thesis. To investigate whether the light-dependent differences in mCherry fluorescence levels are rather a consequence of altered mCherry-PAL protein levels upon irradiation, western blot experiments could be performed. In these

experiments, HEK293 cells could be transfected with mCherry or mCherry-PAL and incubated under different light conditions. For all transfections that included PAL, a decreased fluorescence of PAL was observed when the cells were incubated under light conditions (**Figure 4.21b**). However, the underlying mechanistic principle is not entirely clear. As the cell samples were prepared in darkness for the flow cytometry analysis, a procedure that takes more than 10 min, the protein switches back in its dark conformation according to the previous results (**Figure 4.1**). It could also be likely that the extensive exposure of PAL to blue light might lead to photoinduced self-oxidation, similar as it is described for other LOV-based photoreceptors [320]. To investigate the impact of the extended light exposure on the PAL-binding to the aptamer 53.19, *in vitro* binding experiments with a *pre*-incubation step of PAL under light conditions could be performed.

5.3.3.2 Investigation of 3'-isomiR formation after *pre*-miR21-aptamer maturation

The results shown in **Table 4.1** suggest, that the maturation of the *pre*-miR21-53.19 chimera SHA is altered compared to its natural counterpart [321]. This might be a consequence of the additional guanine nucleotide that was embedded into the 5' end of SHA. This additional nucleotide is required for the efficient transcription from the U6 promoter. However, the presence of an additional guanine may also influence the dicer processing [322] which results in altered 3' isomiR formation. To verify the impact of the additional guanine at the 5'end on the *pre*-miR21 processing, ribozyme sequences could be embedded into the *pre*-miR21 to cleave off the additional 5' nucleotide after transcription. Additionally, the impact of the aptamer 53.19 as apical loop domain on the 3'-isomiR formation has to be tested in parallel. Taken together, the additional optimization of light-responsive *pre*-miR sequences is necessary to mimic the natural 3'-isomiR formation precisely.

5.3.4 Light-control of shRNA activity

As further studies are necessary to ensure the correct maturation for the *pre*-miR21 construct SHA and to create a more generalizable and modular approach for the regulation of distinct target genes, light responsive shRNAs were developed next. In **Figure 4.23**, different siRNA core sequences were taken from literature and conjoined with the PAL aptamer 53.19 as apical loop domain. Several siRNAs were tested as usually only one to two out of four newly designed siRNAs are highly functional [323] even when designing rules are taken into account [324-326]. From three tested shRNAs (SH2 [327], SH3 [299], SH4 [328], **Figure 4.23a**), only one displayed an intermediate fold change of 4.0 and a strong suppression of eGFP in darkness (SH2, **Figure 4.23b**,**c**). Without a light-responsiveness, this suppression could be recapitulated when SH2's siRNA was conjoined with a standard loop sequence (SH1) and no suppression could be observed for SHA due to the absence of miR21 binding sites in the 3'UTR of the eGFP reporter mRNA (**Figure 4.23b**,**c**). Almost irrespective to the light state, SH3 and SH4 weakly suppressed eGFP expression (**Figure 4.23b**,**c**). As the siRNA core elements of SH2 and SH4 were characterized in microscopy experiments to observe the suppression of eGFP fusion protein expression, the results cannot be compared quantitatively with the results that were obtained in this thesis [327, 328]. The gene suppression *via* the siRNA that was used in SH3 was described in flow

cytometry studies before [299]. In this study, a stronger gene suppression was observed compared to suppression that was described in this thesis [299]. As the siRNA was conjoined with another loop sequence and the flow cytometry gating strategies were not shown in this study, a head-to-head comparison of both studies is not possible. Due to initial promising results, SH2 was chosen for investigating the effect of nucleotide implementations between the siRNA core domain and the PAL aptamer 53.19 (hinge region).

For *pre*-miR21 variant SHA, an unpaired adenine was situated upstream to the aptamer in the hinge region. This nucleotide is part of mature miR21-5p. SHA displayed a 9-fold change in eGFP expression in presence of miR21 binding sites (**Figure 4.18b**). Therefore, an adenine was also implemented into the hinge region of SH2 (SH5, **Figure 4.24**). One additional adenine nucleotide was inserted in another construct downstream to the aptamer in order to investigate the impact of two symmetric adenine bulges (SH8, **Figure 4.24**). Both SH5 and SH8 displayed slightly increased fold changes *via* increased eGFP expression under light conditions compared to SH2. These results indicate the relevance of bulge implementations into the hinge region for the light-responsiveness (**Figure 4.24c**,**d**). One explanation for this could be the enhanced accessibility of the aptamer to PAL in these constructs [329], or it could result from altered dicer processing [270]. Published *in vitro* studies in which the stem of the aptamer 53.19 (G19C) was modified indicate increased binding to PAL under light and dark conditions compared to the aptamer 53.19 [237]. When this construct was extended by an additional C-C base pair at the termini of the aptamer, just a weak binding under light conditions and virtually no binding in darkness was obtained [237]. These two aptamer variants were conjoined with the siRNA core element of SH2 in order to form SH6 (G19C) and SH7 (G19C and additional C bases at both termini, **Figure 4.24a**). When these constructs were transfected, the performance of SH6 was similar to SH2 in all three tested parameters (eGFP expression under light and dark conditions, fold changes). This indicates that the implementation of a bulge increases only the light expression of eGFP when it is positioned adjacent to the aptamer 53.19 (**Figure 4.24c**,**d**). Instead, the results for SH7 resembled the results for SH8 closely, which indicates further that the G19C modification does not modulate the light-responsiveness (**Figure 4.24c**,**d**). Therefore, the results from *in vitro* PAL binding studies could not predict the cellular behavior of regulatory RNAs. In the same set of *in vitro* studies, the aptamer 53.19 loop region mutants C9G and C12G bind to a comparable extent to PAL under light conditions as the aptamer 53.19, whereas the binding in darkness was strongly reduced [237]. Thus, the loop region of SH7 was modified with C9G (SH9), C12G (SH10) or both (SH11) mutations simultaneously (**Figure 4.24b**). Unexpectedly, all three constructs displayed low eGFP expression irrespective to the light irradiation state and the level of eGFP suppression varied only slightly among these constructs (**Figure 4.24c**). Thus, the strong binding observed *in vitro* from these aptamer variants was no reliable prediction to generate shRNA variants which would induce a high level of eGFP positive cells under light conditions. This further indicates that the *in vitro* PAL binding studies of the aptamers could not predict the cellular behavior of regulatory RNAs.

As the highest fold change was observed for a single adenine bulge adjacent to the aptamer (SH5, **Figure 4.24d**), the impact of asymmetrically implemented bulge nucleotides into the hinge region of SH2 was investigated in detail (**Figure 4.25**). Thus, the nucleotide identity was permutated up- and

downstream to the aptamer as it was suspected that this could have an influence on corresponding protein interactions [329]. In both positions (up- and downstream to the aptamer), the implementation of a uridine led to the highest number of eGFP expressing cells for the respective position (SH12 and SH16, **Figure 4.25b**). This indicates that structural rearrangements which were caused by unpaired uridines might facilitate either PAL binding under light conditions or dicer processing/accuracy in darkness [330, 331]. The implementation of a uridine (SH12) or a guanine (SH13) upstream to the aptamer resulted in the highest number of eGFP expressing cells under light conditions among all constructs (**Figure 4.25b**).

In all tested shRNA variants of SH2, a hydrogen bond formation of the U4G16 Wobble base pair in the aptamer 53.19 could be predicted (**Figure 4.26a**,**b**). This suggests that the aptamer folds into similar conformations independent to the surrounding nucleotides. For SH12 and SH13, tertiary structure predictions revealed strong structural deviations from the original construct SH2 by a shift of the two abundant apical loops towards the opposite side of the radial axis compared to the single loop observed for SH2 (**Figure 4.26c**). Structural deviations for other tested constructs (SH5, SH15, SH16 and SH18) were less pronounced and cells that have been transfected with these constructs indicated comparable amounts of eGFP expression under both light conditions (**Figure 4.25b**, **Figure 4.26c**,**d**). Therefore, similar fold changes have been observed for these constructs (6.1 – 6.5-fold, **Figure 4.25c**). Both SH14 and SH17 indicated alternative secondary structures of the aptamer stem according to secondary structure predictions (**Figure 4.25a**). This might explain the strongly reduced level of eGFP expressing cells under light conditions and the reduced fold changes due to altered binding affinities to PAL and/or dicer (**Figure 4.25b**,**c**). Together, the tested shRNAs showed various eGFP expression levels under light and dark conditions at overall similar fold changes. Target control at different expression levels can be of interest because target levels and physiologic observations do not necessarily follow linear correlations [332]. Thus, a fine-tuning of protein concentration at certain levels by the suitable shRNA variant could be of relevance. To identify shRNA variants with increased light-responsiveness, a more efficient way of shRNA screening might be necessary. To this end, a flow cytometry-based re-selection could be performed by using doped shRNA libraries.

The impact of asymmetrically implemented bulge nucleotides into the hinge region was recapitulated by using SH3 as a second model shRNA. Again, for both positions a uridine implementation led to the highest number of eGFP expressing cells under light conditions (SH20 and SH22, **Figure 4.27b**). The implementation of a uridine (SH20) or an adenine (SH19) upstream to the aptamer resulted in the highest numbers of eGFP expressing cells under light conditions among all tested constructs, while the insertion of a downstream adenine (SH21) revealed the lowest eGFP expression (**Figure 4.27b**). For SH19 and SH20, tertiary structure predictions revealed strong structural deviations from the original construct SH3 by a shift of the two abundant apical loops towards the opposite side of the radial axis compared to the single loop which was observed for SH3 (**Figure 4.27e**). SH22 indicated intermediate levels of eGFP expressing cells under light conditions and tertiary structure predictions did not result in the formation of an additional loop 2 as observed for all other constructs (**Figure 4.27b**,**f**). However, loop 3 of SH22 was shifted when compared to loop 1 from SH3. SH21 also indicated structural deviations from SH2, but unlike the rest of the tested variants, loop 2 was aligned perpendicular to loop 1 from SH3

(**Figure 4.27e**,**f**). Also, the distance from loop 1 from SH3 to loop 3 was relatively small for SH21 compared to other tested constructs (**Figure 4.27e**,**f**). In contrast to the rest of the tested constructs, a loop 4 was observed in tertiary structure predictions for SH21 (**Figure 4.27f**). Some of these unique structural features could impede shRNA transcription, nuclear export or PAL binding for SH21 and result in low levels of eGFP positive cells under light conditions (**Figure 4.27b**). To investigate the impact of altered shRNA transcription, the nuclear export could be inhibited and the nuclear fraction of shRNA could be quantified by RT-qPCR, whereas the impact of a cytosolic export on the shRNA localization could be investigated by fluorescence *in situ* hybridization (FISH). As expected, a low number of eGFP positive cells was found for SH23 under light conditions (**Figure 4.27b**). This was in accordance with an alternative predicted secondary structure of the aptamer stem (**Figure 4.27a**). Similar results would be expected for the implementation of a cytosine upstream to the aptamer (but this was not tested in cells). Compared to the hinge region variants, the aptamer point mutant SH24 indicated higher levels of eGFP expressing cells irrespective to the light irradiation state (**Figure 4.27b**). This again shows the beneficial effect of bulge implementations into the shRNA hinge regions for increased target suppression. Other than for SH2 variants, the number of eGFP expressing cells under light conditions did not correlate with the number of eGFP expressing cells in darkness. Consequently, a variety of fold changes for the tested constructs have been calculated (**Figure 4.27b**,**c**). This might be caused by an altered shRNA transcription efficiency, nuclear export and altered processing by dicer. Furthermore, the regulatory RNA processing could be affected by altered PAL binding [270]. These differences could correlate with the nucleotide composition of the siRNA that flanks the aptamer and the hinge region. It would be interesting to screen the implications of all canonical nucleotide insertions up-and downstream to the aptamer in conjunction with all possible neighboring base pair configurations. This could be performed together with tertiary structure predictions to reveal the predictive power and limitations of forecasting the shRNA structures that are expected to show high numbers of eGFP positive cells under light conditions. If the crystal structure of PAL in its light state bound to the aptamer 53.19 is solved, the orientation of PAL binding and its consequences on dicer processing might be easier to understand. Among all tested shRNA variants, SH22 indicated the highest fold change (15.3-fold, **Figure 4.27c**) which is within the range of the highest levels for conditional systems for post-transcriptional gene expression control that has been described to date (~19-fold, [197, 205]). SH22 exceeds previously described fold changes for the conditional control of regulatory RNAs (3.1-fold [137]).

Subsequently, microscopy studies were performed to verify the light-responsiveness of selected shRNA variants (**Figure 4.28**, **Figure 10.4**). Indeed, light-dependent differences in eGFP expression could be observed for shRNA constructs that induced high fold changes in the flow cytometry studies (> 4.0-fold, **Figure 4.24**, **Figure 4.25**). No differences in the eGFP fluorescence could be observed for SH2, SH4 and SH9. These constructs also indicated small fold changes in flow cytometry analysis (**Figure 4.22**, **Figure 4.23**). As fluorescence microscopy is less sensitive than flow cytometry [271], it is not possible to detect fold changes in the eGFP fluorescence that are below or equal to 4.0. SH1 indicated slightly increased eGFP fluorescence when these cells were incubated in darkness (**Figure 4.28**). Because eGFP absorbs blue light, bleaching of eGFP could occur when the cells are incubated under light conditions [319] and this effect gets obvious when only marginal levels of eGFP are expressed. As a consequence of the gating strategy that excludes trace eGFP fluorescence, eGFP bleaching was not

observed in flow cytometry (**Figure 7.1**). A Hoechst 33342 nuclear staining was performed to underpin the presence of a comparable cell number and a similar focusing for all image acquisitions. However, a decreased mCherry fluorescence from mCherry-PAL in HEK293PAL cells which were incubated under light conditions could be observed (**Figure 4.28**). This is in accordance with the flow cytometry measurements of the mCherry fluorescence in HEK293 cells that were transiently transfected with mCherry-PAL and incubated under different light conditions (**Figure 4.21a**).

Selected eGFP shRNA variants that indicated different levels of eGFP expression under light or dark conditions as well as a variety of fold changes in cellular experiments were subsequently tested for *in vitro* binding to PAL (**Figure 4.29**). All aptamer 53.19-modified constructs indicated less binding to PAL in darkness to a similar extent and a similar binding under light conditions compared to the full length aptamer 53 (**Figure 4.29**). These results suggest that the hinge region modifications do not directly interfere with the PAL binding *in vitro*, but rather affect the shRNA processivity in cells. Given the large variety of loop orientations which were observed in tertiary structure predictions for hinge region variants, the PAL binding might modulate the steric hindrance of the dicer cleavage under light conditions [196]. It seems that the *in vitro* PAL binding assays to regulatory RNAs should only be considered as a qualitative indication for PAL binding, because no correlation between the *in vitro* binding of shRNAs and the eGFP expression in cells could be determined under light conditions. For example, the aptamer point mutant SH9 displayed 49 % of binding in light (and virtually no binding in darkness) which was only slightly below the binding of SH18 in light (77 %, **Figure 4.29b**). However, no light dependency could be observed for SH9 in cell assays, but a light-dependency was observed for SH18 (**Figure 4.24d**, **Figure 4.25c**). Furthermore, the eGFP expression in cells varied strongly under light conditions among the tested SH2- and SH3- derived single hinge nucleotide variants (**Figure 4.25**, **Figure 4.27**). To demonstrate the impact of shRNA hinge nucleotide variations on the processivity by dicer more clearly, *in vitro* dicer cleavage experiments in presence and absence of PAL need to be performed. To study the interaction of shRNA variants with PAL *in vitro* quantitatively, SPR measurements could be performed as well.

It had been demonstrated before that the three-dimensional orientation of a RNA-binding protein that interacts with the apical loop domain of a shRNA impacts dicer cleavage. In this case, the efficiency of dicer cleavage is dictated by the binding protein's orientation which is conveyed by the shRNA's loop orientation [196]. As it was predicted within this thesis that the folding of the apical loop of the shRNAs influences the numbers of eGFP positive cells under light conditions, RNA sequence motifs which lead to structural kink turns (k-turn) were implemented into the hinge region of SH2. According to the structure predictions, the k-turn motifs mediated altered loop orientations (**Figure 4.30c**) whereas the Wobble base pair of aptamer 53.19 remained intact (**Figure 4.30b**). K-turns had been used in shRNA engineering before [157] and can also be found in natural *pre*-miRs [333]. Indeed, the kink-shRNA variants SH25 and SH26 indicated high numbers of eGFP positive cells under light conditions (**Figure 4.30d**). However, both constructs also showed elevated levels of eGFP positive cells in darkness which were paired with low fold changes (**Figure 4.30e**). This could indicate a decreased dicer processing or cleavage accuracy or less steric hindrance between the regulatory RNAs and PAL. *In vitro* dicer cleavage experiments in presence and absence of PAL could be performed to answer these open

questions. To reveal the impact of kinked hinge regions on processed siRNA composition, NGS analysis could be performed as well.

Besides the Motif2 variant 53.19, Nm60 was found within the next generation sequencing data of the PAL SELEX[9] and the genome of *Nakamurella multipartita*. To test its functionality as light-responsive apical loop domain of shRNAs, Nm60 was conjoined with the siRNA core domain of SH2 and with three hinge regions. These constructs were subjected to eGFP reporter assays in mammalian cells (**Figure 4.31**). According to tertiary structure predictions, the apical loop folding of the generated shRNA variants deviated strongly from the variant that has no nucleotide insertion into the hinge region (**Figure 4.31b**). Indeed, a light-responsive expression of eGFP could be observed for all tested constructs (**Figure 4.31c**). 60_2 and 60_3 indicated nearly similar eGFP expression under light conditions and similar orientations of loop 2 at the opposite side of the radial axis compared to loop 1 from the shRNA analogue that has no hinge region insertion (**Figure 4.31b**,**c**). 60_1 showed decreased eGFP expression under light conditions and a perpendicular orientation of loop 2 compared to loop 1 (**Figure 4.31b**,**c**). 60_2, the simplest variant in which a uridine moiety was implemented upstream to the aptamer, indicated the highest fold change (**Figure 4.31d**). All three tested constructs (60_1-3) displayed relatively high levels of eGFP positive cells in darkness (23 % - 32 %, **Figure 4.31c**). This points towards a general decrease in dicer processing or accuracy when Nm60 is used instead of the aptamer 53.19. One reason could be that the shRNA processing by dicer is generally facilitated by flexible terminal loop regions [330]. Indeed, the loop region of Nm60 consists of six nucleotides, whereas the loop region of aptamer 53.19 consists of 9 nucleotides. This might decrease the shRNA processing by dicer due to a more rigid apical loop domain. Another reason for the weak suppression in darkness could be the altered 3'isomiR formation. For example, it was shown in **Table 4.1** that nucleotides from the aptamer may become part of the processed siRNA. Whereas the Nm60's first nucleotide (cytosine) cannot hybridize with the eGFP mRNA binding site of the conjoined siRNA, the aptamer 53.19's first nucleotide (guanine) matches this binding site. Again, to delineate the impact of PAL and dicer on these shRNA variants, *in vitro* dicer cleavage experiments in presence and absence of PAL could be performed along with NGS analysis of siRNA processing.

5.4 Impact of light intensity and timing on light-dependent reporter protein abundance

In this section it was found that the application of 100 µW/cm^2 constant blue light led to the highest number of eGFP expressing cells and consequently to the highest achievable light-dependent fold changes (**Figure 4.32**). Similar LOV-based photoreceptors used for optogenetic approaches in mammalian cells were illuminated with intensities of ~1 mW/cm^2 (EL222, [334]) or one order of magnitude below (LOV2, [80]). This indicates that PAL operates within the same range of light-sensitivity compared to existing LOV-proteins. Furthermore, the present study suggests that it is worthwhile to tune the light dose, as decreased fold changes had been observed when the light intensity was increased

[9] NGS analysis by Anna Maria Weber.

(**Figure 4.32**). This could be due to unwanted light-induced oxidative damage of the PAL protein which had also been described for other LOV proteins before [320, 335]. To reduce possible light-induced oxidative damages of the photoreceptor, pulsed protocols for the light-illumination were applied (**Figure 4.33**). In principle, this could increase the regulatory output [74, 80]. However, this was not observed in eGFP reporter assays (**Figure 4.33**). Instead, a constant application of blue light resulted in the highest number of eGFP positive cells. The observation that pulsing of light over the period of 44 h decreases reporter expression indicates that the PAL photochemistry remains intact over the entire period of the assay and that the conformation of PAL switches back and forth during seconds in darkness (**Figure 4.33**). However, for this assay a decreased fold change was observed compared to the assay before (3.3-fold *vs*. 4.1-fold, **Figure 4.32** *vs.* **Figure 4.33**). The underlying reason might be the changes of the pH in the culture medium after opening. This might decrease the efficiency of lipofection [263, 336, 337]. Additionally, the fold changes for both experiments which were described in section 4.4 were below the fold changes that were described for SH5 in section 4.3.2.1 (6.4-fold, **Figure 4.24c**,**d**). One reason might be that different light setups were used among these experiments. In section 4.4, the LPA device was used. This device utilizes one LED pin as spot-light source for the illumination of the well from the bottom. Instead, a light array was used in section 4.3.2.1 which consists of a multitude of LED pins that are arranged to illuminate transparent 24-well plates homogeneously from the top. Thus, increased eGFP expression levels were found when the LED array was used probably due to a more homogenous illumination.

5.5 Optoribogenetic control of cell cycle

Next, it was decided to target cell cycle proteins *via* light-responsive shRNAs in transient transfection experiments. Because the half-lives of the corresponding mRNAs and proteins are relatively short this could facilitate the observation of regulatory events in a time frame within two days after transfection [105, 338]. For the initial screening of shRNA sequences which target CDK1, two sequences (SHCDKi and SHCDKii) were selected from the RNAi consortium database [339]. For the initial screening of shRNA sequences which target cyclin B1, two sequences (SHCBi and SHCBii) were selected from the homepage of a lentiviral shRNA vector manufacturer (Applied Biological Materials). These sequences were cloned into the pSilencer plasmid backbone and co-transfected with a plasmid that expresses AGO2 (**Figure 4.34**). For both targets only one out of two shRNA sequences was found to be functional which means that the cells did accumulate in the G_2/M phase of the cell cycle compared to the controls (SH5, None, **Figure 4.34**). The co-transfection of these two functional shRNAs (SHCBi and SHCDKi) together did not increase the accumulation of the cells in the G_2/M phase notably when 50 ng of each plasmid was transfected but the accumulation increased when 100 ng of each plasmid was used which indicates a concentration-dependent effect (**Figure 4.34**).

To render SHCBi and SHCDKi light dependent, the loop sequences were exchanged by the aptamer 53.19 and an adenine nucleotide upstream to the aptamer to form SHCB1 and SHCDK1. An adenine was chosen as the hinge region nucleotide, as at that time the eGFP screening assays were only performed until section 4.3.2.1. Therefore, the impact of the nucleotide identity and its positioning up- or

downstream of the aptamer was still unknown at that time point. SHCB1 and SHCDK1 indicated a binding to PAL *in vitro* to a comparable extent as the full length aptamer 53 (**Figure 4.35c**,**d**). Interestingly, the binding in darkness was reduced for both constructs compared to aptamer 53 (**Figure 4.35c**,**d**). As expected, the G11C aptamer point mutants SHCB1m and SHCDK1m did not show a binding irrespective to the light irradiation state (**Figure 4.35c**,**d**). All these constructs were tested in HEK293PAL cells in presence of elevated AGO2 levels and indicated an accumulation of cells in the G_2/M phase (**Figure 4.35e**). However, no light-dependency was observed for SHCB1 and SHCDK1. Together with the observation for eGFP shRNAs (**Figure 4.24**), this result indicates that functional siRNA sequences can be conjoined with the PAL aptamer in a general and simple manner without the risk to destroy the siRNA's suppressive capacity. Other than before, no increased accumulation of cells in the G_2/M phase could be observed when 100 ng of both SHCB1 and SHCDK1 were co-transfected compared to single transfections (100 ng, **Figure 4.35e**). Instead, SHCDK1m and the co-transfection of 100 ng SHCB1m and SHCDK1m showed higher levels of cells in the G_2/M phase compared to other transfections that target cyclin B1 and CDK1 (**Figure 4.35e**). This could indicate that SHCDK1m is the most effective shRNA for the target gene suppression under these conditions. As no light-dependency was observed in cells (**Figure 4.35e**) but the binding to PAL was shown to be light-dependent *in vitro* (**Figure 4.35c**,**d**), it was doubted that the elevated levels of AGO2 are beneficial for the light-regulation of these intrinsic target genes.

It had been described before, that altered AGO2 expression levels influence the cell proliferation and the cell cycle distribution in cancer cells [340]. However, in HEK293PAL cells no significant differences in G_2/M phase accumulation could be determined for the SH5/AGO2 co-transfection compared to untransfected cells (None, **Figure 4.34** and **Figure 4.35e**). The mRNA levels of CDK1 and cyclin proteins are of low abundance (~45 transcripts/cell for CDK1 and ~10 - 100 transcripts/cell for cyclin proteins, [105]), whereas the transcript levels for eGFP mRNA which are transcribed from a CMV promoter are several magnitudes above the expectation for these intrinsic mRNAs [276]. Thus, only gene expression from strong promoters may require elevated levels of AGO2 for efficient target suppression. Therefore, shRNA experiments in absence of elevated AGO2 levels have been re-performed in HEK293PAL cells and extended for additional hinge region shRNA variants that target cyclin B1 (**Figure 4.36**, **Figure 10.5**). Here, SHCB1 indicated an accumulation of cells in the G_2/M phase only in darkness and to a comparable extent as SHCB1m under both light conditions (**Figure 4.36b**). Under light conditions, the accumulation was reduced in cells that harbor SHCB1 and this level was comparable to SHCB2 (uridine insertion upstream to the aptamer) and SHCB3 (uridine insertion downstream to the aptamer) and the latter two constructs did not show light-dependency (**Figure 4.36a**,**b**). The reason for the inability of SHCB2 and SHCB3 to accumulate cells in G_2/M phase might be explained by an altered processivity by dicer which leads to siRNAs of various lengths and suppressive capacities [270, 341]. As the adenine insertion upstream to the aptamer was functional in the case of SHCB1, this hinge variant was also tested to control the CDK1 expression (SHCDK1, **Figure 4.36c**) and the light-dependent difference in G_2/M phase accumulation was found to be superior as for cyclin B1 (e.g. 3.9 % for SHCB1 *vs*. 5.4 % for SHCDK1, **Figure 4.36d**). The degree of the cell cycle inhibition by either SHCB1 and SHCDK1 could depend on the suppressive capacity of the respective shRNA as well as the cell line [342] and is in line with previous observations for similar cell lines [295, 343, 344].

Therefore, the suppressive capacity is also dependent on the gene delivery efficiency. For HEK293 cells, a transient plasmid transfection efficiency of 70-80 % has been described [345]. In hard-to-transfect cells such as stem cells, this number may be further decreased. Typically, the efficiency of gene delivery by viral vectors is superior to transient transfection methods. Thus, improved cell cycle regulation could be achieved using viral vectors. For example, in stem cells a transduction efficiency of ~90 % may be achieved when adeno-associated vectors are used [346].

The expression of cyclin B1 and CDK1 expression is necessary for the initiation of mitosis [347]. It was then asked whether the accumulation of cells in G_2/M phase can be increased by suppressing the PLK1 protein which is an essential regulator throughout mitosis [348]. To this end, a published siRNA that targets PLK1 [339] was conjoined with the aptamer 53.19 and various hinge region modifications of which the double-nucleotide insertions were generated by hazard during cloning (SHPLK3-5) (**Figure 4.37a**). These constructs were screened for light-dependent G_2/M phase accumulation 29 h after transfection (**Figure 4.37b**) and all constructs led to a strong accumulation of cells in the G_2/M phase to a comparable extent as it was observed before [274, 349, 350]. However, only SHPLK2, and to a slighter extent, SHPLK4 and SHPLK5 indicated a reduced accumulation under light conditions (**Figure 4.37b**). Therefore, a point mutant of SHPLK2 was generated (SHPLK2m) and for better comparison both constructs were tested at the same time point after transfection that was also applied in **Figure 4.36** (44 h after transfection, **Figure 4.37c, Figure 10.5**). Similar to previous observations, the accumulation of cells in the G_2/M phase was increased for SHPLK2 in darkness compared to light conditions (**Figure 4.37c**). However, other than for the previous PLK1 shRNA screening assay, the light-dependent differences decreased when SHPLK2 was transfected (**Figure 4.37b** *vs.* **c**). This might be due to kinetic aspects of the transfection, as prolonged suppression of PLK1 can lead to cell apoptosis. Therefore, a smaller transfected cell population remains [348]. Another aspect might be that varying transfection efficiencies could account for a relatively large scattering of the values between the assay repetitions (**Figure 4.37b**,**c**).

As light-dependent physiologic effects could be observed when cyclin B1, CDK1 and PLK1 were targeted with optoribogenetically active shRNAs (**Figure 4.36** and **Figure 4.37**), it should be further verified whether this effect correlates with the target protein abundances. Therefore, western blot experiments were performed with lysates from cells that had been transfected with the different shRNAs and incubated in a similar way as for the cell cycle experiments (**Figure 4.38**, **Figure 10.6**). Indeed, altered protein levels for cyclin B1 and CDK1 correlated with the G_2/M phase accumulation which was observed in cell cycle experiments (**Figure 4.38a**,**c**,**d**). However, cyclin B1 and CDK1 protein levels could not be completely restored under light conditions (**Figure 4.38a**,**c**,**d**). This suggests that the suppressive activity of the shRNAs is not completely inhibited under light conditions, probably due to incomplete shRNA binding to PAL. As the K_d values for PAL and dicer to their RNA substrates are similar, a competition between these two proteins for the shRNA binding may occur (~153 nM for PAL/53.19 [237] and ~50 nM for dicer/dsRNA [351]). In darkness, only faint cyclin B1 and CDK1 protein expression levels could be detected (**Figure 4.38a**,**c**,**d**, for full range blots see **Figure 10.6**) which might be a consequence of an unaffected protein expression in untransfected cells [347]. This observation had been described before for the suppression of cyclin B1 and CDK1 which was mediated by transient

transfection of regulatory RNAs [352, 353]. One possibility to increase the light-dependent differences in gene expression might be the generation of a stable cell line that expresses the shRNA under the control of an inducible promoter [219, 295, 354]. For SHPLK2 and SHPLK2m, a slight protein suppression irrespective to the light irradiation state could be observed (**Figure 4.38b**,**e**). However, SHPLK2 was found to be light-responsive in cell cycle assays (**Figure 4.37b**,**c**). This contradiction could be explained by the limited sensitivity of western blot experiments [355] which masks small changes in the PLK1 protein expression. Techniques, such as single cell mass cytometry [356], could be useful to reveal changes in protein expression in more detail. These methods enable multiparametric measurements (e.g. measurement of protein levels *via* antibody-based detection and cell cycle determination) per cell rather than the generation of average values for the cell population as it is obtained from western blot analysis. However, this experiment indicated that the light-responsiveness of shRNAs targeting PLK1 need to be further improved. This could be achieved by the generation of a stable cell line that would enable an inducible shRNA expression as described above or by further testing of different siRNA core domains [274, 349, 357].

6 Outlook

6.1 Examples for multiplexing optoribogenetic RNA elements

As it had been described before, several protein-driven RNA switches can be used to control two mRNAs simultaneously [157]. The polarity of the translational switch upon light irradiation can be determined by integration of the RNA switch in *cis* (the embedding of the PAL-aptamer in 5'UTR results in an off-switch) or *trans* (the embedding of the PAL-aptamer into the apical loop domain of a regulatory RNA results in an on-switch, **Figure 6.1a**). In principle, the switches with both polarities can be used in parallel. For example, the simultaneous regulation of two mRNAs that target a pathway can be used to increase the output effect. In one scenario, the simultaneous regulation of a protein (protein A) which suppresses the activity of a second protein (protein B, **Figure 6.1b**) could be anticipated. Under light conditions, the expression of protein A is increased by an on-switch, and protein B is decreased by an off-switch and *vice versa* in darkness. In another attempt, the output effect could be increased by the opposite regulation of two protein levels that regulate a pathway of interest inversely (**Figure 6.1c)**. One of these proteins could be inhibited under light conditions whereas the other protein is activated under these conditions. An increased output effect could be especially useful when regulatory leakiness of the pathway of interest would have irreversible effects such as cell death or differentiation [157].

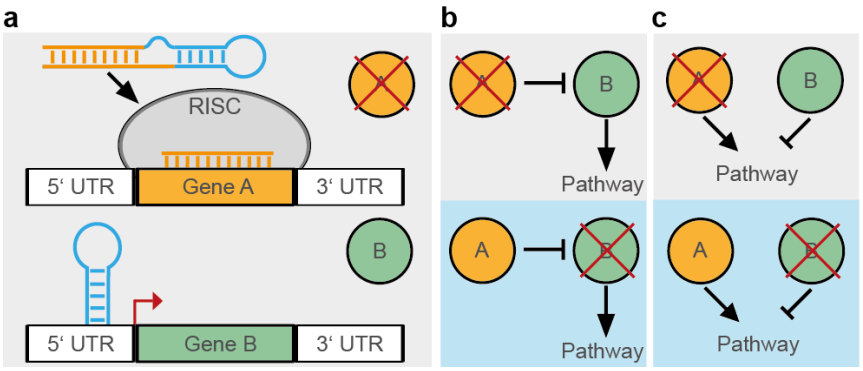

Figure 6.1: Multiplexed optoribogenetic systems that regulate the translational activity of two target genes in the opposite direction. a, Gene expression can be controlled by regulatory RNAs to suppress the expression of protein A in darkness whereas another target gene encodes for protein B, which was set under the control of a riboregulator which is located in its 5'UTR leads to the gene expression in darkness. Under light conditions, the expression status of both genes is inverted. **b**,**c**, Light-dependent pathway regulation *via* simultaneous control of two interacting proteins (**b**) or two proteins that both act on the pathway of interest (**c**).

Furthermore, two light-responsive regulatory RNAs could be applied simultaneously to control two mRNAs in parallel which would lead to a restored protein expression in light and a decrease protein expression for both targets in darkness. The induced effect depends on whether the regulated target proteins either activate or inactivate a cellular pathway (**Figure 6.2)**. For example, this strategy could be used to increase effects on the cell cycle as it was shown by the application of single shRNAs in **Figure 4.36b**,**d** and **Figure 4.37c** in this thesis. Here, cells had been transfected with SHCB1 or SHPLK2 and

the incubation in light led to decreased accumulation of cells in the G_2/M phase which was similar to the control levels. The co-transfection of these two regulatory RNAs might increase the range of light-responsiveness by an increase of the cell accumulation in the G_2/M phase in darkness while the accumulation might still drop to the levels for the control that were observed under light conditions. This idea is supported by the observation that the simultaneous suppression of cyclin B1 and PLK1 in HeLa cells led to an increased accumulation of cells in the G_2/M phase [219].

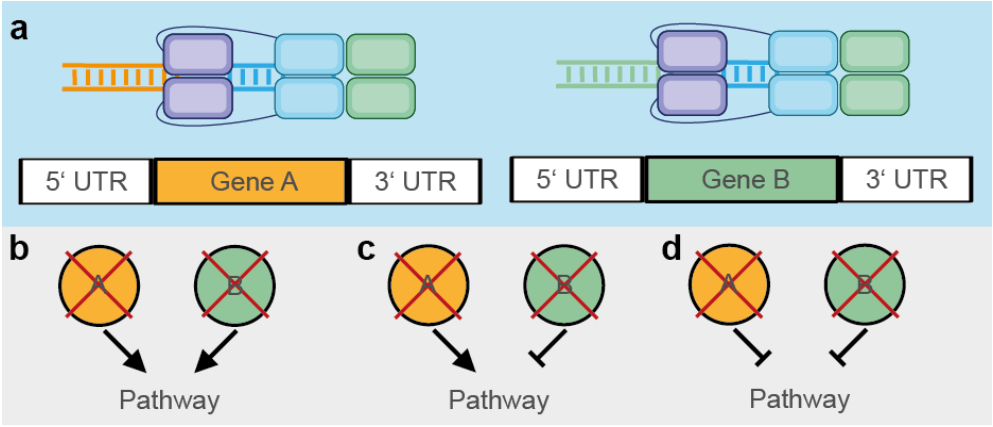

Figure 6.2: Multiplexed optoribogenetic shRNAs can be used to restore protein expression in light and decrease protein expression in darkness. a, Two regulatory RNA molecules are bound by PAL under light conditions. In darkness, the target genes are suppressed which may inactivate (**b**), modulate (**c**) or activate (**d**) the targeted pathway.

6.2 Optoribogenetics for spatiotemporally controlled studies of miR and protein function

One interesting application for addressing a multitude of gene targets may be the photocontrol of endogenous miR maturation. Tools have been developed to observe miR maturation kinetics in a cellular context. These tools help to understand the subcellular organization and functionality of endogenous miRs [250, 358]. Oppositely, optoribogenetic approaches are well-suited for precise and reversible manipulation of *pre*-miR processing. Optoribogenetic approaches may be useful to broaden our understanding in the spatiotemporal organization of miR function (**Figure 6.3**). The precise subcellular control of miR maturation paired with single cell RNA sequencing [359, 360] could help to decipher miR-associated target gene control, e.g. in their regulatory activity on subsets of target genes at different cellular compartments at different time points [358].

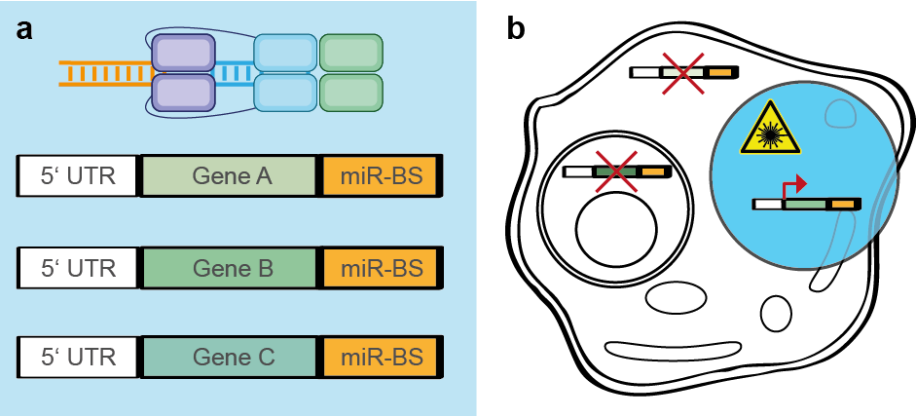

Figure 6.3: Optoribogenetic control of *pre*-miR processing may be used to study the spatiotemporal role of mature miR abundance and corresponding protein expression. a, Under light conditions, the processing of an optoribogenetic *pre*-miR is altered through PAL-binding which limits the suppressive activity on target gene abundances. **b**, Spatial regulation of mature miR activity is enabled by subcellular illumination of a cell.

Besides the studying of miR maturation, protein function can be studied by using optoribogenetics. It is difficult to study the role of genes when their knockout results in lethality at certain stages of the embryonic development [361]. To circumvent lethality, conditional gene expression systems were developed for several animals [362-364]. However, the induction of these systems is notably slow (e.g. at least a 24 h delay in gene expression after induction, [310]). To study genetic dynamics at a more resolved timescale it is necessary to quickly, reversibly and precisely control gene expression [365]. In these cases, optoribogenetic modalities may enlarge current toolboxes.

6.3. Optoribogenetic therapies

T-cell responses are controlled by multiple factors, integrating several input protein levels. Thus, efficient T-cell activation may be increased by multifactorial regulation, e.g. the suppression of inhibitory proteins paired with the induction of activating proteins at the same time (**Figure 6.2c)** [366]. As an alternative to the exogenous addition of proteins, genetic engineering of T-cells has recently entered clinical trials [367, 368] and was furthermore extended for optogenetic modalities and so founding the field of optoimmunoengineering [369]. The multifactorial control in combination with optoribogenetic modalities features local and timed immunomodulation which may reduce off-target effects that are caused by constant and systemic immunomodulation [370]. A key drawback of *in vivo* approaches using optogenetics is the difficult administration of light into deep tissues. However, recent advantages in wireless implantable optoelectronic devices may help to overcome these obstacles [371, 372].

Besides T-cells, other cell types can be genetically modified and implanted into a host organism for example to secrete bioactive molecules upon light illumination [373, 374]. Such “designer” cells may be programmed to produce endocrinal molecules (e.g. insulin) that impact the whole organism’s hoemeostasis. Another option to program would be the production of paracrine molecules with the aim to induce high local concentrations that enable spatially restricted therapies. For example, the local

modulation of the tumor microenvironment *via* CCL4 secretion may lead to an increased invasion of $CD8^+$ T cells that could kill cancer cells [375]. Finally, cell-based treatment could be targeted to regions of spinal cord injuries. The controlled secretion of modulatory molecules that act on diverse pathways (axonal sprouting, synapse formation, promoting axon regeneration) may improve the recovery of functional tissue after lesion in these regions [376, 377].

6.4 Optoribogenetics in biotechnology and biomaterial development

The optoribogenetic control of RNA could be used to modulate biotechnological pathways for biomolecule production in yeast cells. It had been shown before that a switching from the growth to the production phase by light could improve product yields [378] and relevant target genes could be set under the control of optoribogenetic control elements such as shRNAs or aptamer-engineered 5'UTRs (**Figure 6.4**). Rather than small molecule-based compounds for the induction of the production phase, the use of light may also help to circumvent purification steps to separate the product from inducer molecules. This would render the purification step more cost-effective [379].

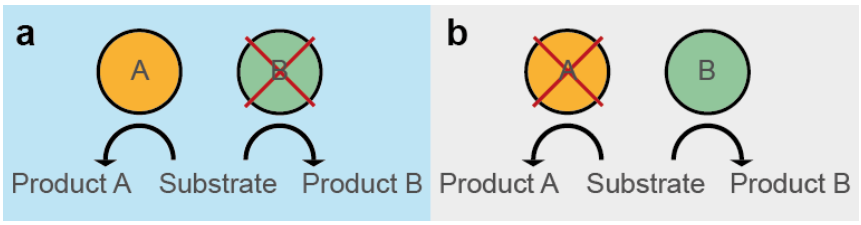

Figure 6.4: Light-controlled alternative substrate production could be used in biotechnological applications for a switching between a "production" phase under light conditions (**a**) and a "growth" phase in darkness (**b**) which would lead to the formation of different products, e.g. product a under light conditions **(a**) and product b in darkness (**b**). To reach this goal, genetic modalities that are depicted in **Figure 6.a** could be used for pathway engineering.

Another idea would be the application of optoribogenetics in tissue engineering. Recently, a technique has been developed to control the cell interaction with the extracellular matrix by light in order to modulate the cell attachment [380]. Complementary systems could be developed for the light-controlled production of biomolecules that act on cell migration [381], proliferation [382] or differentiation [383] within a given cell matrix. These systems can be potentially multiplexed with each other by using orthogonal optogenetic modalities that respond to different wavelengths [384].

7 Methods

7.1 Working with nucleic acids

7.1.1 Agarose gel electrophoresis

Depending on the size of the nucleic acids to separate, 1%, 2% or 4% agarose powder was dissolved in 0.5x TBE buffer by boiling of the mixture. 5 µl ethidium bromide was added into 50 ml agarose solution which was subsequently poured into a gel casting chamber to solidify. Samples were prepared by mixing the corresponding nucleic acid solution with either DNA or RNA loading dye, respectively. Gels were routinely run for 15-30 min at 150 V and visualized using UV transillumination (BioRad). Nucleic acid sizes were compared to 1 kb Plus DNA Ladder or Ultra Low Range DNA Ladder.

7.1.2 Polymerase Chain Reaction (PCR)

Routine PCR reactions for amplification of trace DNA was performed using homemade Pfu DNA polymerase enzyme.

Table 7.1: Pipetting scheme for PCR reaction using Pfu polymerase.

Reagent name	Volume [µl]	Stock concentration	Final
Pfu reaction buffer	10	10 x	1x
$MgCl_2$	8	25 mM	2 mM
dNTPs	1	25 mM	0.25 mM
5'- Primer	1	100 µM	1 µM
3'- Primer	1	100 µM	1 µM
dsDNA template	1		1 – 20 nM
Pfu polymerase	1	2.5 U/µl	2.5 U
ddH_2O	*ad* 100 µl		

DNA amplification was achieved by using a standard PCR cycling protocol assuming an extension time of 0.5 kb per minute for Pfu polymerase.

Table 7.2: Standard cycling protocol for DNA amplification using Pfu polymerase.

Step	Temperature	Time	Repeat
Initial denaturation	95 °C	30 sec	
Denaturation	95 °C	30 sec	
Annealing	T_m – 5 °C	30 sec	20 – 25 cycles
Elongation	72 °C	0.5 kb/min	
Final elongation	72 °C	Elongation time + 1 min	

For amplification of plasmid backbones as well as integration of single point mutations to plasmids, Flash Phusion polymerase was used due to its high fidelity and rapid extension time (1 kb/15 sec) according to the protocol provided by the manufacturer.

7.1.3 Purification of nucleic acids

Purification of nucleic acids by phenol-chloroform extraction was performed by adding an equal volume of phenol to the aqueous nucleic acid solution. After brief vortexing and centrifugation at 4 °C for 5 min and 14.000 rpm, the aqueous, upper phase was mixed with two volumes of chloroform in a 2 ml reaction tube. After another round of brief vortexing and centrifugation at 4 °C for 5 min and 14.000 rpm, the upper aqueous phase was subjected to ethanol precipitation. For ethanol precipitation, the aqueous phase was supplemented with 1/10 volume of 3M NaOAc, pH 5.4 and three volumes of 100 % ethanol. After incubation for 20 min at – 80 °C, the mixture was centrifuged at 4 °C for 30 min at 20.000 g. Next, the supernatant was decanted, and 1500 µl of 70 % ice-cold ethanol was added. After another round of centrifugation at 4 °C for 30 min at 20.000 g, the pellet was air-dried under a fume hood and resuspended in ddH_2O or MilliQ water (10 – 100 µl). PCR reactions, digested plasmids as well as cut-out gel slices from agarose gel electrophoresis containing a DNA of interest were purified using NucleoSpin Gel and PCR Clean-up kit according to the manufacturer's instructions.

7.1.4 *In vitro* transcription (IVT)

RNA molecules of interest were produced from dsDNA templates using the in-house generated T7-RNA polymerase enzyme. dsDNA templates were modified upstream by implementing a T7 promoter sequence and two additional guanine residues (bold) after the transcription start site to ensure transcription (TAATACGACTCACTATA<u>G</u>**GG**, underlined G: transcription start site, [385]). IVT reactions were performed at 37 °C either for 4 h or overnight.

Table 7.3: Pipetting scheme for *in vitro* transcriptions.

Reagent name	Volume [µl]	Stock concentration	Final
Tris pH 7.9	20	200 mM	40 mM
$MgCl_2$	2.5	1 M	25 mM
NTPs	10	25 mM	2.5 mM
DTT	5	100 µM	5 mM
Inorganic Pyrophosphatase	0.2	2 U/µl	0.4 U
RNasin	1.24	40 U/µl	50 U
dsDNA template	9		100-300 pmol
T7 RNA polymerase	5	50 U/µl	250 U
ddH_2O	*ad* 100 µl		

7.1.5 RNA workup

For purification of IVT reactions, 10 µl 3 M NaOAc, pH 5.4 was added followed by addition of 300 µl ethanol. After 30 min incubation at -80 °C, samples were centrifuged for 30 min at 4°C for 20.000 g. The supernatant was decanted, and the pellet was washed with 100 µl 70 % ethanol. After an additional centrifugation step, the supernatant was carefully removed, and the pellet was dried for 30 min at room temperature using air ventilation of a fume hood. Then, the pellet was resuspended in 70 µl RNAse free MilliQ water. After further addition of 8 µl DNAseI buffer and 1 µl DNAseI, the reaction was incubated for 30 min at 37 °C.

7.1.6 Urea polyacrylamide gel electrophoresis

Short RNA oligonucleotides (50 – 150 bases) were separated using a 10 % Urea polyacrylamide gel (Urea PAGE). Urea PAGE gel casting solution was prepared freshly for each gel, quickly poured between two glass slides and allowed to rest until polymerization was accomplished. The gel was then mounted into a chamber filled with 1x TBE. Gel was pre-run for 30 min at 375 V. Samples were mixed with PAA loading buffer, heated for 5 min to 95 °C. After rinsing the gel pockets with a syringe and loading of the samples onto the gel, electrophoresis was performed for 90 min at 375 V. Then, RNA was visualized by UV shadowing using a handlamp. Cut out gel pieces containing RNA of interest were then subjected to electroelution or stored at -20 °C until needed.

7.1.7 Electroelution

Gel pieces containing RNA were positioned into an electroelution chamber filled with 1x TBE buffer. Channels connecting cathode and anode were filled with 170 µl 8 M ammonium acetate. After 45 min at 150 V, the RNA migrated towards the anode accumulating in the channels filled with high salt content. RNA was isolated by first closing the channels using pipette tips, discarding residual buffer, reopening the channels by discarding the pipette tips and pipetting the RNA out of the channels. After another round of ethanol precipitation (described in section 7.1.5), RNA was dried and resuspended in 60 µl MilliQ water.

7.1.8 Concentration determination

Nucleic acid concentrations were measured on a NanoQuant Infinite 200 plate reader (Tecan) by UV absorption. Nucleic acid concentration was calculated using Lambert-Beer law:

$$\frac{A_{260\ nm}}{l \bullet \varepsilon_{DNA\ or\ RNA}} = c[\text{DNA or RNA}]\ \text{in M} \qquad (1)$$

with $\varepsilon_{DNA\ or\ RNA}$ = extinction coefficient in $\frac{1}{M \bullet cm}$ and l = pathlength in cm

Purity of nucleic acids were estimated by calculating absorption ratio of $\frac{A_{260\ nm}}{A_{230\ nm}}$. Values ranging from 1.7 – 1.9 for DNA and 1.9 – 2.1 for RNA were considered as "pure" and used for downstream experiments.

7.1.9 5'(De-)phosphorylation

Classical cloning using only one restriction enzyme to cut plasmid backbone is prone to re-ligation. In these cases, dephosphorylation of the plasmid backbone was performed using calf intestinal alkaline phosphatase (CIAP) according to the manufacturer's instructions.

In cases, re-ligation of the plasmid backbone (for example after whole plasmid PCR amplification) was intended or dsDNA should be ligated into a dephosphorylated plasmid backbone, 5'- phosphorylation reactions were performed at 37 °C for 30 min.

Table 7.4: Pipetting scheme for 5' phosphorylation.

Reagent name	Volume [µl]	Stock concentration	Final
T4 PNK buffer	2	10 x	1 x
DNA template			up to 300 pmol
T4 PNK (NEB)	1	10 U/µl	10 U
ddH_2O	*ad* 20 µl		

7.1.10 Molecular cloning

Classical restriction cloning was performed according to the manufacturer's instructions of the respective enzymes (e.g. New England Biolabs or Promega). Purification was performed according to section 7.1.3. Subsequent ligation was performed using T4 DNA ligase (New England Biolabs). For AQUA cloning and whole plasmid PCR reactions, in-house protocols were elaborated by Christian Renzl, which were derived from [386]. In-Fusion and NEBuilder cloning reactions were performed according to the manufacturer's instructions and exclusively with purified nucleic acid samples. Typically, 75 - 100 ng of linearized vector was used in concert with a two- to threefold molar excess of insert.

7.1.11 *In silico* 3D shRNA structure predictions

In silico 3D shRNA structure predictions were performed by pasting expected RNA primary sequences transcribed from U6 promoter in eukaryotic cells into the RNAfold WebServer form [387]. Obtained secondary structure prediction were pasted into the RNAComposer WebServer form [388, 389]. Resulting PDB files were either separately visualized or aligned to control PDB files using UCSF CHIMERA modeling software [390].

7.2 Working with Escherichia coli

7.2.1 LB Medium and agar plates

LB Medium (Luria/Miller) was prepared by dissolving 10 g powder in 1 l ddH_2O followed by autoclaving for 15 min at 121 °C. For preparation of LB-Agar plates, 7.5 g agarose was added additionally to the LB Medium before autoclaving. Solution was cooled down to 65 °C before an antibiotic of choice was added. Final antibiotic concentrations usually were 100 µg/ml for ampicillin and 50 µg/ml for kanamycin, respectively. Plates were casted under sterile conditions and stored at 4 °C for several weeks.

7.2.2 Cultivation and long-term storage of bacteria

E. coli bacteria were obtained from agar plates or glycerol stocks. For subsequent plasmid preparation, either 6 ml or 400 ml LB medium containing an antibiotic compatible to the plasmid to be expressed was inoculated with bacteria and incubated over night at 37 °C under agitation (120 – 160 rpm). Afterwards, glycerol stocks were prepared for long-term storage of bacteria by mixing 500 µl of the solution containing bacteria with 500 µl 50 % glycerol. After mixing, samples were stored at -80 °C. For PAL protein expression, 100 ml LB medium containing 20 µg/ml gentamycin and 50 µg/ml kanamycin was inoculated with pET28c-6xHis-PAL glycerol stock and incubated over night at 120 rpm and 37 °C.

7.2.3 Generation of chemically competent bacteria

E. coli strains HST08 or SCS110 were rendered competent in-house. 100 ml main culture was inoculated with 1 ml pre-culture and incubated overnight. The main culture was then incubated until the OD_{600} has reached 0.4. Then, the culture was incubated for 5 min on ice followed by centrifugation for 7 min at 3000 rpm and 4 °C. The supernatant was discarded and the pellet was resuspended in 20 ml ice-cold $CaCl_2$ solution. After another centrifugation step (2500 rpm, 4°C, 5 min), the supernatant was discarded, the pellet was resuspended in 20 ml ice-cold $CaCl_2$ and incubated for 30 min on ice. The last centrifugation step was repeated, the supernatant was discarded, and the pellet was resuspended in 4 ml $CaCl_2$ solution. The solution was aliquoted in tubes à 50 µl, snap-frozen using liquid nitrogen and stored at -80 °C.

7.2.4 Transformation

For transformation, 50 µl competent *e. coli* bacteria were thawed on ice and mixed with 2.5 µl (In-Fusion), 2 µl (TOPO TA) or 20 µl of classical restriction ligation and incubated for 20 – 30 min. After heat shock (42°C for 90 sec) and a 2 min cooldown period on ice, 450 µl LB medium was added and the mixture was incubated for 1 h at 37 °C and 800 rpm. For cloning, 75 µl per solution was distributed onto agar-plates. For re-transformation, 10 µl per solution was distributed onto agar-plates. Plates were incubated over night at 37 °C.

7.2.5 Plasmid preparation

Small (6 ml culture) and medium (400 ml culture) plasmid preparations were purified using NucleoSpin Plasmid or NucleoBond Xtra Midi kits, respectively. Purification was performed according to the manufacturer's instructions.

7.2.6 Sanger sequencing

Purified plasmid samples were sent for sequencing at concentrations ranging from 50 to 90 ng/µl to either Eurofins (formerly GATC Biotech) or Seqlab (Microsynth).

7.3 Working with proteins

7.3.1 Induction and protein overexpression

For *in vitro* PAL protein overexpression, 4 l LB medium containing 50 µM riboflavin, 20 µg/ml gentamycin and 50 µg/ml kanamycin were inoculated with 40 ml pre-culture and incubated at 30 °C, 120 rpm, until an OD_{600} of 0.6 was reached. After further supplementing the medium with 1 mM IPTG, bacteria solution was incubated for three days in darkness at 12 °C and 120 rpm. Then, bacteria solution was centrifuged for 30 min at 4 °C and 3700 rpm. Thereafter, supernatant was discarded, and pellet subjected to protein purification.

7.3.2 Protein purification

Bacteria pellet containing overexpressed PAL was resuspended in 40 ml ice-cold lysis buffer by vortexing for 15 min. Cell walls were disrupted by sonification (50 % instrument power, alternating every 30 sec between pulses and rest on ice for 4 min in total). Subsequently, the lysate was cleared by centrifugation (18.000 rpm, 45 min, 4 °C) and the supernatant was incubated with 6 ml Ni-NTA beads for 1 h at 4 °C while overhead shaking. Subsequently, beads were centrifuged at 1600 rpm for 10 min and 4 °C. Then, supernatant was discarded, and beads were resuspended in 10 ml lysis buffer. After repeating this washing and centrifugation step, beads were resuspended in 3 ml lysis buffer and loaded onto a disposable column. Excess liquid could pass through the column by gravity flow. Then, 9 ml elution buffer was added, column was sealed and incubated for 30 min whilst overhead shaking at 4 °C. Next, column was re-opened, and flow-through was collected, dialyzed two times against 1x ICB for 4 h and overnight, respectively. Lastly, protein was analyzed on SDS-PAGE, concentration was determined, and protein was subjected to biotinylation (section 7.3.7) or long-term storage at -80 °C after freezing in liquid nitrogen.

7.3.4 Concentration determination and protein switching

Protein concentration of whole cell lysates was routinely determined using Pierce BCA Protein Assay Kit following the manufacturer's recommendations. PAL protein concentration was calculated using absorption spectroscopy measurements:

$$\frac{A_{447nm}-A_{580nm}}{\varepsilon_{Riboflavin447nm} \bullet l} = c[PAL] \text{ in M} \quad (2)$$

$$\text{with } \varepsilon_{Riboflavin447} = 12500 \frac{1}{M \bullet cm} \text{ and } l = \text{pathlength in cm}$$

The conformational state of PAL protein was also determined by recording of the absorption spectrum from 405 – 504 nm. The conformation of PAL was switched to the light conformation by exposing the protein to blue light (405 nm) at an intensity of 1 mW/cm^2 for 1 min at room temperature. PAL was switched back to the dark conformation by incubating the protein for 1 h in the dark at room temperature.

Purity of the PAL protein was estimated using following formula:

$$\frac{A_{280}}{A_{447}} \approx \text{Purity} \quad (3)$$

Values from 3.8 to 4.2 were considered as "pure". These values are obtained due to PAL's amino acid composition. The tyrosine, tryptophane and cystine residues in PAL were considered to absorb light at 280 nm together with Riboflavin. At 447 nm, only riboflavin was considered to absorb light.

7.3.5 SDS-PAGE

For separation of proteins according to their molecular weight and for subsequent Western Blot experiments, SDS-PAGE was performed. 10 or 12.5 % PAA gels were prepared by subsequent casting of separating and stacking gel between two glass slides. After polymerization, gels were loaded into a running chamber filled with 1x SDS gel running buffer. Samples were mixed with Laemmli buffer and heated to 95 °C for 5 min before cooling down on ice. Gels loaded with samples were pre-run for 5 min at 50 V and subsequently run for 45 min at 150 V.

7.3.6 Coomassie Staining

For protein visualization on acrylamide gels, SimplyBlue SafeStain solution was used according to the manufacturer's recommendations.

7.3.7 Biotinylation of PAL protein

In vitro purified PAL protein was biotinylated using Sulfo-NHS-LC-Biotin dissolved in 1x ICB at a 4-molar excess at 4 °C under dark conditions. Biotinylated protein was separated from residual educts using size exclusion chromatography (Zeba columns) according to the manufacturer's recommendations.

7.3.8 Dot Blot

Successful biotinylation was verified using Dot Blot analysis. Therefore, 10, 25 and 50 pmol of non-biotinylated PAL and biotinylated PAL were spotted on a nitrocellulose membrane and allowed to dry for 1 h at room temperature. After membrane blocking in 1x PBS supplemented with 5 % BSA and 0.1 % Tween 20 for 30 min at room temperature, solution was replaced with Streptavidin-HRP complex diluted 1:1000 in 1x PBS supplemented with 5 % BSA, 0.1 % Tween 20 and incubated for 30 min at room temperature. After three washing steps with 1x PBS supplemented with 0.1 % Tween 20 for 5 min, Pierce ECL Western Blotting substrates were added, and chemiluminescence was detected immediately afterwards using a VersaDoc imaging system (BioRad).

7.4 *In vitro* RNA-protein interaction assay (RiboGreen assay)

For *in vitro* PAL protein/RNA aptamer interaction studies, biotinylated PAL was first immobilized to streptavidin-coated well plates. To this end, wells were washed three times with 200 µl 1x ICB before 125 pmol biotinylated PAL protein dissolved in 100 µl 1x ICB was added per well and incubated at 4 °C for 4 h or overnight. Then, wells were washed three times with 200 µl 1x ICB. Next, RNA was diluted to final concentrations of 1000, 100 and 10 nM in 1x ICB in absence or presence of 0.5 mg/ml Heparin and 0.5 mg/ml BSA to reach a final volume of 100 µl per well. After incubation for 30 min at 25 °C under either blue light (465 nm, 2.15 mW/cm^2) or dark conditions, wells were washed three times for 3 min with 200 µl 1x ICB. Subsequently, RiboGreen reagent was diluted 1:500 in 1x TE-buffer and 150 µl was added to each well and incubated for 1 h under dark conditions. Finally, fluorescence intensity (ex/em: 500/525 nm) was measured using a Tecan Ultra plate reader. Values were processed by subtracting background fluorescence from equally treated wells without immobilized PAL and subsequent normalization to full length aptamer 53 incubated under light conditions.

7.5 Working with mammalian cells

7.5.1 Cultivation and long-term storage of cells (seeding, freezing, thawing)

Hek293, HEK293PAL and HeLa cells were cultured in DMEM medium, supplemented with 1 % non-essential amino acids, 1 % Sodium Pyruvate and 10 % fetal calf serum at 37 °C in a humidified 5 % CO_2 atmosphere and were passaged every 2–3 days. HEK293PAL cells were cultured one week before and

after cell sorting with 1 % penicillin/streptomycin and permanently in presence of Geneticin (G418, 400 µg/mL).

7.5.2 Mycoplasma testing

Mycoplasma testing was performed every three months using PCR detection.

7.5.3 Transient plasmid transfection

Cells were transfected either immediately after seeding in 500 µl DMEM supplemented with 1 % NEAA and 1 % Sodium Pyruvate containing 10 % FCS or 24 h after seeding in 500 µl DMEM supplemented with 1 % NEAA and 1 % Sodium Pyruvate. In the latter case, 60 µl FCS were added per well 4 h after transfection. For transfection, 1.5 µL Lipofectamine2000 was used per well in a 24-well plate format. Cells were transfected with various amounts of plasmid DNA (see in the following). Plasmids and Lipofectamine2000 were each diluted in 50 µl Opti-MEM per well and incubated 5 min before mixing at room temperature. After 20 min further incubation at room temperature, 100 µl transfection mix was added per well. For microscopy experiments investigating the PAL (fusion-) protein photochemistry or localization, cells were transfected with 500 ng of the respective pmCherry-C1 plasmid construct. For experiments comprising of aptamer-modified *Metridia* Luciferase mRNA, cells were transfected with 500 ng plasmid DNA (e.g. pmCherry-C1 plasmid variant and PMetLuc2-Control reporter plasmid variant at a mass ratio of 10:1). For the *pre*-miR/reporter plasmid titration experiment (section 4.2.2.2), 500 ng plasmid DNA was transfected per well. pSilencer plasmid was transfected in excess (100:1, 75:1, 50:1, 25:1, 10:1) or in equal amounts (1:1) to the PMetLuc2-Control plasmid variant. For *pre*-miR/shRNA reporter assays without AGO2 overexpression, cells were transfected with 500 ng plasmid DNA (e.g. pSilencer and pEGFP-N1 or PMetLuc2-Control plasmid at a mass ratio of 100:1). For reporter assays without AGO2 overexpression, cells were transfected with 500 ng plasmid DNA (e.g. pSilencer and pEGFP-N1 or PMetLuc2-Control plasmid at a mass ratio of 100:1). For experiments involving AGO2, cells were transfected with 250 ng plasmid DNA (e.g., pSilencer, AGO2 and pEGFP-N1 plasmid at a mass ratio of 2:2:1) in case of eGFP regulation and 200 ng plasmid in case of intrinsic target regulation (e.g., pSilencer and AGO2 and pEGFP-N1 at a mass ratio of 1:1). In case of miR21 mimic co-transfection with reporter plasmid, 495 ng of pEGFP-N1 or PMetLuc2-Control plasmid was co-transfected with 10 nM miR21 mimic (24 pmol/well). For the experiment investigating the impact of light on mCherry-PAL fluorescence (section 4.2.3.2), cells were transfected with a total amount of 500 ng plasmid DNA comprising of a single pmCherry-C1 construct or a two constructs mixed at a mass ratio of 1:1 (250 ng of each). For transfections of shRNAs targeting intrinsic mRNAs without additional AGO2 overexpression, 500 ng of the corresponding pSilencer plasmid variant was transfected.

7.5.4 Generation of the HEK293PAL cell line

For the generation of a stable monoclonal HEK293 cell line expressing mCherry-PAL (HEK293PAL), 1 × 10^6 cells were seeded into each well of a 6-well plate and transfected by Lipofectamine2000

transfection on the following day using 2.5 µg plasmid DNA and 8 µl Lipofectamine2000. Four hours after transfection, the supernatant was discarded, and cells were washed with PBS before the addition of 3 ml cell medium. After three days, the medium was supplied with 400 µg/ml G418. One week before and after cell sorting, cell medium was supplemented with 1 % penicillin/streptomycin. After five weeks of selection, single cells, which strongly express mCherry, were sorted *via* fluorescence activated cell sorting into a well of a 96-well plate. Cells were cultivated until 80 % confluency was reached in a T-175 culture flask. Then, cells were frozen or used in further experiments.

7.5.5 Determination of 3'isomiR formation by 3' miR-RACE

For 3' miR-RACE (rapid amplification of cDNA ends), 1 × 10^5 HEK293PAL cells were seeded in a 24-well plate. 24 h later, transfection with SHA and luciferase reporter plasmid was performed according to section 7.5.3 and cells were further incubated in darkness. 19 h after transfection total RNA extraction with TRIzol was performed according to the manufacturer's instructions. 1,5 µg total DNase-treated RNA was poly-adenylated using Poly-A Polymerase according to the manufacturer's instructions. The reaction was purified by phenol/chloroform extraction followed by ethanol precipitation (section 7.1.3). Reverse transcription was performed using 1 µg poly-adenylated cDNA and Bioscript Reverse Transcriptase (RT-Primer: ATTCTAGAGGCCGAGGCGGCCGACATGTTTTTTTTTTTTTTTTTTTT-TTTTTTTTT) according to the manufacturer's instructions. After another round of phenol/chloroform extraction followed by ethanol precipitation, PCR amplification was performed using Taq Polymerase (Forward Primer: CGCCTAGCTTATCAGACTGATGT, reverse Primer: ATTCTAGAGGCCGAGGCGG-CCGACATG). Cloning was performed using TOPO TA cloning kit according to the manufacturer's instructions. Plasmids were isolated from individual clones, purified as described in section 7.1.3 and sent for sequencing.

7.5.6 Protein isolation

Whole protein lysates were prepared from eukaryotic cell material. Therefore, cell supernatant was aspirated and replaced with 500 µl ice-cold 1x PBS per well using 24-well plates. After pipetting up and down, cells were transferred to reaction tubes and centrifuged for 5 min at 200 rpm at 4 °C. The supernatant was aspirated, and the pellet was resuspended in 20 µl RIPA buffer containing 1 mM PMSF. After 5 min incubation on ice, cells were centrifuged for 15 min at 14.000 rpm and 4 °C. Then, supernatant was transferred to a fresh tube.

7.5.7 mCherry quantification assay

1 × 10^6 HEK293PAL cells were lysed in 250 µl RIPA buffer containing 1 mM Phenylmethylsulfonyl fluoride (PMSF). Lysates were cleared by centrifugation (14.000 g for 15 min, 4°C). Generation of a mCherry standard curve and fluorescence measurements were performed using mCherry Quantification Kit according to the manufacturer's instruction with the exception that RIPA buffer containing 1 mM

PMSF was used instead of mCherry Assay Buffer. For calculation, a cell volume of 4000 µm^3 was assumed as well as the cytosol to occupy one third of the cell's volume [256].

7.5.8 Semi-dry Western Blot

HEK293PAL cells were lysed 44 h after transfection as described in 7.5.6 Protein isolation. Cleared lysates in 1x Laemmli buffer were incubated at 95 °C for 5 min before loading on SDS-PAGE gels. Protein quantification was performed as described in section 7.3.4. 5 µg of protein per lane was loaded onto 10 % or 12,5 % SDS-PAGE gels and blotted in 1x Transfer buffer onto a nitrocellulose membrane using a Bio-Rad Trans-Blot SD Semi-Dry Transfer Cell for 75 min at 20 V and 30 W. Membranes were blocked with 1x TBS-T buffer containing 5 % BSA (Western Blot grade) under agitation at room temperature for 1 h. Blots were cut according to the protein ladder in a way that all target proteins can be individually incubated with the respective primary antibody (mouse *anti*-cdc2 (CDK1, 1:1000); mouse *anti*-GAPDH (1:4000); goat *anti*-Cyclin B1 (1:1000); rabbit *anti*-PLK (1:1000); rabbit *anti*-Histone H3 (1:2000); mouse *anti*-Phospho Histone H3/Ser10 (1:1000)) at 4 °C overnight or at room temperature for 1 h in 1x TBS-T containing 5 % BSA. Detection was performed with IRDye 800CW goat *anti*-mouse, donkey *anti*-goat and goat *anti*-rabbit at a dilution of 1:15.000, respectively.

Antibody-stained blot pieces were arranged, and fluorescence images were acquired using an Odyssey Imaging System's 800 nm channel (ex/em: 785/810 nm) to visualize bound 800CW secondary antibodies. Pixel densitometry of blot bands was performed using Fiji software by creating rectangles of equal sizes for each sample lane followed by quantification of the area under the peak of each protein spot. Relative density was calculated by dividing values obtained from putative cyclin B1, CDK1 or PLK1 protein bands through the values obtained from the putative GAPDH band of each lane. Relative density values were normalized to untransfected cells incubated in darkness.

7.5.9 Luciferase Assay

Seeding, transfection and light application. For luciferase assays in which cells were seeded and transfected the same day (in presence of FCS), 0.75 × 10^5 HEK293 or HEK293PAL cells were seeded and transfected according to section 7.5.3. 18 h after transfection and incubation under blue light (465 nm, 106 µW cm^{-2}, 30 s pulses) or in darkness, 50 µl cell supernatant was harvested per sample and subjected to luciferase assay. For luciferase assays in which cells were seeded and transfected the next day (in absence of FCS), 1 × 10^5 HEK293 or HEK293PAL cells were seeded in two separate 24-well plates. Cells were transfected according to section 7.5.3. 18 h - 19 h after transfection and incubation under blue light (465 nm, 106 µW cm^{-2}, 30 s pulses) or in darkness, 50 µl cell supernatant was harvested per sample and subjected to luciferase assay. For reversibility assays, one control plate was kept constantly in darkness. Another plate was incubated under varying light conditions after transfection as indicated by the corresponding time lines (section 4.2.3.1). Immediately before the light irradiation status was altered for one plate, cell medium was exchanged for both plates involved in the assay (plate incubated constantly in darkness and plate exposed to varying light conditions).

Chemiluminescent luciferase assay. For the luciferase assay, 50 µl of the cell culture supernatant was transferred to wells of a white 96-well plate. 5 µl luciferase substrate dissolved in buffer according to the manufacturer's instructions was added and the reaction was incubated for 3 min at room temperature. The luminescence signal was measured using an EnSpire plate reader with an integration time of 5 s.

Data normalization. For normalization strategies, please see the corresponding figure captions.

7.5.10 eGFP Assay

eGFP reporter assays in mammalian cells. 1 × 10^5 HEK293PAL cells were seeded per well in two separate 24-well plates. After 24 h, transfection was performed as indicated in section 7.5.3. For the miR21-based reporter assays, the 3'UTR of pEGFP-N1 bearing both miR21-5p and -3p binding sites (eGFP-5p-3p, **Figure 4.17a**) was used. For shRNA-based reporter assays, unmodified pEGFP-N1 was used. Cells were incubated for 44 h in the presence of blue light (465 nm, 106 µW cm^{-2}, 30 s pulses) using the LED array or in darkness. Then, the cell supernatant was aspirated, cells were washed and resuspended in PBS (25 °C). Subsequent quantification of eGFP positive cells was performed using flow cytometry. For evaluation, single cells were identified as described in section 7.5.15. The percentage of eGFP positive cells was normalized to control *pre*-miR transfection (SHD) incubated in darkness where no influence on eGFP expression was expected for miR experiments. For SHRNA experiments, the percentage of eGFP positive cells was normalized to aptamer-modified *pre*-miR21 transfection (SHA) and incubated in darkness as no influence on eGFP expression due to the absence of miR21 binding sites in the 3'UTR sequence of the eGFP mRNA was expected in this case.

7.5.11 Optimization of light intensity and timing on light-dependent reporter protein abundance

1 × 10^5 HEK293PAL cells were seeded in black 24-well plates with clear bottom (VisionPlate, 4titude). Transfection was performed as indicated in section 7.5.3. Then, the plate was mounted onto the custom-made LPA device. For optimization of light doses, constant light (λ_{max}= 465 nm) at the indicated intensity was applied for 44 h. For optimization of light pulses, cells were incubated with 30 sec light pulses at 100 µW/cm^2 followed by time intervals of the indicated lengths where cells were incubated in darkness. Subsequent quantification of eGFP positive cells was performed using flow cytometry. For evaluation, single cells were identified as described in section 7.5.15. The threshold for eGFP positive cells (Fluorescein isothiocyanate area channel, FITC-A) was set to 5 % for cells that have been translated with SH5 and incubated in darkness.

7.5.12 Fluorescence microscopy

PAL protein switching and PAL particle microscopy. 5 × 10^4 Hek293 cells were seeded in black 24-well plates with clear bottom (µ-plate, ibidi). After 24 h, cells were transfected with 500 ng of the indicated plasmid as described in section 7.5.3 or left untransfected in case of HEK293PAL cells. For PAL protein

switching, cells were incubated only in darkness. For PAL particle microscopy, cells were incubated for further 48 h in darkness or in presence of blue light (465 nm, 106 µW/cm^2, 30 s pulses) and subjected to fluorescence microscopy 24 h and 48 h after transfection. Next, cells were analyzed by confocal laser scanning microscopy (LSM 710, Zen Black software, Zeiss) using a 20x/0.8 objective for PAL protein switching and a 40x/1.2 water immersion objective for PAL particle microscopy. PAL protein conformation was switched to the light state by applying 1 min light pulses at 458 nm (100 % laser power) followed by a 10 min recovery step in darkness which allows the protein to switch back to its initial conformation. Fluorescence of mCherry (excitation (ex)/emission (em): 543/578–696 nm) and PAL (ex/em: 405/488-529 nm) was monitored, respectively. Imaging was performed at 37 °C.

Table 7.5: LSM settings used for particle microscopy of protein constructs with different expression levels.

Construct type	Laser power at 543 nm [%]	Gain	Histogram
CMV plasmids	1	600	0 – 3000
UBC plasmids	2	700	0 – 4000
CMV_4E-BP1-mCherry-PAL plasmid	3	700	0 – 7500
HEK293PAL cell line	5	700	0 – 2000
MT plasmids/Untransfected cells	5	700	0 - 1000

Fluorescence microscopy of shRNA variants controlling eGFP expression in Hek293PAL cells. 5 × 10^4 cells were seeded in black 24-well plates with clear bottom (µ-plate, ibidi). After 24 h, cells were transfected with shRNA, AGO2 and eGFP expressing plasmids as described in section 7.5.3. Cells were incubated for 44 h in the presence of blue light (465 nm, 106 µW/cm^2, 30 s pulses) or in darkness. Then, the supernatant was replaced by cell medium containing 5 µg/mL Hoechst 33342. After a 10 min incubation at 37 °C, the supernatant was replaced with cell medium. Next, cells were analyzed by confocal laser scanning microscopy (LSM 710, Zen Black software, Zeiss) using a 20x/0.8 objective. Fluorescence of mCherry (excitation (ex)/emission (em): 543/578–696 nm), Hoechst 33342 (ex/em: 405/410-494) and eGFP (ex/em: 488/494-574 nm) was monitored, respectively. Imaging was performed at 37 °C.

Photomask experiment. 7.5 × 10^4 HEK293PAL cells were seeded in black 24-well plates with clear bottom (VisionPlate, 4titude). After 24 h, cells were transfected with *pre*-miR, AGO2 and eGFP expressing plasmids as described in section 7.5.3. Then, the plate was mounted onto the custom-made LPA device and irradiated with 10 µW/cm2 of constant light (λmax= 465 nm). After 48 h, cells were analyzed by confocal laser scanning microscopy (LSM 710) using a 10x/0.45 objective and image concatenation (10% overlay). Imaging was performed at 37 °C. eGFP fluorescence was visualized as green color and image histograms were adjusted to 5/10 before .tiff picture export (Zen Black software, Zeiss). Image brightness was adjusted to + 150 and image sizes were adjusted to 300 x 300 pixels using Adobe Photoshop CS5 software.

7.5.13 mCherry-PAL bleaching

1 × 10^5 Hek293 cells were seeded in two separate 24-well plates and incubated for 24 h. Transfection was performed as described in section 7.5.3. Cells were further incubated for 44 h in the presence of blue light (465 nm, 106 µW/cm^2, 30 s pulses) using the LED array or in darkness. Then, cell supernatant was aspirated, and cells were washed and resuspended PBS (25 °C). Subsequent quantification of mCherry or PAL positive cells was performed using flow cytometry. For evaluation, single cells were identified as described in section 7.5.15. The threshold for mCherry (Allophycocyanin area channel, APC-A) and PAL (Fluorescein isothiocyanate area channel, FITC-A) positive cells was set to 1 % for untransfected HEK293 cells incubated in darkness.

7.5.14 Cell cycle assay

1 × 10^5 HEK293PAL cells per well were seeded in two separate 24-well plates. 24 h after seeding, transfection was performed as indicated in section 7.5.3. Afterwards, cells were incubated for 29 h or 44 h in the presence of blue light (465 nm, 106 µW/cm^2, 30 s pulses) or in darkness. Then, cells were fixed in 70% ice-cold Methanol in PBS and incubated for at least 30 min at 4 °C followed by RNAse A (50 µg/mL) and propidium iodide (PI, 50 µg/mL) treatment for 30 min at 37 °C under mild agitation. Subsequent analysis of cell cycle distribution quantified by PI fluorescence per cell was performed using flow cytometry and the gating strategy described in section 7.5.15 was used for evaluation.

7.5.15 Flow cytometry analysis

Usually, at least 30.000 cells were analyzed from each sample. eGFP and propidium iodide were excited with a 488 nm laser and detected with a 530/30 or 585/42 filter set, respectively. mCherry was excited with a 633 nm laser and detected with a 660/20 filter set:

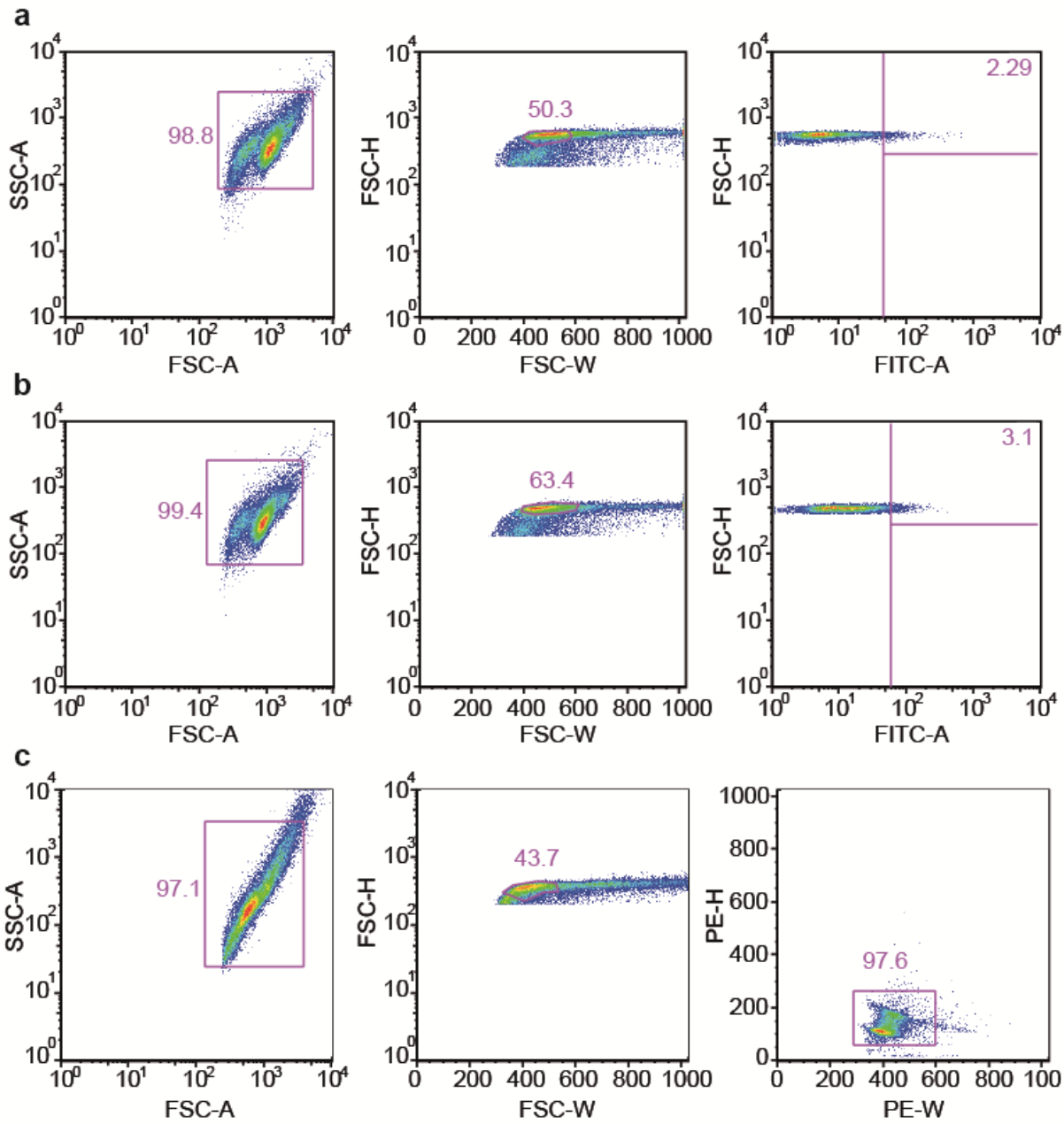

Figure 7.1: Gating strategies to identify eGFP positive cells for miR21 (a), shRNA experiments (b) and cell cycle phases (c). a-c, Cell debris was excluded using side scatter area (SSC-A) *vs*. forward scatter area (FSC-A). Singlet cells were detected using forward scatter height (FSC-H) *vs*. forward scatter width (FSC-W). For miR21 and shRNA experiments (**a**, **b**), eGFP positive cells were identified using FSC-H *vs*. Fluorescein isothiocyanate area (FITC-A). **a**, Cells transfected with SHA and incubated in darkness were set to 2.29 % eGFP positive cells and gating was applied to all other tested samples. **b**, Cells transfected with SH1 and incubated in darkness were set to 3.1 % eGFP positive cells and gating was applied to all other tested samples. **c**, Cell cycle debris and apoptotic cells were excluded using Phycoerythrin height (PE-H) *vs*. Phycoerythrin width (PE-W). Flow cytometry was performed using a BD FACS Canto II instrument (BD Bioscience). Data processing was performed using FlowJo (9.6.3) and GraphPad Prism (6.01).

7.6 Data treatment and blinding

7.6.1 Calculation of fold changes

Light-dependent fold changes were calculated by dividing values (crude values for luciferase assay, percentage of eGFP positive cells for eGFP assays) of samples incubated under light conditions through samples incubated in darkness (duplicates) to obtain four values for each independent experiment.

7.6.2 Blinded experiments

The identity of SHCB1, SHCB1m, SHCDK1, SHCDK1m and SH3 were blinded and double-blinded in one experiment, each. The identity of SHPLK2 and SHPLK2m was double-blinded in one experiment. For the blinded experiment, the identity of these PSilencer plasmids have been blinded before transfection by a second person. For the double-blinded experiment, another experimenter performed the assay that was blinded by a third person in a similar way. Identity of the samples was confirmed after data evaluation between the experimenter and the person who performed the blinding.

7.6.3 Statistics and reproducibility

Prism 6.01 (GraphPad Software, Inc.) was used to generate graphs and calculate *P* values. For all statistical analysis, no gaussian distributions were assumed due to limited sample sizes. Wilcoxon two-sided signed-rank test was used to compare equally treated cell samples incubated under the indicated light conditions. Therefore, a paired observation was assumed. Two-sided Mann-Whitney *U* test was used to compare light-dependent fold changes between differently treated groups (e.g. different time points). Therefore, an unpaired observation was assumed. Cohen's *d* effect size was used to calculate effect sizes in Western Blot analysis derived from equally treated cell samples incubated under the indicated light conditions. In this case, sample size was too small to test for significance. Datasets are presented as mean ± s.d., if not otherwise stated.

8. Materials

8.1 Buffers and solutions

Table 8.1: Buffers and solutions used within this dissertation.

Solution	Ingredient	Amount
0.5x TBE	Tris, pH 8.0	45 mM
	Boric acid	45 mM
	EDTA	1 mM
6x DNA loading buffer	Tris pH 8.0	10 mM
	Glycerol	60 %
	EDTA	60 mM
	Bromophenol Blue	
	Xylene cyanol	
2x RNA loading buffer	Formamide	47.5 %
	SDS	0.01 %
	EDTA	0.5 mM
	Bromophenol Blue	
	Xylene cyanol	
Pfu PCR buffer 10x	Tris/HCl pH 8.8	200 mM
	KCl	100 mM
	Triton X-100	1 %
	$(NH_4)_2SO_4$	100 mM
	BSA	1 mg/ml
TE-buffer 10x	Tris/HCl pH 7.4	0.1 M
	EDTA	10 mM
Urea PAGE gel	Urea	8.3 M
casting solution	Urea in 10x TE	8.3 M
	Rotiphorese sequencing gel concentrate	28 ml
	10 % APS	560 µl
	TEMED	28 µl
PAA loading buffer	Formamide	60 %
	SDS	5 %
	EDTA	0.25 mM
1x TBE	Tris, pH 8.0	90 mM
	Boric acid	90 mM
	EDTA	2 mM
$CaCl_2$-solution	$CaCl_2$	60 mM
	Glycerol	15 %
	PIPES pH 7.0	10 mM
Lysis buffer	Tris pH 7.8	50 mM

	NaCl	300 mM
	Imidazole	20 mM
	Glycerol	10 %
Elution buffer	Tris pH 7.8	50 mM
	NaCl	300 mM
	Imidazole	500 mM
	Glycerol	10 %
1x ICB buffer	Hepes pH 7.2 (at 37 °C)	12 mM
	KCl	135 mM
	NaCl	10 mM
	$MgCl_2$	1 mM
	Glycerol	10 %
6x Laemmli buffer	Tris pH 6.8	375 mM
	SDS	6 %
	Glycerol	48 %
	β-Mercaptoethanol	9 %
	Bromophenol blue	
10 % Separating gel (SDS-PAGE)	Acrylamide/Bis-solution (30 %)	2000 µl
	Water	2440 µl
	Tris pH 8.8, 1.5 M	1500 µl
	SDS, 10 %	60 µl
	TEMED	6 µl
	APS	60 µl
4 % Stacking gel (SDS-PAGE)	Acrylamide/Bis-solution (30 %)	540 µl
	Water	2440 µl
	Tris pH 6.8, 1 M	1000 µl
	SDS, 10 %	20 µl
	TEMED	5 µl
	APS	20 µl
10x SDS gel running buffer	Tris, pH 8.2	250 mM
	Glycine	2 M
	SDS	1 %
10x TBS	Tris pH 7.6	200 mM
	NaCl	150 mM
1x TBS-T	Tris pH 7.6	20 mM
	NaCl	15 mM
	Tween 20	0.05 %
Blocking buffer	TBS-T	1x
	BSA	5 %

10x Transfer buffer	Tris	25 mM
	Gylcine	20 %
	Urea	9 M

8.2 Reagents and Chemicals

Table 8.2: Reagents and Chemicals used within this dissertation.

Reagent or Chemical name	Supplier
Agar, bacteriology grade	AppliChem
Agarose	Bio-Budget technologies
Ammonium acetate	Sigma Aldrich
Ammonium peroxodisulfate (APS)	Roth
Ampicillin	Roth
BioScript reverse transcriptase	Bioline
Boric acid	AppliChem
Bovine serum albumin	Calbiochem
Bromophenol blue	Merck
Calf intestine alkaline phosphatase (CIAP)	Promega
CIAP 10x buffer	Promega
Cell culture media	Thermo Fisher Scientific
DMEM (high glucose, GutaMAX)	Thermo Fisher Scientific
dNTP-mix	Jena Bioscience
1,4-dithiothreitol (DTT)	Roth
Dimethylsulfoxide (DMSO)	Sigma Aldrich
DNAse I	Roche
EZ-Link Sulfo-NHS-Biotin	Thermo Fisher Scientific
EDTA	AppliChem
Ethanol	VWR
Ethidium bromide	Roth
Fetal calf serum (FCS)	Sigma-Aldrich
Flash Phusion polymerase	Thermo Fisher Scientific
Geneticin (G418)	Thermo Fisher Scientific
Gentamicin	Roth
Glycerol	Roth
Glycine	Roth
GoTaq DNA Polymerase	Promega
GoTaq 10x buffer	Promega
Heparin	VWR
Hepes	Roth
Hoechst 33342	Thermo Fisher Scientific

Hydrochlorid acid (HCl)	Roth
Imidazol	Roth
Isopropanol	Merck
Inorganic pyrophosphatase (iPP)	Sigma Aldrich
Kanamycin	Roth
LB powder	Sigma Aldrich
Lipofectamine 2000	Thermo Fisher Scientific
Magnesium chloride ($MgCl_2$)	Roth
MeOH	VWR
MISSION microRNA21 Mimic	Sigma Aldrich
Non-essential amino acids (MEM NEAA)	Thermo Fisher Scientific
NTPs	Jena Bioscience
Ni-NTA agarose	Macherey-Nagel
Pfu polymerase	Homemade
Phenol	Roth
Poly(A) Polymerase	NEB
Potassium chloride (KCl)	Roth
Propidium Iodide	Thermo Fisher Scientific
(-)-Riboflavin	Sigma Aldrich
Quant-iT RiboGreen RNA Reagent	Thermo Fisher Scientific
RIPA buffer	Thermo Fisher Scientific
RNAse A	Thermo Fisher Scientific
RNAsin	Promega
Rotiphorese sequencing gel concentrate	Roth
SimplyBlue SafeStain	Thermo Fisher Scientific
Sodium acetate (NaOAc)	VWR
Sodium chloride (NaCl)	Roth
Sodium pyruvate	Thermo Fisher Scientific
Streptavidin Coated High Capacity Plates	Thermo Fisher Scientific
T4 Polynucleotide kinase (PNK)	NEB
T4 PNK 10x buffer	NEB
T7 RNA polymerase	Homemade
TEMED	Roth
Tris	Roth
TRIzol	Thermo Fisher Scientific
Trypsin/EDTA (10x)	Thermo Fisher Scientific
Tween-20	Calbiochem
Urea	Roth
Xylenecyanole	Merck
Zeba Spin Desalting Columns, 7K MWCO	Thermo Fisher Scientific

8.3 Standards

Table 8.3: Standards used within this dissertation.

Name	Purpose	Manufacturer
Ultra Low Range DNA ladder	Detection of 10-300 bp DNA	Thermo Fisher Scientific
1 kb Plus DNA Ladder	Detection of 0.1-10 kbp DNA	NEB
Low Range RNA ladder	Detection of 0.1-1 kbp RNA	Thermo Fisher Scientific
Prestained Protein Ladder – Mid-range molecular weight	Detection of 10-180 kDa Proteins	abcam

8.4 Commercially available kits

Table 8.4: Commercially available kits used within this dissertation.

Name	Purpose	Manufacturer
NEBuilder	Assembly Cloning	New England Biolabs
NucleoSpin Gel and PCR Clean-up	PCR purification	Marcherey-Nagel
NucleoSpin Plasmid	Small scale plasmid preparation	Marcherey-Nagel
NucleoBond Xtra Midi	Medium scale plasmid preparation	Marcherey-Nagel
In-Fusion HD EcoDry Cloning	In-Fusion cloning	Takara Clontech
TOPO TA cloning	TOPO TA cloning	Life Technologies
Ready-To-Glow Secreted Luciferase	Luciferase reporter assay	Takara Clontech
Pierce BCA Protein Assay	Protein quantification	Thermo Fisher Scientific
mCherry Quantification	mCherry quantification	BioVision
VenorGeM Classic	Mycoplasma detection	Minerva biolabs

8.5 Synthetic Oligonucleotides

8.5.1 DNA sequence of 4E-BP1-mCherry-PAL

In the following, the DNA sequence of 4E-BP1-mCherry-PAL is depicted. Green: 4E-BP1 coding region, red: mCherry coding region, blue: PAL coding region, grey: glycine-serine linker, white: spacer sequences. 4E-BP1 was cloned into *NheI* restriction site and PAL was cloned between the *EcoRI* and *BamHI* restriction sites:

5’ATGTCCGGGGGCAGCAGCTGCAGCCAGACTCCCAGCCGGGCTATCCCCACTCGCCGCGTAGC
CCTCGGCGACGGCGTGCAGCTCCCGCCCGGGGACTACAGCACCGCGCCCGGCGGCACGCTCT
TCAGCACCGCGCCGGGAGGAACCAGAATCATCTATGACCGGAAATTCCTGATGGAGTGTCGGAA
CGCGCCTGTGGCCAAAGCACCCCCAAAGGACCTGCCAACCATTCCAGGGGTCACTAGCCCTACC
AGCGATGAGCCTCCCATGCAGGCCAGCCAGAGCCATCTGCACAGCAGCCCGGAAGATAAGCGG
GCAGGTGGTGAAGAGTCACAGTTTGAGATGGACATTGGTGGCGGAGGCTCGCTAGCGCTACCG
GTCGCCACCATGGTGAGCAAGGGCGAGGAGGATAACATGGCCATCATCAAGGAGTTCATGCGCT

TCAAGGTGCACATGGAGGGCTCCGTGAACGGCCACGAGTTCGAGATCGAGGGCGAGGGCGAGG
GCCGCCCCTACGAGGGCACCCAGACCGCCAAGCTGAAGGTGACCAAGGGTGGCCCCCTGCCCT
TCGCCTGGGACATCCTGTCCCCTCAGTTCATGTACGGCTCCAAGGCCTACGTGAAGCACCCCGC
CGACATCCCCGACTACTTGAAGCTGTCCTTCCCCGAGGGCTTCAAGTGGGAGCGCGTGATGAAC
TTCGAGGACGGCGGCGTGGTGACCGTGACCCAGGACTCCTCCCTGCAGGACGGCGAGTTCATC
TACAAGGTGAAGCTGCGCGGCACCAACTTCCCCTCCGACGGCCCCGTAATGCAGAAGAAGACCA
TGGGCTGGGAGGCCTCCTCCGAGCGGATGTACCCCGAGGACGGCGCCCTGAAGGGCGAGATC
AAGCAGAGGCTGAAGCTGAAGGACGGCGGCCACTACGACGCTGAGGTCAAGACCACCTACAAG
GCCAAGAAGCCCGTGCAGCTGCCCGGCGCCTACAACGTCAACATCAAGTTGGACATCACCTCCC
ACAACGAGGACTACACCATCGTGGAACAGTACGAACGCGCCGAGGGCCGCCACTCCACCGGCG
GCATGGACGAGCTGTACAAGTCCGGACTCAGATCTCGAGCTCAAGCTTCGAATTCTATGAAGGTG
AACCGGCCCGCGGAGCGCGCCTCGTTCGGTTCGTTCGTGCTCGACGCCGGGTCCGCCCGGTTC
GTCGGCTCCGACGAGTTGGCGCTGGTGCTTGGCTTCGCCCCGGGTGATGTGGTGCTGACGCCG
GCCGTGGTGCTGGCCCACCTGCATCCGGACGATCGGCTGGAATGGCAGGCCGGTCTGCAGCGA
TGCCTGGCCACCGGGCGACCCGTGGTGGTCAACCACCTGCTGCTGACCGCGGAGGCCGAGCC
GCGCCCCGCGATGACGACGCTGACCGCGCTGACCGAGCAGGACCGGGTGCGAGCGGTCACCG
GTGTGATCACCGACCTGAGCGACCGCGTCCGGCGGGCGACCGAGGCCGAGATCCGCCAGGCG
GTCCGGGCGGCGGCCGCGACCCGCAGCGAGATCGACCAGGCCAAGGGCATCGTGATGGCCGC
CTTCGACGTCGACGCCGACCAGGCGTTTGCCCTGCTCAAGTGGCACTCCTCGCAGAGCAACCGC
AAGCTGCGGGACCTGGCCACCGGGATGATCGAGGGCTTGGCAGCGGCCAACTCCGCGTTGCCA
CTGCGGCGGCGGCTGTCCACCGTCTTCACCGACATGGGTTGCCCGGCGCCCTCCACCAAGGGC
TGGACCGTGCCGGTCACCGACATCGGCCTGCCGCCCACGTCGGGGCTGATCCCGACCGCGTTG
CTCCCGGGCATCCTGACCCGGGCCGCGCACGACGCATCGGTTGCCATCACCGTCGCCGACGTC
ACCGCACCGGACCAGCCGCTGGTCTACGCCAACCCGGCCTTCGAACGCCTGACCGGTTACGCC
GCGGCCGAGGTGCTGGGCCGCAACTGCCGCTTCCTGCAGGCCGAGTCCGGCGATCCGCACGA
GCGGTCGGCGATTCGCTCGGCGATCGCCAACGGCGACGCGGTCACCACCCTGATCCGCAACTT
CCGCCAGGACGGGCACGCCTTCTGGAACGAGTTCCACCTGTCCCCCGTGCGCAACGGGGCCGG
CCGGGTCACCCATTACATCGGCTACCAGCTCGACGTCACCGAGCGGGTCGAGCGCGATCAGCA
GTTGGAGCAGCTGGCGTCGTAG3’

8.5.2 DNA sequence of aptamer 53.19-modified *Metridia* luciferase 5’UTR

In the following, parts of the Mot2 plasmid DNA sequence derived from the pMetLuc2-Control plasmid are shown. Shown is the 5’UTR of the *Metridia* luciferase gene with the aptamer 53.19 insertion (blue). Aptamer 53.19 was cloned into the single *AgeI* restriction site (grey) resulting in a second *AgeI* restriction scar. Five additional nucleotides (green) have been implemented up- and downstream to the aptamer to increase the stability of the stem-loop (-30.1 kcal/mol), which are not present on the unmodified plasmid (Luc). The underlined bold nucleotides have been mutated to the corresponding Watson-Crick base pairing nucleotides to yield the aptamer control plasmid (M4). Red nucleotides: Start codon:

5’TCAGATCCTCAGATCCGCTAGCGCTACCGGACTCAGATCCACCGGTGAGTGCGGTAC**AG**C**AG**C
GATGCCGCACTCACCGGTCGCCACC**ATG**3’

8.5.3 DNA sequences of miR21 binding sites

In the following, part of the 3’UTR of reporter genes is shown, indicating how miR21 binding sites where incorporated into the plasmid sequence. Four binding sites (blue) complementary to miR21-5p were cloned into the NotI restriction site (grey). Four binding sites (green) complementary to miR21-3p were cloned into the MfeI restriction site (grey) of pMetLuc2-Control or pEGFP-N1, respectively:

5’GCGGCCGCTCAACATCAGTCTGATAAGCTACTAATCAACATCAGTCTGATAAGCTACTAATCAA
CATCAGTCTGATAAGCTACTAATCAACATCAGTCTGATAAGCTAGCGGCCGCGACTCTAGATCAT
AATCAGCCATACCACATTTGTAGAGGTTTTACTTGCTTTAAAAAACCTCCCACACCTCCCCCTGAA
CCTGAAACATAAAATGAATGCAATTGACAGCCCATCGACTGGTGTTGCTAAACAGCCCATCGACT
GGTGTTGCTAAACAGCCCATCGACTGGTGTTGCTAAACAGCCCATCGACTGGTGTTGCAATTG3’

8.5.4 Regulatory RNA sequences

Table 8.5: List of *pre*-miR21 and shRNAs used within this dissertation. Blue: Aptamer sequence, red: Aptamer Mutations, orange: Hinge Region nucleotides, brown (bold): control loop sequences.

Name	RNA Sequence (5’ - 3’)
04	GGGAGGACGAUGCGGGGGCAGCAUGUGUCGUUCCUUCGCGUCCGGCGGGUUGAAGCAGACGACUCGCUGAGGAUCC GAGA
46mu	GGGAGGACGAUGCGGUAGGGUCCUGCCUGUUGCGAUCCUGGGCAUGCAAAUUCCAGACGACUCGCUGAGGAUCCGA GA
53	GGGAGGACGAUGCGGCCGUACAGCAGCGAUGCGGGUCGCGUGUCCACCCCGGCUCAGACGACUCGCUGAGGAUCC GAGA
SHA	GUAGCUUAUCAGACUGAUGUUGACGGUACAGCAGCGAUGCCGCAACACCAGUCGAUGGGCUGUUU
SHB	GAAGGCAAGCUGACCCUGAAGUUCGGUACAGCAGCGAUGCCGAAGGCAAGCUGACCCUGAAGUUU
SHC	GUAGCUUAUCAGACUGAUGUUGACGGUACAGCACCGAUGCCGCAACACCAGUCGAUGGGCUGUUU
SHC_M4	GUAGCUUAUCAGACUGAUGUUGACGGUACUCCUCCGAUGCCGCAACACCAGUCGAUGGGCUGUUU
SHD	GAAGGCAAGCUGACCCUGAAGUUCGGUACAGCACCGAUGCCGAAGGCAAGCUGACCCUGAAGUUU
SHA_V1	GAUAGCUUAUCAGACUGAUGUUGACGGUACAGCAGCGAUGCCGCAACACCAGUCGAUGGGCUGUCUU
SHA_V2	GAUAGCUUAUCAGACUGAUGUUGACGGUACAGCAGCGAUGCCGCAACACCAGUCGAUGGGCUGUCUUGGCCGGCAUG GUCCCAGCCUCCUCGCUGGCGCCGGCUGGGCAACAUGCUUCGGCAUGGCGAAUGGGACUU
SHA_V3	GUAGCUUAUCAGACUGAUGUUGAGUACAGCAGCGAUGCUCAACACCAGUCGAUGGGCUGUUU
SHA_V4	GUAGCUUAUCAGACUGAUGUUGACGGUACAGCAGCGAUGCCGUCAACAUCAGUCUGAUAAGCUAUU
SHI	GUAGCUUAUCAGACUGAUGUUGAGGUUGAAGCAGACGACCCAACACCAGUCGAUGGGCUGUUU
SHI_V1	GUAGCUUAUCAGACUGAUGUUGAGCGGGUUGAAGCAGACGACUCGCCAACACCAGUCGAUGGGCUGUUU
SHI_V2	GUAGCUUAUCAGACUGAUGUUGACGGCGGGUUGAAGCAGACGACUCGCUGCAACACCAGUCGAUGGGCUGUUU
SHJ	GUAGCUUAUCAGACUGAUGUUGAGGUUGAUGCAGACGACCCAACACCAGUCGAUGGGCUGUUU
SHK	GAAGGCAAGCUGACCCUGAAGUUGGUUGAAGCAGACGACCAAGGCAAGCUGACCCUGAAGUUU
SH1	GCAAGCUGACCCUGAAGUUCA**UUCAAGAGA**UGAACUUCAGGGUCAGCUUGCUU
SH2	GCAAGCUGACCCUGAAGUUCAUCGGUACAGCAGCGAUGCCGAUGAACUUCAGGGUCAGCUUGCUU
SH3	GCACAAGCUGGAGUACAACUACGGUACAGCAGCGAUGCCGUAGUUGUACUCCAGCUUGUGCUU
SH4	GCUGGAGUACAACUACAACAGCGGUACAGCAGCGAUGCCGCUGUUGUAGUUGUACUCCAGCUU
SH5	GCAAGCUGACCCUGAAGUUCAUACGGUACAGCAGCGAUGCCGAUGAACUUCAGGGUCAGCUUGCUU
SH6	GCAAGCUGACCCUGAAGUUCAUCGGUACAGCAGCGAUGCCCAUGAACUUCAGGGUCAGCUUGCUU
SH7	GCAAGCUGACCCUGAAGUUCAUCCGGUACAGCAGCGAUGCCCCAUGAACUUCAGGGUCAGCUUGCUU

SH8	GCAAGCUGACCCUGAAGUUCAUACGGUACAGCAGCGAUGCCGAAUGAACUUCAGGGUCAGCUUGCUU
SH9	GCAAGCUGACCCUGAAGUUCAUCCGGUACAGGAGCGAUGCCCCAUGAACUUCAGGGUCAGCUUGCUU
SH10	GCAAGCUGACCCUGAAGUUCAUCCGGUACAGCAGGGAUGCCCCAUGAACUUCAGGGUCAGCUUGCUU
SH11	GCAAGCUGACCCUGAAGUUCAUCCGGUACAGGAGGGAUGCCCCAUGAACUUCAGGGUCAGCUUGCUU
SH12	GCAAGCUGACCCUGAAGUUCAUUCGGUACAGCAGCGAUGCCGAUGAACUUCAGGGUCAGCUUGCUU
SH13	GCAAGCUGACCCUGAAGUUCAUGCGGUACAGCAGCGAUGCCGAUGAACUUCAGGGUCAGCUUGCUU
SH14	GCAAGCUGACCCUGAAGUUCAUCCGGUACAGCAGCGAUGCCGAUGAACUUCAGGGUCAGCUUGCUU
SH15	GCAAGCUGACCCUGAAGUUCAUCGGUACAGCAGCGAUGCCGAAUGAACUUCAGGGUCAGCUUGCUU
SH16	GCAAGCUGACCCUGAAGUUCAUCGGUACAGCAGCGAUGCCGUAUGAACUUCAGGGUCAGCUUGCUU
SH17	GCAAGCUGACCCUGAAGUUCAUCGGUACAGCAGCGAUGCCGGAUGAACUUCAGGGUCAGCUUGCUU
SH18	GCAAGCUGACCCUGAAGUUCAUCGGUACAGCAGCGAUGCCGCAUGAACUUCAGGGUCAGCUUGCUU
SH19	GCACAAGCUGGAGUACAACUAACGGUACAGCAGCGAUGCCGUAGUUGUACUCCAGCUUGUGCUU
SH20	GCACAAGCUGGAGUACAACUAUCGGUACAGCAGCGAUGCCGUAGUUGUACUCCAGCUUGUGCUU
SH21	GCACAAGCUGGAGUACAACUACGGUACAGCAGCGAUGCCGAUAGUUGUACUCCAGCUUGUGCUU
SH22	GCACAAGCUGGAGUACAACUACGGUACAGCAGCGAUGCCGUUAGUUGUACUCCAGCUUGUGCUU
SH23	GCACAAGCUGGAGUACAACUACGGUACAGCAGCGAUGCCGGUAGUUGUACUCCAGCUUGUGCUU
SH24	GCACAAGCUGGAGUACAACUACGGUACAGCACCGAUGCCGUAGUUGUACUCCAGCUUGUGCUU
SH25	GCAAGCUGACCCUGAAGUUCAUAGAGCGGUACAGCAGCGAUGCCGAAUGAACUUCAGGGUCAGCUUGCUU
SH26	GCAAGCUGACCCUGAAGUUCAUAGAAGCGGUACAGCAGCGAUGCCGAGAUGAACUUCAGGGUCAGCUUGCUU
60_1	GCAAGCUGACCCUGAAGUUCAUAGAGGGUUCAGCAGCGAGCCAAUGAACUUCAGGGUCAGCUUGCUU
60_2	GCAAGCUGACCCUGAAGUUCAUUGGUUCAGCAGCGAGCCAUGAACUUCAGGGUCAGCUUGCUU
60_3	GCAAGCUGACCCUGAAGUUCAUUGGGUUCAGCAGCGAGCCCAUGAACUUCAGGGUCAGCUUGCUU
SHCBi	GACACCAACUCUACAAUAUUAGUUA**AUAUUCA**UAGCUAAUGUUGUAGAGUUGGUGUCUU
SHCBii	GACUGACAACACUUAUACUAAGGUUA**AUAUUCA**UAGCCUUAGUAUAAGUGUUGUCAGUU
SHCDKi	GUGGAAUCUUUACAGGACUAU**CUCGAG**AUAGUCCUGUAAAGAUUCCACUU
SHCDKii	GCUGUACUUCGUCUUCUAAUU**CUCGAG**AAUUAGAAGACGAAGUACAGCUU
SHCB1	GACACCAACUCUACAAUAUUAGUUAACGGUACAGCAGCGAUGCCGUAGCUAAUGUUGUAGAGUUGGUGUCUU
SHCB1m	GACACCAACUCUACAAUAUUAGUUAACGGUACAGCACCGAUGCCGUAGCUAAUGUUGUAGAGUUGGUGUCUU
SHCB2	GACACCAACUCUACAAUAUUAGUUAUCGGUACAGCAGCGAUGCCGUAGCUAAUGUUGUAGAGUUGGUGUCUU
SHCB3	GACACCAACUCUACAAUAUUAGUUACGGUACAGCAGCGAUGCCGUUAGCUAAUGUUGUAGAGUUGGUGUCUU
SHCDK1	GUGGAAUCUUUACAGGACUAUCACGGUACAGCAGCGAUGCCGGAUAGUCCUGUAAAGAUUCCACUU
SHCDK1m	GUGGAAUCUUUACAGGACUAUCACGGUACAGCACCGAUGCCGGAUAGUCCUGUAAAGAUUCCACUU
SHPLK1	GUUCUUUACUUCUGGCUAUAUACGGUACAGCAGCGAUGCCGGAUAUAGCCACAAGUAAAGAACUU
SHPLK1m	GUUCUUUACUUCUGGCUAUAUACGGUACAGCAGCGAUGCCGGAUAUAGCCACAAGUAAAGAACUU
SHPLK2	GUUCUUUACUUCUGGCUAUAUUCGGUACAGCAGCGAUGCCGGAUAUAGCCACAAGUAAAGAACUU
SHPLK2m	GUUCUUUACUUCUGGCUAUAUUCGGUACAGCAGCGAUGCCGGAUAUAGCCACAAGUAAAGAACUU
SHPLK3	GUUCUUUACUUCUGGCUAUAUACGGUACAGCAGCGAUGCCGGAAUAUAGCCACAAGUAAAGAACUU
SHPLK4	GUUCUUUACUUCUGGCUAUAUACGGUACAGCAGCGAUGCCGGUAUAUAGCCACAAGUAAAGAACUU
SHPLK5	GUUCUUUACUUCUGGCUAUAUAUCGGUACAGCAGCGAUGCCGGAUAUAGCCACAAGUAAAGAACUU
SHPLK6	GUUCUUUACUUCUGGCUAUAUCGGUACAGCAGCGAUGCCGGAAUAUAGCCACAAGUAAAGAACUU
SHPLK7	GUUCUUUACUUCUGGCUAUAUCGGUACAGCAGCGAUGCCGGUAUAUAGCCACAAGUAAAGAACUU

8.6 Plasmid backbones

Table 8.6: Plasmid backbones used within this dissertation.

Reagent name	Purpose	Supplier
pmCherry-C1	Expression of mCherry-(PAL) fusion proteins	Takara Clontech
pMetLuc-2 Control	Expression of *Metridia* Luciferase reporter protein	Takara Clontech
pEGFP-N1	Expression of eGFP reporter protein	Takara Clontech
pSilencer 2.0-U6	Expression of pre-miR and shRNA variants	Ambion
pET28c-6xHis-PAL	*In vitro* overexpression of PAL protein	Novagen
pIRESneo-FLAG/HA Ago2 corrected	Expression of AGO2 protein	Thomas Tuschl (*via* Addgene)

pRRL pMT ASC-EGFP Puro	PCR template for cloning of the Metallothionein promoter	Florian I. Schmidt
pRRLUbCp ASC-EGFP	PCR template for cloning of the Ubiquitin promoter	Florian I. Schmidt

8.7 Antibodies

Table 8.7: Antibodies used within this dissertation.

Antigen	Clone/Host species	Type	Supplier
GAPDH	Sc-47724/mouse	Primary AB	Santa Cruz Biotechnology
Histone H3	D1H2/rabbit	Primary AB	Cell Signaling
Phospho-Histone H3 (Ser10)	6G3/mouse	Primary AB	Cell Signaling
	POH1/mouse	Primary AB	Cell Signaling
Cdc2	AF6000/goat	Primary AB	R&D Systems
CCNB1	EPR19534/rabbit	Primary AB	Abcam
PLK1	926-32210/goat	800CW	Li-cor
Anti-mouse	926-32214/donkey	800CW	Li-cor
Anti-goat	926-32211/goat	800CW	Li-cor
Anti-rabbit			

8.8 Bacterial strains

Table 8.8: *E. coli* strains used within this dissertation.

Name	Strain	Purpose	Supplier
Stellar	HST08	Plasmid cloning	Takara Clontech
NEB Stable		Plasmid cloning	NEB
One Shot TOP10	DH10B	Plasmid cloning	Thermo Fisher Scientific
SCS110	JM110	Unmethylated plasmid preparation	Stratagene
Arctic express	BL21 (DE3)	Protein overexpression	Agilent

8.9 Human cell lines

All cell lines were purchased from CLS cell lines service. Hek293 cells expressing mCherry-PAL were additionally cultured in presence of 400 µg/ml Geneticin (G418).

Table 8.9: Human cell lines used within this dissertation.

Cell line name	Cultivation medium
Hek293 HEK293PAL HeLa	DMEM supplemented with 1 % MEM Non-Essential Amino Acids, 1 % Sodium Pyruvate and 10 % Fetal Calf Serum

8.10 Equipment

Table 8.10: Equipment used within this dissertation.

Equipment	Manufacturer
Agarose gel camera, UV-transilluminator	Bio-Rad Laboratories
Agarose running chamber	In house construction
Analytical balance	Sartorius
Autoclave	Systec
Bacterial incubator shaker	Innova
BioMate 3 photometer	Thermo Spectronic
Cell culture media	Thermo Fisher Scientific
Centrifuges	Eppendorf, Sigma
Culture flasks	Sarstedt
Culture plates	Sarstedt, ibidi
D-Tube Dialyzer Maxi, MWCO 6-8 kDa	Merck
Disposable cuvettes	Roth
DPBS, pH 7.4	Thermo Fisher Scientific
Electrophoresis power supply	Consort
EnSpire multimode reader	PerkinElmer
Reaction tube racks	Roth
Erlenmeyer flask	Schott
Flow Cytometer FACSCanto II	BD Biosciences
Glass plates for PAGE	Baack
Head-top-tumbler	Heidolph
Hood (bacteria culture)	Antares
Hood (cell culture)	Hera
Incubator (bacteria)	VWR
Incubator (cell culture)	Hera
LED array	In house construction
Light plate apparatus (LPA)	Dr. Hanns-Martin Schmidt
LUMITRAC 200 plates (white)	Greiner
Plates for LPA	4titude
Magnetic stirrer	IKA
Micro Bio-Spin columns	Bio-Rad
Microwave	Bosch
Multichannel pipette	Eppendorf
NanoQuant infinite M200	Tecan
NanoQuant Plate	Tecan
Nitrocellulose membrane	GE Healthcare
Odyssey blot imager	LI-COR
PAGE running chamber	In house construction

Parafilm	Faust
PCR stripes	Sarstedt
PCR Thermocycler	Applied Biosystems, Eppendorf
Petri dishes (94 x 16 mm)	Labomedic
pH meter	Inolab
Pipette tips	Sarstedt
Pipetteboy Accu-Jet Pro	Brand
Pipettes	Eppendorf
Poly-Prep Chromatography Columns	BioRad
Reaction tubes 0.2 ml, 0.5 ml, 1.5 ml, 2 ml	Sarstedt
Refrigerators and Freezer 4°C, -20°C, -80°C	AEG, New Brunswick, Liebherr
Scalpel blades	Labormedic
Serological pipettes	Sarstedt
Sonification device Sonopuls HD70	Bandelin
Spectrophotometer Biomate 3	Thermo Fisher Scientific
Speedvac (Concentrator 5301)	Eppendorf
Sterile filters (0.2 µm)	Merck Millipore
Tecan Ultra	Tecan
Thermomixer 1.5 ml, 2 ml	Eppendorf, HLC
Tube rotator, REAX 2	Heidolph
Vortex	Neolab
Water bath	GFL, Julabo
Water purification system	Thermo Fisher Scientific

8.11 Software

Table 8.11: Software used within this dissertation.

Software	Developer
Adobe Illustrator CS5	Adobe Inc.
ChemDraw Prime 16.0	PerkinElmer Inc.
EndNote X7	Thomson Reuters
GraphPad Prism 6.01	Graphpad Software Inc.
Fiji (ImageJ)	Open Source
FlowJo 9.6.3	BD Biosciences
RNAComposer	Institute of Computing Science, Poznan University
RNAfold WebServer	Institute for Theoretical Chemistry, University of Vienna
SnapGene 3.2.1	GSL Biotech LLC
Microsoft Office 365	Microsoft
Zen 2012 (blue and black edition)	Zeiss

9 Bibliography

1. Grewe, B.F., et al., *High-speed in vivo calcium imaging reveals neuronal network activity with near-millisecond precision.* Nature methods, 2010. **7**(5): p. 399.
2. Willig, K.I., et al., *STED microscopy reveals that synaptotagmin remains clustered after synaptic vesicle exocytosis.* Nature, 2006. **440**(7086): p. 935-939.
3. *Method of the Year 2010.* Nature Methods, 2011. **8**(1): p. 1-1.
4. Yang, Y., et al., *In vitro and in vivo uncaging and bioluminescence imaging by using photocaged upconversion nanoparticles.* Angewandte Chemie, 2012. **124**(13): p. 3179-3183.
5. Kand, D., et al., *Water-soluble BODIPY photocages with tunable cellular localization.* Journal of the American Chemical Society, 2020. **142**(11): p. 4970-4974.
6. Heckel, A., et al., *An anticoagulant with light-triggered antidote activity.* Angew Chem Int Ed Engl, 2006. **45**(40): p. 6748-50.
7. McMillan, T., et al., *Cellular effects of long wavelength UV light (UVA) in mammalian cells.* Journal of Pharmacy and Pharmacology, 2008. **60**(8): p. 969-976.
8. Miesenböck, G., *Optogenetic control of cells and circuits.* Annual review of cell and developmental biology, 2011. **27**: p. 731-758.
9. Adamantidis, A.R., et al., *Neural substrates of awakening probed with optogenetic control of hypocretin neurons.* Nature, 2007. **450**(7168): p. 420-4.
10. Deisseroth, K., *Optogenetics.* Nature methods, 2011. **8**(1): p. 26-29.
11. Rost, B.R., et al., *Optogenetic tools for subcellular applications in neuroscience.* Neuron, 2017. **96**(3): p. 572-603.
12. Aravanis, A.M., et al., *An optical neural interface: in vivo control of rodent motor cortex with integrated fiberoptic and optogenetic technology.* J Neural Eng, 2007. **4**(3): p. S143-56.
13. Nagel, G., et al., *Channelrhodopsin-2, a directly light-gated cation-selective membrane channel.* Proceedings of the National Academy of Sciences, 2003. **100**(24): p. 13940-13945.
14. DeBerry, J.J., et al., *Differential regulation of bladder pain and voiding function by sensory afferent populations revealed by selective optogenetic activation.* Frontiers in integrative neuroscience, 2018. **12**: p. 5.
15. Natasha, G., et al., *Channelrhodopsins: visual regeneration and neural activation by a light switch.* New biotechnology, 2013. **30**(5): p. 461-474.
16. Pan, Z.-H., et al., *ChR2 mutants at L132 and T159 with improved operational light sensitivity for vision restoration.* PLoS One, 2014. **9**(6).
17. Schultheis, C., et al., *Optogenetic long-term manipulation of behavior and animal development.* PloS one, 2011. **6**(4).
18. Shirai, F. and A. Hayashi-Takagi, *Optogenetics: Applications in psychiatric research.* Psychiatry and clinical neurosciences, 2017. **71**(6): p. 363-372.
19. Schild, L.C. and D.A. Glauser, *Dual color neural activation and behavior control with chrimson and CoChR in Caenorhabditis elegans.* Genetics, 2015. **200**(4): p. 1029-1034.

20. Lin, J.Y., et al., *ReaChR: a red-shifted variant of channelrhodopsin enables deep transcranial optogenetic excitation.* Nature neuroscience, 2013. **16**(10): p. 1499.
21. Sengupta, A., et al., *Red-shifted channelrhodopsin stimulation restores light responses in blind mice, macaque retina, and human retina.* EMBO molecular medicine, 2016. **8**(11): p. 1248-1264.
22. Govorunova, E.G., et al., *Natural light-gated anion channels: A family of microbial rhodopsins for advanced optogenetics.* Science, 2015. **349**(6248): p. 647-650.
23. Mauss, A.S., C. Busch, and A. Borst, *Optogenetic neuronal silencing in Drosophila during visual processing.* Scientific reports, 2017. **7**(1): p. 1-12.
24. Arrenberg, A.B., F. Del Bene, and H. Baier, *Optical control of zebrafish behavior with halorhodopsin.* Proceedings of the National Academy of Sciences, 2009. **106**(42): p. 17968-17973.
25. Mohamed, G.A., et al., *Optical inhibition of larval zebrafish behaviour with anion channelrhodopsins.* BMC biology, 2017. **15**(1): p. 103.
26. Chow, B.Y., et al., *High-performance genetically targetable optical neural silencing by light-driven proton pumps.* Nature, 2010. **463**(7277): p. 98-102.
27. Rost, B.R., et al., *Optogenetic acidification of synaptic vesicles and lysosomes.* Nature neuroscience, 2015. **18**(12): p. 1845.
28. Kralj, J.M., et al., *Optical recording of action potentials in mammalian neurons using a microbial rhodopsin.* Nature methods, 2012. **9**(1): p. 90.
29. Adam, Y., et al., *Voltage imaging and optogenetics reveal behaviour-dependent changes in hippocampal dynamics.* Nature, 2019. **569**(7756): p. 413-417.
30. Fan, L.Z., et al., *All-optical electrophysiology reveals the role of lateral inhibition in sensory processing in cortical layer 1.* Cell, 2020. **180**(3): p. 521-535. e18.
31. Alberio, L., et al., *A light-gated potassium channel for sustained neuronal inhibition.* Nature methods, 2018. **15**(11): p. 969-976.
32. Cosentino, C., et al., *Engineering of a light-gated potassium channel.* Science, 2015. **348**(6235): p. 707-710.
33. Airan, R.D., et al., *Temporally precise in vivo control of intracellular signalling.* Nature, 2009. **458**(7241): p. 1025-1029.
34. Makowka, P., et al., *Optogenetic stimulation of G s-signaling in the heart with high spatio-temporal precision.* Nature communications, 2019. **10**(1): p. 1-9.
35. Spangler, S.M. and M.R. Bruchas, *Optogenetic approaches for dissecting neuromodulation and GPCR signaling in neural circuits.* Current opinion in pharmacology, 2017. **32**: p. 56-70.
36. Siuda, E.R., et al., *Optodynamic simulation of β-adrenergic receptor signalling.* Nature communications, 2015. **6**(1): p. 1-13.
37. Beiert, T., T. Bruegmann, and P. Sasse, *Optogenetic activation of Gq signalling modulates pacemaker activity of cardiomyocytes.* Cardiovascular research, 2014. **102**(3): p. 507-516.
38. Pashaie, R., et al., *Optogenetic brain interfaces.* IEEE reviews in biomedical engineering, 2013. **7**: p. 3-30.

39. Tsukamoto, H. and Y. Furutani, *Optogenetic Modulation of Ion Channels by Photoreceptive Proteins*, in *Optogenetics*. 2021, Springer. p. 73-88.
40. Klapper, S.D., et al., *Biophysical properties of optogenetic tools and their application for vision restoration approaches.* Frontiers in systems neuroscience, 2016. **10**: p. 74.
41. Hansen, J.N., et al., *Nanobody-directed targeting of optogenetic tools to study signaling in the primary cilium.* Elife, 2020. **9**: p. e57907.
42. Jansen, V., et al., *Controlling fertilization and cAMP signaling in sperm by optogenetics.* Elife, 2015. **4**: p. e05161.
43. Stierl, M., et al., *Light modulation of cellular cAMP by a small bacterial photoactivated adenylyl cyclase, bPAC, of the soil bacterium Beggiatoa.* Journal of Biological Chemistry, 2011. **286**(2): p. 1181-1188.
44. Ruggiero, E., et al., *Upconverting nanoparticles for the near infrared photoactivation of transition metal complexes: new opportunities and challenges in medicinal inorganic photochemistry.* Dalton Transactions, 2016. **45**(33): p. 13012-13020.
45. Ash, C., et al., *Effect of wavelength and beam width on penetration in light-tissue interaction using computational methods.* Lasers in medical science, 2017. **32**(8): p. 1909-1918.
46. Ryu, M.-H. and M. Gomelsky, *Near-infrared light responsive synthetic c-di-GMP module for optogenetic applications.* ACS synthetic biology, 2014. **3**(11): p. 802-810.
47. Gasser, C., et al., *Engineering of a red-light–activated human cAMP/cGMP-specific phosphodiesterase.* Proceedings of the National Academy of Sciences, 2014. **111**(24): p. 8803-8808.
48. Avci, P., et al. *Low-level laser (light) therapy (LLLT) in skin: stimulating, healing, restoring*. in *Seminars in cutaneous medicine and surgery*. 2013. NIH Public Access.
49. Wu, Y.I., et al., *A genetically encoded photoactivatable Rac controls the motility of living cells.* Nature, 2009. **461**(7260): p. 104-108.
50. Niopek, D., et al., *Engineering light-inducible nuclear localization signals for precise spatiotemporal control of protein dynamics in living cells.* Nature communications, 2014. **5**: p. 4404.
51. Renicke, C., et al., *A LOV2 domain-based optogenetic tool to control protein degradation and cellular function.* Chem Biol, 2013. **20**(4): p. 619-26.
52. Wu, Y.I., et al., *A genetically encoded photoactivatable Rac controls the motility of living cells.* Nature, 2009. **461**(7260): p. 104-8.
53. Berlew, E.E., et al., *Optogenetic Rac1 engineered from membrane lipid-binding RGS-LOV for inducible lamellipodia formation.* Photochemical & Photobiological Sciences, 2020. **19**(3): p. 353-361.
54. Valon, L., et al., *Optogenetic control of cellular forces and mechanotransduction.* Nature communications, 2017. **8**(1): p. 1-10.
55. Niopek, D., et al., *Optogenetic control of nuclear protein export.* Nature communications, 2016. **7**(1): p. 1-9.
56. Krueger, D., et al., *Principles and applications of optogenetics in developmental biology.* Development, 2019. **146**(20).

57. Strickland, D., et al., *TULIPs: tunable, light-controlled interacting protein tags for cell biology.* Nat Methods, 2012. **9**(4): p. 379-84.
58. Ye, H., et al., *A synthetic optogenetic transcription device enhances blood-glucose homeostasis in mice.* Science, 2011. **332**(6037): p. 1565-1568.
59. Moglich, A., R.A. Ayers, and K. Moffat, *Design and signaling mechanism of light-regulated histidine kinases.* J Mol Biol, 2009. **385**(5): p. 1433-44.
60. Muller, K., et al., *A red/far-red light-responsive bi-stable toggle switch to control gene expression in mammalian cells.* Nucleic Acids Res, 2013. **41**(7): p. e77.
61. Yamada, M., et al., *Light control of the Tet gene expression system in mammalian cells.* Cell reports, 2018. **25**(2): p. 487-500. e6.
62. Baaske, J., et al., *Dual-controlled optogenetic system for the rapid down-regulation of protein levels in mammalian cells.* Scientific reports, 2018. **8**(1): p. 1-10.
63. Konermann, S., et al., *Optical control of mammalian endogenous transcription and epigenetic states.* Nature, 2013. **500**(7463): p. 472-6.
64. Müller, K., et al., *Optogenetics for gene expression in mammalian cells.* Biological chemistry, 2015. **396**(2): p. 145-152.
65. Liu, H., et al., *Optogenetic control of transcription in zebrafish.* PloS one, 2012. **7**(11).
66. Müller, K., M.D. Zurbriggen, and W. Weber, *An optogenetic upgrade for the Tet-OFF system.* Biotechnology and bioengineering, 2015. **112**(7): p. 1483-1487.
67. Strickland, D., K. Moffat, and T.R. Sosnick, *Light-activated DNA binding in a designed allosteric protein.* Proc Natl Acad Sci U S A, 2008. **105**(31): p. 10709-14.
68. Strickland, D., et al., *Rationally improving LOV domain–based photoswitches.* Nature methods, 2010. **7**(8): p. 623.
69. Kaberniuk, A.A., A.A. Shemetov, and V.V. Verkhusha, *A bacterial phytochrome-based optogenetic system controllable with near-infrared light.* Nature methods, 2016. **13**(7): p. 591.
70. Cashmore, A.R., et al., *Cryptochromes: blue light receptors for plants and animals.* Science, 1999. **284**(5415): p. 760-765.
71. Jung, A., et al., *Structure of a bacterial BLUF photoreceptor: insights into blue light-mediated signal transduction.* Proceedings of the National Academy of Sciences, 2005. **102**(35): p. 12350-12355.
72. Che, D.L., et al., *The dual characteristics of light-induced cryptochrome 2, homo-oligomerization and heterodimerization, for optogenetic manipulation in mammalian cells.* ACS synthetic biology, 2015. **4**(10): p. 1124-1135.
73. Taslimi, A., et al., *Optimized second-generation CRY2–CIB dimerizers and photoactivatable Cre recombinase.* Nature chemical biology, 2016. **12**(6): p. 425.
74. Wang, X., X. Chen, and Y. Yang, *Spatiotemporal control of gene expression by a light-switchable transgene system.* Nature methods, 2012. **9**(3): p. 266.
75. Nash, A.I., et al., *Structural basis of photosensitivity in a bacterial light-oxygen-voltage/helix-turn-helix (LOV-HTH) DNA-binding protein.* Proceedings of the National Academy of Sciences, 2011. **108**(23): p. 9449-9454.

76. Kawano, F., et al., *Fluorescence imaging-based high-throughput screening of fast-and slow-cycling LOV proteins.* PloS one, 2013. **8**(12): p. e82693.
77. Schwerdtfeger, C. and H. Linden, *VIVID is a flavoprotein and serves as a fungal blue light photoreceptor for photoadaptation.* The EMBO journal, 2003. **22**(18): p. 4846-4855.
78. Motta-Mena, L.B., et al., *An optogenetic gene expression system with rapid activation and deactivation kinetics.* Nature chemical biology, 2014. **10**(3): p. 196.
79. Möglich, A. and P. Hegemann, *Biotechnology: programming genomes with light.* Nature, 2013. **500**(7463): p. 406-408.
80. Bubeck, F., et al., *Engineered anti-CRISPR proteins for optogenetic control of CRISPR–Cas9.* Nature methods, 2018. **15**(11): p. 924-927.
81. Renzl, C., A. Kakoti, and G. Mayer, *Aptamer-mediated reversible transactivation of gene expression by light.* Angewandte Chemie, 2020. **132**(50): p. 22600-22604.
82. Cao, J., et al., *Light-inducible activation of target mRNA translation in mammalian cells.* Chem Commun (Camb), 2013. **49**(75): p. 8338-40.
83. Cao, J., et al., *Bidirectional regulation of mRNA translation in mammalian cells by using PUF domains.* Angew Chem Int Ed Engl, 2014. **53**(19): p. 4900-4.
84. Kim, N.Y., et al., *Optogenetic control of mRNA localization and translation in live cells.* Nature cell biology, 2020. **22**(3): p. 341-352.
85. Lee, S., et al., *Reversible protein inactivation by optogenetic trapping in cells.* Nature methods, 2014. **11**(6): p. 633-636.
86. Wu, Z., H. Yang, and P. Colosi, *Effect of genome size on AAV vector packaging.* Molecular Therapy, 2010. **18**(1): p. 80-86.
87. Sedlmayer, F., D. Aubel, and M. Fussenegger, *Synthetic gene circuits for the detection, elimination and prevention of disease.* Nature biomedical engineering, 2018. **2**(6): p. 399-415.
88. Re, A., *Synthetic gene expression circuits for designing precision tools in oncology.* Frontiers in cell and developmental biology, 2017. **5**: p. 77.
89. Gardner, T.S., C.R. Cantor, and J.J. Collins, *Construction of a genetic toggle switch in Escherichia coli.* Nature, 2000. **403**(6767): p. 339-342.
90. Goñi-Moreno, A. and P.I. Nikel, *High-performance biocomputing in synthetic biology–integrated transcriptional and metabolic circuits.* Frontiers in bioengineering and biotechnology, 2019. **7**: p. 40.
91. Germer, K., M. Leonard, and X. Zhang, *RNA aptamers and their therapeutic and diagnostic applications.* International journal of biochemistry and molecular biology, 2013. **4**(1): p. 27.
92. Liu, J., et al., *Recent developments in protein and cell-targeted aptamer selection and applications.* Current medicinal chemistry, 2011. **18**(27): p. 4117-4125.
93. Kalra, P., et al., *Simple methods and rational design for enhancing aptamer sensitivity and specificity.* Frontiers in molecular biosciences, 2018. **5**: p. 41.
94. Tuerk, C. and L. Gold, *Systematic evolution of ligands by exponential enrichment: RNA ligands to bacteriophage T4 DNA polymerase.* Science, 1990. **249**(4968): p. 505-510.
95. Ellington, A.D. and J.W. Szostak, *In vitro selection of RNA molecules that bind specific ligands.* nature, 1990. **346**(6287): p. 818-822.

96. Pfeiffer, F., et al., *Systematic evaluation of error rates and causes in short samples in next-generation sequencing.* Scientific reports, 2018. **8**(1): p. 1-14.
97. Wrzesinski, J. and J. Ciesiolka, *Characterization of structure and metal ions specificity of Co2+-binding RNA aptamers.* Biochemistry, 2005. **44**(16): p. 6257-6268.
98. Paige, J.S., K.Y. Wu, and S.R. Jaffrey, *RNA mimics of green fluorescent protein.* Science, 2011. **333**(6042): p. 642-6.
99. Gragoudas, E.S., et al., *Pegaptanib for neovascular age-related macular degeneration.* New england journal of medicine, 2004. **351**(27): p. 2805-2816.
100. Mayer, G., et al., *Fluorescence-activated cell sorting for aptamer SELEX with cell mixtures.* Nature protocols, 2010. **5**(12): p. 1993.
101. Breuers, S., et al., *Robotic assisted generation of 2'-deoxy-2'-fluoro-modifed RNA aptamers–High performance enabling strategies in aptamer selection.* Methods, 2019. **161**: p. 3-9.
102. Tolle, F. and G. Mayer, *Preparation of SELEX Samples for Next-Generation Sequencing.* Methods Mol Biol, 2016. **1380**: p. 77-84.
103. Famulok, M., M. Blind, and G. Mayer, *Intramers as promising new tools in functional proteomics.* Chemistry & biology, 2001. **8**(10): p. 931-939.
104. Yu, D., et al., *Optogenetic activation of intracellular antibodies for direct modulation of endogenous proteins.* Nature methods, 2019. **16**(11): p. 1095-1100.
105. Schwanhäusser, B., et al., *Global quantification of mammalian gene expression control.* Nature, 2011. **473**(7347): p. 337-342.
106. Burke, D.H. and D.G. Nickens, *Expressing RNA aptamers inside cells to reveal proteome and ribonome function.* Briefings in Functional Genomics, 2002. **1**(2): p. 169-188.
107. Sullenger, B.A., et al., *Overexpression of TAR sequences renders cells resistant to human immunodeficiency virus replication.* Cell, 1990. **63**(3): p. 601-608.
108. Lennarz, S., et al., *Selective Aptamer‐Based Control of Intraneuronal Signaling.* Angewandte Chemie, 2015. **127**(18): p. 5459-5463.
109. Filonov, G.S., et al., *In-gel imaging of RNA processing using broccoli reveals optimal aptamer expression strategies.* Chemistry & biology, 2015. **22**(5): p. 649-660.
110. Mi, J., et al., *H1 RNA polymerase III promoter-driven expression of an RNA aptamer leads to high-level inhibition of intracellular protein activity.* Nucleic acids research, 2006. **34**(12): p. 3577-3584.
111. Stefanovic, B., et al., *Assemble, nuclear import and function of U7 snRNPs studied by microinjection of synthetic U7 RNA into Xenopus oocytes.* Nucleic acids research, 1995. **23**(16): p. 3141-3151.
112. Farokhzad, O.C., et al., *Targeted nanoparticle-aptamer bioconjugates for cancer chemotherapy in vivo.* Proceedings of the National Academy of Sciences, 2006. **103**(16): p. 6315-6320.
113. Li, M.-J., et al., *Inhibition of HIV-1 infection by lentiviral vectors expressing Pol III-promoted anti-HIV RNAs.* Molecular Therapy, 2003. **8**(2): p. 196-206.
114. Blind, M., W. Kolanus, and M. Famulok, *Cytoplasmic RNA modulators of an inside-out signal-transduction cascade.* Proceedings of the National Academy of Sciences, 1999. **96**(7): p. 3606-3610.

115. Thiel, K.W. and P.H. Giangrande, *Intracellular delivery of RNA-based therapeutics using aptamers.* Therapeutic delivery, 2010. **1**(6): p. 849-861.
116. Auslander, D., et al., *Rational design of a small molecule-responsive intramer controlling transgene expression in mammalian cells.* Nucleic Acids Res, 2011. **39**(22): p. e155.
117. Kumar, D., C.-I. An, and Y. Yokobayashi, *Conditional RNA interference mediated by allosteric ribozyme.* Journal of the American Chemical Society, 2009. **131**(39): p. 13906-13907.
118. Auslander, S., et al., *Engineering a ribozyme cleavage-induced split fluorescent aptamer complementation assay.* Nucleic Acids Res, 2016. **44**(10): p. e94.
119. Ponchon, L. and F. Dardel, *Recombinant RNA technology: the tRNA scaffold.* Nature methods, 2007. **4**(7): p. 571-576.
120. Litke, J.L. and S.R. Jaffrey, *Highly efficient expression of circular RNA aptamers in cells using autocatalytic transcripts.* Nature biotechnology, 2019. **37**(6): p. 667-675.
121. Hafner, M., et al., *Displacement of protein-bound aptamers with small molecules screened by fluorescence polarization.* Nature protocols, 2008. **3**(4): p. 579.
122. Huang, D.-B., et al., *Crystal structure of NF-κB (p50) 2 complexed to a high-affinity RNA aptamer.* Proceedings of the National Academy of Sciences, 2003. **100**(16): p. 9268-9273.
123. Thomas, M., et al., *Selective targeting and inhibition of yeast RNA polymerase II by RNA aptamers.* Journal of Biological Chemistry, 1997. **272**(44): p. 27980-27986.
124. Seiwert, S.D., et al., *RNA aptamers as pathway-specific MAP kinase inhibitors.* Chemistry & biology, 2000. **7**(11): p. 833-843.
125. Mayer, G., et al., *Controlling small guanine–nucleotide-exchange factor function through cytoplasmic RNA intramers.* Proceedings of the National Academy of Sciences, 2001. **98**(9): p. 4961-4965.
126. Shi, H., B.E. Hoffman, and J.T. Lis, *RNA aptamers as effective protein antagonists in a multicellular organism.* Proceedings of the National Academy of Sciences, 1999. **96**(18): p. 10033-10038.
127. Srinivasan, J., et al., *ADP-specific sensors enable universal assay of protein kinase activity.* Chemistry & biology, 2004. **11**(4): p. 499-508.
128. Burke, D.H. and L. Gold, *RNA aptamers to the adenosine moiety of S-adenosyl methionine: structural inferences from variations on a theme and the reproducibility of SELEX.* Nucleic acids research, 1997. **25**(10): p. 2020-2024.
129. An, C.-I., V.B. Trinh, and Y. Yokobayashi, *Artificial control of gene expression in mammalian cells by modulating RNA interference through aptamer–small molecule interaction.* Rna, 2006. **12**(5): p. 710-716.
130. Hanson, S., et al., *Tetracycline-aptamer-mediated translational regulation in yeast.* Molecular microbiology, 2003. **49**(6): p. 1627-1637.
131. Wang, S., et al., *An RNA-aptamer-based two-color CRISPR labeling system.* Sci Rep, 2016. **6**: p. 26857.
132. Fusco, D., et al., *Single mRNA molecules demonstrate probabilistic movement in living mammalian cells.* Current Biology, 2003. **13**(2): p. 161-167.

133. Hunsicker, A., et al., *An RNA aptamer that induces transcription.* Chemistry & biology, 2009. **16**(2): p. 173-180.
134. Weigand, J.E. and B. Suess, *Tetracycline aptamer-controlled regulation of pre-mRNA splicing in yeast.* Nucleic acids research, 2007. **35**(12): p. 4179-4185.
135. Vogel, P., A. Hanswillemenke, and T. Stafforst, *Switching protein localization by site-directed RNA editing under control of light.* ACS synthetic biology, 2017. **6**(9): p. 1642-1649.
136. Lunse, C.E., et al., *An aptamer targeting the apical-loop domain modulates pri-miRNA processing.* Angew Chem Int Ed Engl, 2010. **49**(27): p. 4674-7.
137. Atanasov, J., et al., *Design and implementation of a synthetic pre-miR switch for controlling miRNA biogenesis in mammals.* Nucleic Acids Res, 2017. **45**(22): p. e181.
138. Hockenberry, A.J. and M.C. Jewett, *Synthetic in vitro circuits.* Current opinion in chemical biology, 2012. **16**(3-4): p. 253-259.
139. Keeley, M.B., et al., *TetR hybrid transcription factors report cell signaling and are inhibited by doxycycline.* BioTechniques, 2005. **39**(4): p. 529-536.
140. Gossen, M., et al., *Transcriptional activation by tetracyclines in mammalian cells.* Science, 1995. **268**(5218): p. 1766-1769.
141. Wright, D.A., et al., *Standardized reagents and protocols for engineering zinc finger nucleases by modular assembly.* Nature protocols, 2006. **1**(3): p. 1637-1652.
142. Sanjana, N.E., et al., *A transcription activator-like effector toolbox for genome engineering.* Nature protocols, 2012. **7**(1): p. 171-192.
143. Nakamura, M., et al., *CRISPR technologies for precise epigenome editing.* Nature Cell Biology, 2021. **23**(1): p. 11-22.
144. Collias, D. and C.L. Beisel, *CRISPR technologies and the search for the PAM-free nuclease.* Nature communications, 2021. **12**(1): p. 1-12.
145. Pickar-Oliver, A. and C.A. Gersbach, *The next generation of CRISPR–Cas technologies and applications.* Nature reviews Molecular cell biology, 2019. **20**(8): p. 490-507.
146. Wang, H., et al., *CRISPR-mediated live imaging of genome editing and transcription.* Science, 2019. **365**(6459): p. 1301-1305.
147. Moreno, A.M., et al., *In situ gene therapy via AAV-CRISPR-Cas9-mediated targeted gene regulation.* Molecular Therapy, 2018. **26**(7): p. 1818-1827.
148. Beyer, H.M., et al., *Red Light-Regulated Reversible Nuclear Localization of Proteins in Mammalian Cells and Zebrafish.* ACS Synth Biol, 2015. **4**(9): p. 951-8.
149. Babendure, J.R., et al., *Control of mammalian translation by mRNA structure near caps.* RNA, 2006. **12**(5): p. 851-61.
150. Kozak, M., *Circumstances and mechanisms of inhibition of translation by secondary structure in eucaryotic mRNAs.* Molecular and cellular biology, 1989. **9**(11): p. 5134-5142.
151. Yoon, H. and T.F. Donahue, *The suil suppressor locus in Saccharomyces cerevisiae encodes a translation factor that functions during tRNA (iMet) recognition of the start codon.* Molecular and cellular biology, 1992. **12**(1): p. 248-260.
152. Gray, N.K. and M. Wickens, *Control of translation initiation in animals.* Annual review of cell and developmental biology, 1998. **14**(1): p. 399-458.

153. Kaufman, R.J., *Control of gene expression at the level of translation initiation.* Current opinion in biotechnology, 1994. **5**(5): p. 550-557.
154. Cigan, A.M., E.K. Pabich, and T.F. Donahue, *Mutational analysis of the HIS4 translational initiator region in Saccharomyces cerevisiae.* Molecular and Cellular Biology, 1988. **8**(7): p. 2964-2975.
155. Baim, S. and F. Sherman, *mRNA structures influencing translation in the yeast Saccharomyces cerevisiae.* Molecular and cellular biology, 1988. **8**(4): p. 1591-1601.
156. Sugiyama, T. and D. Nakada, *Translational control of bacteriophage MS2 RNA cistrons by MS2 coat protein: polyacrylamide gel electrophoretic analysis of proteins synthesized in vitro.* Journal of molecular biology, 1968. **31**(3): p. 431-440.
157. Saito, H., et al., *Synthetic human cell fate regulation by protein-driven RNA switches.* Nature communications, 2011. **2**(1): p. 1-9.
158. DE GREGORIO, E., et al., *Tethered-function analysis reveals that eIF4E can recruit ribosomes independent of its binding to the cap structure.* Rna, 2001. **7**(1): p. 106-113.
159. Dreyfuss, G., V.N. Kim, and N. Kataoka, *Messenger-RNA-binding proteins and the messages they carry.* Nature reviews Molecular cell biology, 2002. **3**(3): p. 195-205.
160. Muckenthaler, M.U., B. Galy, and M.W. Hentze, *Systemic iron homeostasis and the iron-responsive element/iron-regulatory protein (IRE/IRP) regulatory network.* Annu. Rev. Nutr., 2008. **28**: p. 197-213.
161. Werstuck, G. and M.R. Green, *Controlling gene expression in living cells through small molecule-RNA interactions.* Science, 1998. **282**(5387): p. 296-298.
162. Harvey, I., P. Garneau, and J. Pelletier, *Inhibition of translation by RNA-small molecule interactions.* RNA, 2002. **8**(4): p. 452-63.
163. Kallunki, T., et al., *How to Choose the Right Inducible Gene Expression System for Mammalian Studies?* Cells, 2019. **8**(8): p. 796.
164. Bayer, T.S. and C.D. Smolke, *Programmable ligand-controlled riboregulators of eukaryotic gene expression.* Nat Biotechnol, 2005. **23**(3): p. 337-43.
165. Winkler, W., A. Nahvi, and R.R. Breaker, *Thiamine derivatives bind messenger RNAs directly to regulate bacterial gene expression.* Nature, 2002. **419**(6910): p. 952-956.
166. Lynch, S.A. and J.P. Gallivan, *A flow cytometry-based screen for synthetic riboswitches.* Nucleic Acids Res, 2009. **37**(1): p. 184-92.
167. Desai, S.K. and J.P. Gallivan, *Genetic screens and selections for small molecules based on a synthetic riboswitch that activates protein translation.* Journal of the American Chemical Society, 2004. **126**(41): p. 13247-13254.
168. Weigand, J.E., et al., *Screening for engineered neomycin riboswitches that control translation initiation.* RNA, 2008. **14**(1): p. 89-97.
169. Auslander, S., et al., *A general design strategy for protein-responsive riboswitches in mammalian cells.* Nat Methods, 2014. **11**(11): p. 1154-60.
170. Yen, L., et al., *Exogenous control of mammalian gene expression through modulation of RNA self-cleavage.* Nature, 2004. **431**(7007): p. 471-476.

171. Yen, L., et al., *Identification of inhibitors of ribozyme self-cleavage in mammalian cells via high-throughput screening of chemical libraries.* Rna, 2006. **12**(5): p. 797-806.
172. Wurmthaler, L.A., et al., *A tetracycline-dependent ribozyme switch allows conditional induction of gene expression in Caenorhabditis elegans.* Nature communications, 2019. **10**(1): p. 1-8.
173. Beilstein, K., et al., *Conditional control of mammalian gene expression by tetracycline-dependent hammerhead ribozymes.* ACS Synth Biol, 2015. **4**(5): p. 526-34.
174. Auslander, S., P. Ketzer, and J.S. Hartig, *A ligand-dependent hammerhead ribozyme switch for controlling mammalian gene expression.* Mol Biosyst, 2010. **6**(5): p. 807-14.
175. Isaacs, F.J., et al., *Engineered riboregulators enable post-transcriptional control of gene expression.* Nature biotechnology, 2004. **22**(7): p. 841-847.
176. Liu, Y., et al., *Targeting cellular mRNAs translation by CRISPR-Cas9.* Sci Rep, 2016. **6**: p. 29652.
177. Consortium, I.H.G.S., *Finishing the euchromatic sequence of the human genome.* Nature, 2004. **431**(7011): p. 931.
178. Shen, H. and Z. Li, *miRNAs in NMDA receptor-dependent synaptic plasticity and psychiatric disorders.* Clinical Science, 2016. **130**(14): p. 1137-1146.
179. Wilson, R.C. and J.A. Doudna, *Molecular mechanisms of RNA interference.* Annual review of biophysics, 2013. **42**: p. 217-239.
180. Krichevsky, A.M. and G. Gabriely, *miR-21: a small multi-faceted RNA.* Journal of cellular and molecular medicine, 2009. **13**(1): p. 39-53.
181. Winter, J., et al., *Many roads to maturity: microRNA biogenesis pathways and their regulation.* Nature cell biology, 2009. **11**(3): p. 228-234.
182. Fabian, M.R., N. Sonenberg, and W. Filipowicz, *Regulation of mRNA translation and stability by microRNAs.* Annual review of biochemistry, 2010. **79**: p. 351-379.
183. Krutzfeldt, J., et al., *Silencing of microRNAs in vivo with 'antagomirs'.* Nature, 2005. **438**(7068): p. 685-9.
184. Ebert, M.S., J.R. Neilson, and P.A. Sharp, *MicroRNA sponges: competitive inhibitors of small RNAs in mammalian cells.* Nature methods, 2007. **4**(9): p. 721-726.
185. Velagapudi, S.P., S.M. Gallo, and M.D. Disney, *Sequence-based design of bioactive small molecules that target precursor microRNAs.* Nature chemical biology, 2014. **10**(4): p. 291-297.
186. Diederichs, S., et al., *Coexpression of Argonaute-2 enhances RNA interference toward perfect match binding sites.* Proceedings of the National Academy of Sciences, 2008. **105**(27): p. 9284-9289.
187. Elbashir, S.M., et al., *Duplexes of 21-nucleotide RNAs mediate RNA interference in cultured mammalian cells.* nature, 2001. **411**(6836): p. 494-498.
188. Weiss, W.A., S.S. Taylor, and K.M. Shokat, *Recognizing and exploiting differences between RNAi and small-molecule inhibitors.* Nature chemical biology, 2007. **3**(12): p. 739-744.
189. Paddison, P.J., et al., *Short hairpin RNAs (shRNAs) induce sequence-specific silencing in mammalian cells.* Genes Dev, 2002. **16**(8): p. 948-58.
190. Siolas, D., et al., *Synthetic shRNAs as potent RNAi triggers.* Nat Biotechnol, 2005. **23**(2): p. 227-31.

191. Nakashima, Y., et al., *Branched RNA nanostructures for RNA interference.* Chemical Communications, 2011. **47**(29): p. 8367-8369.
192. Bramsen, J.B., et al., *Improved silencing properties using small internally segmented interfering RNAs.* Nucleic acids research, 2007. **35**(17): p. 5886-5897.
193. Setten, R.L., J.J. Rossi, and S.-p. Han, *The current state and future directions of RNAi-based therapeutics.* Nature Reviews Drug Discovery, 2019. **18**(6): p. 421-446.
194. Herold, M.J., et al., *Inducible and reversible gene silencing by stable integration of an shRNA-encoding lentivirus in transgenic rats.* Proceedings of the National Academy of Sciences, 2008. **105**(47): p. 18507-18512.
195. An, C.I., V.B. Trinh, and Y. Yokobayashi, *Artificial control of gene expression in mammalian cells by modulating RNA interference through aptamer-small molecule interaction.* RNA, 2006. **12**(5): p. 710-6.
196. Kashida, S., T. Inoue, and H. Saito, *Three-dimensionally designed protein-responsive RNA devices for cell signaling regulation.* Nucleic acids research, 2012. **40**(18): p. 9369-9378.
197. Mou, H., et al., *Conditional regulation of gene expression by ligand-induced occlusion of a microRNA target sequence.* Molecular Therapy, 2018. **26**(5): p. 1277-1286.
198. Hartig, J.S., *Aptamer-Based Control of Gene Expression Utilizing Endogenous miRNAs.* Molecular Therapy, 2018. **26**(5): p. 1178-1180.
199. Deiters, A., *Light activation as a method of regulating and studying gene expression.* Current opinion in chemical biology, 2009. **13**(5-6): p. 678-686.
200. Mikat, V. and A. Heckel, *Light-dependent RNA interference with nucleobase-caged siRNAs.* Rna, 2007. **13**(12): p. 2341-2347.
201. Shah, S., S. Rangarajan, and S.H. Friedman, *Light-activated RNA interference.* Angewandte Chemie International Edition, 2005. **44**(9): p. 1328-1332.
202. Govan, J.M., et al., *Optochemical control of RNA interference in mammalian cells.* Nucleic acids research, 2013. **41**(22): p. 10518-10528.
203. Shah, S., et al., *Light-activated RNA interference using double-stranded siRNA precursors modified using a remarkable regiospecificity of diazo-based photolabile groups.* Nucleic acids research, 2009. **37**(13): p. 4508-4517.
204. Jain, P.K., S. Shah, and S.H. Friedman, *Patterning of gene expression using new photolabile groups applied to light activated RNAi.* Journal of the American Chemical Society, 2011. **133**(3): p. 440-446.
205. Ji, Y., et al., *Photochemical regulation of gene expression using caged siRNAs with single terminal vitamin E modification.* Angewandte Chemie International Edition, 2016. **55**(6): p. 2152-2156.
206. Blidner, R.A., et al., *Photoinduced RNA interference using DMNPE-caged 2'-deoxy-2'-fluoro substituted nucleic acids in vitro and in vivo.* Molecular BioSystems, 2008. **4**(5): p. 431-440.
207. Kala, A. and S.H. Friedman, *Enhanced light-activated RNA interference using phosphorothioate-based dsRNA precursors of siRNA.* Pharmaceutical research, 2011. **28**(12): p. 3050-3057.

208. Kimura, Y., et al., *Intracellular build-up RNAi with single-strand circular RNAs as siRNA precursors.* Chemical Communications, 2020. **56**(3): p. 466-469.
209. Tang, X., et al., *Regulating gene expression in zebrafish embryos using light-activated, negatively charged peptide nucleic acids.* Journal of the American Chemical Society, 2007. **129**(36): p. 11000-11001.
210. Huang, X., et al., *Light-activated RNA interference in human embryonic stem cells.* Biomaterials, 2015. **63**: p. 70-79.
211. Hammill, M.L., G. Islam, and J.-P. Desaulniers, *Reversible control of RNA interference by siRNAzos.* Organic & Biomolecular Chemistry, 2020. **18**(1): p. 41-46.
212. Lapenna, S. and A. Giordano, *Cell cycle kinases as therapeutic targets for cancer.* Nature reviews Drug discovery, 2009. **8**(7): p. 547-566.
213. Imoto, Y., et al., *The cell cycle, including the mitotic cycle and organelle division cycles, as revealed by cytological observations.* Journal of electron microscopy, 2011. **60**(suppl_1): p. S117-S136.
214. Vermeulen, K., D.R. Van Bockstaele, and Z.N. Berneman, *The cell cycle: a review of regulation, deregulation and therapeutic targets in cancer.* Cell proliferation, 2003. **36**(3): p. 131-149.
215. Banfalvi, G., *Overview of cell synchronization*, in *Cell Cycle Synchronization*. 2011, Springer. p. 1-23.
216. Terzi, M.Y., M. Izmirli, and B. Gogebakan, *The cell fate: senescence or quiescence.* Molecular biology reports, 2016. **43**(11): p. 1213-1220.
217. Malumbres, M. and M. Barbacid, *To cycle or not to cycle: a critical decision in cancer.* Nature Reviews Cancer, 2001. **1**(3): p. 222-231.
218. Davis, P.K., A. Ho, and S.F. Dowdy, *Biological methods for cell-cycle synchronization of mammalian cells.* Biotechniques, 2001. **30**(6): p. 1322-1331.
219. Yuan, J., et al., *Stable gene silencing of cyclin B1 in tumor cells increases susceptibility to taxol and leads to growth arrest in vivo.* Oncogene, 2006. **25**(12): p. 1753-1762.
220. Harper, J.V., *Synchronization of Cell Populations in G1/S and G 2/M Phases of the Cell Cycle*, in *Cell Cycle Control*. 2005, Springer. p. 157-166.
221. Jin, D., et al., *Combining CDK4/6 inhibitors ribociclib and palbociclib with cytotoxic agents does not enhance cytotoxicity.* PloS one, 2019. **14**(10): p. e0223555.
222. Vassilev, L.T., *Cell cycle synchronization at the G2/M phase border by reversible inhibition of CDK1.* Cell cycle, 2006. **5**(22): p. 2555-2556.
223. Vassilev, L.T., et al., *Selective small-molecule inhibitor reveals critical mitotic functions of human CDK1.* Proceedings of the National Academy of Sciences, 2006. **103**(28): p. 10660-10665.
224. Malumbres, M. and M. Barbacid, *Cell cycle, CDKs and cancer: a changing paradigm.* Nature reviews cancer, 2009. **9**(3): p. 153-166.
225. Chopra, P., et al., *Polo-like kinase inhibitors: an emerging opportunity for cancer therapeutics.* Expert opinion on investigational drugs, 2010. **19**(1): p. 27-43.
226. Liu, X. and R.L. Erikson, *Polo-like kinase (Plk) 1 depletion induces apoptosis in cancer cells.* Proceedings of the National Academy of Sciences, 2003. **100**(10): p. 5789-5794.

227. Petronczki, M., P. Lénárt, and J.-M. Peters, *Polo on the rise—from mitotic entry to cytokinesis with Plk1.* Developmental cell, 2008. **14**(5): p. 646-659.
228. Affatato, R., et al., *Identification of PLK1 as a New Therapeutic Target in Mucinous Ovarian Carcinoma.* Cancers, 2020. **12**(3): p. 672.
229. Kondo, S. and N. Perrimon, *A genome-wide RNAi screen identifies core components of the G2-M DNA damage checkpoint.* Science signaling, 2011. **4**(154): p. rs1-rs1.
230. Wei, K.Y. and C.D. Smolke, *Engineering dynamic cell cycle control with synthetic small molecule-responsive RNA devices.* Journal of biological engineering, 2015. **9**(1): p. 1-13.
231. Silva, J.M., et al., *Profiling essential genes in human mammary cells by multiplex RNAi screening.* Science, 2008. **319**(5863): p. 617-620.
232. Raab, M., et al., *Toxicity modelling of Plk1-targeted therapies in genetically engineered mice and cultured primary mammalian cells.* Nature communications, 2011. **2**(1): p. 1-11.
233. Krauss, U., et al., *Distribution and phylogeny of light-oxygen-voltage-blue-light-signaling proteins in the three kingdoms of life.* Journal of bacteriology, 2009. **191**(23): p. 7234-7242.
234. Herrou, J. and S. Crosson, *Function, structure and mechanism of bacterial photosensory LOV proteins.* Nat Rev Microbiol, 2011. **9**(10): p. 713-23.
235. Heintzen, C., J.J. Loros, and J.C. Dunlap, *The PAS protein VIVID defines a clock-associated feedback loop that represses light input, modulates gating, and regulates clock resetting.* Cell, 2001. **104**(3): p. 453-464.
236. Christie, J.M., et al., *Arabidopsis NPH1: a flavoprotein with the properties of a photoreceptor for phototropism.* Science, 1998. **282**(5394): p. 1698-1701.
237. Weber, A.M., et al., *A blue light receptor that mediates RNA binding and translational regulation.* Nature chemical biology, 2019. **15**(11): p. 1085-1092.
238. Takahashi, F., et al., *AUREOCHROME, a photoreceptor required for photomorphogenesis in stramenopiles.* Proceedings of the National Academy of Sciences, 2007. **104**(49): p. 19625-19630.
239. Möglich, A., R.A. Ayers, and K. Moffat, *Addition at the Molecular Level: Signal Integration in Designed Per–ARNT–Sim Receptor Proteins.* Journal of molecular biology, 2010. **400**(3): p. 477-486.
240. Ramesh, A., et al., *The mechanism for RNA recognition by ANTAR regulators of gene expression.* PLoS Genet, 2012. **8**(6): p. e1002666.
241. Salomon, M., et al., *Photochemical and mutational analysis of the FMN-binding domains of the plant blue light receptor, phototropin.* Biochemistry, 2000. **39**(31): p. 9401-9410.
242. Swartz, T.E., et al., *The photocycle of a flavin-binding domain of the blue light photoreceptor phototropin.* J Biol Chem, 2001. **276**(39): p. 36493-500.
243. Thomsen, D.R., et al., *Promoter-regulatory region of the major immediate early gene of human cytomegalovirus.* Proceedings of the National Academy of Sciences, 1984. **81**(3): p. 659-663.
244. Deneke, C., S. Rudorf, and A. Valleriani, *Transient phenomena in gene expression after induction of transcription.* PLoS One, 2012. **7**(4): p. e35044.
245. Jackson, R.J., C.U. Hellen, and T.V. Pestova, *The mechanism of eukaryotic translation initiation and principles of its regulation.* Nat Rev Mol Cell Biol, 2010. **11**(2): p. 113-27.

246. Richter, J.D. and N. Sonenberg, *Regulation of cap-dependent translation by eIF4E inhibitory proteins.* Nature, 2005. **433**(7025): p. 477-480.
247. Haghighat, A., et al., *Repression of cap-dependent translation by 4E-binding protein 1: competition with p220 for binding to eukaryotic initiation factor-4E.* The EMBO journal, 1995. **14**(22): p. 5701-5709.
248. Cha, Y.L., et al., *EIF4EBP1 overexpression is associated with poor survival and disease progression in patients with hepatocellular carcinoma.* PLoS One, 2015. **10**(2): p. e0117493.
249. Hannon, G.J., *RNA interference.* Nature, 2002. **418**(6894): p. 244-51.
250. Sambandan, S., et al., *Activity-dependent spatially localized miRNA maturation in neuronal dendrites.* Science, 2017. **355**(6325): p. 634-637.
251. Hausser, J. and M. Zavolan, *Identification and consequences of miRNA–target interactions—beyond repression of gene expression.* Nature Reviews Genetics, 2014. **15**(9): p. 599-612.
252. Cheng, Y. and C. Zhang, *MicroRNA-21 in cardiovascular disease.* Journal of cardiovascular translational research, 2010. **3**(3): p. 251-255.
253. Sheedy, F.J., *Turning 21: induction of miR-21 as a key switch in the inflammatory response.* Frontiers in immunology, 2015. **6**: p. 19.
254. Pofahl, M., J. Wengel, and G. Mayer, *Multifunctional nucleic acids for tumor cell treatment.* Nucleic acid therapeutics, 2014. **24**(2): p. 171-177.
255. Henique, C., et al., *Genetic and pharmacological inhibition of microRNA-92a maintains podocyte cell cycle quiescence and limits crescentic glomerulonephritis.* Nature communications, 2017. **8**(1): p. 1-15.
256. Mateus, A., P.r. Matsson, and P. Artursson, *Rapid measurement of intracellular unbound drug concentrations.* Molecular pharmaceutics, 2013. **10**(6): p. 2467-2478.
257. Mitra, R., et al., *Concordant dysregulation of miR-5p and miR-3p arms of the same precursor microRNA may be a mechanism in inducing cell proliferation and tumorigenesis: a lung cancer study.* Rna, 2015. **21**(6): p. 1055-1065.
258. Flores-Jasso, C.F., et al., *First step in pre-miRNAs processing by human Dicer.* Acta Pharmacol Sin, 2009. **30**(8): p. 1177-85.
259. Gao, Z., E. Herrera-Carrillo, and B. Berkhout, *Delineation of the exact transcription termination signal for type 3 polymerase III.* Molecular Therapy-Nucleic Acids, 2018. **10**: p. 36-44.
260. Park, J.-E., et al., *Dicer recognizes the 5' end of RNA for efficient and accurate processing.* Nature, 2011. **475**(7355): p. 201-205.
261. Prody, G.A., et al., *Autolytic processing of dimeric plant virus satellite RNA.* Science, 1986. **231**(4745): p. 1577-1580.
262. Yamano, S., J. Dai, and A.M. Moursi, *Comparison of transfection efficiency of nonviral gene transfer reagents.* Molecular biotechnology, 2010. **46**(3): p. 287-300.
263. Sato, T., T. Ishii, and Y. Okahata, *In vitro gene delivery mediated by chitosan. Effect of pH, serum, and molecular mass of chitosan on the transfection efficiency.* Biomaterials, 2001. **22**(15): p. 2075-2080.
264. Reid, D.W. and C.V. Nicchitta, *Diversity and selectivity in mRNA translation on the endoplasmic reticulum.* Nature reviews Molecular cell biology, 2015. **16**(4): p. 221-231.

265. Meister, G., et al., *Human Argonaute2 mediates RNA cleavage targeted by miRNAs and siRNAs.* Molecular cell, 2004. **15**(2): p. 185-197.
266. Dickins, R.A., et al., *Tissue-specific and reversible RNA interference in transgenic mice.* Nature genetics, 2007. **39**(7): p. 914-921.
267. Wilson, R.C., et al., *Dicer-TRBP complex formation ensures accurate mammalian microRNA biogenesis.* Molecular cell, 2015. **57**(3): p. 397-407.
268. Brummelkamp, T.R., R. Bernards, and R. Agami, *A system for stable expression of short interfering RNAs in mammalian cells.* science, 2002. **296**(5567): p. 550-553.
269. Warf, M.B., W.E. Johnson, and B.L. Bass, *Improved annotation of C. elegans microRNAs by deep sequencing reveals structures associated with processing by Drosha and Dicer.* RNA, 2011. **17**(4): p. 563-77.
270. Gu, S., et al., *The loop position of shRNAs and pre-miRNAs is critical for the accuracy of dicer processing in vivo.* Cell, 2012. **151**(4): p. 900-911.
271. Cheng, L., et al., *Use of green fluorescent protein variants to monitor gene transfer and expression in mammalian cells.* Nature biotechnology, 1996. **14**(5): p. 606-609.
272. Klein, D., et al., *The kink-turn: a new RNA secondary structure motif.* The EMBO journal, 2001. **20**(15): p. 4214-4221.
273. Schroeder, K.T., et al., *A structural database for k-turn motifs in RNA.* Rna, 2010. **16**(8): p. 1463-1468.
274. Higuchi, T., et al., *Differential gene expression profiling linked to tumor progression of splenic marginal zone lymphoma.* Scientific reports, 2017. **7**(1): p. 1-14.
275. Wang, Z., et al., *Cyclin B1/Cdk1 coordinates mitochondrial respiration for cell-cycle G2/M progression.* Developmental cell, 2014. **29**(2): p. 217-232.
276. Qin, J.Y., et al., *Systematic comparison of constitutive promoters and the doxycycline-inducible promoter.* PLoS One, 2010. **5**(5): p. e10611.
277. van Vugt, M.A., et al., *Polo-like kinase-1 is required for bipolar spindle formation but is dispensable for anaphase promoting complex/Cdc20 activation and initiation of cytokinesis.* Journal of biological chemistry, 2004. **279**(35): p. 36841-36854.
278. Kopka, B., et al., *Electron transfer pathways in a light, oxygen, voltage (LOV) protein devoid of the photoactive cysteine.* Sci Rep, 2017. **7**(1): p. 13346.
279. Suzuki, N., et al., *Enhancement of a σB-dependent stress response in Bacillus subtilis by light via YtvA photoreceptor.* The Journal of general and applied microbiology, 2007. **53**(2): p. 81-88.
280. Vitor, M.T., et al., *Tracking the evolution of transiently transfected individual cells in a microfluidic platform.* Scientific reports, 2018. **8**(1): p. 1-9.
281. Zago, G., et al., *RalB directly triggers invasion downstream Ras by mobilizing the Wave complex.* Elife, 2018. **7**: p. e40474.
282. Asrican, B., et al., *Next-generation transgenic mice for optogenetic analysis of neural circuits.* Frontiers in neural circuits, 2013. **7**: p. 160.
283. Westin, G. and W. Schaffner, *A zinc-responsive factor interacts with a metal-regulated enhancer element (MRE) of the mouse metallothionein-I gene.* The EMBO journal, 1988. **7**(12): p. 3763-3770.

284. Schneider, C. and B. Suess, *Identification of RNA aptamers with riboswitching properties.* Methods, 2016. **97**: p. 44-50.

285. Ferré-D'Amaré, A.R., *Synthetic biology: An RNP switch raises a roadblock.* Nature chemical biology, 2010. **6**(1): p. 5.

286. Beretta, L., et al., *Rapamycin blocks the phosphorylation of 4E-BP1 and inhibits cap-dependent initiation of translation.* The EMBO journal, 1996. **15**(3): p. 658-664.

287. Yanagiya, A., et al., *Translational homeostasis via the mRNA cap-binding protein, eIF4E.* Mol Cell, 2012. **46**(6): p. 847-58.

288. Lawrence, R.E., et al., *A nutrient-induced affinity switch controls mTORC1 activation by its Rag GTPase–Ragulator lysosomal scaffold.* Nature cell biology, 2018. **20**(9): p. 1052-1063.

289. Huston, J.S., et al., *Protein engineering of antibody binding sites: recovery of specific activity in an anti-digoxin single-chain Fv analogue produced in Escherichia coli.* Proceedings of the National Academy of Sciences, 1988. **85**(16): p. 5879-5883.

290. Fingar, D.C., et al., *mTOR Controls Cell Cycle Progression through Its Cell Growth Effectors S6K1 and 4E-BP1/Eukaryotic Translation Initiation Factor 4E.* Molecular and Cellular Biology, 2003. **24**(1): p. 200-216.

291. Andersen, K.R., N.C. Leksa, and T.U. Schwartz, *Optimized E. coli expression strain LOBSTR eliminates common contaminants from His-tag purification.* Proteins: Structure, Function, and Bioinformatics, 2013. **81**(11): p. 1857-1861.

292. Kerruth, S., et al., *Aureochrome 1 illuminated: structural changes of a transcription factor probed by molecular spectroscopy.* PLoS One, 2014. **9**(7): p. e103307.

293. Gauden, M., et al. *Low-temperature and time-resolved spectroscopic characterization of the LOV2 domain of Avena sativa phototropin 1*. in *Femtosecond Laser Applications in Biology*. 2004. International Society for Optics and Photonics.

294. Cadart, C., et al., *Size control in mammalian cells involves modulation of both growth rate and cell cycle duration.* Nature communications, 2018. **9**(1): p. 1-15.

295. Matthess, Y., et al., *Conditional inhibition of cancer cell proliferation by tetracycline-responsive, H1 promoter-driven silencing of PLK1.* Oncogene, 2005. **24**(18): p. 2973-2980.

296. Guryanova, O., et al., *Optimization of a genome-wide disordered lentivector-based short hairpin RNA library.* Molecular biology, 2006. **40**(3): p. 396-405.

297. Ou, W., et al., *Specific targeting of human interleukin (IL)-13 receptor α2-positive cells with lentiviral vectors displaying IL-13.* Human Gene Therapy, Part B: Methods, 2012. **23**(2): p. 137-147.

298. Schagat, T., A. Paguio, and K. Kopish, *Normalizing genetic reporter assays: approaches and considerations for increasing consistency and statistical significance.* Cell Notes, 2007. **17**: p. 9-12.

299. He, J., et al., *A new design of a lentiviral shRNA vector with inducible co-expression of ARGONAUTE 2 for enhancing gene silencing efficiency.* Cell & bioscience, 2015. **5**(1): p. 67.

300. Baez-Vega, P.M., et al., *Targeting miR-21-3p inhibits proliferation and invasion of ovarian cancer cells.* Oncotarget, 2016. **7**(24): p. 36321-36337.

301. Jo, A., H.E. Lee, and H.S. Kim, *Genomic Analysis of miR-21-3p and Expression Pattern with Target Gene in Olive Flounder.* Genomics Inform, 2017. **15**(3): p. 98-107.
302. Tseng, H.H., et al., *Next-generation Sequencing for microRNA Profiling: MicroRNA-21-3p Promotes Oral Cancer Metastasis.* Anticancer Res, 2017. **37**(3): p. 1059-1066.
303. Hockberger, P.E., et al., *Activation of flavin-containing oxidases underlies light-induced production of H2O2 in mammalian cells.* Proceedings of the National Academy of Sciences, 1999. **96**(11): p. 6255-6260.
304. Ge, Q., et al., *Minimal-length short hairpin RNAs: the relationship of structure and RNAi activity.* Rna, 2010. **16**(1): p. 106-117.
305. Okada, C., et al., *A high-resolution structure of the pre-microRNA nuclear export machinery.* Science, 2009. **326**(5957): p. 1275-1279.
306. Chakravarthy, S., et al., *Substrate-specific kinetics of Dicer-catalyzed RNA processing.* J Mol Biol, 2010. **404**(3): p. 392-402.
307. Cruse, W., et al., *Structure of a mispaired RNA double helix at 1.6-A resolution and implications for the prediction of RNA secondary structure.* Proceedings of the National Academy of Sciences, 1994. **91**(10): p. 4160-4164.
308. Mcintyre, G.J., et al., *The effects of stem length and core placement on shRNA activity.* BMC molecular biology, 2011. **12**(1): p. 34.
309. Ribas, J., et al., *A novel source for miR-21 expression through the alternative polyadenylation of VMP1 gene transcripts.* Nucleic acids research, 2012. **40**(14): p. 6821-6833.
310. Börner, K., et al., *Robust RNAi enhancement via human Argonaute-2 overexpression from plasmids, viral vectors and cell lines.* Nucleic acids research, 2013. **41**(21): p. e199-e199.
311. Jin, H.Y., et al., *Transfection of microRNA mimics should be used with caution.* Frontiers in genetics, 2015. **6**: p. 340.
312. Guennewig, B., et al., *Properties of N 4-Methylated Cytidines in miRNA Mimics.* Nucleic acid therapeutics, 2012. **22**(2): p. 109-116.
313. Hirschberg, K., et al., *Kinetic analysis of secretory protein traffic and characterization of Golgi to plasma membrane transport intermediates in living cells.* The Journal of cell biology, 1998. **143**(6): p. 1485-1503.
314. Haugwitz, M., et al., *Multiplexing bioluminescent and fluorescent reporters to monitor live cells.* Curr Chem Genomics, 2008. **1**: p. 11-9.
315. Bail, S., et al., *Differential regulation of microRNA stability.* Rna, 2010. **16**(5): p. 1032-1039.
316. Marshall, W.F., *Modeling recursive RNA interference.* PLoS computational biology, 2008. **4**(9).
317. Quirk, R.A., et al., *Poly (l-lysine)–GRGDS as a biomimetic surface modifier for poly (lactic acid).* Biomaterials, 2001. **22**(8): p. 865-872.
318. Shaner, N.C., et al., *Improved monomeric red, orange and yellow fluorescent proteins derived from Discosoma sp. red fluorescent protein.* Nature biotechnology, 2004. **22**(12): p. 1567-1572.
319. Boudreau, C., et al., *Excitation light dose engineering to reduce photo-bleaching and photo-toxicity.* Scientific reports, 2016. **6**: p. 30892.
320. Hernández-Candia, C.N., S. Casas-Flores, and B. Gutierrez-Medina, *Light induces oxidative damage and protein stability in the fungal photoreceptor Vivid.* PloS one, 2018. **13**(7).

321. Kozomara, A., M. Birgaoanu, and S. Griffiths-Jones, *miRBase: from microRNA sequences to function.* Nucleic acids research, 2019. **47**(D1): p. D155-D162.
322. MacRae, I.J., K. Zhou, and J.A. Doudna, *Structural determinants of RNA recognition and cleavage by Dicer.* Nature structural & molecular biology, 2007. **14**(10): p. 934-940.
323. Chalk, A.M., C. Wahlestedt, and E.L. Sonnhammer, *Improved and automated prediction of effective siRNA.* Biochemical and biophysical research communications, 2004. **319**(1): p. 264-274.
324. Tiscornia, G., et al., *A general method for gene knockdown in mice by using lentiviral vectors expressing small interfering RNA.* Proceedings of the National Academy of Sciences, 2003. **100**(4): p. 1844-1848.
325. Bertrand, J.-R., et al., *Comparison of antisense oligonucleotides and siRNAs in cell culture and in vivo.* Biochemical and biophysical research communications, 2002. **296**(4): p. 1000-1004.
326. Song, E., et al., *RNA interference targeting Fas protects mice from fulminant hepatitis.* Nature medicine, 2003. **9**(3): p. 347-351.
327. Sancak, Y., et al., *The Rag GTPases bind raptor and mediate amino acid signaling to mTORC1.* Science, 2008. **320**(5882): p. 1496-1501.
328. Jeffery, J., et al., *Centrobin regulates the assembly of functional mitotic spindles.* Oncogene, 2010. **29**(18): p. 2649-2658.
329. Barthel, A. and M. Zacharias, *Conformational transitions in RNA single uridine and adenosine bulge structures: a molecular dynamics free energy simulation study.* Biophysical journal, 2006. **90**(7): p. 2450-2462.
330. Zhang, X. and Y. Zeng, *The terminal loop region controls microRNA processing by Drosha and Dicer.* Nucleic acids research, 2010. **38**(21): p. 7689-7697.
331. Tsutsumi, A., et al., *Recognition of the pre-miRNA structure by Drosophila Dicer-1.* Nature structural & molecular biology, 2011. **18**(10): p. 1153.
332. Johnson, H.E., et al., *The spatiotemporal limits of developmental Erk signaling.* Developmental cell, 2017. **40**(2): p. 185-192.
333. Nam, Y., et al., *Molecular basis for interaction of let-7 microRNAs with Lin28.* Cell, 2011. **147**(5): p. 1080-1091.
334. Nash, A.I., et al., *Structural basis of photosensitivity in a bacterial light-oxygen-voltage/helix-turn-helix (LOV-HTH) DNA-binding protein.* Proc Natl Acad Sci U S A, 2011. **108**(23): p. 9449-54.
335. Buckley, A.M., et al., *LOV-based reporters for fluorescence imaging.* Curr Opin Chem Biol, 2015. **27**: p. 39-45.
336. Budker, V., et al., *pH-sensitive, cationic liposomes: a new synthetic virus-like vector.* Nature biotechnology, 1996. **14**(6): p. 760-764.
337. Hardy, J.G., et al., *Synergistic effects on gene delivery–co-formulation of small disulfide-linked dendritic polycations with Lipofectamine 2000™.* Organic & biomolecular chemistry, 2009. **7**(4): p. 789-793.
338. Chen, C.Y.A., N. Ezzeddine, and A.B. Shyu, *Messenger RNA half-life measurements in mammalian cells.* Methods in enzymology, 2008. **448**: p. 335-357.

339. Root, D.E., et al., *Genome-scale loss-of-function screening with a lentiviral RNAi library.* Nature methods, 2006. **3**(9): p. 715-719.
340. Zhang, Y., et al., *AGO2 involves the malignant phenotypes and FAK/PI3K/AKT signaling pathway in hypopharyngeal-derived FaDu cells.* Oncotarget, 2017. **8**(33): p. 54735.
341. Song, Y., et al., *Overexpression of cyclin B1 in human esophageal squamous cell carcinoma cells induces tumor cell invasive growth and metastasis.* Carcinogenesis, 2008. **29**(2): p. 307-315.
342. Rajput, S., et al., *Inhibition of cyclin dependent kinase 9 by dinaciclib suppresses cyclin B1 expression and tumor growth in triple negative breast cancer.* Oncotarget, 2016. **7**(35): p. 56864.
343. Lu, S., et al., *Tivantinib (ARQ 197) affects the apoptotic and proliferative machinery downstream of c-MET: role of Mcl-1, Bcl-xl and Cyclin B1.* Oncotarget, 2015. **6**(26): p. 22167.
344. Premsrirut, P.K., et al., *A rapid and scalable system for studying gene function in mice using conditional RNA interference.* Cell, 2011. **145**(1): p. 145-158.
345. Molinas, M.d.l.M.B., et al., *Optimizing the transient transfection process of HEK-293 suspension cells for protein production by nucleotide ratio monitoring.* Cytotechnology, 2014. **66**(3): p. 493-514.
346. Ling, C., et al., *High-efficiency transduction of primary human hematopoietic stem/progenitor cells by AAV6 vectors: strategies for overcoming donor-variation and implications in genome editing.* Scientific reports, 2016. **6**(1): p. 1-8.
347. Yuan, J., et al., *Cyclin B1 depletion inhibits proliferation and induces apoptosis in human tumor cells.* Oncogene, 2004. **23**(34): p. 5843-5852.
348. Hartsink-Segers, S.A., et al., *Inhibiting Polo-like kinase 1 causes growth reduction and apoptosis in pediatric acute lymphoblastic leukemia cells.* Haematologica, 2013. **98**(10): p. 1539-1546.
349. Guan, R., et al., *Small interfering RNA–mediated Polo-like kinase 1 depletion preferentially reduces the survival of p53-defective, oncogenic transformed cells and inhibits tumor growth in animals.* Cancer research, 2005. **65**(7): p. 2698-2704.
350. Liu, J., et al., *MicroRNA-100 is a potential molecular marker of non-small cell lung cancer and functions as a tumor suppressor by targeting polo-like kinase 1.* BMC cancer, 2012. **12**(1): p. 519.
351. Vermeulen, A., et al., *The contributions of dsRNA structure to Dicer specificity and efficiency.* RNA, 2005. **11**(5): p. 674-82.
352. Xie, X., et al., *Downregulation of G2/mitotic-specific cyclinB1 triggers autophagy via AMPK-ULK1-dependent signal pathway in nasopharyngeal carcinoma cells.* Cell death & disease, 2019. **10**(2): p. 1-10.
353. Sala, R., et al., *Phosphorylation status of thymidine kinase 1 following antiproliferative drug treatment mediates 3'-deoxy-3'-[18F]-fluorothymidine cellular retention.* PloS one, 2014. **9**(7).
354. Kappel, S., et al., *Silencing of mammalian genes by tetracycline-inducible shRNA expression.* Nature protocols, 2007. **2**(12): p. 3257.

355. Ghosh, R., J.E. Gilda, and A.V. Gomes, *The necessity of and strategies for improving confidence in the accuracy of western blots.* Expert review of proteomics, 2014. **11**(5): p. 549-560.
356. Behbehani, G.K., et al., *Single-cell mass cytometry adapted to measurements of the cell cycle.* Cytometry Part A, 2012. **81**(7): p. 552-566.
357. McCarroll, J.A., et al., *Therapeutic targeting of polo-like kinase 1 using RNA-interfering nanoparticles (iNOPs) for the treatment of non-small cell lung cancer.* Oncotarget, 2015. **6**(14): p. 12020.
358. Pitchiaya, S., et al., *Resolving subcellular miRNA trafficking and turnover at single-molecule resolution.* Cell reports, 2017. **19**(3): p. 630-642.
359. Wu, A.R., et al., *Quantitative assessment of single-cell RNA-sequencing methods.* Nature methods, 2014. **11**(1): p. 41.
360. Lee, J.H., et al., *Highly multiplexed subcellular RNA sequencing in situ.* Science, 2014. **343**(6177): p. 1360-1363.
361. Davies, S.A., et al., *Analysis and inactivation of vha55, the gene encoding the vacuolar ATPase B-subunit in Drosophila melanogaster reveals a larval lethal phenotype.* Journal of Biological Chemistry, 1996. **271**(48): p. 30677-30684.
362. Fisher, Y.E., et al., *FlpStop, a tool for conditional gene control in Drosophila.* Elife, 2017. **6**: p. e22279.
363. Lewandoski, M., *Conditional control of gene expression in the mouse.* Nature Reviews Genetics, 2001. **2**(10): p. 743-755.
364. Calixto, A., C. Ma, and M. Chalfie, *Conditional gene expression and RNAi using MEC-8–dependent splicing in C. elegans.* Nature methods, 2010. **7**(5): p. 407.
365. Knopf, F., et al., *Dually inducible TetON systems for tissue-specific conditional gene expression in zebrafish.* Proceedings of the National Academy of Sciences, 2010. **107**(46): p. 19933-19938.
366. Gao, J., et al., *Advances in the development of cancer immunotherapies.* Trends in immunology, 2013. **34**(2): p. 90-98.
367. Sahin, U., K. Karikó, and Ö. Türeci, *mRNA-based therapeutics—developing a new class of drugs.* Nature reviews Drug discovery, 2014. **13**(10): p. 759.
368. Bernards, R., et al., *A roadmap for the next decade in cancer research.* Nature Cancer, 2020. **1**(1): p. 12-17.
369. Tan, P., et al., *Optogenetic immunomodulation: shedding light on antitumor immunity.* Trends in biotechnology, 2017. **35**(3): p. 215-226.
370. Zhao, B., et al., *An Optogenetic Controllable T Cell System for Hepatocellular Carcinoma Immunotherapy.* Theranostics, 2019. **9**(7): p. 1837.
371. Mickle, A.D., et al., *A wireless closed-loop system for optogenetic peripheral neuromodulation.* Nature, 2019. **565**(7739): p. 361-365.
372. Shin, G., et al., *Flexible near-field wireless optoelectronics as subdermal implants for broad applications in optogenetics.* Neuron, 2017. **93**(3): p. 509-521. e3.

373. Shao, J., et al., *Smartphone-controlled optogenetically engineered cells enable semiautomatic glucose homeostasis in diabetic mice.* Science Translational Medicine, 2017. **9**(387): p. eaal2298.
374. Kushibiki, T., et al., *Optogenetic control of insulin secretion by pancreatic β-cells in vitro and in vivo.* Gene therapy, 2015. **22**(7): p. 553-559.
375. Binnewies, M., et al., *Understanding the tumor immune microenvironment (TIME) for effective therapy.* Nature medicine, 2018. **24**(5): p. 541-550.
376. Courtine, G. and M.V. Sofroniew, *Spinal cord repair: advances in biology and technology.* Nature medicine, 2019. **25**(6): p. 898-908.
377. Park, S., et al., *Optogenetic control of nerve growth.* Sci Rep, 2015. **5**: p. 9669.
378. Zhao, E.M., et al., *Optogenetic regulation of engineered cellular metabolism for microbial chemical production.* Nature, 2018. **555**(7698): p. 683-687.
379. Mansouri, M., T. Strittmatter, and M. Fussenegger, *Light-Controlled Mammalian Cells and Their Therapeutic Applications in Synthetic Biology.* Advanced Science, 2019. **6**(1): p. 1800952.
380. Baaske, J., et al., *Optogenetic control of integrin-matrix interaction.* Communications biology, 2019. **2**(1): p. 1-8.
381. Zimmerman, S.P., et al., *Cells lay their own tracks–optogenetic Cdc42 activation stimulates fibronectin deposition supporting directed migration.* J Cell Sci, 2017. **130**(18): p. 2971-2983.
382. Wang, S.J., et al., *Effect of optogenetic stimulus on the proliferation and cell cycle progression of neural stem cells.* The Journal of membrane biology, 2014. **247**(6): p. 493-500.
383. Ono, K., et al., *Optogenetic control of cell differentiation in channelrhodopsin-2-expressing OS3, a bipotential glial progenitor cell line.* Neurochemistry international, 2017. **104**: p. 49-63.
384. Redchuk, T.A., et al., *Near-infrared optogenetic pair for protein regulation and spectral multiplexing.* Nature chemical biology, 2017. **13**(6): p. 633.
385. Myers, J.W., et al., *Recombinant Dicer efficiently converts large dsRNAs into siRNAs suitable for gene silencing.* Nat Biotechnol, 2003. **21**(3): p. 324-8.
386. Beyer, H.M., et al., *AQUA cloning: a versatile and simple enzyme-free cloning approach.* PloS one, 2015. **10**(9): p. e0137652.
387. Gruber, A.R., et al., *The vienna RNA websuite.* Nucleic acids research, 2008. **36**(suppl_2): p. W70-W74.
388. Antczak, M., et al., *New functionality of RNAComposer: application to shape the axis of miR160 precursor structure.* Acta Biochimica Polonica, 2016. **63**(4): p. 737-744.
389. Popenda, M., et al., *Automated 3D structure composition for large RNAs.* Nucleic acids research, 2012. **40**(14): p. e112-e112.
390. Pettersen, E.F., et al., *UCSF Chimera—a visualization system for exploratory research and analysis.* Journal of computational chemistry, 2004. **25**(13): p. 1605-1612.

10 Appendix

10.1 Abbreviations

Table 10.1: List of abbreviations.

APS	Ammonium peroxodisulfate
ATP	Adenosine triphosphate
bp	Base pair
BSA	Bovine serum albumin
CIAP	Calf intestine alkaline phosphatase
DMSO	Dimethyl sulfoxide
dsDNA	Double stranded DNA
DNA	Deoxyribnucleic acid
dNTP	Dexoynucleoside triphosphate
DTT	1,4-dithiothreitol
EDTA	Ethylenediaminetetraacetic acid
EtOH	Ethanol
g	Gram
eGFP	Enhanced green fluorescent protein
HCl	Hydrochloric acid
iPP	Inorganic pyrophosphatase
KCl	Potassium chloride
l	Litre
LB	Lysogeny broth
M	Concentration in mol/l
MeOH	Methanol
Min	Minute
$MgCl_2$	Magnesium chloride
mRNA	Messenger RNA
NaCl	Sodium chloride
NaOAc	Sodium acetate
nt	Nucleotides
NTC	No template control
NTP	Nucleoside triphosphate
PAA	Polyacrylamide
PAGE	Polyacrylamide gel electrophoresis
PBS	Phosphate-buffered saline
PCR	Polymerase chain reaction
PDB	Protein data bank
pH	Negative logarithm of the H^+-concentration

PNK	Polynucleotide kinase
qPCR	Quantitative PCR
R^2	Coefficient of determination
RNA	Ribonucleic acid
RT	Room temperature
SD	Standard deviation
SDS	Sodium dodecylsulfate
SELEX	Systematic evolution of ligands by exponential enrichment
ssDNA	Single-stranded DNA
TEMED	N,N,N’,N’-tetramethylethylenediamine
U	Units
UV	Ultraviolet
V	Volt
W	Watt

10.2 Supporting Information

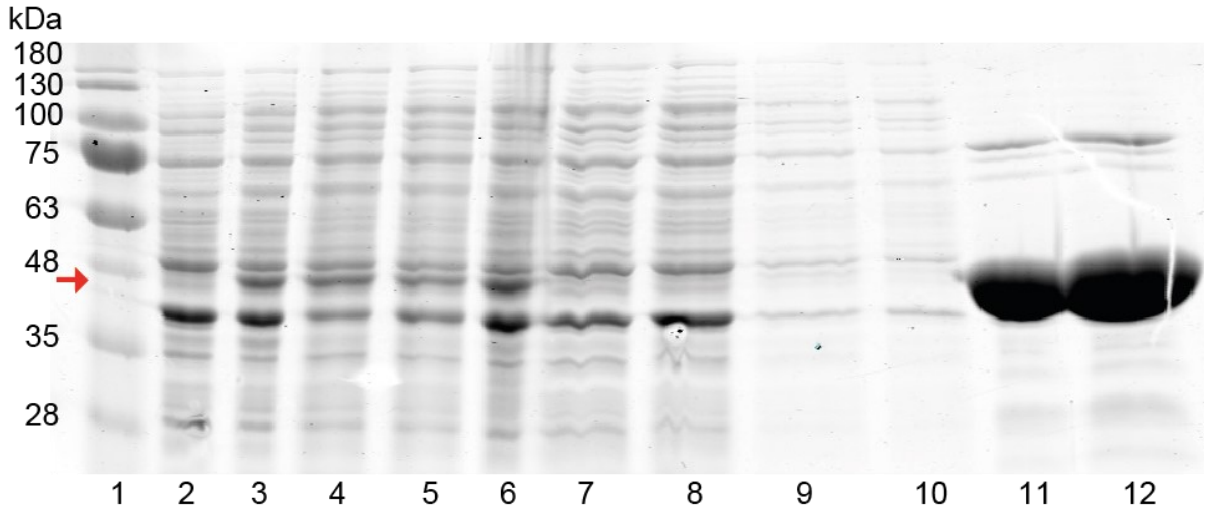

Figure 10.1: Verification of PAL protein expression by gel electrophoresis. Samples at different PAL purification steps (1: Prism Protein Ladder, 2: Cells before induction, 3: Cells after induction, 4, 5: Cell lysate, 6 Cell pellet, 7, 8: Supernatant after bead incubation, 9, 10: Washes, 11: Elution before dialysis, 12: Elution after dialysis). Red arrow: putative PAL band.

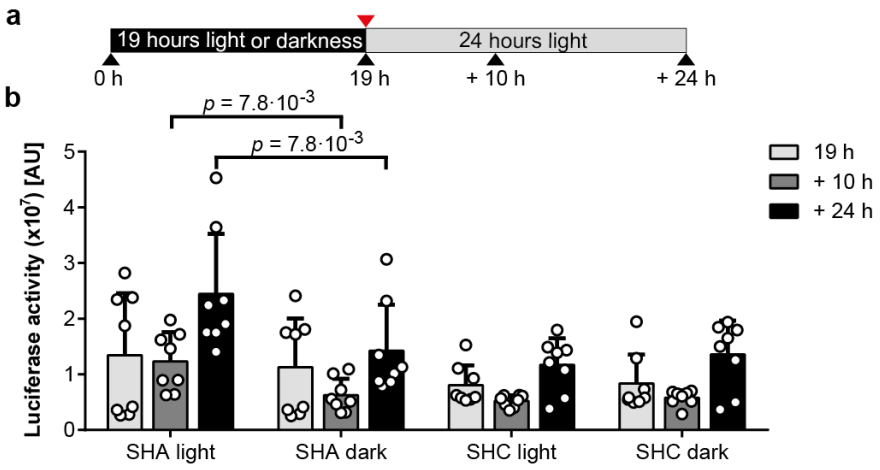

Figure 10.2: Luciferase activity is inducible. a, Illumination protocol applied in (**b**). Red arrow: time point of medium exchange, black arrows, time points of sample collection. **b**, Luciferase activity after transient transfection of the indicated *pre*-miR21 variants. A normalized variant of this dataset is shown in **Figure 4.19e**, in which values were normalized to aptamer point mutant *pre*-miR21 variant (SHC) incubated in darkness, where no light-dependency was expected. Normalization was performed to each time point. HEK293PAL cells were either incubated under conditions shown in (**a**) or constantly in darkness prior to measurement. **b**, Wilcoxon two-sided signed-rank test was used for statistical analysis as a paired observation was assumed. Experiment was performed in duplicates and four independent replicates. Values are means ± s.d.

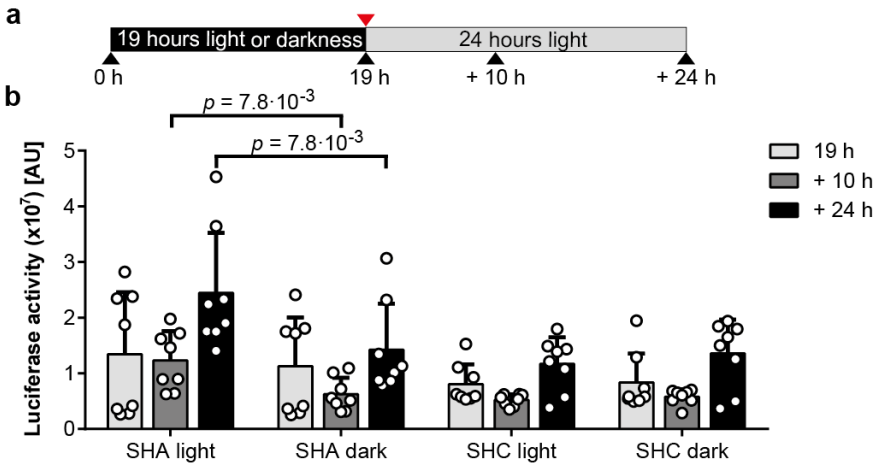

Figure 10.3: Luciferase activity is inducible. a, Illumination protocol applied in (**b**). Red arrow: time point of medium exchange, black arrows, time points of sample collection. **b**, Luciferase activity after transient transfection of the indicated *pre*-miR21 variants. A normalized variant of this dataset is shown in **Figure 4.19e**, in which values were normalized to aptamer point mutant *pre*-miR21 variant (SHC) incubated in darkness, where no light-dependency was expected. Normalization was performed to each time point. HEK293PAL cells were either incubated under conditions shown in (**a**) or constantly in darkness prior to measurement. **b**, Wilcoxon two-sided signed-rank test was used for statistical analysis as a paired observation was assumed. Experiment was performed in duplicates and four independent replicates. Values are means ± s.d.

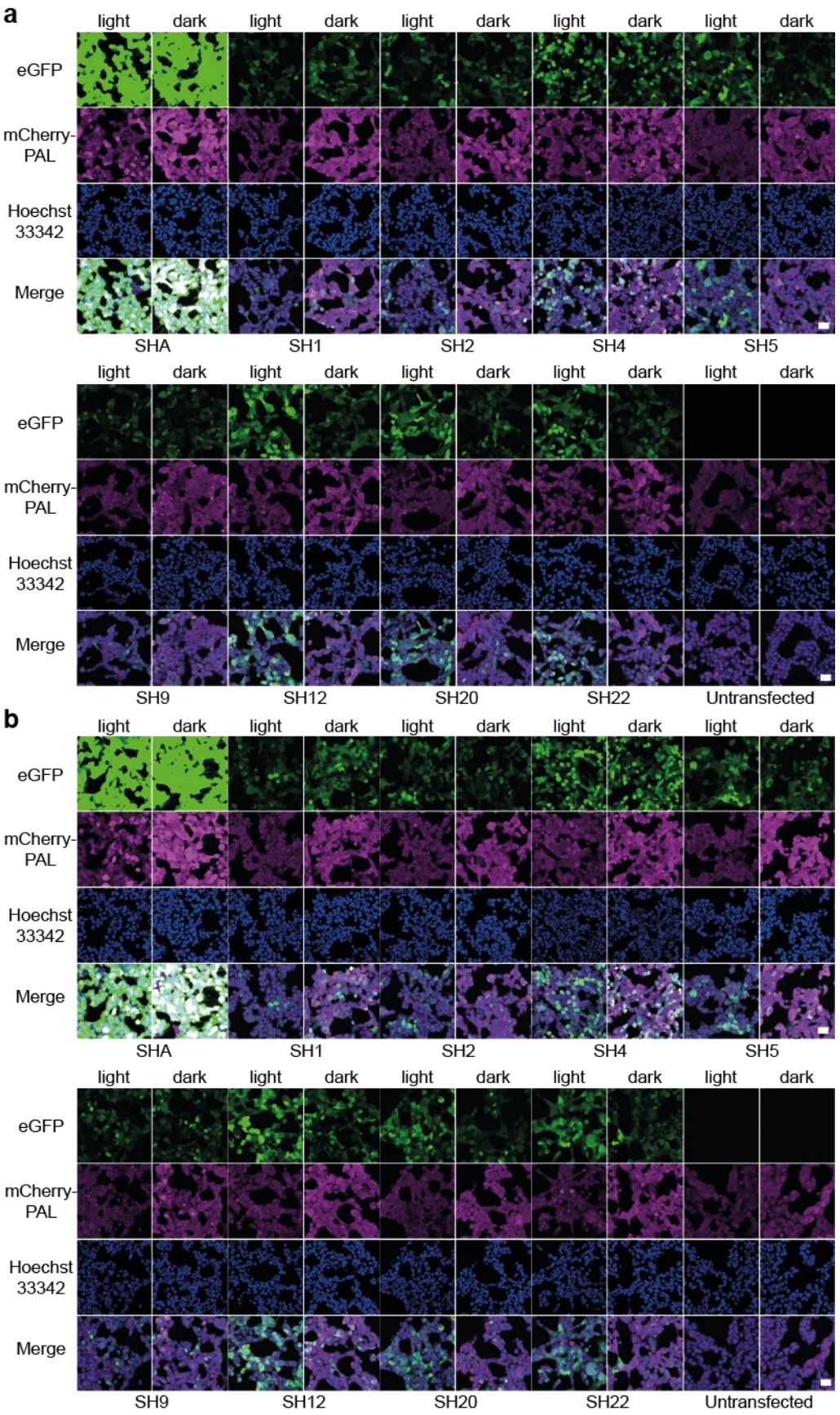
a
light
dark
eGFP
mCherry-PAL
Hoechst 33342
Merge
SHA
SH1
SH2
SH4
SH5
SH9
SH12
SH20
SH22
Untransfected
b

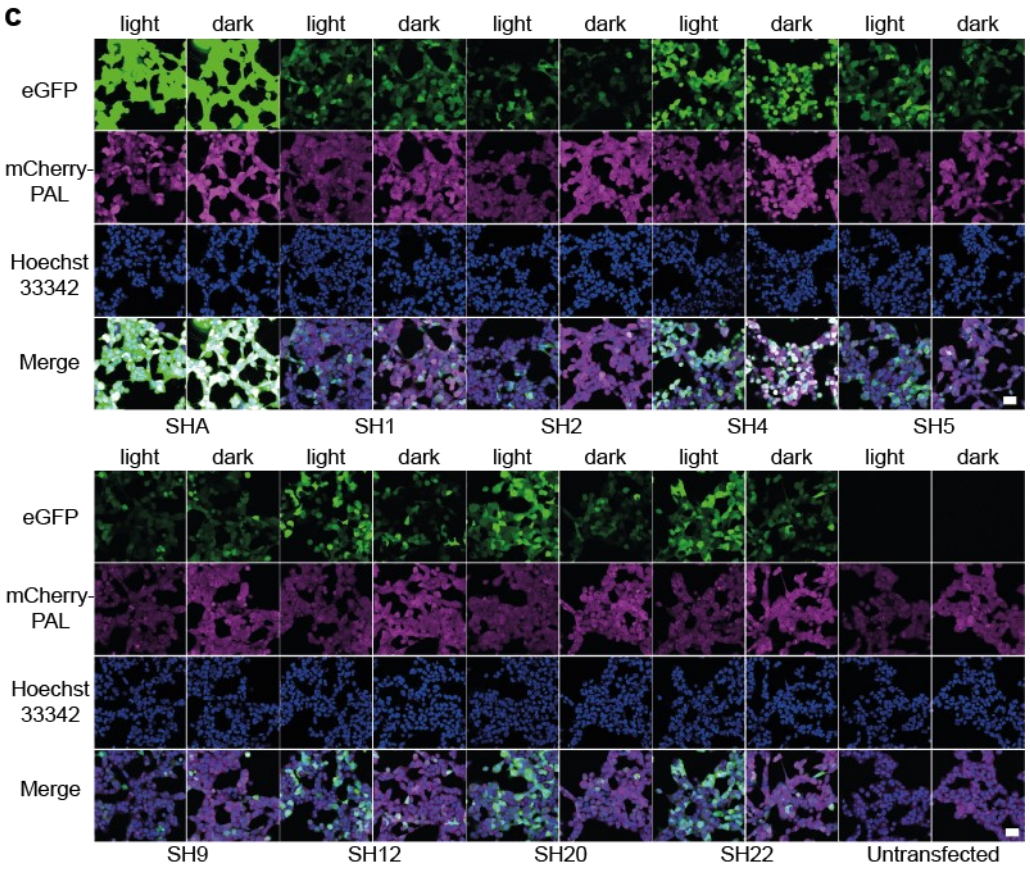

Figure 10.4: Fluorescence microscopy pictures of HEK293PAL cells transfected with eGFP shRNAs indicate light-dependent eGFP expression. Fluorescence microscopy images of HEK293PAL cells transfected with the indicated shRNAs. N = three independent experiments performed in duplicates. Cells were incubated in presence of blue light or in darkness. **a**, **b**, **c**, representatives of first, second and third repetition, respectively. Data corresponds to **Figure 4.28**, where parts of **a** are shown. Scale bar: 40 µm.

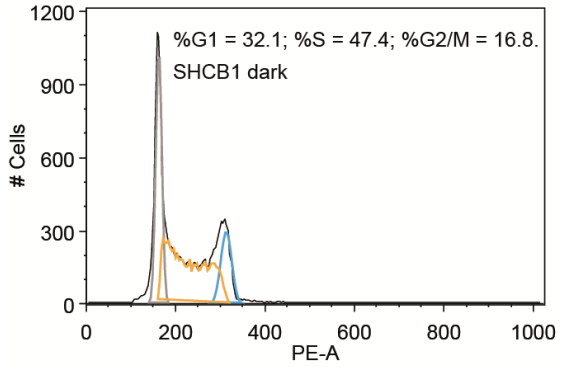
%G1 = 32.1; %S = 47.4; %G2/M = 16.8.
SHCB1 dark
Cells
PE-A

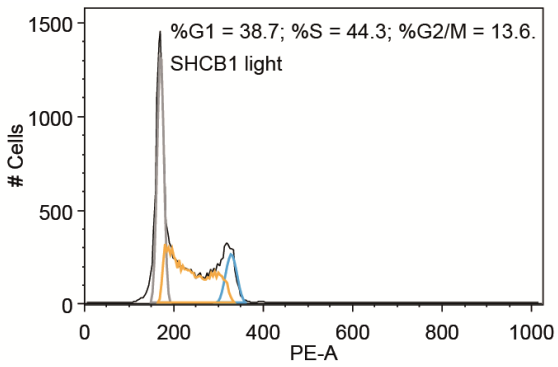
%G1 = 38.7; %S = 44.3; %G2/M = 13.6.
SHCB1 light
Cells
PE-A

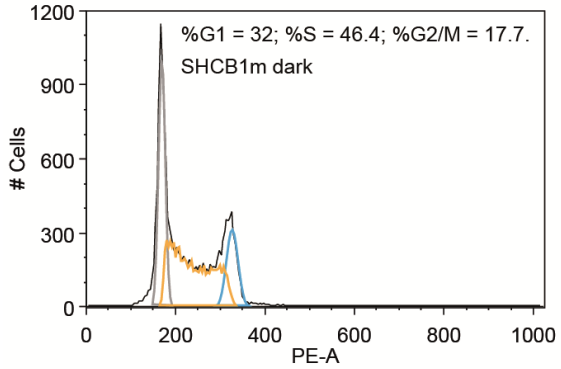
%G1 = 32; %S = 46.4; %G2/M = 17.7.
SHCB1m dark
Cells
PE-A

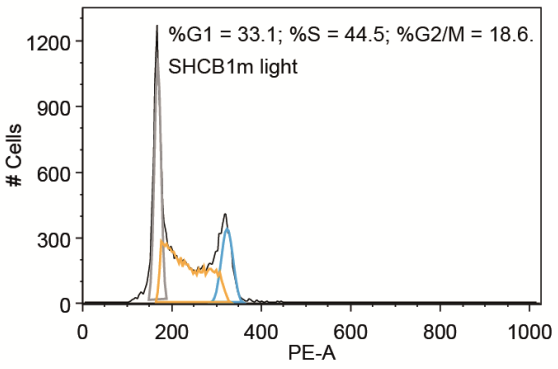
%G1 = 33.1; %S = 44.5; %G2/M = 18.6.
SHCB1m light
Cells
PE-A

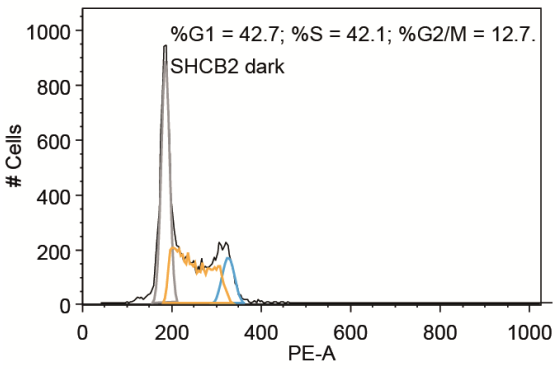
%G1 = 42.7; %S = 42.1; %G2/M = 12.7.
SHCB2 dark
Cells
PE-A

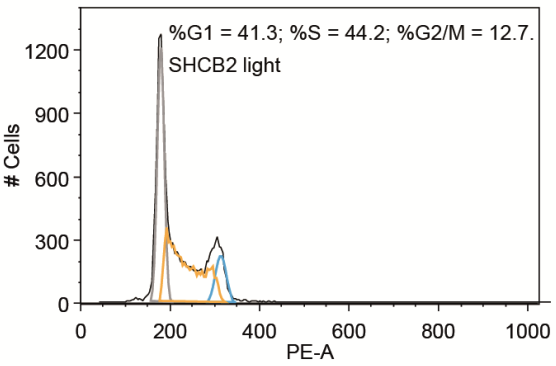
%G1 = 41.3; %S = 44.2; %G2/M = 12.7.
SHCB2 light
Cells
PE-A

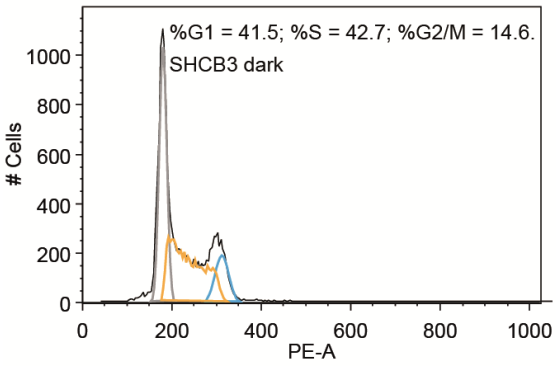
%G1 = 41.5; %S = 42.7; %G2/M = 14.6.
SHCB3 dark
Cells
PE-A

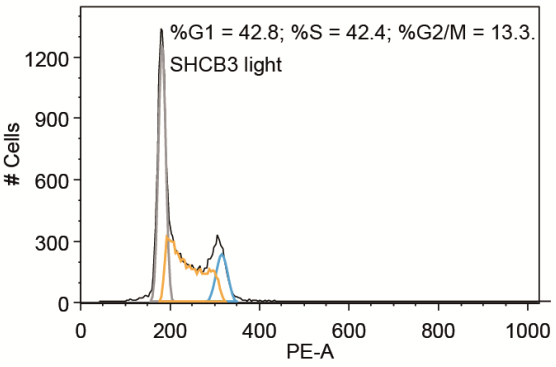
%G1 = 42.8; %S = 42.4; %G2/M = 13.3.
SHCB3 light
Cells
PE-A

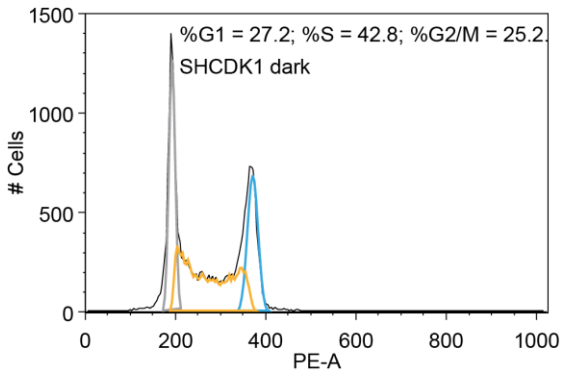
%G1 = 27.2; %S = 42.8; %G2/M = 25.2.
SHCDK1 dark
Cells
PE-A

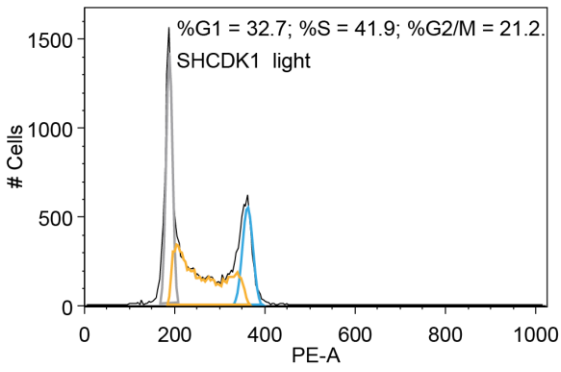
%G1 = 32.7; %S = 41.9; %G2/M = 21.2.
SHCDK1 light
Cells
PE-A

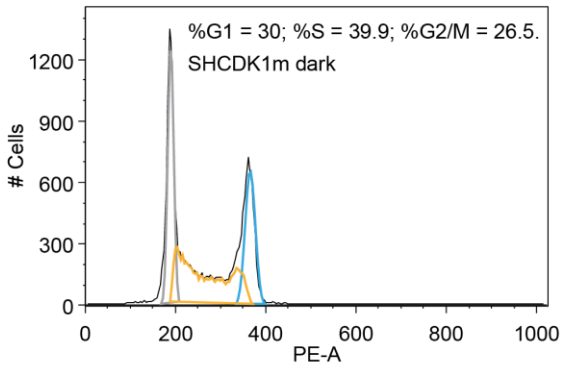
%G1 = 30; %S = 39.9; %G2/M = 26.5.
SHCDK1m dark
Cells
PE-A

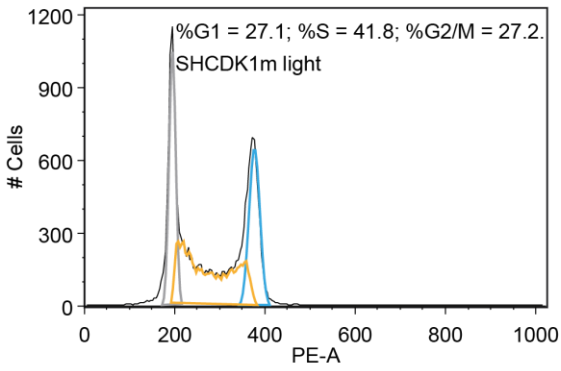
%G1 = 27.1; %S = 41.8; %G2/M = 27.2.
SHCDK1m light
Cells
PE-A

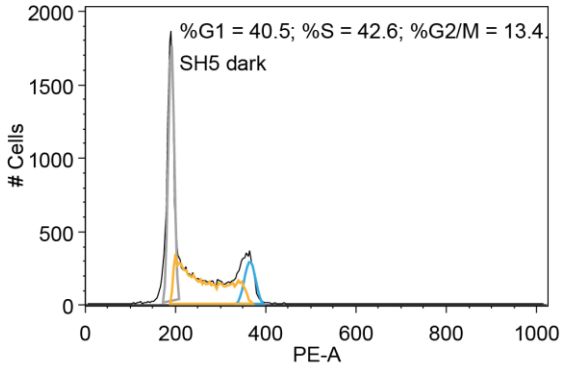
%G1 = 40.5; %S = 42.6; %G2/M = 13.4.
SH5 dark
Cells
PE-A

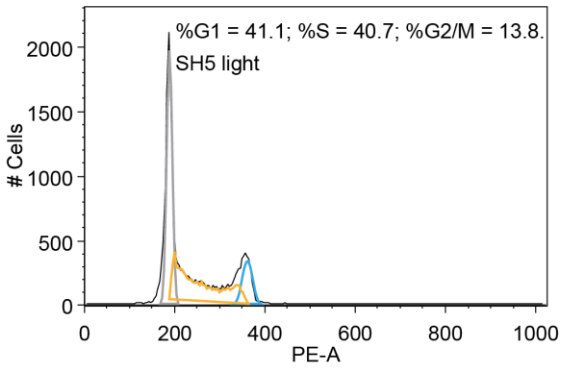
%G1 = 41.1; %S = 40.7; %G2/M = 13.8.
SH5 light
Cells
PE-A

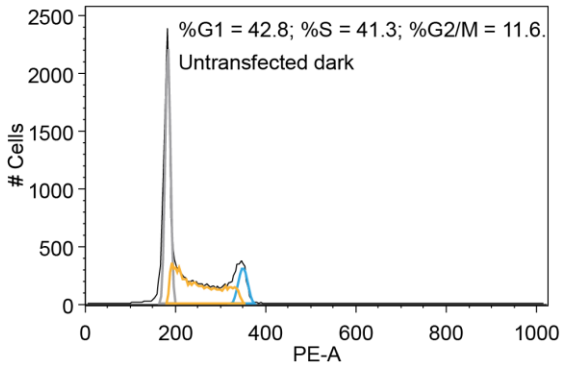
%G1 = 42.8; %S = 41.3; %G2/M = 11.6.
Untransfected dark
Cells
PE-A

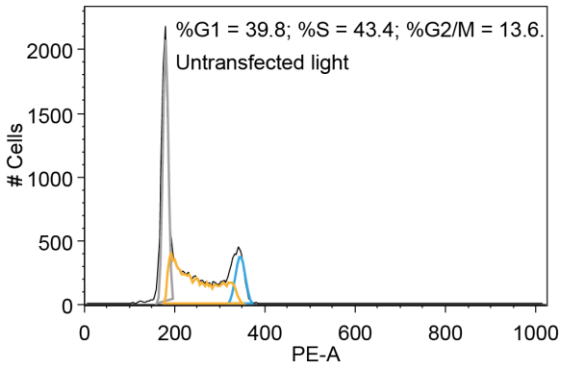
%G1 = 39.8; %S = 43.4; %G2/M = 13.6.
Untransfected light
Cells
PE-A

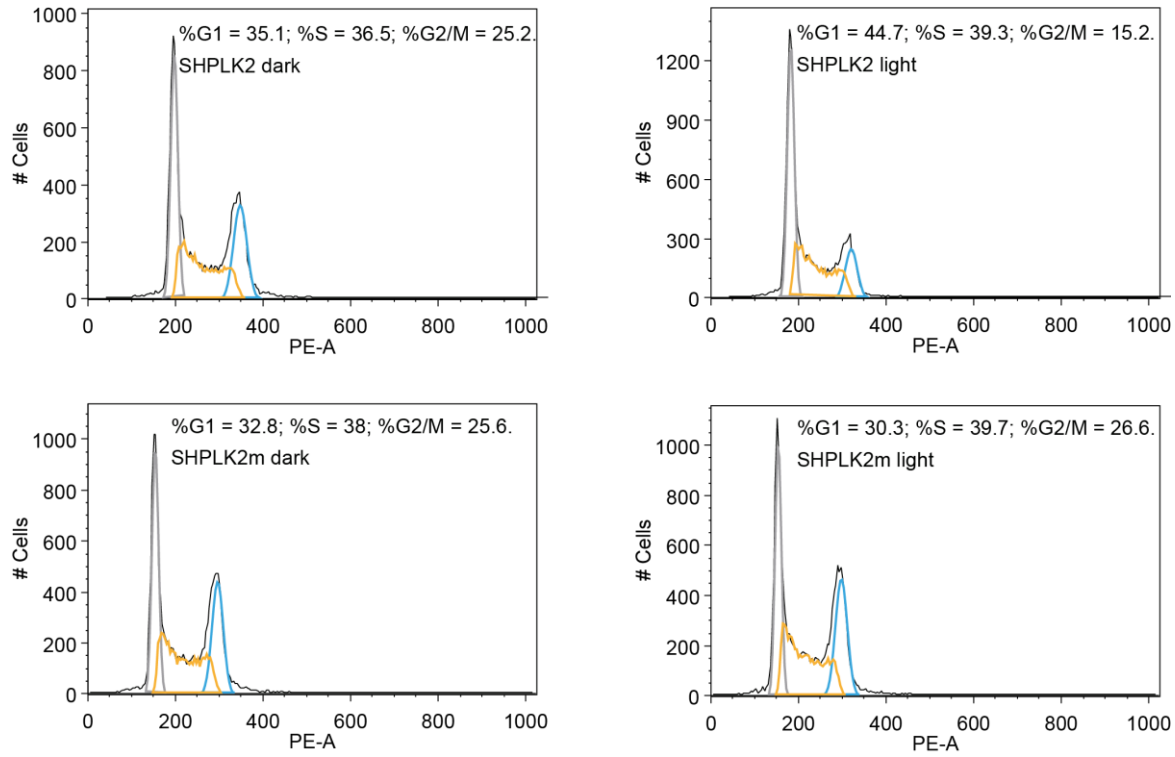

Figure 10.5: Cell cycle phase distribution is optoribogenetically controllable. Representative crude flow cytometry diagrams of HEK293PAL cells transfected with the indicated shRNA variants or non-treated. Cell cycle phase percentages were calculated using Watson pragmatic algorithm. Grey: G_1 phase, orange: S phase, blue: G_2/M phase. N = At least three independent experiments performed in duplicates.

a

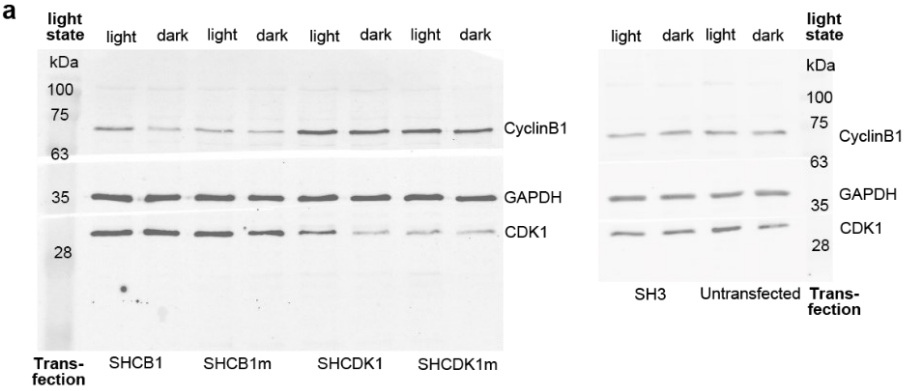
light state
light dark light dark light dark light dark
kDa
100
75
63
35
28
CyclinB1
GAPDH
CDK1
Trans-fection
SHCB1
SHCB1m
SHCDK1
SHCDK1m
light dark light dark
light state
kDa
100
75
63
35
28
CyclinB1
GAPDH
CDK1
SH3
Untransfected
Trans-fection

b

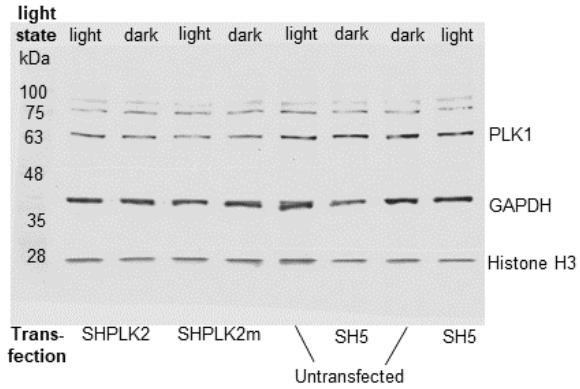
light state
light dark light dark light dark dark light
kDa
100
75
63
48
35
28
PLK1
GAPDH
Histone H3
Trans-fection
SHPLK2
SHPLK2m
SH5
SH5
Untransfected

c

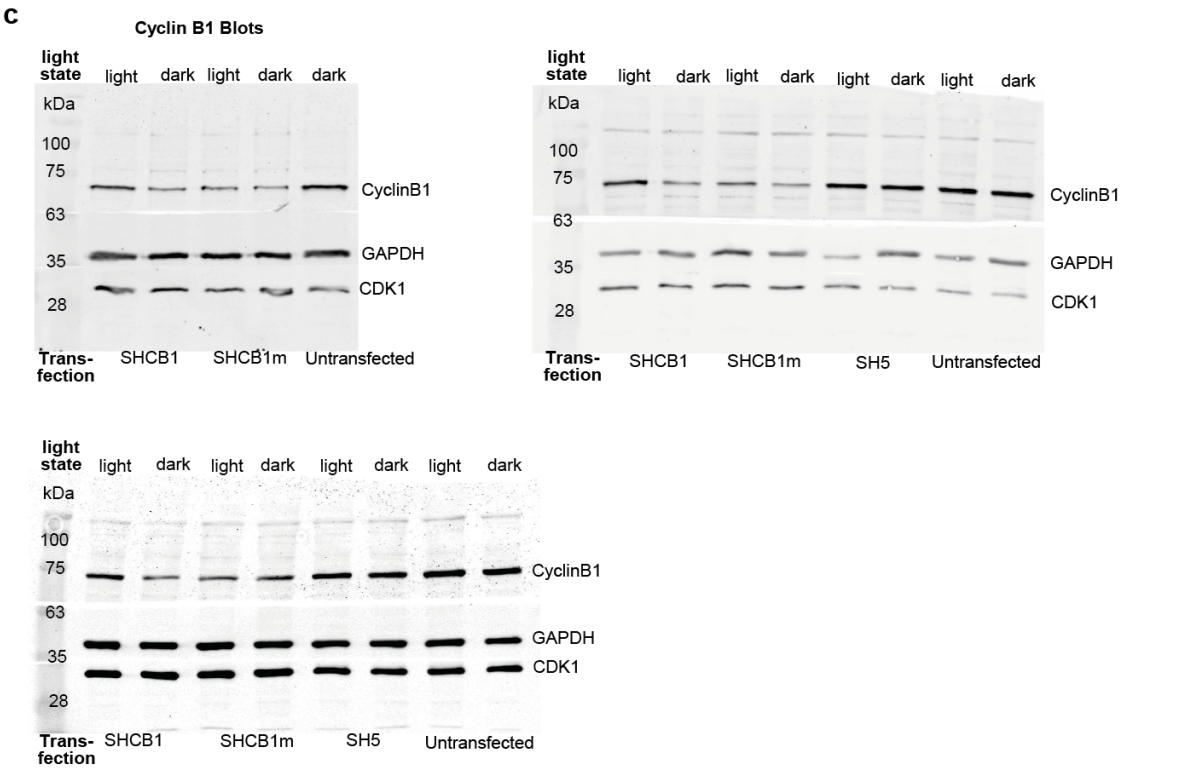
Cyclin B1 Blots
light state
light dark light dark dark
kDa
100
75
63
35
28
CyclinB1
GAPDH
CDK1
Trans-fection
SHCB1
SHCB1m
Untransfected
light state
light dark light dark light dark light dark
kDa
100
75
63
35
28
CyclinB1
GAPDH
CDK1
Trans-fection
SHCB1
SHCB1m
SH5
Untransfected
light state
light dark light dark light dark light dark
kDa
100
75
63
35
28
CyclinB1
GAPDH
CDK1
Trans-fection
SHCB1
SHCB1m
SH5
Untransfected

d

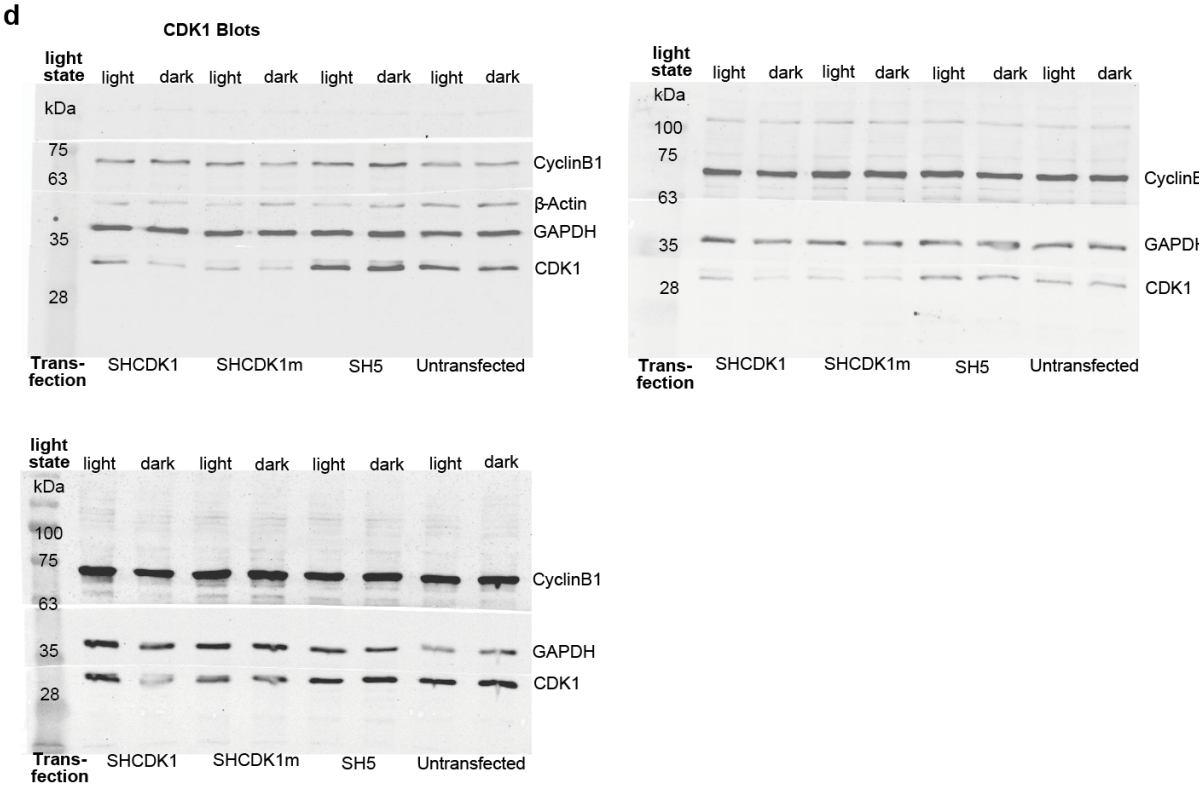
CDK1 Blots
light state
light dark light dark light dark light dark
kDa
75
63
35
28
CyclinB1
β-Actin
GAPDH
CDK1
Trans-fection
SHCDK1
SHCDK1m
SH5
Untransfected
light state
light dark light dark light dark light dark
kDa
100
75
63
35
28
CyclinB1
GAPDH
CDK1
Trans-fection
SHCDK1
SHCDK1m
SH5
Untransfected
light state
light dark light dark light dark light dark
kDa
100
75
63
35
28
CyclinB1
GAPDH
CDK1
Trans-fection
SHCDK1
SHCDK1m
SH5
Untransfected

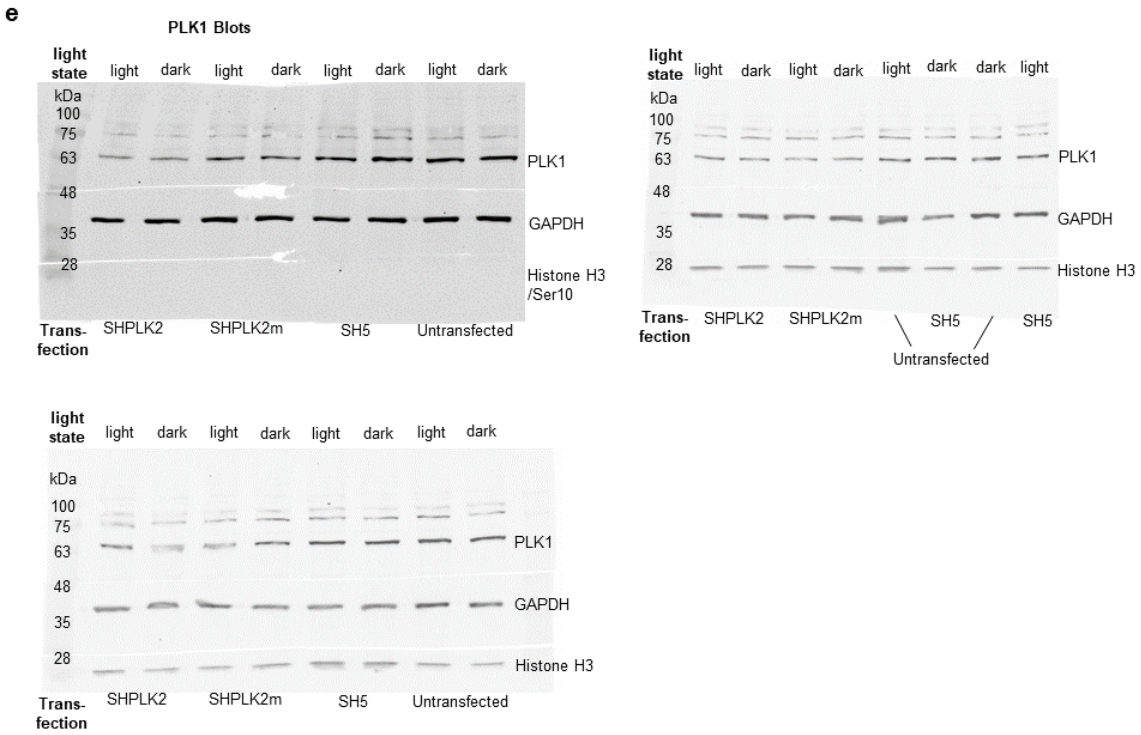

Figure 10.6: Optoribogenetic control of target protein expression. Full range Western Blots showing cyclin B1, CDK1, PLK1, GAPDH, Histone H3 and HistoneH3/Ser10 protein expression after transfection with the indicated shRNAs and incubation with the indicated light state. Parts of (**a**) were shown in **Figure 4.38a**. Parts of (**b**) were shown in **Figure 4.38b**. **c**,**d**,**e**, Western blots shown were used for quantification of cyclin B1 (**Figure 4.38c**), CDK1 (**Figure 4.38d**) and PLK1 (**Figure 4.38e**) protein levels using pixel densitometry. N = Three independent experiments.

10.3 Acknowledgements

First, I want to thank my thesis supervisor Prof. Dr. Günter Mayer, who profoundly contributed to my development as a scientist in never-ending discussions and Zoom conferences. Thank you so much!

It was a great experience to collaborate with the working group of Prof. Dr. Andreas Möglich. Thank you, Andreas, for your support and willingness to become my co-corrector.

For becoming part of my committee, I also want to thank Prof. Dr. Eva Kiermaier and Prof. Dr. Anton Bovier.

This work was funded by the SFB1926 “Next Generation Optogenetics”. Thank you for the funding and the opportunity to meet great scientists.

My gratitude also goes to the thesis proofreaders Christian Renzl, Anna Maria Weber, Anna Will and Ignazio Geraci. You did a great job!

Furthermore, I want to thank Dr. Stephanie Kath-Schorr, Dr. Florian Schmidt, Prof. Dr. Oliver Gruß, Dr. Silvana Haßel and Moujab Choukeife for the time they invested and fruitful discussions with me about my project.

Thank you, Dr. Christoph Domnick and Nikolas Hochheimer for hanging out with me frequently in the bouldering hall. That was a great time! Thank you, Dr. Mark Kerzhner, Dr. Daniel Matzner, Laura Lledo Bryant and Julia Siegl for the great “extracurricular activities” outside of the lab.

To Dr. Laia Civit, Dr. Malte Rosenthal, Dr. Franziska Ersoy, Dr. Anna Schüller, Anna Jonczyk, Tjasa Legen, Milena Mund and all members of the Mayer, Kath-Schorr and Famulok group: It is always a pleasure to meet and discuss with you.

I also want to thank Kordula Bellinghausen, Dr. Sven Freudenthal, Stefan Breuers and Sandra Ullrich for their great effort and success to keep the lab organized. Thank you, Justina Stark for keeping the buffers and the smile on stock.

Also, I want to express my gratitude to my students Charles Morgan and Léa Angèle Dugrosprez. All the best for your careers!

Thank you, dear Julia Patricia Deisinger for your mental support and your photomask gift which made it into the publication. I admire your scientific skills and personality! My biggest gratitude also goes to both of our families and my friends that helped me to keep on track.